Thermomechanical Characterization of Energy Geostructures with Emphasis on Energy Piles

THÈSE N^{O} 6452 (2014)

PRÉSENTÉE LE 28 NOVEMBRE 2014

À LA FACULTÉ DE L'ENVIRONNEMENT NATUREL, ARCHITECTURAL ET CONSTRUIT
LABORATOIRE DE MÉCANIQUE DES SOLS - CHAIRE GAZ NATUREL PETROSVIBRI
PROGRAMME DOCTORAL EN MÉCANIQUE

ÉCOLE POLYTECHNIQUE FÉDÉRALE DE LAUSANNE

POUR L'OBTENTION DU GRADE DE DOCTEUR ÈS SCIENCES

PAR

Thomas MIMOUNI

acceptée sur proposition du jury:

Prof. I. Botsis, président du jury
Prof. L. Laloui, directeur de thèse
Prof. F. Maréchal, rapporteur
Prof. J. S. McCartney, rapporteur
Prof. J.-M. Pereira, rapporteur

ÉCOLE POLYTECHNIQUE
FÉDÉRALE DE LAUSANNE

Suisse
2014

A ma mère, Annick,

A mon père, Ali,

A mon frère, Bertrand,

A ma compagne, Catherine

"A mes montagnes, reconnaissant, infiniment, pour le bien-être intérieur que ma jeunesse a retiré de leur sévère école"

(Walter Bonatti)

Acknowledgements

I first thank my Ph.D. advisor, Prof. Lyesse Laloui, for offering me the opportunity to carry out stimulating research studies in the best conditions. I also warmly thank him for his confidence and for involving me into several interesting projects in collaboration with public partners.

I would like to thank the members of my thesis jury, Prof. Ioannis Botsis and Prof. François Maréchal from Ecole Polytechnique Fédéreal de Lausanne, Prof. John S. McCartney from the University of Colorado Boulder and Prof. Jean-Michel Pereira from Ecole des Ponts ParisTech for the time they spent on my dissertation and for their pertinent comments.

I am thankful to Energie Ouest Suisse Holding for its financial support during my entire thesis, to the Swiss Federal Institute of Technology Lausanne for financing the experimental site on the campus and to the Swiss Federal Office for Energy for its financial support during field campaigns.

I would like to thank Mr. Gilbert Steinmann, head of Swiss Geo Testing Sàrl, for his close collaboration and availability either during the construction of the experimental site or for the maintenance of the heating modules. Gilbert, your expertise was much appreciated.

I thank all the persons who helped me during and after the construction of the experimental site. First, Fabrice who took care of the construction site during my absence and who actively participated to the sensor installation on the reinforcing cages of the test piles. I warmly thank Patrick, Gilbert and Laurent, as well as the apprentices Quazim, Bastien, Julien and Swann for their availability when something had to be installed or fixed on the test site during and after the site construction. Gentlemen, your help was more than necessary to hold the deadlines for the site construction and tests, thank you very much.

I particularly thank Mr. Sylvain Demierre for generously lending me the ICOM (EPFL) SOFO reading unit with which I could take measurements from the optical fibers.

I thank Mr. Samuel Vurpillot from De Cérenville Géotechnique SA for his help using the SOFO reading unit and its software.

I would like to thank Alice and Alessandro with who I had very interesting discussions about energy geostructures.

I salute my two officemates Suzanne and Valentina.

I thank the secretaries of the laboratory, Rosa Ana, Barbara and Jessica, for their help in administrative tasks.

I thank Mr. Thibaud Meney from Karakas & Français, Mr. Samuel Cooper from HRS Real Estate and Mr. Erhard Riegler from Marti Sa for their collaboration during the construction of the test site.

I thank Ms. Elena Ruffato, Mr. Ivan Cottone and Mr. Fabio Zanini from SMARTEC Sa for their expertise and consulting when designing the experimental site.

I am grateful to Dr. Sidiqui from the Swiss Federal Office of Energy, Prof. Marc Randolph from the University of Western Australia, Prof. Kenichi Soga from Cambridge University and Prof. Peter Bourne Webb from the Instituto Superior Técnico in Lisbon for the fruitful discussions we had.

I thank all my colleagues for their kind attention and discussions: Donatela, Ali, Samuel, Dimitrios, Alberto, Timur, Chao, Abdushalam, Paul, Albin, Antoine, Yafei, Sen, Roman, Samila, Alessio, John, Azad, Jérôme, Jonas.

I finally thank my family which was very supportive during my studies as well as Catherine with who I shared these last 8 years.

Abstract

Suitable developments of sustainable energy sources are drawn by analysing the Energy sector, considering environmental, economic and social aspects. The particular example of Switzerland is detailed with a focus on the energy consumption in the buildings. Based on the statistics from the Swiss Federal Office of Energy, the majority of the energy consumed by the Swiss households and in office and retail spaces is used for space conditioning as well as hot water production. However, still $3/4^{th}$ of this demand is satisfied using fossil energies (i.e. fuel oil and gas). Therefore, developing and promoting sustainable heat sources for the buildings may have a major impact on energy sustainability.

In this scope, energy geostructures represent the next generation of ground heat exchangers for ground source heat pump systems. These are more cost effective than conventional ground heat exchangers (e.g. geothermal boreholes) because they save the specific drilling operations and take advantage of the ground structures required anyway. Studies also suggest that the concrete of the geostructures may enhance the thermal contact with the ground. Turning conventional geostructures into energy geostructures is achieved by installing polyethylene absorber pipes into foundation and underground concrete structures, generally attached to the reinforcing cages. Circulating a heat carrier fluid into these tubes allows heat exchanges with the ground for heating and cooling purposes, using the natural ground temperature that is relatively fresh during hot spells and hot during cold spells. Seasonal heat storage is also possible when ground conditions are favorable. Finally, monovalent or bivalent systems are designed according to local ground conditions mainly characterized by the natural ground temperature, ground thermal properties and groundwater.

Geotechnical operational design of energy piles is discussed using Thermo-Pile software, a tool developed at the Laboratory of Soil Mechanics of the Swiss Federal Institute of Technology Lausanne (Switzerland) and based on the load-transfer method. This tool is used to investigate the evolution of energy pile bearing mechanisms under non cyclic thermal loads as well as energy pile serviceability. The importance of cyclic mechanisms for piles under conventional mechanical loads is highlighted by discussing the back analysis of the Lambeth College test pile (London, United Kingdom). Then, a thermal unloading path is proposed, implemented in Thermo-Pile and validated against the discussed case study. Next, we propose a simple mathematical framework in which we can estimate the asymptotic position of the null point (i.e. the point which does not move under thermal load) based on the pile constraints such as friction and tip compression. Group effects are then addressed by coupling Thermo-Pile software with the Euler-Bernoulli beam model. The obtained tool allows investigating piled beams with energy piles. Finally, the impact of 2 dimensional effects in load-transfer analyses is discussed. It is found that the conventional 1 dimensional analysis intrinsically postulates that radial thermal strains are free to develop whereas

the mobilizable axial thermal expansion could increase by 50 % when they are totally blocked. Therefore, we propose a method based on lateral load-transfer to account for these radial effects.

The effects of pore water pressure build under temperature variations on the bearing capacities of energy piles are investigated using thermo-hydro-mechanical finite element analyses. This phenomenon, not accounted for in the load-transfer method, could have a significant impact by reducing cyclically the effective contact stress at the pile-soil interface. The study investigates a single pile subjected to different mechanical loads selected based on the modelled load-settlement curve. Two drained cases were tested with permeabilities of 10^{-16} m^2 and 10^{-18} m^2 plus the fully drained case used as a reference. It was found that yearly temperature variations between -10 and +10 °C induce little pore water pressure variations of +/- 4 kPa for a permeability of 10^{-16} m^2 and significant variations, around +/- 40 kPa, for a permeability of 10^{-18} m^2. Therefore, the evolution of ultimate bearing capacities is driven by soil and concrete expansion for permeabilities greater or equal to 10^{-16} m^2, that is to say they increase during heating and decrease during cooling. Conversely, when these are driven by pore water pressure, which is the case for the permeability of 10^{-18} m^2, ultimate bearing capacities decrease during heating and increase during cooling. As a result, long term evolutions of the pile serviceability differ even if thermal loads are the same and uncontrolled pile settlements can be observed in soils with very low permeability. Finally, comparing design resistances estimated based on the Eurocode 7 to the analyses suggests that, except in soils with very low permeability, the current design codes remain conservative for the design of energy piles.

Heat production is investigated on shallow urban tunnels. These geostructures may represent a significant heat source because of their extension. Several solutions were experimentally tested mainly in Austria, considering thermoactive tunnel linings, geotextiles, slabs, walls and prototype self-drilling bolts. The present thesis proposes to deepen the knowledge about heat exchanger anchors as they are the least investigated. Indeed, thermoactive slabs, linings and walls were extensively used on real structures while heat exchanger anchors have only been tested in an embankment in Vienna (Austria). The investigations are carried out using thermohydraulic and thermohydromechanical finite element analyses on a cut and cover tunnel and a bored tunnel. Mechanical effects on the cut and cover tunnel are not considered because of the buffer effect of the backfill but the impact of the soil-atmosphere thermal interactions are accounted for as well as unsaturated conditions. Conversely, the bored tunnel is investigated under saturated conditions only while considering mechanical effects because of the confinement induced by the surrounding ground. The heat production cycles are of two types: the first type only considers heat production, letting the ground at thermal rest during hot spells; the second type considers seasonal heat storage. These two types of cycles were designed based on air temperature to capture a realistic building heat demand, and these are optimized by maximizing the heat extraction while not freezing the ground in between the ground anchors and bolts. It is found that seasonal heat storage is necessary on the cut and cover tunnel to maintain a sufficient heat production level while it is not efficient on the bored tunnel. Produced heat ranges from 0.6 to 4.2 GWh per kilometer of tunnel and per year.

A method based on a periodic pumping procedure, inspired from hydraulic engineering, was evaluated for the *in situ* determination of the bulk soil thermal diffusivity using a scaled model at

the laboratory scale. The evaluation was carried out in a tank filled with Bioley silt. The test consisted in periodically heating and cooling (+/-15 °C) a scaled borehole heat exchanger while recording the temperature in the ground at different distances from the heat exchanger with thermocouples. Two thermocouples were used to measure the inlet and outlet borehole temperatures. The observed delay and attenuation between the borehole temperature and the temperature in the silt are then used to retrieve the silt thermal diffusivity based on the heat conduction theory. Estimates obtained from the tests were in general agreement with values reported in the literature using different methods. However, the full-scale deployment of this technic is discussed and a sensitivity analyses is carried out to quantify the impact of the accuracy in installing the temperature sensors around the borehole heat exchanger.

Full-scale experimental investigations of the thermomechanical response of energy piles are carried out. Four 28 m long test piles were built below a water retention tank that is also supported by conventional piles. The test piles are gathered in a tank corner to allow studying group effects. Three thermomechanical response tests are analysed. The first consisted in heating the piles when no structure was built on top of them. This test provided information about the pile constraints induced by the ground (i.e. side friction and tip compression). Next, each test pile was individually tested once the tank was built. When heating one pile at a time, the evolution of top strains and tip compression were monitored on the neighbouring test piles in order to quantify the pile to pile interactions. Then, the entire group was heated in order to observe the relief of pile to pile interactions as a result of a global group expansion. Comparisons of the different thermomechanical response test are achieved in term of pile tip compression, pile top strains and degree of freedom profiles. It is found that the tank construction influences the thermomechanical response of the piles down to the stiff soil layers while their respective position below the raft impacts their responses down to 10 m. The pile to pile interactions are clearly visible on the first level of neighbouring piles (i.e. directly adjacent) and down to the pile tips. Group effects observed during the heating of the entire group doubled the degree of freedom of each test pile, inducing greater pile heaves but reducing differential settlements, therefore reducing internal thermal efforts. Individual thermomechanical response tests leaded to pile head heaves around 0.5 mm while the group test induced pile top heaves up to 1 mm for temperature variations along the pile between 6 and 10 °C. Thermal responses of the piles are also analysed. A method to account for thermal capacitive effects is proposed in order to interpret thermal response test from large diameter energy piles. This method was used to estimate the ground thermal conductivity. Finally, the thermohydraulic response of the soil is discussed based on measurements from piezometers deployed in between the test piles.

Keywords

Geotechnics, shallow geothermal energy, foundation structure, ground source heat pump, pile foundation, tunnel, anchor, geostructure, bearing capacity, group effect, long term cyclic effect, thermomechanical response, design tool, numerical analysis, full-scale experiment, scaled model

Résumé

Ce travail analyse tout d'abord le secteur énergétique dans sa globalité en considérant les aspects environnementaux, sociaux et économiques dans le but d'identifier les changements souhaitables afin d'en améliorer la durabilité. Prenant l'exemple de la Suisse, l'accent est mis sur la consommation énergétique dans les bâtiments. Les statistiques de l'Office Fédéral Suisse de l'Energie montrent que la majorité (75 %) de l'énergie consommée dans les ménages suisses ainsi que dans les espaces commerciaux et de bureau est utilisée pour le chauffage ou la climatisation des locaux ; en second plan vient la production d'eau chaude sanitaire. Toutefois, ¾ de ces demandes sont satisfaites en utilisant des énergies fossiles, c'est-à-dire du gaz ou du mazout. Dès lors, le développement et la promotion de sources de chaleur durables pour les bâtiments apparait comme une action à fort impact dans ce secteur.

Dans cette optique, les géostructures représentent la prochaine génération d'échangeur de chaleur avec le sol pour les pompes à chaleur géothermiques. Leur installation est plus économique que celle des échangeurs de chaleur conventionnels comme les sondes géothermiques car elles ne requièrent pas d'opération de forage dédiée et profitent de la construction de structures nécessaires. Des études montrent de plus que le béton des géostructure améliore le contact thermique entre les tubes échangeurs et le sol. Les tubes échangeurs en polyéthylène sont généralement attachés aux cages d'armature des géostructures avant la coulée du béton. La circulation d'un fluide caloporteur, généralement de l'eau glycolée, permet les échanges de chaleur avec le sol pour tirer avantage des températures relativement fraiches durant l'été et chaudes durant l'hiver. Le stockage saisonnier de chaleur est aussi possible quand les conditions du sous-sol sont favorables.

Le dimensionnement géotechnique opérationnel des géostructures énergétiques est illustré en utilisant le logiciel Thermo-Pile développé au Laboratoire de Mécanique des Sols de l'Ecole Polytechnique Fédérale de Lausanne (Suisse). Cet outil, basé sur la méthode de transfert de charge, est utilisé pour étudier l'évolution des capacités portantes mobilisées par un pieu sous chargement thermique non cyclique. L'importance des mécanismes cycliques sous chargement mécanique conventionnel est mise en avant en discutant la rétro-analyse du pieu test du Lambeth College à Londres (Royaume-Uni). Un mécanisme de déchargement thermique est alors proposé, implémenté dans Thermo-Pile et validé contre le test discuté. Ensuite, la position asymptotique du point nul est exprimée en termes de friction et compression ultimes ainsi que chargement du pieu. Les effets de groupe sont abordés en couplant le logiciel Thermo-Pile au modèle de poutre de Euler-Bernoulli afin d'étudier des longrines sur pieux comprenant un pieu échangeur de chaleur. Enfin, l'impact des effets bidimensionnels sur les analyses de transfert de charge sont discutés. Il est conclu que l'approche unidimensionnelle postule intrinsèquement que les dilatations thermiques radiales sont libres de se développer alors que leur blocage entrainerait une augmentation du coefficient de

dilatation thermique axial de près de 50 %. Une méthode pour prendre en compte ces effets est alors proposée sur la base du transfert de charge latéral utilisant les courbes *p-y*.

L'impact des variations de pression d'eau dans les pores du sol sur les capacités portantes des pieux est étudié grâce à des analyses aux éléments finis thermohydromécaniques. Ce phénomène, non pris en compte par la méthode des transferts de charge, pourrait avoir un impact significatif en réduisant de manière cyclique la contrainte effective de contact entre le sol et le pieu. Cette étude s'intéresse à un pieu isolé soumis à différentes charges mécaniques sélectionnées selon la courbe de chargement-tassement simulée. Deux différentes perméabilités du sol sont testées : 10^{-16} m^2 and 10^{-18} m^2 ainsi que la condition totalement drainée qui sert de référence. Il a été observé que, pour des variations cycliques annuelles de température entre -10 et +10 °C, la perméabilité de 10^{-16} m^2 entraine des variations de pression d'environ 4 kPa à l'interface sol-pieu alors que la perméabilité de 10^{-18} m^2 entraine des variations de 40 kPa. Toutefois, les variations de pression d'eau observées jusqu'à une perméabilité de 10^{-16} m^2 ont une faible influence sur les capacités portantes du pieu. Elles sont alors dictées par les dilatations thermiques du pieu et du sol et ainsi, la capacité ultime en friction augmente lors de l'échauffement du pieu et diminue lors de son refroidissement. Par contre, on observe l'évolution inverse lorsque les variations de pressions d'eau sont plus importantes. Effet, l'échauffement du pieu et de l'eau dans son pourtour entraine une réduction de la contrainte effective normale à la paroi du pieu, réduisant ainsi la friction ultime mobilisable. C'est alors que l'on peut observer des tassements incontrôlés lors de l'échauffement du pieu. La comparaison des analyses et des résistances estimées à partir de l'Eurocode 7 suggère que les règles de dimensionnement restent conservatives quand elles sont appliquées aux pieux échangeurs, mis à part les sols de perméabilité très faible.

La production de chaleur via des tunnels urbains est aussi étudiée. Ce type de géostructure pourrait représenter une source de chaleur significative de par leur extension. Plusieurs solutions ont été testées expérimentalement, surtout en Autriche, dont des corps de tunnels thermoactifs, des géotextiles équipés de tubes échangeurs, des radiers et murs thermoactifs et des prototypes d'ancrages échangeurs de chaleur. La présente thèse propose d'étudier l'efficacité énergétiques et la réponse thermomécanique de tels ancrages. En effet, les murs, corps de tunnels et radier thermoactifs ont bénéficié d'un intérêt important et de nombreux sites expérimentaux grandeur réelle ont vu le jour, principalement en Autriche et particulièrement à Vienne, tandis que des prototypes d'ancrages échangeurs de chaleur n'ont été testés que sur un talus. L'étude a été menée en utilisant des analyses aux éléments finis thermohydrauliques et thermohydromécaniques d'une tranchée couverte et d'un tunnel foré. Les implications mécaniques de la production de chaleur ont été négligées pour la tranchée couverte à cause de l'effet tampon du remblai alors que les interactions thermiques ainsi que des conditions insaturées ont été considérées. En revanche, le tunnel foré a été considéré suffisamment profond pour négliger l'influence thermique de la surface sur sol mais les implications mécaniques de la production de chaleur ont été estimées à cause du confinement plus important de la structure. Deux types de cycles de production de chaleur sont étudiés : le premier considère uniquement la production de chaud et le sol est au repos durant les périodes chaudes tandis que le second considère le stockage saisonnier. Ces deux types de cycles sont basés sur l'évolution de la température de l'air afin de représenter au mieux une demande réelle et l'optimisation de la production de chaleur se fait en maximisant la chaleur extraite tout en ne

gelant pas le sol entre les ancrages. Il est montré que le stockage saisonnier est nécessaire pour assurer une production durable sur la tranchée couverte alors qu'il n'est pas efficace pour le tunnel foré. L'énergie extraite via les ancrages varie de 0.6 à 4.2 GWh par an et par kilomètre de tunnel.

Une méthode basée sur une procédure de pompage périodique, inspirée d'un test de pompage cyclique, a été évaluée sur un modèle réduit pour la détermination *in situ* de la diffusivité thermique du sol. Le test a été conduit dans un conteneur remplit de limon Bioley. L'expérience consistait à chauffer et refroidir périodiquement (+/-15 °C) un modèle réduit de sonde géothermique et à enregistrer l'évolution de la température à différentes distances de celui-ci. Deux thermocouples ont aussi été utilisés pour mesurer les températures d'entrée et de sortie de la sonde. Le délai et l'atténuation observés entre les variations de température dans la sonde et celles mesurées dans l'échantillon sont utilisées pour estimer la diffusivité thermique du limon Bioley. Nos estimations sont en accord avec les valeurs reportées dans la littérature et basées sur d'autres méthodes. Toutefois, le déploiement à l'échelle réelle d'un tel test est discuté et la sensibilité des estimations par rapport à la position des mesures dans le sol est étudiée.

La réponse thermomécanique d'un groupe de pieux échangeurs a été étudiée sur un site expérimental grandeur nature. Quatre pieux tests longs de 28 m ont été construits sous un bassin de rétention qui est aussi supporté par des pieux conventionnels. Les pieux tests sont regroupés au coin nord-ouest du bassin de rétention afin d'étudier les effets de groupe entre eux. Trois tests de réponse thermomécanique ont été menés. Le premier caractérise les contraintes appliquées par le sol sur les pieux tests (friction et compression), lorsqu'aucune structure n'est construite par-dessus les pieux. Ensuite, la réponse thermomécanique de chacun des pieux tests a été évaluée une fois le bassin de rétention construit. De plus, lorsqu'un pieu test était chauffé, les déformations en tête et les compressions en pointe des pieux adjacents ont été mesurées afin de quantifier les interactions pieu-pieu. Puis, le groupe entier a été chauffé afin d'observer l'évolution des interactions pieu-pieu. Les comparaisons des différents tests sont discutées en termes de déformations en tête, compression en pointe et profils de degré de liberté. Il a été observé que la construction du bassin de rétention influence la réponse thermomécanique des pieux jusqu'aux couches dures du sol alors que la position des pieux sous le radier impacte uniquement les dix premiers mètres des pieux à partir de la tête. Les interactions pieu-pieu sont visibles tout au long des pieux directement adjacents, de la tête à la pointe. Le chauffage du groupe entier de pieux tests a pour effet de doubler le degré de liberté des pieux, induisant des soulèvements de pieux plus importants mais réduisant les soulèvements différentiels ainsi que les efforts thermiques internes. Le chauffage individuel de chacun des pieux a conduit à des soulèvements de l'ordre de 0.5 mm tandis que le chauffage du groupe de pieux a entrainé des soulèvements d'environ 1 mm, cela pour des variations de températures entre +6 et +10 C. La réponse thermique des pieux a aussi été analysée. Une méthode pour tenir compte des effets capacitifs est proposée afin d'interpréter correctement les tests de réponse thermique sur des pieux de large diamètre. Cette méthode a été utilisée pour estimer la conductivité thermique du sol. Enfin, la réponse thermohydraulique du sol est discutée en s'appuyant sur des mesures piézométriques entre les pieux tests.

Mots-clés

Géotechnique, géothermie de surface, ouvrage de soutènement, pompe à chaleur géothermique, pieu de fondation, tunnel, ancrage, géostructure, capacités portantes, effet de groupe, effet cyclique au long terme, réponse thermomécanique, outils de dimensionnement, analyse numérique, expérience grandeur nature, modèle réduit

Content

List of Figures

List of Tables

List of Equations

List of symbols

Greek symbols

$\alpha^T_{\mu w}$	Rate of increase in water viscosity with temperature	(Pa·s)/K
β_{Lode}	Lode angle	Deg.
β^T_{ax}	Maximum mobilizable axial thermal expansion coefficient	K^{-1}
β^T_c	Concrete linear thermal expansion coefficient	K^{-1}
β^T_L	Porous media linear thermal expansion coefficient	K^{-1}
β^T_{mob}	Mobilised thermal expansion coefficient	K^{-1}
β^T_{rad}	Maximum mobilizable radial thermal expansion coefficient	K^{-1}
β^T_w	Water thermal expansion coefficient	K^{-1}
β^T_{wire}	Vibrating wire thermal expansion coefficient	K^{-1}
γ	Euler constant (= 0.5772)	-
γ_t	Partial factor of safety for the total pile resistance	-
δ	Interface friction angle	Deg.
δ_{ij}	Kronecker delta	-
δ_{TT}	Signal attenuation	-
ε	Strain	-
$\boldsymbol{\varepsilon}$	Total strain tensor	-
ε_{ax}	Axial strain	-
$\varepsilon_{ax,blo}$	Blocked axial thermal strain	-
$\varepsilon_{ax,free}$	Free axial thermal strain	-
$\varepsilon_{ax,obs}$	Observed axial thermal strain	-
$\boldsymbol{\varepsilon^p}$	Plastic strain tensor	-
ε_{rad}	Radial strain	-
$\varepsilon_{rad,blo}$	Blocked radial thermal strain	-
$\varepsilon_{rad,free}$	Free radial thermal strain	-
$\varepsilon_{rad,obs}$	Observed radial thermal strain	-
η_e	Efficiency of heat extraction from the ground	-
η_{fill}	Efficiency of the complementary energy source	-
η_i	Efficiency of heat injection into the ground	-
η_{inj}	Efficiency of seasonal heat storage	-
η_P	Efficiency of pumps	-
θ	Soil temperature anomaly	K
θ_i	Temperature at the GHE-soil interface	K
θ_0	Amplitude of the heat source temperature variations	K
θ_r	Radial dependence of temperature anomaly	K
λ	Thermal conductivity	W/(m·K)
$\boldsymbol{\lambda}$	Thermal conductivity tensor	W/(m·K)
λ_a	Air thermal conductivity	W/(m·K)
λ_c	Concrete/grouting material thermal conductivity	W/(m·K)
λ_{eff}	Soil-pile effective thermal conductivity	W/(m·K)
λ_p	Pipe wall thermal conductivity	W/(m·K)
λ_s	Soil grains thermal conductivity	W/(m·K)
λ_w	Water thermal conductivity	W/(m·K)
μ_w	Water viscosity	Pa·s

μ_{w0}	Reference water viscosity	Pa·s
ν	Poisson's ratio	-
ξ_1, ξ_2	Correlation factors	-
ξ_c	Fitting parameter	-
π	Pi	Rad.
Π	Air entry value	Pa
ρ	Density	kg/m^3
ρ_a	Air density	kg/m^3
ρ_c	Concrete density	kg/m^3
ρ_f	Heat-carrier fluid density	kg/m^3
ρ_g	Grout density	kg/m^3
ρ_s	Soil grains density	kg/m^3
ρ_w	Water density	kg/m^3
ρ_w	Water density	kg/m^3
ρ_{w0}	Reference water density	kg/m^3
ς	Characteristic length for heat diffusion under periodic regime	m^{-1}
σ	Stress	Pa
$\boldsymbol{\sigma}$	Total stress tensor	Pa
$\boldsymbol{\sigma'}$	Effective stress tensor	Pa
σ_{ax}	Axial stress	Pa
$\sigma_{ax,th}$	Axial thermal stress	Pa
σ_c	Concrete compressive strength after 28 days of curing	Pa
$\sigma_{c,g}$	Grout compressive strength after 28 days of curing	Pa
σ'_h	Effective horizontal stress	Pa
σ_{rad}	Radial stress	Pa
$\sigma_{rad,th}$	Radial thermal stress	Pa
σ'_v	Vertical effective stress	Pa
τ	Heat source signal period	s
τ_0	Dimensionless time for heat conduction	-
υ_w	Wire linear density	kg/m
φ_{TT}	Phase shift	Cycle
χ_w	Water compressibility coefficient	Pa^{-1}
ω	Heat source signal pulsation	s^{-1}
ϕ'	Internal effective friction angle	Deg.

Roman symbols

a	Pile to pile distances	m
a_λ	Slope of the temperature-ln(time) regression	K or °C
A_{wire}	Wire cross section	m^2
b	Pile to pile distances	m
$\boldsymbol{b}$	Body force vector	Pa/m
b_λ	Y-intercept of the temperature-ln(time) regression	K or °C
c	Specific heat capacity	J/K/kg
c'	Effective cohesion	Pa
c_a	Air specific heat capacity	J/K/kg
c_c	Concrete specific heat capacity	J/K/kg
c_f	Heat-carrier fluid specific heat capacity	J/K/kg
c_s	Soil grains specific heat capacity	J/K/kg
c_w	Water specific heat capacity	J/K/kg

C_1, C_2, C_3, C_4	Integration constants	-
C_{GHE}	GHE total heat capacity	J/K
C_{pump}	Proportionality factor linking E_i to H_i	-
C_{soil}	Soil heat capacity	J/K/m^3
D	Pile diameter	M
D_T	Soil thermal diffusivity	m^2/s
$D_{T,\delta}$	Estimated thermal diffusivity based on attenuation	m^2/s
$D_{T,\varphi}$	Estimated thermal diffusivity based on phase shift	m^2/s
$\boldsymbol{E}$	Elastic tensor	Pa
E_b	Beam Young's modulus	Pa
E_c	Concrete Young's modulus	Pa
E_f	Total energy consumed by the GSHP system	kWh
E_g	Grout Young's modulus	Pa
E_{hp}	Energy consumed by a heat pump	kWh
E_i	Pumping system consumption when the heat pump is bypassed	kWh
E_M	Menard pressuremeter coefficient	Pa
E_{wire}	Wire Young's modulus	Pa
f	Failure surface	Pa
f_{wire}	Wire tension	
$f_{wire,mech}$	Vibrating wire tension due to mechanical processes	N
$f_{wire,obs}$	Observed vibrating wire tension	N
$f_{wire,th}$	Vibrating wire tension due to thermal effects	N
F	Resonant frequency of a vibrating wire	Hz
F_0	Reference vibrating wire frequencies	Hz
F_1	Actual vibrating wire frequencies	Hz
g	Gravity	m/s^2
h_i	Heat transfer coefficient in the absorber pipes	W/(K·m^2)
h_w	Suction	Pa
H	GHE length	m
H_e	Heat amount extracted from the ground through GHEs	kWh or kWh/y/ml
H_f	Energy outcome from a heat pump	kWh
H_i	Heat amount injected into the ground through GHEs	kWh or kWh/y/ml
$\boldsymbol{I}$	Identity matrix	-
I_{Gz}	Beam quadratic moment	m^4
j	Imaginary unit	-
k_σ	Earth pressure coefficient	-
$k_{r,w}$	Relative water permeability	-
k_w	Intrinsic water permeability	m^2
K	Gauge factor	Hz^{-2}
K_b	Load-transfer elastic slope for pile tip compression	Pa/m
K_h	Pile head stiffness	Pa/m
K_s	Load-transfer elastic slope for pile shaft friction	Pa/m
l_k	kth soil layer thickness	m
l_{OF}	Optical fiber length	m
l_{RC}	Reinforcing cage perimeter	m
L	Pile length	m
$\boldsymbol{L}$	Displacement vector gradient	-

L_b	Beam length	m
L_{wire}	Wire length	m
m	Van Genuchten model parameter	-
M_{fz}	Beam bending moment	N·m
n	Porosity	m^3/m^3
N	Number of absorber pipes in a ground heat exchanger	-
N_c	Number of thermal cycles	-
N_r	Ratio between the source-sensor distance and heat source radius	-
p	Pile perimeter	m
p_a	Air pressure	Pa
p_w	Pore water pressure	Pa
p_{w0}	Reference water pressure	Pa
p_y	Horizontal soil reaction	N
P	Pile mechanical load	N
P_{elec}	Electricity price	cts/kWh
P_{eq}	Equivalent price of energy using complementary heat sources	cts/kWh
P_{fill}	Price of the complementary energy	cts/kWh
P_h	Brut price of the produced heat with a GSHP	cts/kWh
P_L	Left isothermal pile total load	N
P_P	Energy pile total load	N
P_R	Right isothermal pile total load	N
P_{T0}	Linear heat rate along anchors	W/m
q	Linear heat rate along ground heat exchanger	W/m
q_b	Pile tip compression bearing capacity	Pa
q_c	Linear heat rate along GHEs	W/m
$\boldsymbol{q_T}$	Heat flux	W/m^2
q_s	Pile friction bearing capacity	Pa
$\boldsymbol{q_w}$	Pore water macroscopic velocity	m/s
Q_{abs}	Absorber heat flux to increase GHE temperature	W
$Q_{b,ult}$	Bearing resistance in compression	N
$Q_{b,mob}$	Mobilised base force	N
Q_h	Total pile mechanical load	N
Q_{mth}	Pile total mobilised bearing force under thermal and mechanical loads	N
Q_{th}	Heating power injected into a GHE	W
Q_T	Volumetric heat source or sink	W/m^3
$Q_{s,mob}$	Mobilised shaft force	N
$Q_{s,mob,low}$	Mobilised bearing force through friction below the null point	N
$Q_{s,mob,up}$	Mobilised bearing force through friction above the null point	N
$Q_{s,ult}$	Bearing resistance in friction	N
Q_{ult}	Pile total bearing capacity	N
r	Radial coordination	m
r_b	Borehole heat exchanger radius	m
r_i	GHE radius	m
r_{int}	Inner absorber pipe radius	m
r_{out}	Outer absorber pipe radius	m
R	Radial distance at which far field condition is applied	m
R_1	Pile top force developed during pile-structure interactions	N
R_b	Thermal resistance	K/(W/m)

R_c	Thermal resistance linked to concrete/grouting material	K/(W/m)
$R_{c,d}$	Pile design resistance	N
$R_{c,k}$	Characteristic pile ultimate compressive resistance	N
$R_{c,m}$	Characteristic pile representative compressive resistance	N
R_L	Left isothermal piles action on the beam	N
R_P	Energy pile action on the beam	N
R_{Pile}	Pile radius	m
R_{pconv}	Thermal resistance linked to convection in absorber pipes	K/(W/m)
R_{pcond}	Thermal resistance linked to pipe wall conduction	K/(W/m)
R_R	Right isothermal piles action on the beam	N
R_{RC}	Reinforcing cage radius	m
s	Pile settlement	m
S_c	Shape factor	-
S_{inf}	Pile asymptotic settlement	m
S_{mech}	Pile settlement under mechanical load	m
S_T	System enthalpy	J
S_w	Soil degree of saturation	-
$S_{w,max}$	Maximum degree of saturation	-
$S_{w,res}$	Residual degree of saturation	-
t	Time	s
t_b	Mobilized pile tip compression	Pa
t_s	Mobilized shaft friction	Pa
$t_{s,mob,static}$	Mobilised shaft friction under mechanical load only	Pa
T	Temperature	K
T_0	Reference temperature	K
T_1	Actual vibrating wire temperature	K
T_f	Mean heat-carrier fluid temperature	K
T_{in}	Heat-carrier fluid temperature at the GHE inlet	K or °C
T_{out}	Heat-carrier fluid temperature at the GHE outlet	K or °C
T_s	Ground temperature	K
$\boldsymbol{u}$	Displacement vector	m
v_L	Left isothermal pile top displacement	m
v_P	Energy pile top thermal displacement	m
v_R	Right isothermal pile top displacement	m
V_c	Concrete volume in a GHE	m^3
V_f	Heat-carrier fluid volume in a GHE	m^3
X	Beam axis coordinate	m
X_{DT}	Variable used to invert the thermal diffusivity interference analyses	-
y	Horizontal soil-pile interface displacement	m
z	Vertical coordinate, depth	m
z_h	Pile top thermal displacement	m
z_{NP}	Null point depth	m

Abbreviations

ACMEG-T	Advanced Constitutive Model for Environmental Geomechanics – Thermal effect
BP	Bâtiment Polyvalent
Ce	Heat production cycle with only heat extraction
Cei	Heat production cycle with seasonal heat storage
Cei,e	Cei cycle starting with heat extraction

Cei,i	Cei cycle starting with heat injection
CFA pile	Continuous Flight Auger pile
CoP	Coefficient of Performance
CSTB	Centre Scientifique et Technique du Bâtiment
EPFL	Ecole Polytechnique Fédérale de Lausanne
FoS	Factor of Safety
GHE	Ground Heat Exchanger
GSHP	Ground Source Heat Pump
HP	Heat Pump
NP soil	Impervious soil
PW	Piezometer
SFP	Seasonal Factor of Performance
SP soil	Slightly permeable soil
TH	Thermohydraulic
THM	Thermohydromechanical
TPC	Total Pressure Cell
TRT	Thermal response test
UTES	Underground Thermal Energy Storage
VW(SG)	Vibrating Wire (Strain Gauge)

Operators/functions

$'$, $''$	First and second derivatives
∂	Partial derivative
∇	Gradient
Δ	Variation
Σ	Sum
cos()	Cosine function
d	Small variation
div()	Divergence
exp()	Exponential function
grad()	Gradient
sin()	Sine function
tan()	Tangent function
tr()	Matrix trace
I_0, K_0	Modified Bessel functions of 0^{th} order
I_1, K_1	Modified Bessel functions of 1^{st} order
Re{}	Real part

Introduction

The heating and cooling of buildings represent a significant part of energy consumption in developed and developing countries. Still, almost 3/4th of this demand is satisfied using fuel oil and gas. Therefore, alternative heat sources are being developed in order to reduce the majoritarian part occupied by fossil fuels. On one hand, district heating permits an opportunity to take advantage of heat sources that require a large scale such as biomass. On another hand, decentralized systems using heat pumps are more and more in use. The most effective, from a thermal standpoint, is the ground source heat pump because of the relatively high temperature levels found in the ground, but installing deep ground heat exchangers (down to a few hundred meters) remains relatively expensive. Therefore, embedding ground heat exchangers into geostructures (i.e. deep foundations or underground structures) would supplement the conventional geothermal systems while reducing the costs by minimizing the earthwork. However, adding the thermal part to the mechanical role that foundations and underground structures requires some precautions. Indeed, the concrete of geostructures may shrink or expand under temperature variations that are applied to allow heat exchanges. As a result, the thermomechanical response of energy geostructures should remain such that its strains and stresses comply with the structural support requirements, the idea being to use as much heat as possible without disturbing the overlying building.

The present thesis examines the thermal and thermomechanical characterisations of energy geostructures in the broad sense and with a particular focus on energy piles which is the most common type of energy geostructure encountered. This is achieved using the different opportunities offered by today's research, that is to say numerical, theoretical and advanced experimental methods.

The environmental, economic, social and technical aspects of ground source heat pumps and energy geostructures are discussed in Section 1. The first chapter analyses the energy sector in Switzerland in order to draw the optimal evolution required to increase its sustainability. This partly justifies the work achieved in the present thesis. Then, the second chapter presents the energy geostructures in the broad sense with their principle and goals as well as an up-to-date review of the characterisation methods and design considerations.

Section 2 regroups numerical analyses of energy geostructures using finite differences and finite element methods. Chapter 3 presents the developments carried out on Thermo-Pile software during this thesis. Representative studies as well as development of coupled algorithm are presented, among which an thermal loading-unloading algorithm validated on experimental data, a coupling between Thermo-Pile software and the Euler-Bernoulli beam model to study pile-to-pile interactions through the supported structure, and a method to account for radial thermal strains based on lateral load-transfer curves. Chapter 4 investigated the long term effects of pore water pressure build up on a single pile serviceability as well as the conservativeness of the conventional design codes regarding energy piles. Finally, Chapter 5 presents finite element analyses of thermoactive tunnels using heat exchanger anchors. This study aimed at optimising the heat production while minimizing the mechanical implications on a cut-and-cover tunnel and a bored tunnel.

The third section deals with experimental investigations. Chapter 6 presents a method to estimate the soil thermal diffusivity using interference analyses and based on pumping tests. The method was

evaluated on a scaled borehole (at laboratory scale). Chapter 7 regroups the observations and analyses carried out on the experimental group of energy piles built on the EPFL campus in 2011. The experimental site is first described as well as the sensors used and the data processing methods. Then, the tests are detailed. The first test was carried out on the piles without any structures on top of them which allowed us to characterise the constraints applied by the ground only. Next, the piles were tested individually once the overlying structure was finished. Comparing the two first tests allowed quantifying the constraints induced by the top structure as well as the pile-to-pile interactions. Finally, the pile group was heated as a whole and compared to the single tests in order to quantify the group effects.

Concluding remarks are gathered in Section 4.

Section 1: Background

Chapter 1 Improving Energy Sustainability

1.1 Identifying the needed changes

The concept of Sustainability allows appreciating the long term (i.e. over a human time frame) impacts of a process as well as its ability to continue in time. Sustainability is strongly linked to the concept of Development: we then talk about Sustainable Development. This does not only include the use of green technologies to reduce the anthropogenic impact on the Environment but also involves Social and Economic aspects. Indeed, Development based only on Environmental concerns may not be bearable or even viable. Conversely, Development omitting the Environmental aspect in favour of Social and Economic aspects may be equitable but not sustainable. Therefore, Sustainability stands at the crossroad of Environmental, Social and Economic concerns. This can be represented using the so-called overlapping (or interlocking, see Adams (2006)) circles of Sustainability (Figure 1:1).

The overlapping area between the circles represents the Sustainability. It can vary depending on the relative diameters of these three pillars and Adams (2006) suggests a method to represent ideally balanced and unbalanced models of Development. The ideal balance is reached when the three pillars have the same diameter, which maximizes the overlapping area. Unbalances are observed as in Figure 1c of Adams (2006) when the pillars have different diameters. Adams (2006) represents the situation in 2006 using the greatest diameter for the Economic pillar, an intermediate diameter for the Social pillar and the smallest diameter for the Environmental pillar. Therefore, the Sustainability, represented by the overlapping area of the circles, is not optimum. Better Sustainability is therefore achieved by enlarging the Environmental pillar which may better balance the model (see Figure 1:2, “Change needed”).

But going into more detail, Adams (2006) represents the situation in 2006 with the Environmental pillar slightly shifted toward the Social pillar, suggesting that the protection of the environment was more motivated by Social concerns than Economic reasons at this time. Indeed, the main justification for environment protection has been for a long time the protection of our quality of life that was threatened by pollutant emissions, use of chemicals in agriculture, etc. But Adams removes this shift for the “change needed” and aligns the Environmental pillar with the intersection of the Social and Economic pillars (see Figure 1:2, “Change needed”).

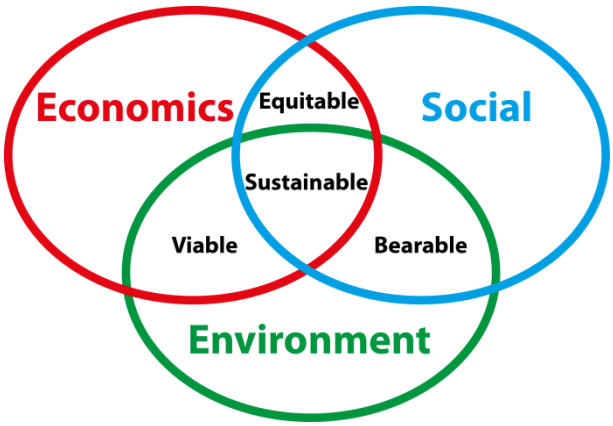

Figure 1:1 Ven diagram of Sustainability

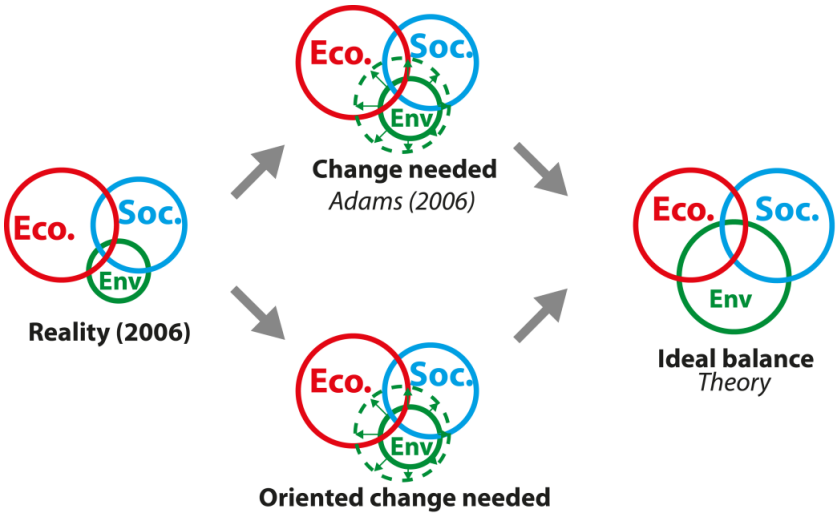

Figure 1:2 Analysis of the situation in 2006 and identification of the change needed using the Ven diagram of Sustainability, partially redrawn from Adams (2006)

As a result, any increase in Sustainability is achieved by simply expanding the Environmental pillar. It would therefore be useful to keep the shift toward the Social pillar in order to define a preferential direction of change needed toward the Economic pillar (see "oriented change needed in Figure 1:2). This would naturally account for the significant rises of energy prices that make, nowadays, the development of alternative and renewable energy sources also an Economic concern.

In conclusion, the change needed should be dedicated to Environmental concerns in order to increase this pillar, and particularly towards Economic aspects in order to make the changes viable.

1.2 Energy in space conditioning: a major impact sector

Despite Sustainability could impact almost every single aspect of our lives, some are more important than others as they touch the basic human needs. Food (including water) habitat and energy are the three most important aspects related to human life. Transport could come as a fourth aspect that has drastically grown since the development of high speed (e.g. train and planes) and efficient individual (e.g. cars) transportation systems though this can be – partially – included in energy.

The present work will mainly focus on energy consumed in buildings and developments needed to improve the sustainability in this domain. Indeed, Pérez-Lombard (2003) suggested to consider building energy consumption as the third pole of energy consumption beside industry and transport because of the important quantities of energy involved (i.e. 20-40 % of the total energy consumption). Therefore, this pole can be subdivided into two main categories which differentiate buildings for habitat from office and retail spaces. End use of the energy in buildings is generally distributed into several end applications which are:

- Space conditioning
- Production of hot water
- Ventilation
- Entertainment
- Cooking / dishwashing
- Lighting
- Washing / drying
- Fridge and freezer
- Other

The split for the different above-mentioned categories are given for the Swiss households, tertiary sector (i.e. office and retail spaces) and industry in Figure 1:3, Figure 1:4 and Figure 1:5, respectively (Kemmler et al., 2013). It comes out that space heating is the main application in the households and tertiary sector, representing 69.7 % and 50 % of the total consumption, respectively.

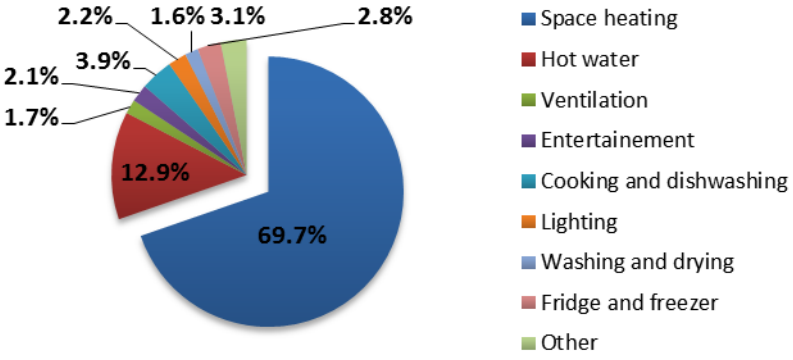

Figure 1:3 Distribution of consumed energy in Swiss households in 2012 according to end use, after (Kemmler et al., 2013)

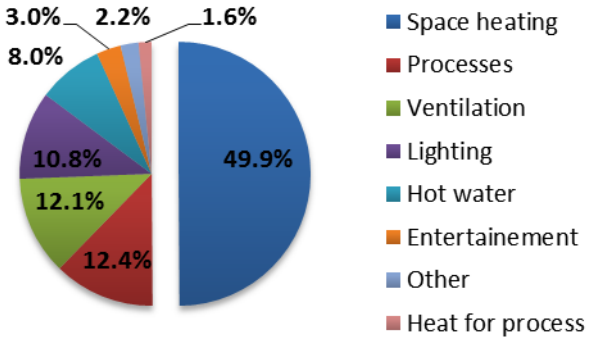

Figure 1:4 Distribution of consumed energy in the tertiary sector and the agriculture in 2012 according to end use, after (Kemmler et al., 2013)

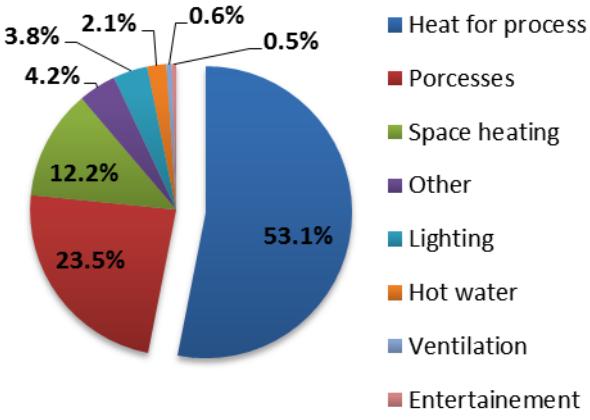

Figure 1:5 Distribution of consumed energy in the industry in 2012 according to end use, after (Kemmler et al., 2013)

The production of hot water is the second end application of energy in the households, representing 12.9 %, and the 5th in the tertiary sector with 8 %. Therefore, space conditioning and production of hot water represent the main energy consumption poles in households and office and retail buildings. However, the major part of this significant demand is still satisfied using fossil fuels (i.e. fuel oil and natural gas):

- 73.1 % of the energy used for space heating in the households and approximately 60 % in office and retails spaces
- 61 % of the energy used for the production of hot water in the households and almost 80 % in office and retails spaces

As a result, it appears that finding, developing and promoting heat sources for the conditioning of buildings represent an important aspect of future energy policies. This includes, inter alia, the development of new energy sources that should:

- be renewable (Environmental impact ++)
- have an optimized life cycle (Environmental impact ++)
- remain cost-effective (Economic impact ++)
- be easy to implement (Economic impact ++)
- be flexible, adaptable to many regions of the Hearth (Social impact +)
- have minimized negative impacts on life quality (Social impact +)

The following section tries to identify the characteristics of shallow geothermal energy related to the above-mentioned requirements.

Chapter 2 Energy Geostructures: Systems and Characterization Overviews

2.1 Principle of energy geostructures

Energy geostructures are used as the ground heat exchanger in ground source heat pump systems in order to provide heat for the heating and cooling of buildings.

2.1.1 Ground source heat pumps with energy geostructures

Ground Source Heat Pump (GSHP) systems take advantage of the relatively constant temperature levels found down to a few hundred meters below the soil surface. Energy geostructures are designed to operate within the very shallow part of the soil (0-50 m) which is in thermal equilibrium with the atmosphere. Therefore, the temperature there is equal to the mean yearly air temperature which depends on the location of the site and GSHP using energy geostructures are operated with temperature levels from 10 to 35 °C 2006 (Murphy and McCartney, 2014).

GSHP systems are composed of 3 main elements: the heat pump, the building and the ground. These different parts are linked through heat exchangers: the one linking the heat pump to the ground is called Ground Heat Exchanger (GHE) and the one linking the building to the heat pump is the heating network. They are detailed and discussed hereafter. In GSHP systems using energy geostructures, foundations have the role of GHE as well as support.

2.1.1.1 Functioning modes

Because energy geostructures are shorter than boreholes but much more numerous, they have particular functioning modes compared to conventional ground loops. Indeed, the proximity and shortness of the GHEs can require, under certain conditions, to seasonally balance the extracted heat from the ground. Therefore, different functioning modes were developed.

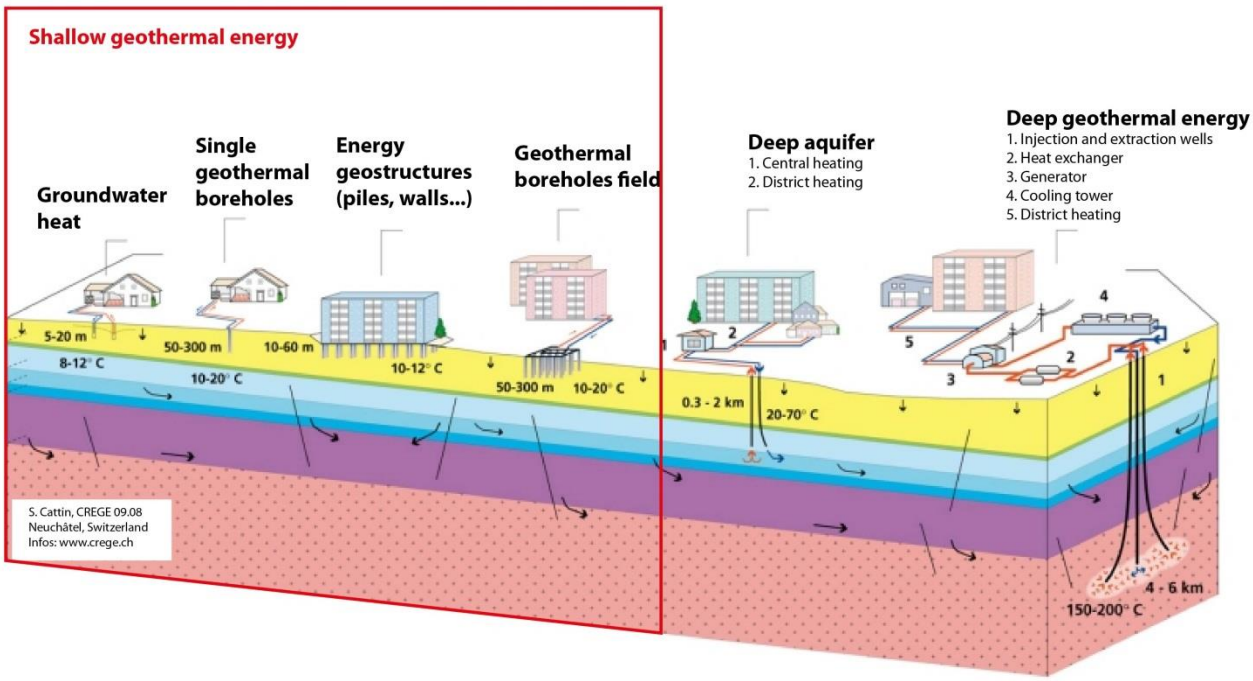

Figure 2:1 Various geothermal systems from very shallow to deep installations, from S. Cattin, CREGE, Neuchâtel, Switzerland

Pure heating or cooling, letting the ground at thermal rest when conditioning is not required, can be achieved when the natural thermal recharge occurring in the ground is high enough. This is generally the case for open loop systems which use an upstream well for production and a downstream well for reinjection and for closed loop systems embedded within permeable soil with significant groundwater flow. Anstett et al. (2005) suggest that a Darcy velocity of 0.5 to 1 m per day is high enough to achieve decoupled heat and cold production using a monovalent (i.e. 100 % of the heating is provided by GHEs) closed-loop system. This mode may represent a great opportunity for heating or cooling dominated climates provided that efficient heat sources are available.

Otherwise, **seasonal heat storage** is required in order to maintain the lift within acceptable limits on the long term operation. This mode is generally applied to closed loop systems but can be considered for very specific cases in trapped aquifers (Paksoy et al., 2000). It includes heat extraction during cold spells which reduces the ground temperature, and heat injection during hot spells which increases the ground temperature. Therefore, this mode of functioning induces cyclic variations in ground temperature on a yearly basis. Heat injection into the ground during hot spells can be achieved according to different methods:

- **Direct cooling**: the heat carrier fluid circulates within the building conditioning network and gets hot at the contact with the building. It then goes into the ground loops and transfers its heat, getting colder. The cold heat carrier fluid is then sent back into the building. This only requires pumps to circulate the heat carrier fluid. The potential of this method relies on the temperature difference between the ground and the building and this type of system can also be coupled with cooling towers in order to limit the heat injection into the ground to keep the direct cooling potential at an efficient level (Anstett et al., 2005).
- **Cooling machine**: when direct cooling does not provide a sufficient capacity, the heat pump used for heating during cold spells can be inverted and turned into a cooling machine where the building is the heat source and the ground the heat sink.
- **Active heat storage**: this mode of storage includes heat harvesting from multiple heat sources at high temperature (> 50 °C) during hot spells (e.g. solar thermal panels and waste heat) and storing it in Underground Thermal Energy Storage (UTES) (Sanner et al., 2003).

Depending on the local potential and on the number of energy geostructures required for a building, two types of systems can be encountered:

- **Monovalent systems** rely only on energy geostructures to provide heating and cooling. This type of system is rare but achievable under certain conditions (i.e. significant ground water flow and favourable conditioning loads). An example of such a monovalent system is the industrial building Lidwil at Altendorf (Zurich, Switzerland) which uses 120 spun energy piles (out of 155 spun pile foundations) with 2 U-loops per pile and filled with fine gravel (Anstett et al., 2005). The installation provides 160 kW of heating using three heat pumps of 18 kW each with CoPs of 2.9–3. The piles are embedded within a gravel layer wherein the Zurich lake groundwater flows with a Darcy's velocity between 100 and 150 m/d.

- **Bivalent systems** use the energy geostructures to provide a part of the heating and cooling loads of a building, the rest being satisfied using conventional heat sources. For example, energy piles at the dock Midfield of the Zurich airport provide 85 % of the heating and 87 % of the cooling through free cooling. The remaining parts come from district heating for heating or a cooling tower for cooling (Anstett et al., 2005; Pahud and Hubbuch, 2007).

For monovalent closed loop systems, Anstett et al. (2005) suggest injecting at least 70 % of the extracted energy when the Darcy velocity is lower than 0.5 m/d. However, injecting more than 90 % of the extracted energy may compromise the long term efficiency of direct cooling.

2.1.1.2 The heat pump

Heat Pumps are thermal devices that convert mechanical work into heat. Simple HPs comprise four main devices that are the condenser, the evaporator, the compressor and a reducing valve. The HP works with a refrigerant which is a special fluid that evaporates at low temperatures. This fluid is in contact with a heat source from which it pumps heat and a heat sink where it delivers the extracted heat.

The efficiency of energy conversion is generally characterised using the Coefficient of Performance (CoP) of the heat pump which says how much units of heat we get using one unit of electricity: as an example, a CoP of 3 means that we process 2 units of heat from the heat source with one unit of electricity, finally getting 3 units of heat (see Section 9.1 for details on the heat pump).

However, CoP varies as it depends on the lift (i.e. the difference between the delivery temperature level and the heat source level): the greater the lift, the lower the CoP. As a result, the seasonal factor of performance (SFP) is used to characterize the efficiency of a GSHP system along seasons.

2.1.1.3 The building heating network

Shallow geothermal power is coupled with HPs because of the low temperature levels encountered at shallow depth in the ground. Therefore, it is suitable to use it combined with heating systems that require moderate to low temperature levels (up to 55 °C) and induce small temperature drops (between 5 and 10 °C). The greater the heating temperature, the lower the CoP as the lift increases (Network, 2002).

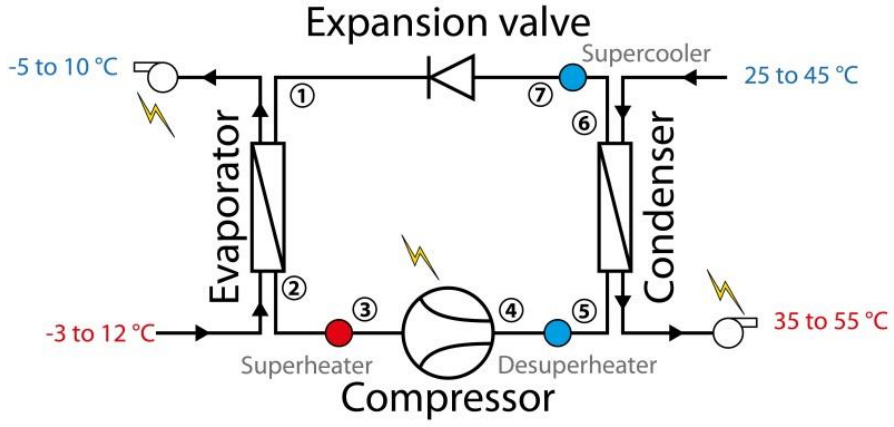

Figure 2:2 Schematic representation of a GSHP system. Temperature levels are those observed using energy geostructures

2.1.2 Energy geostructures as particular ground heat exchangers

2.1.2.1 Energy piles

Energy piles are the most worldwide used energy geostructure. This is mainly due to the fact that this is the most commonly built foundation structure eligible as a GHE. Conceptually, the thermal activation of any type of pile foundation is possible with more or less constraints, depending on the construction method.

Bored piles (Figure 2:3) are built according to the general method: 1/ a temporary casing is pushed into the ground, 2/ the space inside the casing is excavated using an auger, 3/ the reinforcing cage is inserted into the excavated casing, 4/ concrete is poured using a tremie pipe and 5/ the casing is removed. This type of pile is suitable for energy piles as the absorber pipes can be tightened to the reinforcing cages (on the inner face in order to avoid damages during the installation) before they are inserted into the casing. For example, 300 out of the 350 bored piles supporting the dock Midfield of the Zurich airport were turned into energy pile (Anstett et al., 2005; Pahud, 2013). These piles are generally large diameter piles which allow deploying several U-loops within the same pile. As example, 5 U-loops have been installed in the energy piles at the dock Midfield (diameter between 0.9 and 1.5 m) with an average active length of 26.8 m which represents 268 m per pile (Anstett et al., 2005).

Spun piles (Figure 2:3) are also suitable for energy piles. The installation process requires driving the pre-fabricated piles into the ground, therefore, absorber pipes can only be installed once the piles have been driven. They are generally installed within hollow piles which are then filled with wet sand, fine gravel (Anstett et al., 2005) or cement (Park et al., 2013). As an example, the Fully school in Valais (Switzerland) has 41 energy piles out of the 118 driven piles on which it rests. The energy pile diameters range from 20 to 30 cm and they have 2 U-loops sealed with wet sand. The average active length of the energy piles is 23.2 m which represents 92.8 m of absorber pipe per pile.

Continuous Flight Auger (CFA) piles are installed using a continuous auger and no casing. The hollow auger penetrates the ground to the pile depth. Then, concrete is pumped through the hollow bore and the auger is pulled out. Finally, the reinforcing cage is driven into the fresh concrete. Therefore, absorber pipes must be strongly tightened to the reinforcing cage. You et al. (2014) have demonstrated the feasibility of such energy piles.

Pre-installation of absorber pipes on reinforcing cages could be a significant improvement of reinforcing cage manufacturing for projects involving energy piles and it is a driving factor for the technology acceptance as no additional time for pile installation would be required on site when planned early enough. Applications to driven piles will still require on-site installation and grouting of the pipes.

In Switzerland, the installed capacity of energy piles has steadily increased since 2000 to go from 3.7 to 15.1 MW in 2012 (Imhasly et al., 2013). Amis and Loveridge (2014) reported that the number of energy piles in the United-Kingdom has gone from almost 0 in 2005 up to approximately 5000 in 2012. Therefore, interest is growing in this type of energy geostructure.

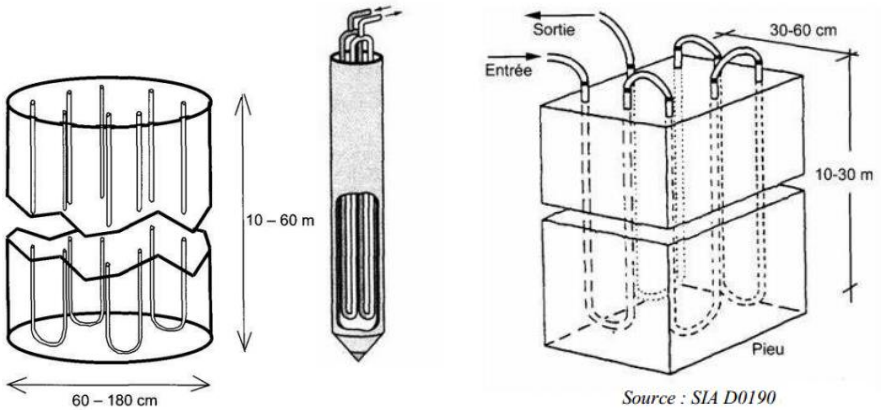

Figure 2:3 Scheme of (left) bored and (middle) spun piles and (right) rectangular piles or walls, from (Anstett et al., 2005) – entrée = inlet and sortie = outlet

2.1.2.2 Thermoactive tunnels

Urban tunnels have been identified as potential energy geostructures because of their lengths and proximity with potential consumers. Several parts of them have been tested on pilot sites, mainly in Austria.

Thermoactive geotextile deployed between the primary and secondary linings have been tested on a portion of the Lainzer tunnel (Vienna, Austria) (Adam and Markiewicz, 2009). Portions of geotextile were equipped with 2 U-loops off-site so that *in situ* installation was not delayed too much. On site work consisted in connecting the geotextile portions to the collection line.

Thermoactive lining segments were used on a 54-m-long portion of the Jenbach tunnel in Austria (Frodl et al., 2010; Rehau, 2012) to provide 43 kW of heating to an overlying municipal building with a peak of 80 kW at -16 °C. The tunnel is 12 m in diameter and is located 27 m below the soil surface. With a mean heat pump CoP of about 3, the heat rate extracted from the ground reaches 15 kW. A total of 189 special lining segments (7 segments plus a keystone per 2-m-wide and 500-mm-thick ring) were moulded in factory with absorber pipes attached to the inside of the reinforcing cage. On site operations consisted in connecting the segments together.

Finally, **heat exchanger anchors** have been tested in an embankment in Vienna (Austria). Those were self-drilling anchor bolts in which coaxial probes were installed into the hollow bore used for flushing and grouting (Adam, 2008b). Some finite element analyses have also been carried out with realistic tunnel embankment geometries (Adam and Markiewicz, 2009).

2.1.2.3 Thermoactive walls and slabs

All types of walls and slabs can be thermally activated by deploying absorber pipes. Brandl (2006) identified more than 37’000 m^2 of thermoactive diaphragm walls and almost 13’000 m^2 of thermoactive foundation rafts in 2006 in Vienna, Austria. These walls and slabs were located below buildings and along the newly built extension of the U2 metro line of Vienna and Lainzer tunnel. Amis and Robinson (2010) reported similar applications in London (United-Kingdom).

2.2 Thermal characterisation of energy geostructures

Thermal characterization of energy geostructures is based on the heat diffusion/convection theory in soils, which is first detailed. Then, characteristics used to compare different configurations of energy geostructures are presented.

2.2.1 Heat transport theory

Provided the relatively low temperature levels reached in the shallow ground using energy geostructures, the two main mechanisms involved in heat transport are heat conduction and advection (i.e. forced convection). The first is linked to molecular vibration while the second is induced by groundwater movements within the soil matrix. Free convection, driven by buoyancy effects, may also develop in permeable soils but may remain relatively marginal in most cases (Hermansson et al., 2009).

Heat conduction is governed by the so called heat equation which takes the following form for an isotropic homogeneous medium:

$$\frac{\partial S_T}{\partial t} = div\left(\mathbf{q_T}\right) + Q_T$$

Equation 2:1 General heat equation

where t is the time, S_T represents the system enthalpy, Q_T represents any volumetric heat source or sink and $\mathbf{q_T}$ is the heat flux density. This equation was established making a heat balance on an elementary volume while considering that heat transport is only achieved through conduction, represented by the Fourier's law giving the heat flux density as:

$$\mathbf{q_T} = -\boldsymbol{\lambda} \cdot \nabla T$$

Equation 2:2 General Fourier's law formulation

where $\boldsymbol{\lambda}$ is the thermal conductivity tensor. This law states that heat goes from hot regions toward cold regions (Fourier, 1822).

The heat equation becomes the heat convection-diffusion equation when forced convection is involved, which yields (ignoring volumetric heat sources and sinks):

$$\frac{\partial S_T}{\partial t} + \rho_w c_w \mathbf{U} \cdot grad\left(T\right) = div\left(\mathbf{q_T}\right)$$

Equation 2:3 Convection-diffusion equation

where ρ_w and c_w are the fluid (i.e. water) density and specific heat and $\boldsymbol{U}$ is the macroscopic fluid velocity.

Based on these theories, different analytical and numerical solutions have been developed for design purposes. First, Ingersoll and Plass (1948) developed the Infinite Line Source (ILS) model in which the heat source has a null radius. In order to account for heat source radius, Carslaw and

Jaeger (1947) then developed the Infinite Cylinder Source (ICS), later improved by Ingersoll et al. (1954) and applied to GHE design by Mogensen (Mogensen, 1983) (1983) and Baudoin (1988). The ICS model was considering a hollow cylinder without heat capacity. Eskilson (1987) proposed a numerical solution using g-functions for the Finite Line Source (FLS), which allowed considering relatively complex geometries of borehole fields and accounting for finite length of GHEs. Philippe et al. (2009) compared these three models (i.e. ILS, FLS and ICS) and determined that the ICS was suitable for short-term impact investigations (less than 1 day) while the advantages of the FLS are mainly on the long-term effects (more than 1000 days) and the ILS is well suited for medium-term operations (1 day to 1 year).

These models were however developed considering only heat conduction and solutions for similar configurations (i.e. ILS, FLS and ICS) were then proposed accounting for groundwater seepage. This is generally achieved by considering a moving heat source. Diao et al. (2004a) proposed a solution for a moving ILS and Molina-Girardo et al. (2011) developed the moving FLS.

In order to account for heat capacity of GHEs, Man et al. (2010) developed Infinite and Finite Solid Cylinder (ISC and FSC) models without groundwater seepage. For this, the cylindrical source was filled with the same material as the surrounding ground. Finally, Zhang et al. (2013) developed the moving FSC model to account for groundwater seepage.

Other models have been developed for special configurations such as the solution proposed by Cui et al. (2011) for energy piles with spiral coils.

But these models aim at estimating the temperature field around the GHEs, in the ground, as a function of the heat rate injected through a GHE. Other models have been developed to draw temperature profiles inside the GHE absorber pipes. Zeng et al. (2003) and Diao et al. (2004b) have used the FLS to get temperature profiles along single and double U-loops connected in parallel or in series.

In conclusion, the heat conduction-advection theory has allowed developing numerical and analytical solutions that are mainly used in design software (see (CSTB)).

2.2.2 Thermal potential of energy geostructures: the example of energy piles

Design methods are illustrated using charts and tools developed for vertical GHEs as these represent the main topic of this thesis. As mentioned in the introduction, the intermediate media between the heat carrier fluid and the ground induce temperature drops that are characterised using the thermal resistance of the system, defined as:

$$R_b = \frac{T_s - T_f}{q}$$

Equation 2:4 Thermal resistance

where T_f is the heat-carrier fluid temperature, T_s is the soil-pile interface temperature and q is the induced heat flow per meter of GHE (in W/m). As a result, the greater R_b, the greater the temperatures difference between the heat carrier fluid and the ground, and therefore the lower the

efficiency. To set the convention, we will consider that R_b values are always positive and that a positive heat flux q corresponds to absorption of heat by the GHE.

The thermal resistance therefore accounts for the number of pipes, their disposition, the concrete cover thickness as well as the thermal conductivity of the grouting material and the thermal properties of the heat-carrier fluid. A general decomposition of R_b is based on resistances in series (Loveridge and Powrie, 2014):

$$R_b = R_{pconv} + R_{pcond} + R_c$$

Equation 2:5 Decomposition of the thermal resistance

where R_{pconv} accounts for the forced convection transfer between the pipe wall and the heat carrier fluid, R_{pcond} accounts for the pipe wall and R_c accounts for the grouting material/concrete and cross section geometry. Analytical expressions of R_{pcond} and R_{pconv} were derived (Loveridge and Powrie, 2014):

$$R_{pcond} = \frac{\ln\left(r_{out} / r_{\text{int}}\right)}{2N\pi\lambda_p}$$

Equation 2:6 Thermal resistance associated with the conduction through the pipe wall

where r_{out} and r_{int} are the outer and inner radius of the pipe, respectively, N is the number of pipes per cross section of GHE and λ_p is the thermal conductivity of the pipe wall material.

$$R_{pconv} = \frac{1}{2N\pi r_{\text{int}} h_i}$$

Equation 2:7 Thermal resistance associated with the forced convection inside the pipe

where h_i it the heat transfer coefficient. Remund (1999) proposed to split the thermal resistance R_c into two terms as:

$$R_c = \frac{1}{\lambda_c S_c}$$

Equation 2:8 Decomposition of the thermal resistance related to the grout/concrete and geometry of the GHE cross section

where λ_c is the thermal conductivity of the grouting material/concrete and S_c is the shape factor accounting for the number of pipes and their positions within the GHE cross section (i.e. concrete cover, see Figure 2:4).

Since the grouting (i.e. R_c) accounts for almost 65 % of the borehole thermal resistance and the pipe wall (i.e. R_{pcond} and R_{pconv}) for 35 %, major improvements are realized by lowering R_c which is potentially achieved by either increasing the thermal conductivity of the grout (Delaleux et al., 2012) and/or increasing the shape factor.

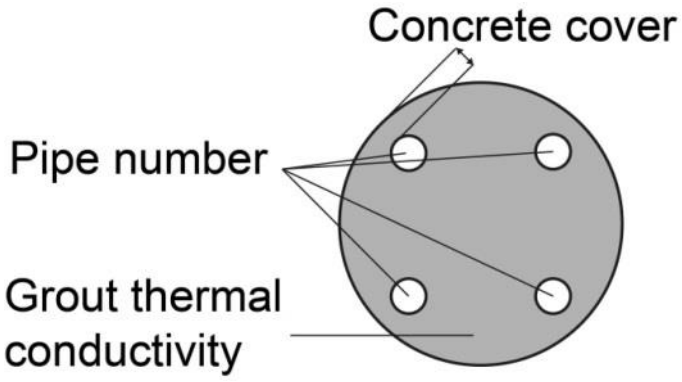

Figure 2:4 Cross section of a vertical GHE (borehole or pile) with the different parameters involved in the thermal resistance of the system

However, concrete cover is generally imposed by the reinforcing cage design while thermal short circuiting (i.e. thermal interactions between cold and hot pipes) is one significant issue faced when increasing the number of pipes per cross section. As a result, the shape factor S_c can only be partially optimised.

Anstett et al. (2005) and then Loveridge and Powrie (2014) have provided charts of thermal resistances for energy piles. Important conclusions are that:

- large diameter piles have lower thermal resistance
- thinner concrete covers yield better thermal contact between the pipes and the ground
- an optimal number of pipes exists as increasing them induces greater thermal interactions which reduces the system potential

If using thermal resistance charts given for characteristic configurations provides a first insight in the thermal optimisation of vertical GHEs, more advanced tools are required to model the whole system and quantify long term heat performances. Design approaches can be divided into two main categories: simple systems using a single vertical GHE and systems using a field of GHEs (e.g. of boreholes and most generally the case for energy geostructures).

Monfort (2012) exposed during the Intersol'2012 meeting in Paris that single geothermal boreholes for small heating demand (i.e. P < 30 kW) are designed based on characteristic extraction rates (e.g. 50 W/m for the given example) and that the GHE length is estimated based on the heating load that is to be satisfied by the shallow geothermal system and its efficiency. Indeed, let consider Monfort's example: a building whose needs are satisfied with a 7.5 kW heat pump whose CoP is 4. As a result, the withdrawn power from the ground is 7.5 kW*(CoP-1)/CoP = 5.62 kW. The required length of GHE is therefore 5.62 kW / 50 W/m ~ 112 m.

However, the assumption of constant linear extraction rate (i.e. 50 W/m) may not be valid when considering fields of vertical GHE as thermal interactions may develop and reduce this value. For the design of such fields, dynamic simulation tools are available and the French Technical and Scientific Center for Buildings (CSTB) makes a relatively complete list of those (CSTB). These tools are based on dynamic simulations accounting for building thermal loads, heat pump capacity and efficiency as well as ground temperature and GHE geometry.

Among the cited models and tools, PILESIM (Pahud, 1999) was developed at the EPFL for the particular design of energy piles. One interesting example of application using PILESIM is the pre-project study carried out on the EPFL campus for the use of energy piles below the BP (Bâtiment Polyvalent) building (Fromentin et al., 1998). The optimization of the HP capacity was achieved in such a way that the annual produced energy was maximised while the fluid temperature at the pile inlet remains greater than 0 °C in order to avoid soil freezing. Therefore, two domains were delimited in the HP capacity – annual produced energy diagram that can be plotted using tools such as PILESIM (Figure 2:5):

- Domain I: this domain represents under-designed HPs which cannot take full advantage of the ground heat: the annually produced energy is limited by the HP capacity
- Domain II: this domain represents over-designed HPs whose capacity is not fully used (i.e. economic losses on the initial investment) because of the temperature limitation in the ground (i.e. 0 °C): the annually produced heat is limited by the ground capacity

Therefore, the direct use of Figure 2:5 would suggest using a HP with a capacity around 86 kW. However, refined analyses showed that using a capacity of 80 kW instead of 86 kW is preferable on the long term even if the annual energy production is slightly reduced.

In conclusion, design charts and tools for vertical GHEs (i.e. piles and boreholes) are nowadays available for the different thermal design steps, namely pre-project design, project design and refined operational design. Studies have also been carried out to determine similar parameters for diaphragm walls (Kürten, 2011; Caichu et al., 2012).

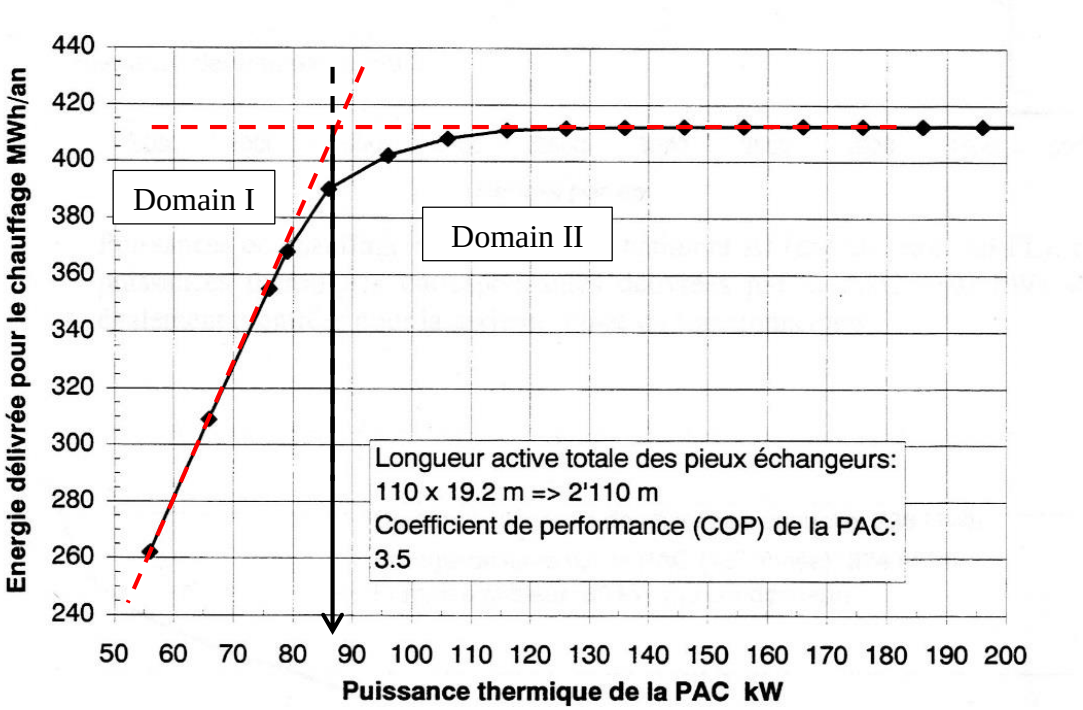

Figure 2:5 Annually delivered energy (in MWh/y) versus heat pump capacity (in kW), from (Fromentin et al., 1998). The legend says: active total length of the energy piles = 2'110 m, heat pump CoP = 3.5

2.3 Thermomechanical characterization of energy geostructures

The thermomechanical response of energy geostructures is of great importance as their first role is to ensure a structural integrity. The thermal expansion and contraction due to temperature variations may produce significant deformations and efforts that must be controlled. Therefore, great effort has been put in characterising the thermomechanical response of energy geostructures in general and of energy piles in particular in order to gain confidence in this technology.

2.3.1 Experimental characterisation

2.3.1.1 In situ characterisation

The thermomechanical response of energy geostructures is generally quantified *in situ* in terms of thermal strains and stresses. Indeed, when a geostructure is heated or cooled, it expands or contracts. However, the observed axial strains are lower than the ones which would occur if the geostructure was out of the ground. This is due to the constraints that the soil applies to the geostructure (i.e. compression and/or friction). These constraints provide to the geostructures their bearing capacities but block a part of the axial thermal strains which are then turned into axial thermal stresses. The relationship between the blocked ($\varepsilon_{ax,blo}$) and observed ($\varepsilon_{ax,obs}$) axial thermal strains is:

$$\varepsilon_{ax,\,free} = \beta_c^T \Delta T = \varepsilon_{ax,obs} + \varepsilon_{ax,blo}$$

Equation 2:9 Free, blocked and observed thermal strains

where $\beta_c{}^T$ is the linear thermal expansion coefficient of the geostructure (i.e. concrete) and ΔT is the temperature variation of the geostructure. As blocked axial thermal strains turn into thermal stresses ($\sigma_{ax,th}$), one may write:

$$\sigma_{ax,th} = E_c \varepsilon_{ax,blo} = E_c \left(\beta_c^T \Delta T - \varepsilon_{ax,obs} \right)$$

Equation 2:10 Axial thermal stress

The global thermomechanical response of the geostructure can be characterised by the mobilised thermal expansion $\beta_{mob}{}^T$ (Murphy et al., 2014a) or the degree of freedom *n* (Laloui et al., 2003):

$$\beta_{mob}^T = \frac{\varepsilon_{ax,obs}}{\Delta T}$$

$$n = \frac{\varepsilon_{ax,obs}}{\beta_c^T \Delta T}$$

Equation 2:11 Mobilised thermal expansion coefficient and degree of freedom

The advantage of the mobilised thermal expansion coefficient is that it does not require any assumption about the linear expansion coefficient of the energy geostructure. Practically, these quantities are derived using linear regressions on the $\varepsilon_{ax,obs}$-ΔT curves.

Such thermomechanical characterisations have been carried out on energy piles in Switzerland (Laloui et al., 2003), United Kingdom (Bourne-Webb et al., 2009) and United States (Murphy et al., 2014a).

2.3.1.2 Laboratory characterisation

Laboratory characterisation of the thermomechanical response of energy geostructures provide specific information and can take two forms: scaled models and laboratory tests.

Tests on pile scaled models were conducted under 1g or in centrifuge boxes. These kinds of test provide a global picture of the scaled model response and have the advantage of being less expansive and test conditions and measurements are better controlled than in full-scale tests. Centrifuge tests have been used by McCartney and Rosenberg (2011) to investigate the impact of radial thermal strains on the bearing capacities of scaled pile models. After applying a temperature increase that was maintained throughout the entire test, they established the load-settlement curves of the piles. It was found that pile heating could increase its ultimate load. Later, Stewart and McCartney (2014) investigated thermal cycles with centrifuge tests on energy piles and evidenced that thermohydromechanical effects could have a significant impact on the soil-pile interface. Goode and McCartney (2014) investigated scaled models of pile with centrifuge tests in clay and sand. Wang et al. performed 1g tests on scaled piles in sand at different moistures (0, 2 and 4 %). The testing procedure was relatively advanced and consisted in cyclic mechanical loading sequences under different temperatures (20, 40 and 60 °C). The successive mechanical cycles carried out at the different temperatures allowed getting rid of variability in pile shaft friction. Finally, Kramer and Basu (2014) carried 1g tests on a scale pile model in sand with lots of thermocouple deploying in the soil tank. This allowed getting the detailed temperature field around the pile. They also performed load tests at 20 °C and 40 °C from which they drawn the same conclusions as McCartney and Rosenberg (2011), that is to say heating slightly enhanced the scaled pile bearing capacity. Finally, Yavari et al. (2014) investigated thermal cycles with 1g tests on a scaled pile in sand.

More specific tests were carried out on soil samples and soil-concrete interfaces. These tests are suited for developing constitutive laws used in numerical models. Cekerevac and Laloui (2004) developed thermal triaxial cells to test Kaolin clay and showed the thermal consolidation of normally consolidated samples. Later, Di Donna and Laloui (2014) developed thermal oedometers to investigate thermal cycles on normally consolidated inorganic clays. After a couple of thermal cycles, between 5 and 60 °C, the irreversible volumetric strains stabilised between 0.5 and 1 %, the following cycles being reversible. A test on an overconsolidated sample showed no irreversible volumetric strain. Also, Di Donna and Laloui (2014) developed a thermal shear box to study the impact of temperature variations on the soil-concrete interface. They found that the concrete-sand interface was not sensitive to temperature variations while the clay-concrete interface showed significant evolution because of thermal consolidation of the clay.

2.3.2 Numerical characterisation

Numerical investigations of the thermomechanical response of energy geostructures allow more flexibility than experimental tests but require dedicated models that are developed based on

experimental evidences. They also permit investigating long term thermal and thermomechanical performances while we have no feedback on such timescales. This section is divided into two parts, the first dealing with complex numerical analyses (mainly finite elements) and the second dealing with design tools based on finite differences.

2.3.2.1 Advanced modelling

If the behaviour of concrete geostructures is generally assumed thermoelastic, the thermoelastoplastic response of soils requires more advanced constitutive laws. They are necessary to accurately reproduce experimental observations. Different models were proposed (Laloui, 2001) and this paragraph will focus on recent advances.

Laloui and Cekerevac (2003) developed an isotropic yield mechanism to model the thermoplasticity of clays based on the experimental evidences reported by Cekerevac and Laloui (2004). Later, they developed a cyclic non-isothermal plasticity model to account for thermal cycles (Laloui and Cekerevac, 2008). Laloui and François (2009) finally proposed the multimechanism plasticity model ACMEG-T, considering a thermoplastic isotropic mechanism along with deviatoric mechanisms of a Cam-clay model. The main feature of ACMEG-T is that the preconsolidation pressure depends on the temperature, which induces thermal consolidation in normally consolidated clays. Di Donna et al. (2013) implemented this model into the finite element code *Lagamine* to model long term evolution of the soil-pile interface along energy piles.

Thermal consolidation at the soil-pile interface was found to reduce the normal stress to the pile shaft, slightly reducing the lateral resistance of the pile and therefore inducing long term settlements of about 10 % of the settlement induced by the mechanical loading.

Interface constitutive laws were also developed in order to reproduce the cyclic degradation of the soil-pile interface. Shahrour and Rezaie (1997) proposed the Modjoin law which includes soils inhomogeneity and non-linearity as well as softening/hardening, dilatancy and cyclic degradation. This model was updated by Cao (2010) to account for stress relaxation and strain ratcheting and accommodation.

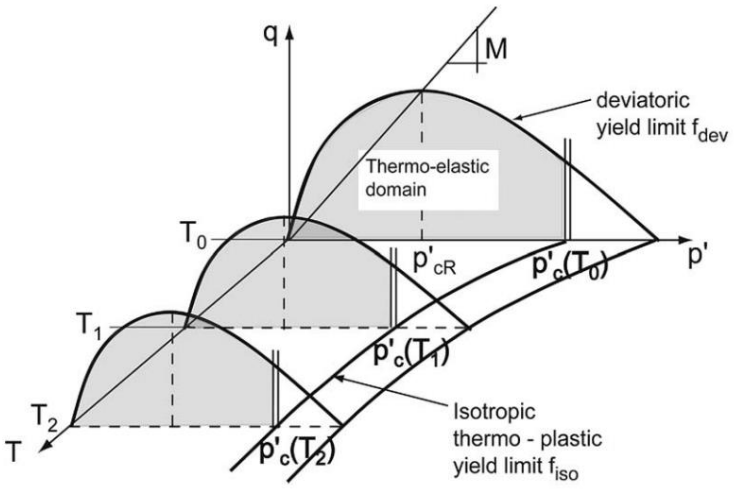

Figure 2:6 Evolution of the yield limit with temperature in the ACMEG-T model, from (Laloui and François, 2009)

Suryatriyastuti et al. (2013) implemented the Modjoin model in FLAC^{3D} and studied the evolution of the mobilised shaft friction and settlements along a 15 m long single pile over 24 thermal cycles between -10 and +10 °C. Head settlements ranged from -5 % and +30 % relatively to the mechanical settlement.

In conclusion, these advanced models were developed based on experimental evidences in order to carry out representative numerical analyses on the long term.

2.3.2.2 Design tools

Aside from advanced numerical codes accounting for complex couplings and geometries, operational tools have been developed for quick estimations of thermal effects on particular energy geostructures: energy piles. These tools consider 1D configuration along the pile axis. They use the load-transfer approach (Coyle and Reese, 1966) and are based on the thermal effect partitioning experimentally observed (see Section 2.3.1.1).

Thermo-Pile was developed by Knellwolf et al. (2011). This software considers a single pile whose cross section is circular, and which is embedded within a layered soil. Ultimate bearing capacities are either estimated using soil geotechnical characteristics (e.g. Lang and Hurder (1978) or specified manually. This tool was validated against the EPFL and Lambeth College test piles. Ouyang et al. (2011) developed a hybrid model using load-transfer curves for the soil-pile interactions and an elastic continuum solution for pile-soil-pile interactions to back analyse the Lambeth College test. Suryatriyastuti et al. (2014) used the Modjoin constitutive law of degradation of the soil-pile interface with the load-transfer method and compared the results with a 3D modelling with FLAC^{3D}.

In conclusion, design tools use simplified but effective load-transfer methods. However, some weaknesses associated with the reductive assumptions still remain to be tackled as highlighted by Ouyang et al. (2011).

Section 2: Numerical Analyses of Energy Geostructures

Chapter 3 Operational Design of Energy Piles

3.1 Introduction

Geothermal piles are pile foundations equipped with absorber pipes to allow heat exchanges with the surrounding ground. Thermal expansion or contraction of the concrete induces thermal strains and stresses that bring new challenges for the design of such structures. Thermal strains are the result of the equilibrium between the thermal efforts and mobilised bearing forces, which depend on the pile's restraint (Laloui et al., 2003; Laloui et al., 2006; Laloui and Di Donna, 2011). Design tools have been developed (Knellwolf et al., 2011; Ouyang et al., 2011; Suryatriyastuti et al., 2014) in order to carry out simplified analyses. These tools are able to provide estimates of thermally induced stresses and strains based on the load-transfer methods using load-transfer curves representing the soil-pile interface behaviour. The EPFL tool, called Thermo-Pile (Knellwolf et al., 2011), first applies the mechanical load to the pile which provides a first set of mobilized bearing forces. Then, the impact of the thermal load is estimated by first finding the null point depth. For this, the software computes as much solutions as the number of pile discrete element, assuming for each solution that the null point is one of the discretization points. The right solution is then the one that produces the lowest resulting force on the assumed null point. This particular method allows using complex load-transfer curves. Ouyang et al. (2011) used a hybrid load-transfer model using load-transfer curves to represent the soil-pile interface behaviour and the elastic continuum solution to model pile-soil-pile interactions. This method was used because it has already been adopted in complex foundation modelling (e.g. rafts, pile group optimization and negative skin friction on pile groups). However, this model only considered linear elastic/perfectly plastic models. Paten and Santamarina (2014) used a simplified method based on the work of Knellwolf et al. (2011) and demonstrated that these methods are suitable for long term evaluation of single pile responses.

This chapter first aims at deepening the understanding of non-cyclic mechanisms linked to monotonic temperature variations in energy piles using Thermo-Pile. This helps illustrating the background linked to the thermomechanical response of these structures. Two full-scale *in situ* experiments were analysed as well as three idealized case studies. The evolution of the mobilised bearing forces along the piles were quantified for temperature variations from -10 °C to +60 °C (the natural ground temperature being taken equal to 11 °C). Profiles of mobilised shaft friction, pile top displacements and null point depths were discussed according to the boundary conditions applied to the piles.

Follows a thorough discussion of the analyses carried out by Knellwolf et al. (2011) about the Lambeth College test pile while validating Thermo-Pile software. We developed a thermal unloading path to investigate this particular test and made its validation against the experimental data.

Next, a mathematical framework is established to estimate the asymptotic position of the null point along energy piles. This formulation helps understanding how energy piles are constrained by the supported mechanical load, the bearing mechanisms and the overlying structure.

Then, a method coupling Thermo-Pile software with the Euler-Bernoulli beam model is proposed for simple analyses of piled beams with energy piles. This section highlights the possible pile to pile

interactions that could occur when the supported structure is rigid enough to allow load redistribution.

Finally, a method to account for thermal radial strains using p-y curves is described. This method can be implemented in load-transfer models and may help tackling limitations of one-dimensional approaches. Indeed, Ouyang et al. (2011) have shown how important can be these radial strains when comparing the results of their model with experimental data.

3.2 Evolution of pile mobilised bearing capacities under non-cyclic temperature variations

3.2.1 Case studies

The different case studies with the related modelling parameters are presented in this section.

3.2.1.1 Real scale in situ case studies

Two real in situ tests have first been investigated: the first EPFL test pile (Laloui et al., 2003) and the Lambeth College test pile (Bourne-Webb et al., 2009).

The EPFL test pile

A geothermal test pile was installed below a building on the campus of the Swiss Federal Institute of Technology, Lausanne (EPFL, Switzerland) in order to monitor real service conditions. The pile is the only geothermal pile connected to its raft and is 25.8 m long and 0.88 m in diameter. The absorber pipes are connected in parallel through collectors at the pile inlet and outlet (Laloui et al., 2003).

The pile concrete Young's modulus was estimated using conventional compression tests on concrete samples (cylinders) and was found to be around 29.2 GPa (Knellwolf et al., 2011). The thermal expansion of the concrete is taken equal to 10^{-5} °C^{-1} (Choi and Chen, 2005; Stewart and McCartney, 2014). The pile is embedded in a layered soil made up of two thin alluvial layers at the top, a thick layer of moraine and the molasse bedrock at the base (Figure 3:1). The different parameters used to model the soil layers were estimated by Knellwolf et al. (2011) and are listed in Table 3:1. The interaction between the pile head and the overlying building is modelled as a linear spring whose stiffness K_h was estimated to be 2 GPa/m (Knellwolf et al., 2011). The mechanical load P applied to the EPFL test pile at the end of the building construction was estimated to 1000 kN (Knellwolf et al., 2011). Based on the soil properties used for the study, the factor of safety (i.e. the ultimate bearing force of the pile divided by the carried load P) of the EPFL test pile is approximately 13. In fact, this test pile was deliberately over-designed in order to prevent any potential damage caused by its heating and cooling.

Table 3:1 Soil parameters used to model the EPFL test pile, after Knellwolf et al. (2011)

Soil layer	A1	A2	B	C	D
Depth (m)	0 – 5.5	5.5 – 12	12 – 22	22 – 25	25 – 25.8
K_s (MPa/m)	16.7	10.8	18.2	121.4	–
q_s (kPa)	102	70	74	160	300
K_b (MPa/m)	–	–	–	–	667.7
q_b (MPa)	–	–	–	–	11

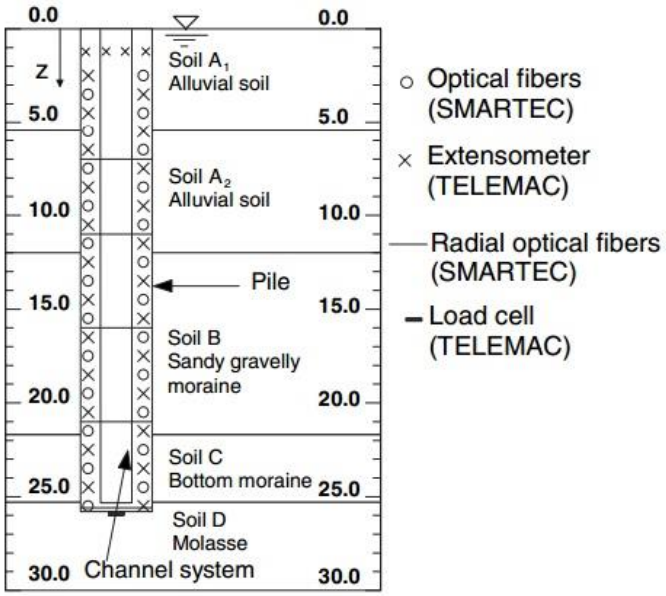

Figure 3:1 Stratigraphy and instrumentation of the EPFL test pile from Laloui et al. (2003)

The Lambeth College test pile [1]

The Lambeth test pile was built away from any existing building. This test pile was 22.5 m long with an upper diameter of 0.61 m and a lower diameter of 0.55 m (Figure 3:2). Mechanical loading was achieved with a jack mounted on a beam linked to anchor piles. The absorber pipes were deployed around the reinforcement cage of the pile; these were connected to a heat sink pile through a heat pump to allow investigating the effects of heating and cooling (Bourne-Webb et al., 2009). The pile thermal expansion and Young's modulus were estimated to 8.5 x 10^{-6} °C^{-1} and 40 GPa, respectively (Bourne-Webb et al., 2009). Knellwolf et al. (2011) back analysed the Lambeth College test pile as a part of the validation of Thermo-Pile software.

[1] Note that the modification of the parameters for the Lambeth College test pile analyses does not appear in the published paper "Towards a secure basis for the design of geothermal piles" by Mimouni T. and Laloui L. in Acta Geotechnica (2014) in which the original parameters proposed by Knellwolf et al. (2011) were used. The analyses presented in this thesis were remade using the boundary conditions proposed by Bourne-Webb et al. (2009), see Section 3.3.

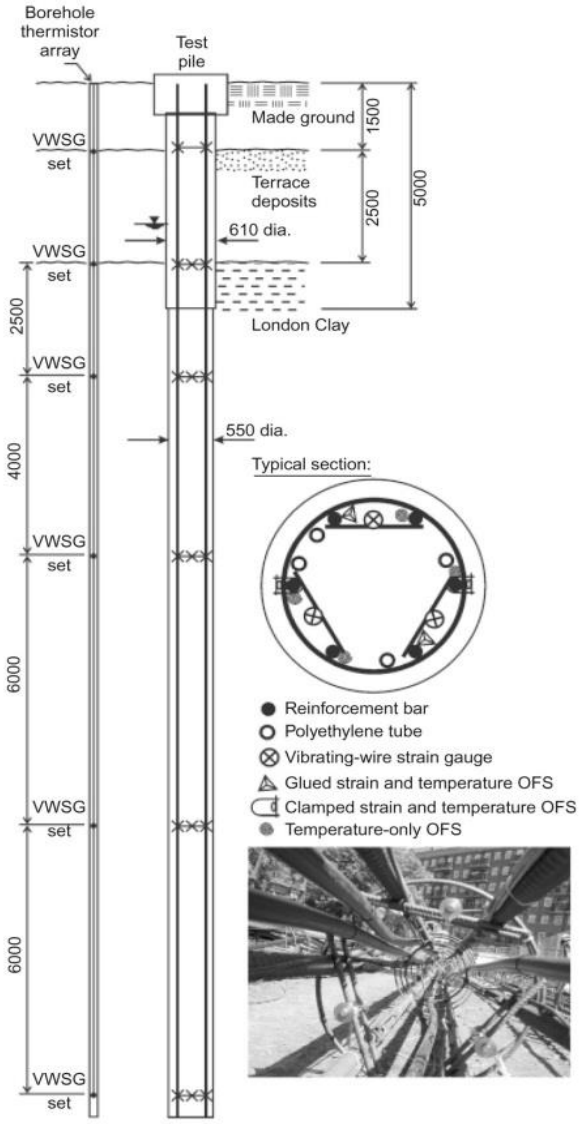

Figure 3:2 Stratigraphy of the Lambeth test pile, from Bourne-Webb et al. (2009)

They decided to ignore the first 6.5 m of soil because of weak mechanical properties and introduced a head resistance K_h despite Bourne-Webb et al. (2009) clearly identified a constant load boundary at the pile top. Therefore, the present study will use the boundary condition identified by Bourne-Webb et al. (2009). The ultimate shaft friction of the first soil layer, between 0 and 6.5 m, is found to be around 35 kPa based on the measurements reported by Bourne-Webb et al. (2009). No head stiffness is used and the rest of the parameters identified by Knellwolf et al. (2011) is used, the Menard modulus of the first layer being assumed to be the same as for the other layers (i.e. 45 MPa). These parameters are listed in Table 3:2. With a mechanical load of 1200 kN, the factor of safety (i.e. the ultimate load – 2472 kN – divided by the carried load) of the Lambeth College test pile was equal to 2.5 (Ouyang et al., 2011).

The impact of the proposed modifications on the analyses carried out by Knellwolf et al. (2011) are thoroughly discussed in the Section 3.3 where a method to account for thermal unloading is proposed.

Table 3:2 Soil parameters used to model the Lambeth test pile, after Knellwolf et al.(2011) and modified according to Bourne-Webb et al. (2009)

Soil layer	1	2	3	4
Depth (m)	0 – 6.5	6.5 – 10.5	10.5 – 16.5	16.5 – 22.5
E_M*(MPa)*	45	45	45	45
q_s (kPa)	35	60	70	80
q_b (kPa)	–	–	–	460

3.2.1.2 Idealized case studies

Three idealized cases outlined in the work of Knellwolf et al. (2011) were slightly modified in order to quantify the sensitivity of the main groups of onshore compression piles to temperature changes: floating piles, which transfer their load to the ground through shaft friction exclusively, end-bearing piles, which transmit their load to a stiff substratum mainly through base compression, and semi-floating piles, which represent an intermediate configuration where both shaft friction and pile tip compression play a significant role in the bearing mechanisms. The selected configurations remain simple in order to properly identify the mechanisms induced by the heating and cooling of the piles. Therefore, a single 10 m long pile with a diameter of 0.5 m is investigated. It is embedded in a homogeneous layer of soil whose characteristics vary according to the pile type; these parameters are listed in Table 3:3. The ultimate shaft friction and base reaction are chosen so that the ultimate bearing forces have the same order of magnitude. The mechanical load P applied to each pile was chosen so that the ultimate bearing force of the piles is equal to 2.5 times P (i.e. the factor of safety for each pile is 2.5). Head stiffnesses were taken equal to 10 GPa/m for all cases. The Young's modulus and thermal expansion coefficient of the pile are taken to be equal to 30 GPa and 10^{-5} °C^{-1}, respectively.

Table 3:3 Soil parameters, pile-structure stiffness and temperature variations considered for the floating pile, end-bearing pile and semi-floating pile

Parameters	Floating pile	Semi-floating pile	End-bearing pile
Ultimate shaft friction q_s (kPa)	100	100	0
Ultimate base reaction q_b (MPa)	0	9	9
Mechanical load P (kN)	628	1335	707
Menard modulus E_M (MPa)	20	60	60
Head stiffness K_h (GPa/m)	10	10	10
Temperature variation ΔT (°C)	-10 – +60	-10 – +60	-10 – +60

3.2.2 Methods

3.2.2.1 Bearing capacities of axially loaded piles

The bearing capacities of conventional axially loaded piles (for a load P) take two forms. The base reaction Q_b transfers a part of the load to the soil through compression of the soil below the pile tip, while the shaft friction Q_s transfers a part of the load to the soil through shear stress at the pile-soil interface.

The mobilisation of bearing capacities can be modelled with the load-transfer approach (Seed and Reese, 1957; Coyle and Reese, 1966). The pile-soil interaction system is represented by an elasto-plastic model, which utilises the load-transfer curves that link the mobilised bearing forces to pile displacements (Randolph and Wroth, 1978; Armaleh and Desai, 1987; Frank et al., 1991). The load-transfer curves employed in the present study were proposed by Frank and Zhao (1982) and are defined using a plateau value q and an initial slope K (Figure 3:3).

The ultimate shaft friction q_s and base reaction q_b represent the maximum resistance that a layer of soil can provide and those quantities can be estimated based on the soil properties (Frank and Zhao, 1982).

The elastic branches K_s and K_b of the load-transfer curves can be estimated from the Menard pressuremeter modulus E_M in cohesive soils with (Frank and Zhao, 1982; Amar et al., 1991):

$$K_b = 11\frac{E_M}{D}$$

$$K_s = 2\frac{E_M}{D}$$

Equation 3:1 Elastic slopes of the load-transfer curves for a cohesive soil as proposed by Frank and Zhao (1982) and Amar et al. (Frank and Zhao, 1982; 1991)

Shaft friction and base reaction are mobilised according to an elastic branch until they reach half of their ultimate values. Then, the slopes of the load-transfer curves change to a fifth of the elastic moduli. When shaft friction or base reaction reaches its ultimate value, the load-transfer curves follows a plateau equal to the ultimate resistance. For both bearing mechanisms, unloading is parallel to the elastic branch (Figure 3:3).

Assuming that the pile cross section is circular and constant with depth, the mobilised bearing forces through shaft friction $Q_{s,mob}$ and base compression $Q_{b,mob}$ can be estimated using:

$$Q_{s,mob} = \pi D\int_0^L t_s.dz$$

$$Q_{b,mob} = \frac{\pi D^2}{4}t_b$$

Equation 3:2 Mobilised shaft friction and base compression

where t_s represents the shaft friction mobilised at a depth z along the pile shaft, t_b represents the compression at the pile tip, which is assumed to be constant across the pile base, and L is the pile length.

Similarly, the bearing resistances $Q_{s,ult}$ and $Q_{b,ult}$ can be computed from the ultimate shaft resistance and base compression with:

$$Q_{s,ult} = \pi D \int_0^L q_s .dz$$
$$Q_{b,ult} = \frac{\pi D^2}{4} q_b$$

Equation 3:3 Ultimate shaft friction and base compression

3.2.2.2 Bearing capacities of geothermal piles

As a foreword to this section, the terms "redistribution" and "variation" of mobilised bearing forces are discussed for a geothermal pile. Indeed, the term "redistribution" implies that no overall variation of the total mobilised bearing resistance is experienced. Conversely, the term "variation" implies a change (i.e. increase or decrease). The following paragraph investigates when redistribution and variation occur.

Let us consider two identical piles that are loaded with the same load *P*. Pile #1 is below a raft that is stiff enough so that load redistribution can occur while pile # 2 is below a soft raft so that the boundary condition at its top is a constant load.

When the piles are heated or cooled, they expand or contract and local variations of the mobilised bearing forces due to thermal displacements will be observed. However, writing the global static equilibrium for each pile after a temperature change yields:

$$P + R_1 = Q_{mth1}$$
$$P = Q_{mth2}$$

Equation 3:4 Static equilibrium of piles under stiff and soft rafts after a temperature variation

where R_1 is the reaction of the raft to the head heave of pile #1, and Q_{mth1} and Q_{mth2} are the mobilised bearing forces under mechanical and thermal loads for pile #1 and pile #2, respectively.

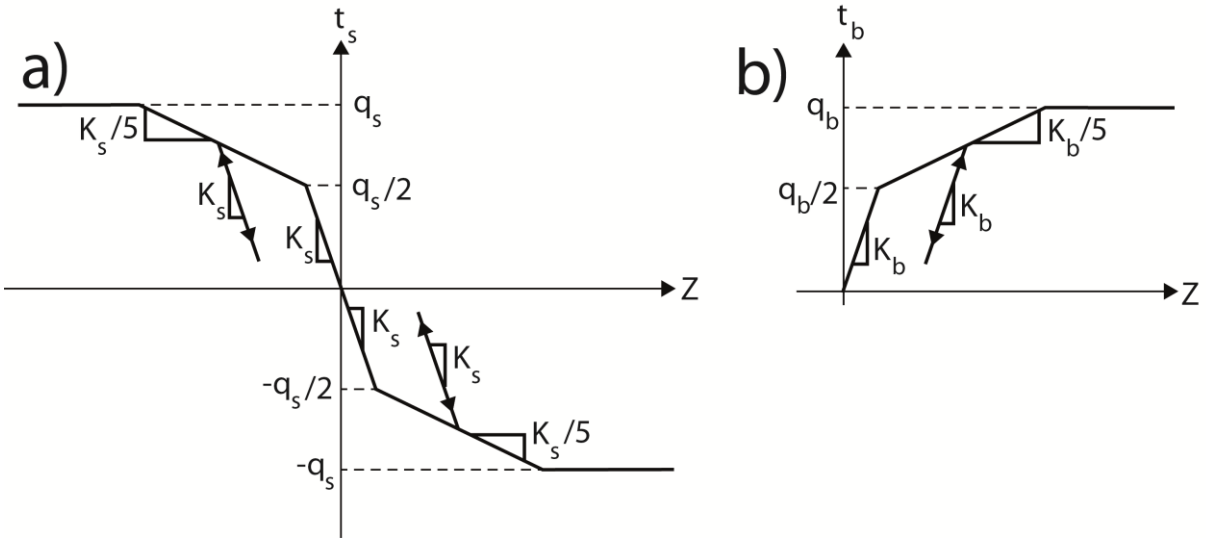

Figure 3:3 Example of load-transfer curves used for shaft friction (a) and base compression (b); z is the displacements, taken positive when downward

Obviously, pile #1 and pile #2 mobilised the same bearing capacities prior to any temperature variation since they were carrying the same dead load *P*. Nevertheless, once they experience a temperature variation, a redistribution of mobilised bearing forces occurs along pile #2 while a variation is observed in pile #1. Indeed, since pile #2 is only subjected to *P* from the exterior, its static equilibrium implies that the mobilised bearing forces remain equal to *P*. Conversely, the head heave of pile #1 induces a new external force on the pile through the raft reaction R_1.

This rationale can also be carried out for large foundations with energy piles. Under temperature changes, each pile will experience variations in their mobilised bearing capacities but, as far as the load carried out by the foundation remains constant, only redistribution will occur across the whole foundation.

Therefore, piles may experience variations in mobilised bearing capacities when load redistribution is possible (i.e. when the raft is rigid enough).

In the present study, geothermal piles are represented as circular axially loaded piles undergoing axial thermal expansion or contraction under thermal loading. Their deformations occur around the null point, which does not move for a given temperature variation. Therefore, the portion of the pile above the null point experiences upward displacements while the part below it experiences downward displacements during thermal expansion of the pile. Conversely, the section of the pile above the null point settles while the part below it heaves when a pile is cooled (i.e. during thermal contraction) (Bourne-Webb et al., 2009; Knellwolf et al., 2011).

Thus, the geothermal pile can be divided into two parts delineated by the null point. The part above the null point will be later called the "upper part of the pile" while the "lower part of the pile" will refer to the section below the null point.

Therefore, the overall mobilised bearing force Q_{mob} can be split into a portion $Q_{mob,up}$ acting on the upper part of the pile and a portion $Q_{mob,low}$ acting on the lower part of the pile. Similarly, the shaft friction can be divided into a portion acting on the upper part of the pile ($Q_{s,mob,up}$) and a portion acting on the lower part of the pile ($Q_{s,mob,low}$) (see Equation 3:5).

Furthermore, a capping force may develop under the reaction of the supported structure (raft, wall…) as the pile head heaves or settles. In Equation 3:5, this action is combined with the mechanical load *P* into a term Q_h, and it is further developed in Equation 3:7.

Thus, Q_{mob}, $Q_{mob,up}$ and $Q_{mob,low}$ can be expressed as follows:

$$Q_{mob} = Q_{mob,up} + Q_{mob,low}$$
$$Q_{mob,up} = Q_h + Q_{s,mob,up}$$
$$Q_{mob,low} = Q_{b,mob} + Q_{s,mob,low}$$

Equation 3:5 Decomposition of mobilised bearing capacities along energy piles

Let z_{NP} be the depth of the null point and *L* the pile length. The terms $Q_{s,mob,low}$ and $Q_{s,mob,up}$ can then be computed from Equation 3:2 as follows:

$$Q_{s,mob,up} = \pi D \int_{0}^{z_{NP}} t_s.dz$$

$$Q_{s,mob,low} = \pi D \int_{z_{NP}}^{L} t_s.dz$$

Equation 3:6 Mobilised shaft friction and base compression

It is obvious that the null point definition does not hold when the temperature variation is zero. Therefore, the graphs presented in the following analyses will exhibit a discontinuity in 0 for the two friction terms given in Equation 3:6 while the base and head reactions are defined for a zero temperature variation (i.e. under mechanical load only).

The head action Q_h includes the mechanical load P and the raft capping reaction, which is modelled as a linear elastic stiffness (K_h) linking the head reaction to the head heave z_h:

$$Q_h = P + \frac{\pi D^2}{4} K_h z_h$$

Equation 3:7 Pile head action

Thus, the mobilised bearing capacities will vary as follows when the pile is heated:

- The mobilised resistance at the head of the pile, Q_h, increases because the pile head heaves.
- The mobilised shaft friction along the upper part of the pile, $Q_{s,mob,up}$, decreases because axial displacements occur in the upward direction. Negative friction can develop depending on the magnitude of the displacements.
- The mobilised shaft friction along the lower part of the pile, $Q_{s,mob,low}$, increases because axial displacements occur in a downward direction. The ultimate shaft friction may be reached depending on the magnitude of the temperature increase.
- The mobilised base resistance, $Q_{b,mob}$, increases because thermally-induced axial displacements in the lower part of the pile occur in the downward direction. The ultimate base reaction may be reached depending on the magnitude of the displacements.

Conversely, when the pile is cooled:

- The mobilised resistance at the head of the pile, Q_h, decreases. The capping reaction of the raft occurs in the upward direction and pulls on the pile head as it settles.
- The mobilised shaft friction along the upper part of the pile, $Q_{s,mob,up}$, increases because the axial displacements occur in the downward direction.
- The mobilised shaft friction along the lower part of the pile, $Q_{s,mob,low}$, decreases because axial displacements occur in the upward direction.
- The mobilised base resistance, $Q_{b,mob}$, decreases because the pile tip heaves. If the pile tip heave is large enough that the contact between the pile base and the soil is broken (i.e., higher than the elastic unloading displacement at the pile base), the base reaction reaches zero.

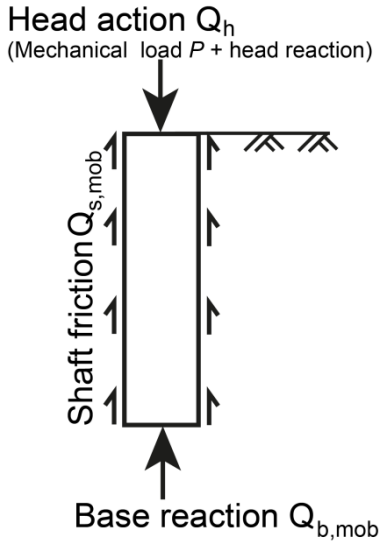

Figure 3:4 Schematic of forces acting on a pile foundation

The sign convention adopted in the analyses is as follow (Figure 3:4):

- Upward shaft friction is taken as positive
- A positive base reaction acts upwards
- The mechanical load P is given as positive but acts downward
- Upward displacements are taken as positive
- K_h is a positive quantity so that the positive head reaction acts downward, in order to have the same sign convention as the mechanical load *P*

These conventions were used in order to obtain positive left and right hand sides in the pile equilibrium equation:

$$P + \frac{\pi D^2}{4} K_h . z_h = Q_{s,mob} + Q_{b,mob}$$

Equation 3:8 Pile static equilibrium with linear elastic interactions with the overlying structure

In summary, the mobilised bearing capacities of geothermal piles are expected to vary with temperature and to be redistributed according to the position of the null point.

3.2.2.3 Variations in mobilised shaft friction

While evolution of the base reaction and head actions are simple to estimate since they occur at single depths, the mobilisation of friction along the pile shaft is less straightforward.

To simplify the analysis, one can split the mobilised shaft friction $t_{s,mob}$ into a static portion $t_{s,mob,static}$ (mobilised under the mechanical load *P*, prior to any temperature change) that is independent from the temperature and a portion $\Delta t_{s,mob}$ that depends on temperature and depth as follows:

$$t_{s,mob}\left(\Delta T, z\right) = t_{s,mob,static}\left(z\right) + \Delta t_{s,mob}\left(\Delta T, z\right)$$

Equation 3:9 Decomposition of the locally mobilised shaft friction

As described above, heating (cooling) the pile causes downward (upward) displacements in the area of the lower part of the pile, while upward (downward) displacements occur in the upper part of the pile. By definition, the null point is the point where thermally-induced displacement is zero and consequently where the shaft friction remains unchanged (i.e., $\Delta t_{s,mob}(\Delta T, z_{NP})=0$).

As a result, thermally-induced displacements always increase from the null point to the pile ends (i.e. head and tip). The shaft friction in homogenous soils layers will vary depending on the location of a layer relatively to the null point as follows:

- The greatest variation in shaft friction, $\Delta t_{s,mob}$, within a layer of soil below the null point occurs at its base, while the smallest variation is located at the top of the soil layer. The friction increases with heating and decreases with cooling.
- The greatest variation in shaft friction within a layer of soil above the null point occurs at its top while the smallest variation is located at the base of the layer. The friction decreases with heating and increases with cooling.

In summary, the shaft friction is divided into a mechanically mobilised portion, which remains constant over all temperatures, and a portion that varies with the temperature of the pile.

3.2.3 Analyses

3.2.3.1 Full scale in situ case studies

The EPFL and Lambeth College test piles were utilized as real case illustrations. Temperature variations in the piles were assumed to be between -10°C and +60°C. Therefore, the absolute temperature of the piles varies between +1°C and + 70°C, the upper limit being representative of extreme solar thermal ground heat storage through geothermal foundations.

Evolution of mobilised bearing capacities with temperature

EPFL test pile

The semi-floating behaviour of the EPFL test pile is evidenced looking at the distribution of bearing capacities with similar bearing forces for base compression and shaft friction. Heating of the pile results in increased head action, base reaction and mobilised shaft friction below the null point while the friction along the upper part of the pile decreases and can even become negative. Cooling the pile reduces the shaft friction in the lower part of the pile as well as the base reaction and head action, but increases the mobilised shaft friction above the null point. This is illustrated in Figure 3:5 for the EPFL test pile. Changes in the slopes of the mobilised bearing capacities are observed at around +20°C, when the null point moves upward (Figure 3:14). Indeed, ascension of the null point along the pile axis enlarges the lower part of the pile while it reduces the upper part of it. As a result, the part of the pile available to generate upward displacements through thermal expansion is shortened. Therefore, the head reaction does not vary linearly despite the fact that the head stiffness K_h is set as a constant.

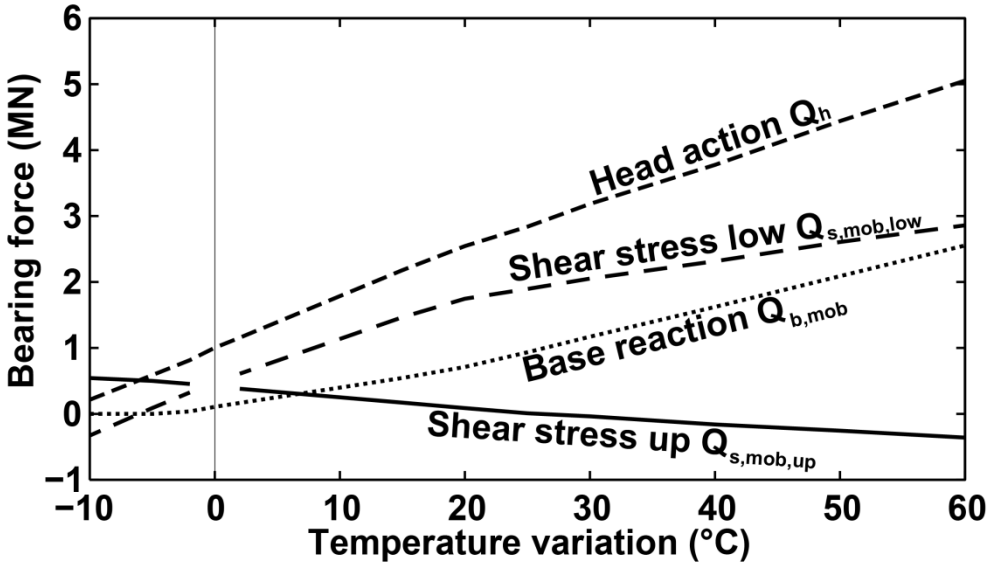

Figure 3:5 Simulated evolution of the bearing forces mobilised by the EPFL test pile under monotonic temperature variation

Sharp variations in shaft friction occur along the pile close to a zero temperature variation, mainly due to the large displacements of the null point with temperature in that narrow interval. Furthermore, it is not possible to differentiate the terms in Equation 3:5 because the null point is not defined for a null temperature variation. However, the sum of friction and base reaction remains equal to the head action (i.e. dead load plus raft reaction), ensuring the static equilibrium of the pile. Therefore, the mobilised bearing capacities increase with temperature. Trends were evaluated by performing linear regressions along linear parts of the curves between +0 °C and +20 °C. These estimates were then compared to those of Amatya et al. (2012) based on field measurements.

The thermal stress induced at the head was estimated to be -150 kPa/°C based on the field data whereas it is equal to -115 kPa/°C based on the numerical analyses. Induced pile tip compression was estimated to be -79 kPa/°C from the field data while the numerical analyses suggest a value of -62.5 kPa/°C.

Lambeth College test pile

Since the Lambeth test pile qualifies as a floating pile, little base compression is observed. The carried load is mainly transmitted to the soil through shaft friction. As expected, an increase in the pile temperature leads to greater mobilised shaft friction in the lower part of the pile since it experiences downward displacements and a relief in the upper part of the pile. Conversely, cooling the pile induces a decrease in the mobilised shaft friction along the lower part of the pile while it increases in the upper portion of the pile. The small amount of base compression can be lost as the pile tip heaves when the pile is cooled, which evidences the floating character of the Lambeth College test pile in Figure 3:6. Finally, the head action remains constant and equal to the pile load as the boundary condition at the pile top is of constant load type.

Trends were estimated along the linear parts during heating (i.e. between +0°C and +20°C). Amatya et al. (2012) estimated that there is no thermally-induced stress at the Lambeth test pile tip or head.

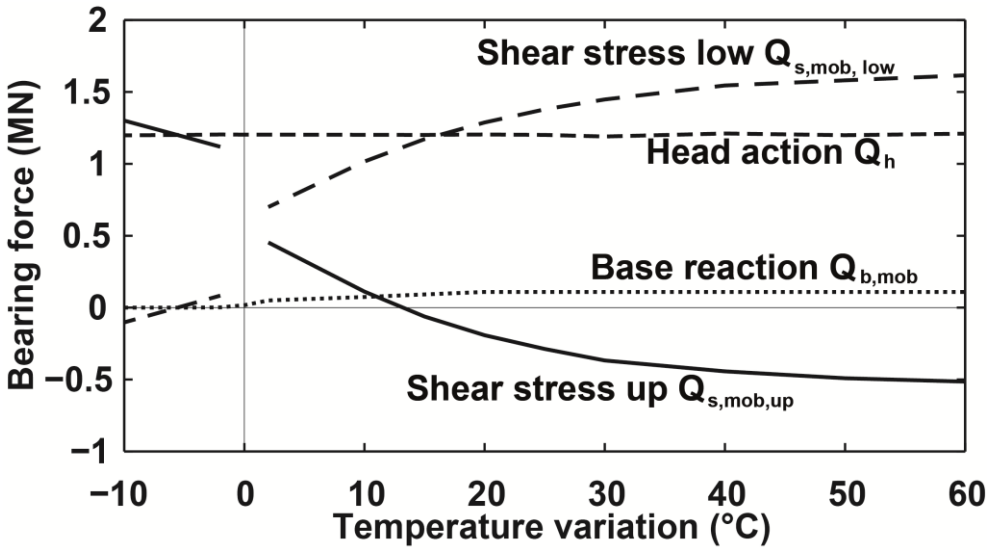

Figure 3:6 Simulated evolution of the bearing forces mobilised by the Lambeth test pile under monotonic temperature changes

Using a constant load boundary condition at the pile top numerically implies that there is also no evolution of the pile mechanical load while a small increase in base reaction of 4.1 kPa/°C was modelled. In conclusion, the estimated variations of mobilised bearing capacities are in agreement with field data.

Shat friction mobilisation process

EPFL test pile

The evolution of the shaft friction along the EPFL test pile is shown in Figure 3:7. As described in Section 3.2.2.3, the variations in shaft friction within a soil layer are greater at the boundary farthest from the null point. Ultimate shaft friction in soil layer B starts being mobilised from the layer base while layer C mobilises all its ultimate force for a temperature variation of +60 °C. Negative friction develops easily in the upper part of the pile during heating because the mechanical loading, prior to temperature variation, does not induce major friction mobilisation in this area (mainly due to the fact that the pile is over-designed). This case study highlights the importance of the initial mechanical loading as a starting point for the thermal loading.

Lambeth College test pile

The impact of heating or cooling on the mobilised shaft friction of the Lambeth College test pile shows that floating piles are very sensitive to thermal loadings. Shaft friction increases below the null point as the pile is heated. The greatest variations in shaft friction are observed at the lower edges of soil layers (Section 3.2.2.3). Ultimate shaft friction along the first soil layer is mobilised under mechanical load only. Therefore, cooling the pile increases this mobilisation and ultimate shaft friction starts being mobilised at the top of the second soil layer. Conversely, the ultimate shaft friction is mobilised along the lower half of the pile while significant negative friction developed along the upper part for a temperature increase of +50 °C (Figure 3:8).Finally, the null point is lower during cooling than during heating.

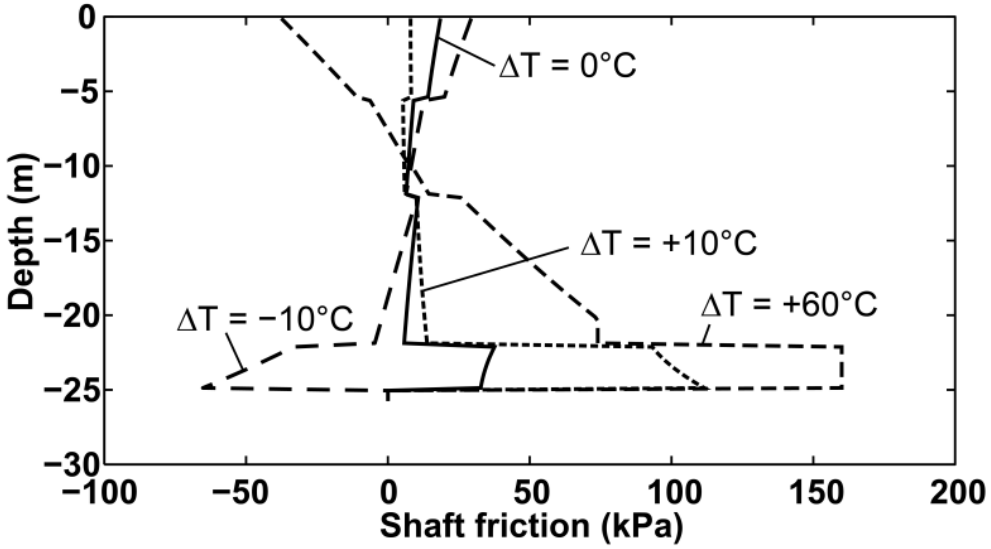

Figure 3:7 Simulated evolution of the profile of mobilised shaft friction along the EPFL test pile

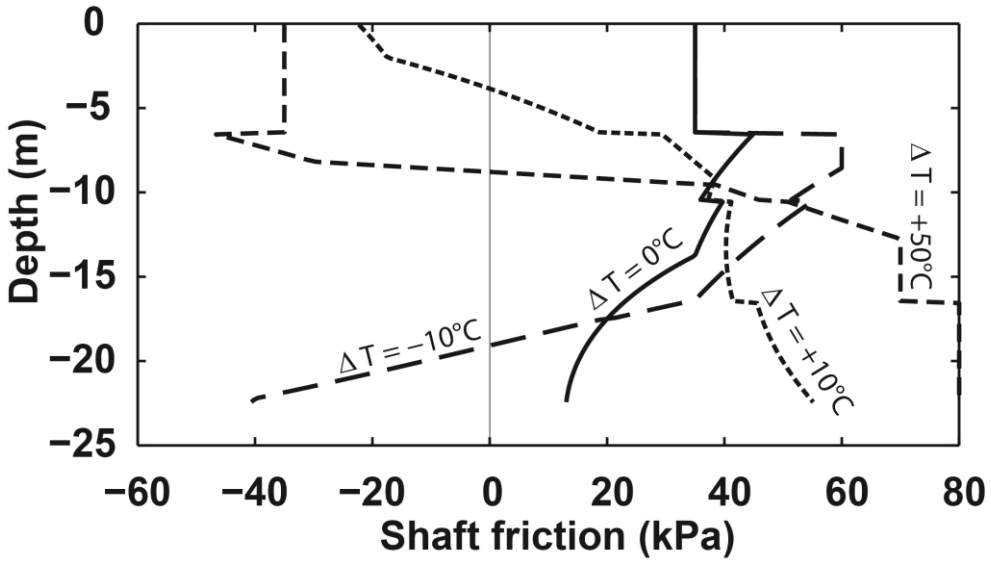

Figure 3:8 Simulated evolution of the profile of mobilised shaft friction along the Lambeth test pile

3.2.3.2 Idealized case studies

Three idealized case studies were investigated in order to evidence the differences in thermomechanical responses of different pile bearing mechanisms: floating, semi-floating and end-bearing piles.

Evolution of mobilised bearing capacities with temperature

Floating pile

The floating pile case study was modelled with no base resistance so that it does not appear on Figure 3:9 (i.e. it is equal to zero). As expected, the head reaction and shaft friction along the lower part of the pile increase with temperature while the shaft friction along the upper section of the pile decreases. The bearing capacity of the idealized floating pile is never reached for the temperature

variations investigated. Indeed, the thermal expansion of the pile induces a reaction at the pile head that is almost equal to the pile mechanical load (i.e. the load on the pile is doubled from 0.6 MN at +0°C to about 1.2 MN at +60°C) while the factor of safety of the pile is equal to 2.5 (i.e. the pile can mobilise forces up to 2.5 times its mechanical load).

The behaviour of a semi-floating pile is shown by the non-negligible base compression observed in Figure 3:10. Base compression and shaft friction along the lower part of the pile increase with temperature while the shaft friction along the upper portion of the pile decreases. The head reaction increases as the pile head heaves with temperature. In that case, the head action is almost doubled for a temperature increase of +60 °C so that the initial factor of safety of 2.5 still prevents the ultimate bearing force from being mobilised. The transition in shaft friction from positive to negative temperature variations is sharper in the semi-floating pile than in the floating pile because of the importance of dissymmetry in the pile confinement.

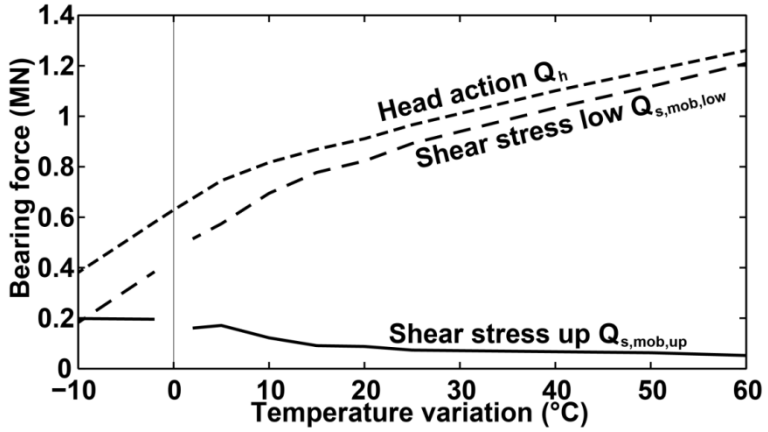

Figure 3:9 Simulated evolution of the bearing forces mobilised by the idealized floating pile under monotonic temperature variations

Semi-floating pile

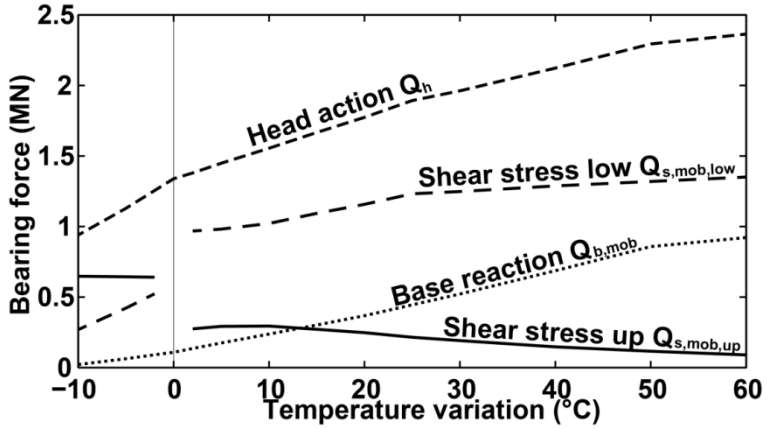

Figure 3:10 Simulated evolution of the bearing forces mobilised by the idealized semi-floating pile under monotonic temperature variation

End-bearing pile

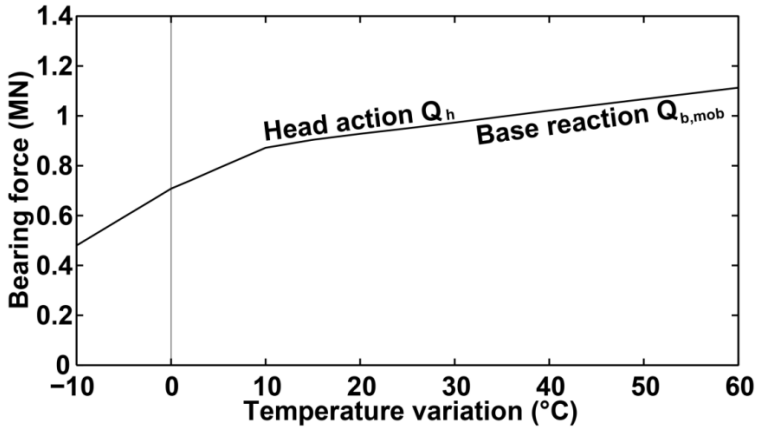

Figure 3:11 Simulated evolution of the bearing forces mobilised by the idealized end-bearing pile under monotonic temperature variation

End-bearing piles are characterized by low shaft friction. Therefore, the load is mainly transferred to the ground through pile tip compression. As a result, the base compression equals the head load at any time. The compression induced by the mechanical load only (i.e. for zero temperature variation) is lower than 0.8 MN so that it remains within the elastic domain of the t_b-z curve (i.e. from 0 to about 8.836 MN). Therefore, the single slope change observed during heating for a temperature increase of +10 °C suggests that:

- for a temperature increase between 0 and +10 °C, the pile tip compression remains elastic;
- for a temperature increase between +10 and +60 °C, the pile tip compression is elasto-plastic.

Unloading of the pile tip during pile thermal contraction is expected to occur according to the same slope as elastic loading. However, Figure 3:11 shows a small slope change when changing from heating to cooling. This effect is attributed to the accuracy of the numerical analyses. Indeed, the determination of the null point depth, which drives the expansion or contraction of the pile, is achieved with an accuracy of 0.2 m in the present analysis (i.e. the 10 m long pile is divided into 50 identical elements).

Shaft friction mobilisation process

Floating pile

Evolution of the shaft friction profile with temperature is described in Figure 3:12. Mobilised shaft friction increases along the upper part of the pile and decreases along the lower part of it during heating, and vice-versa during cooling. The ultimate positive shaft friction starts to be mobilised from the pile tip during heating and negative friction can develop when cooling because of the relatively weak shaft friction mobilisation under mechanical loading.

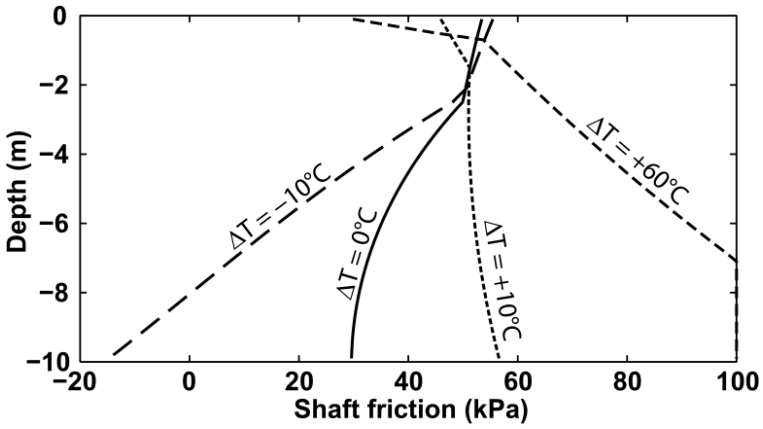

Figure 3:12 Simulated evolution of the profile of mobilised shaft friction along the idealized floating pile

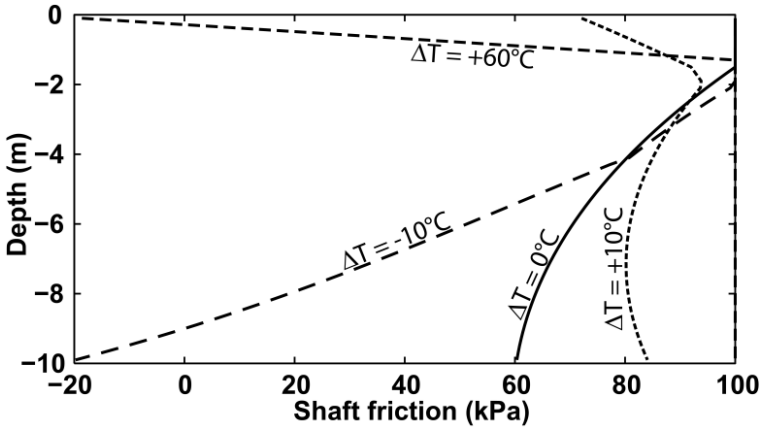

Figure 3:13 Simulated evolution of the profile of mobilised shaft friction along the idealized semi-floating pile

Semi-floating pile

The mechanical load applied to the semi-floating pile is two times greater than the loads applied to the two other idealized case studies in order to keep a safety factor of about 2.5. As a result, the shaft friction mobilised under mechanical loading is greater than that observed for the floating pile. Therefore, ultimate positive shaft friction is mobilised along the whole lower portion of the pile for a temperature increase of +60 °C while negative friction develops close to the pile head (Figure 3:13).

3.2.4 Non-failing mechanisms and pile serviceability

3.2.4.1 In situ test piles

When an energy pile is heated, its null point will tend to rise (Figure 3:14) because of the evolution of the different stiffnesses representing the soil (i.e. base compression and shaft friction stiffnesses K_b and K_s) and the structure (head stiffness K_h). Indeed, the pile-structure interaction is represented by a linear spring whose value does not change, while the soil is modelled with nonlinear springs whose stiffnesses decrease with the magnitude of the pile displacements. As a result, monotonically expanding the pile induces a reduction in the load-transfer stiffness while the head stiffness remains

constant. The soil representative stiffness can attain zero when the ultimate bearing force is mobilised. Therefore, since the apparent stiffness of the soil decreases during heating or cooling, the null point moves toward the pile head in order to maintain the pile equilibrium. Values of null point depth observed in the analyses are similar to those found when analysing field data. Amatya et al. (2012) give null point depths of -6 m and -12.5 m for temperature variations of +10 °C and +18 °C, respectively, while the analyses give depths of -9.5 m and -12.75 m for the Lambeth and EPFL test piles, respectively. The differences between the observations and the model may come from the fact that the Lambeth College test consisted in a cooling-heating sequence (see Section 3.3).

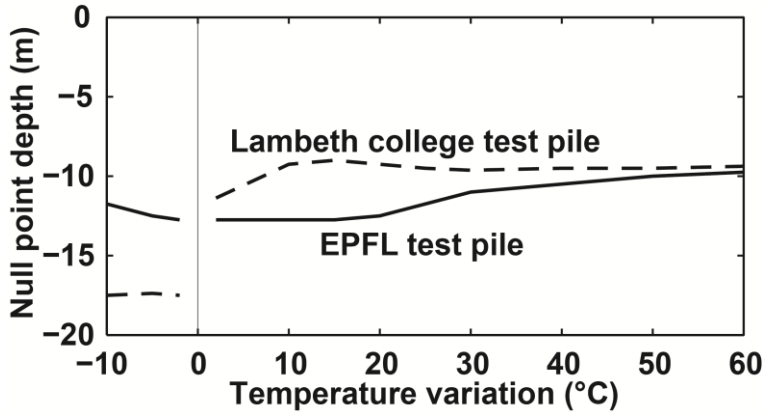

Figure 3:14 Simulated evolution of the depth of the null point with temperature variation for the EPFL and Lambeth test piles

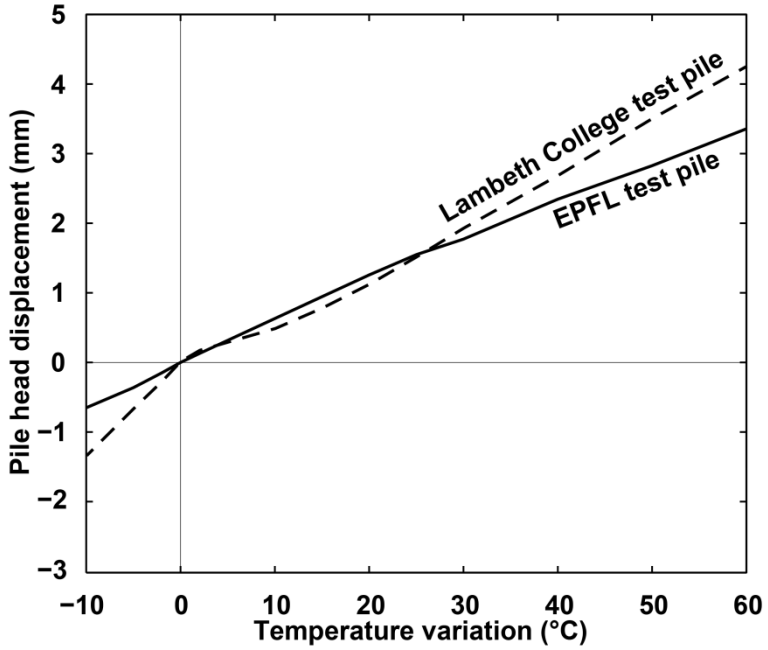

Figure 3:15 Simulated thermally-induced pile head displacements for the EPFL and Lambeth test piles. Displacements are taken relative to the pile settlement after mechanical loading. Positive displacements represent heave

The serviceability of the two test piles was also investigated and head displacements are plotted against temperature variations in Figure 3:15. The test piles experience head displacements up to 3-4 mm for extreme temperature variations of +60 °C. These displacements are to be tempered by the fact that the EPFL test pile was largely overdesigned, inducing greater thermal forces, while the Lambeth college test pile has no reaction structure at its top so that its head is free to move. Therefore, no geotechnical failure is observed under the stated assumption.

As a result, the design of energy piles is a question of serviceability limits as well as thermal efficiency and it reduces to make sure that the differential settlements remain within acceptable limits under thermal loading.

3.2.4.2 Idealized case studies

The pile serviceability was assessed for the three idealized piles whose head movements with temperature are given in Figure 3:16. These have similar serviceability and the head displacements do not exceed 0.5 mm (i.e. 1000 times less than the pile diameter). The non-failing mechanisms taking place within geothermal piles during non-cyclic temperature variation (i.e. increase or decrease) were described in the previous sections and it was shown that over-designing a geothermal pile might not be efficient from a serviceability standpoint. Therefore, the idealized cases were utilised to further investigate this aspect.

Different values of factor of safety (2.5, 5 and 10) were adopted for each of the three case studies and the comparisons are presented in Figure 3:16. Modifying the factor of safety is achieved by dividing the mechanical load P applied to the piles by 2 and 4 to obtain factors of safety equal to 5 and 10, respectively. Results of the simulations show that over-designing geothermal piles does not have a positive influence from a serviceability standpoint and it can even have a negative impact as serviceability limits are enlarged. This is mainly attributed to the greater internal forces generated by large pile diameters under the same temperature increase. For the three cases investigated, the factor of safety starts having a significant effect for temperature increases greater than +20 °C and the end-bearing pile seems to be more sensitive than the others. In conclusion, over-sizing geothermal piles may not provide better serviceability while it does increase the cost.

3.2.5 Conclusions

The present study gives some insight into the bearing mechanisms induced by non-cyclic temperature variations that occur in single geothermal piles.

Dividing the geothermal pile into two parts delimited by the null point allows a better understanding of the evolution of mobilised bearing capacities under either heating or cooling. Indeed, the section of the pile above the null point experiences upward displacement when heated and downward displacement during cooling. Conversely, the part of the pile that is below the null point settles during heating and heaves when cooled.

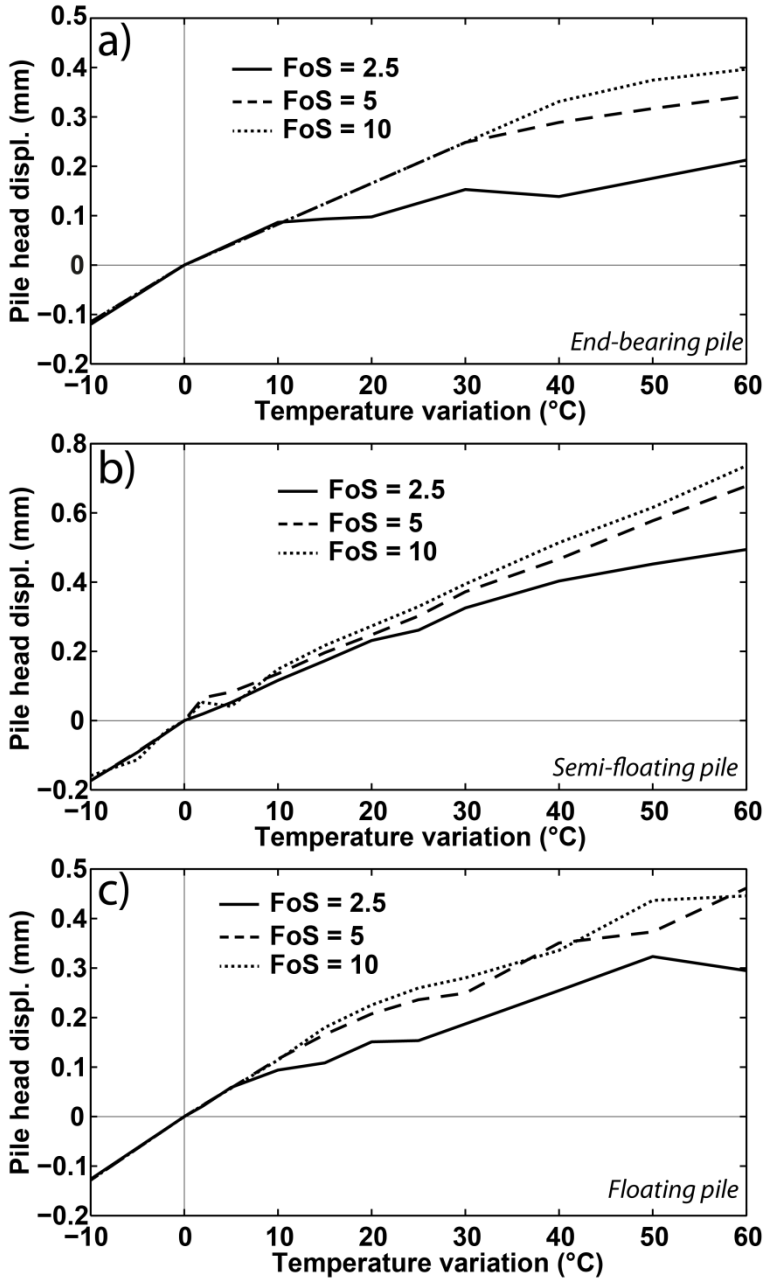

Figure 3:16 Simulated pile head displacements with temperature for () the end-bearing pile, (b) the semi-floating pile and (c) the floating pile. Pile head displacements are relative to the pile settlements after mechanical loading

Therefore, heating induces an increase in shaft friction along the lower part of the pile and leads to greater pile tip compression while it relieves the shaft friction along the upper part of the pile and increases the pile head heave. On the other hand, cooling induces a reduction in shaft friction along the lower part of the pile with a release of the pile tip compression while the shaft friction along the upper portion of the pile is increased and the pile head settles.

It is shown that the pile head heave or settlement induces a reaction from the supported structure that brings load variations to the pile. As a result, the bearing force mobilised by the pile varies with temperature.

Because the pile head heaves during heating, the capping effect of the structure on top of the pile induces an additional (downward) load which must be balanced by the mobilised bearing force. Therefore, the total mobilised bearing force increases when the pile is heated. Conversely, the pile head settlements observed when cooling induce a pulling (i.e. upward) reaction that relieves a part of the pile mechanical load. As a result, the overall mobilised bearing force of the pile is reduced.

However, if the pile-structure interaction is neglected in order to maximise the pile head movements so that the design remains conservative under monotonic thermal loads, it should not be ignored when cyclic thermal changes are considered. Indeed, the pile-structure stiffness determines the additional load applied to the pile head. Therefore, unloading after a monotonic temperature change will strongly depend on the mobilised bearing force prior to unloading. In this case, neglecting the pile-structure interaction may lead to a non-conservative design as the pile load prior to unloading could be badly estimated and the accumulated unrecoverable settlements might be underestimated. However it is not an easy task to estimate the head stiffness as it may involve the entire supported structure as well as the position and displacements of the other piles. As a conclusion, this particular aspect needs further investigation in order to estimate whether or not the differences between the two design methods, i.e. with and without head stiffness, are significant.

The mechanisms involved in the variations of the pile mobilized bearing forces under non-cyclic temperature variations were found to not induce failure because at least one point of the pile does not move, i.e. the null point, thus preventing excessive pile settlements in the investigated range of temperature variations. Finally, it is shown that increasing the factor of safety of geothermal piles may not improve the pile serviceability, while it can significantly increase the costs.

3.3 Accounting for thermal unloading with Thermo-Pile software

Knellwolf et al. (2011) have back analysed two major in situ tests on energy piles:

- The EPFL test pile below a 4 storey building (Laloui et al., 2003)
- The Lambeth College test pile (Bourne-Webb et al., 2009)

However, the assumptions linked to the Lambeth College test pile were not satisfactory when comparing with the conclusions drawn by Bourne-Webb et al. (2009). Indeed, Knellwolf et al. (2011) used a head reaction stiffness while Bourne-Webb et al. (2009) clearly stated that the boundary condition at the pile top was of constant load type. As a result, Knellwolf et al. (2011) decided to ignore the first 6.5 m of soil because of weak mechanical properties. But, one important aspect is that the experimental results from the Lambeth College test pile represent a cooling followed by a heating (Ouyang et al., 2011). As a result, plastic deformations along the pile should be expected. Nevertheless, Thermo-Pile as used by Knellwolf et al. (2011) did not include a thermal unloading/reloading path. As a result, trying to model the cooling and subsequent heating of the Lambeth College test pile as two separate phases was not the correct approach. However, the analyses they carried out for the EPFL test pile are still valid because the pile had such a high factor of safety (around 13, see Mimouni and Laloui) that heating and cooling remained within the elastic domain of the pile response, a fact previously suggested by Laloui et al. (2006) with finite element analyses.

Therefore, agreement between the numerical analysis using the improved version of Thermo-Pile and the experimental data was investigated.

3.3.1 Description of the model

The model presented in this section was developed to account for irreversible displacements observed at the soil-pile interface during heating and cooling cycles. The present analyses only consider one thermal loading and unloading after the mechanical initialisation.

Let consider that the heating represents the thermal loading phase and the cooling is the thermal unloading. We can then expect that:

- A point above both the heating and cooling null points will experience heave during heating with subsequent unloading of the shaft friction and will settle during cooling with the subsequent increase in mobilised shaft friction (Figure 3:17a)
- A point below both the heating and cooling null points will settle during heating with the subsequent increase in shaft friction and will heave during cooling, relieving the mobilised shaft friction (Figure 3:17b)
- A point above the heating null point and below the cooling null point will only heave with the subsequent unloading in mobilised shaft friction (Figure 3:17c)
- A point below the heating null point and above the cooling null point will only settle with the subsequent increase in mobilised shaft friction (Figure 3:17d)

Considering that cooling corresponds to the thermal loading and heating is the thermal unloading would lead to similar mechanisms but in a different order.

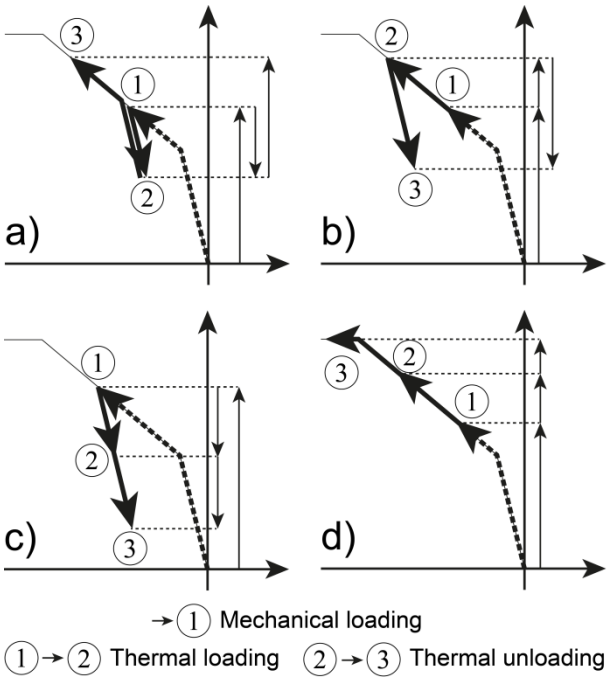

Figure 3:17 Possible sequences of thermal loading and unloading

These sequences have been implemented into Thermo-Pile software and simulations of tests 1 and 7 of the EPFL test pile and the cooling-heating test on the Lambeth College test pile were modelled. Comparisons of the experimental results with numerical analyses are given in the next section.

3.3.2 The new validation

3.3.2.1 EPFL tests 1 and 7

Test 1 was achieved when no structure was built on top of the test pile ("free head"). A constant temperature profile and a null pile load were used similarly to Knellwolf et al. (2011) . Initial mean temperature of the pile was 12.9 °C. Temperature variations and experimental strain profiles were estimated based on the measurements reported by Laloui et al. (1999; 2003). We used three profiles taken during heating (19, 22 and 26 May 1998) and three during cooling (27, 29 May and 11 June 1998). During this test, pile temperature increased from 12.9 °C to 34.7 °C and then cooled down to 15.6 °C. Eventually, it cooled down to its natural temperature but this was neither measured nor modelled.

Agreement between the numerical analyses and the experimental results (Figure 3:18) is good. Discrepancies are observed at the pile end during the passive cooling (Figure 3:18b) because we used constant temperature variations along the pile while experimental results suggest that the pile end cool faster than the pile middle (see Laloui et al. (2003)). Comparison between the measured and modelled pile top movements is also relatively good during heating and less satisfactory during cooling (Figure 3:20). This might arise from the fact that radial strains are not considered as discussed by Ouyang et al. (2011) about the analyses of the Lambeth College test pile.

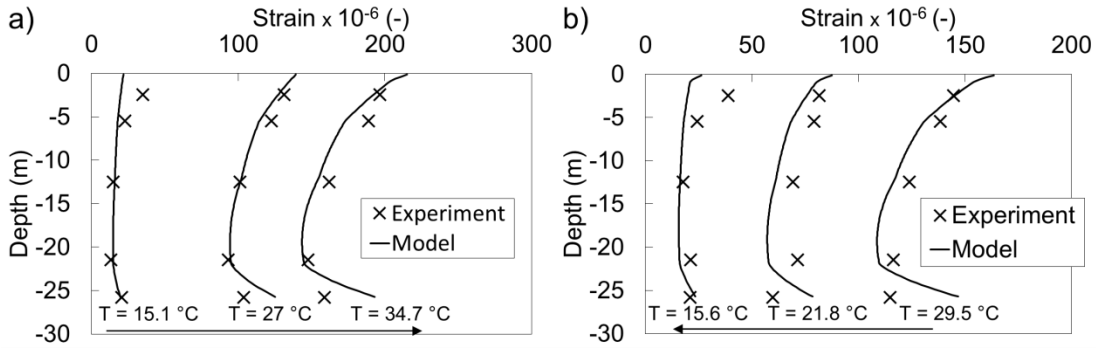

Figure 3:18 EPFL test 1 heating (a) and cooling (b). The mean pile temperature is indicated below each profile

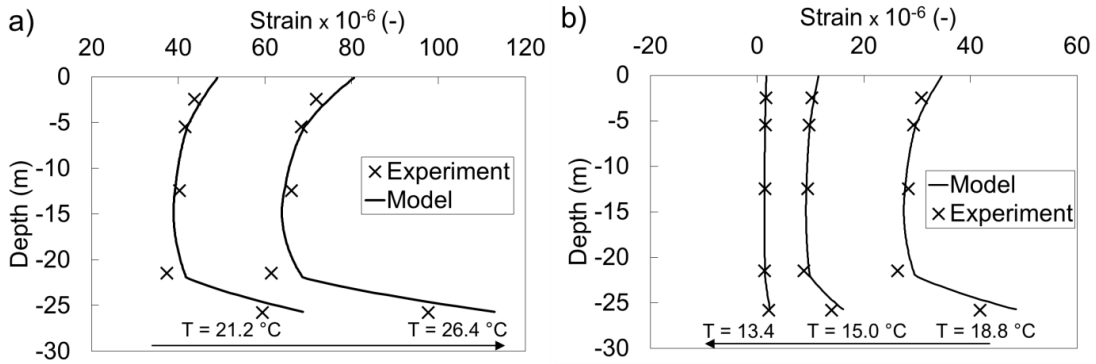

Figure 3:19 EPFL test 7 heating (a) and cooling (b)

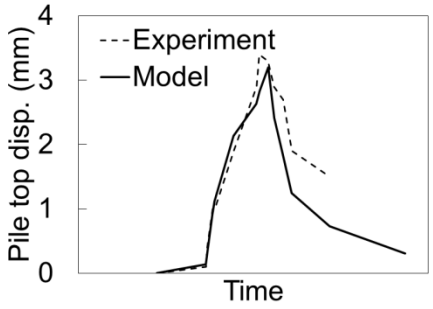

Figure 3:20 EPFL test 1, pile top displacement

Similar work was achieved for test 7 on the EPFL test pile. Data were taken from Laloui et al. (1999) and two profiles during heating (8 and 25 February 1998) and three during cooling (2 March and 6 April 1999, and 17 January 2000) were modelled. The numerical analyses correctly represent the experimental data (Figure 3:19).

3.3.2.2 Lambeth College test

The Lambeth College test pile, as modelled by Knellwolf et al. (2011) was not really representative for the test conditions reported by Bourne-Webb et al. (2009). We therefore decided to remake the validation of Thermo-Pile using the correct boundary conditions, that is to say:

- Null reaction stiffness at the pile top
- Constant pile load equal to 1200 kN
- Account for the first layer of soil (0 – 6.5 m) with an ultimate shaft friction of 35 kPa deduced from Bourne-Webb et al. (2009)
- Consider the thermal loading/unloading sequence $T_g \rightarrow T_g - 19$ °C $\rightarrow T_g + 10$ °C

The modelled strains show relatively good agreement with the measurements reported by Bourne-Webb et al. (2009). Ouyang et al. (2011) developed a tool similar to Thermo-Pile, but using different load-transfer curves with which they back analysed this test. The pile and ground properties were such that the initial mechanical settlement was well reproduced by the model. However, divergence was observed when cooling and then heating the pile. We reproduced the same simulations using Thermo-Pile software with the thermal unloading and the comparisons are given in Figure 3:22. The modelled mechanical settlement is around 1.3 mm while the observed and back-analysed settlements are around 2.3 mm. This might come from the fact that the test pile was first subjected to a load of 1800 kN and then unloaded down to 1200 kN, accumulating irreversible settlements, which was not modelled in the present analyses. Indeed, the settlement predicted by Thermo-Pile with a load of 1800 kN is of 2.5 mm, therefore consistent with this suggestion. However, the evolution trough cooling and heating is in agreement with the experimental observations when we shift the modelled curve upward to match the mechanical settlement (Figure 3:22).

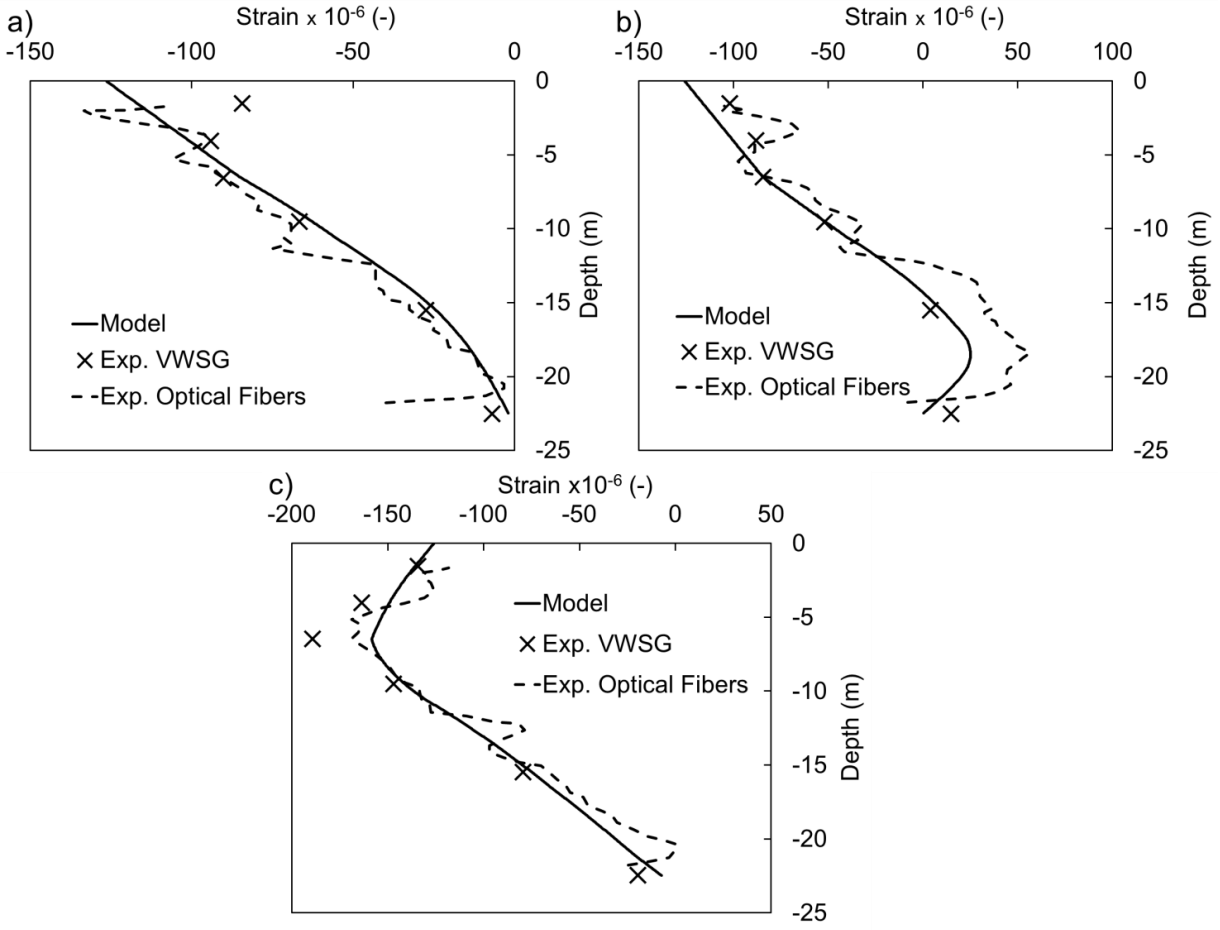

Figure 3:21 Strain profiles after (a) mechanical loading, (b) cooling and (c) heating

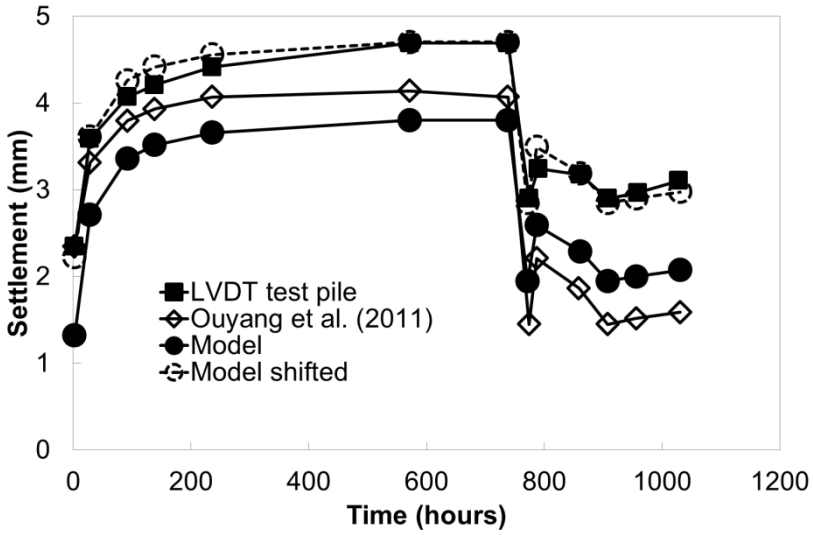

Figure 3:22 Pile top heave during the cooling and heating sequence T_g → T_g - 19 °C → T_g + 10 °C from experimental (Bourne-Webb et al., 2009) and numerical analyses (Ouyang et al., 2011)

3.3.3 Conclusions of the discussion

The loading/unloading path implemented in Thermo-Pile was validated against the EPFL and Lambeth College test piles. It was shown that the model is able to reproduce *in situ* observations. The proposed method was also tested for long term cyclic analyses but the accuracy of it did not allow getting consistent results and numerical propagation of error along the cycles prevented analyses to be achieved. Indeed, cumulated inaccuracy in determining the exact null point depth because of the pile discretisation leads to numerical deviation and inconsistent results (e.g. continuous and infinite pile settlement).

3.4 Asymptotic position of the null point

This section provides a mathematical formulation in which the asymptotic depth of the null point is expressed as a function of the soil characteristics and pile load under the same assumptions as Thermo-Pile (Knellwolf et al., 2011). We only consider piles subjected to a constant mechanical load. Indeed, for piles with a head stiffness, the asymptotic position of the null point is at the pile top as this is the only way to fully mobilise shaft friction (Mimouni and Laloui, 2014). The general expression of the pile external force equilibrium after a temperature variation is therefore given by:

$$P + \int_0^{z_{NP}} p(z)\,t_s(z)\,dz = \int_{z_{NP}}^{L} p(z)\,t_s(z)\,dz + A(z=L)\,t_b(z=L)$$

Equation 3:10 General pile equilibrium after a temperature change

where $p(z)$ and $A(z=L)$ are the pile perimeter at the depth z and pile base cross section, respectively, and $t_s(z)$ and $t_b(z=L)$ are the mobilised shaft friction at the depth z and base compression at the depth L, respectively. The idea of this section is to determine where the null point is located when the ultimate bearing capacities are mobilised locally (i.e. either positive or negative). Also, assuming that the pile cross section is circular (diameter D) and constant with depth leads to:

$$P + \pi D \int_0^{z_{NP}} q_s(z)\,dz = \pi D \int_{z_{NP}}^{L} q_s(z)\,dz + \frac{\pi D^2}{4} q_b(z=L)$$

Equation 3:11 Developed pile equilibrium after a temperature change

where $q_s(z)$ and $q_b(z=L)$ are the ultimate shaft friction at the depth z and ultimate base compression at the pile tip, respectively. This expression will be declined according to different cases presented in the next sections. For sake of simplicity, we consider that the ultimate shaft friction is constant for each of the soil layers. First, a pile embedded within a homogeneous soil is investigated. Then, a method for layered soils is proposed.

3.4.1 Pile embedded within a single homogeneous layer

Assuming that the ultimate shaft friction is constant throughout the soil and equal to q_{s0}, Equation 3:11 becomes:

$$P + \pi D q_{s0} z_{NP} = \pi D q_{s0} \left(L - z_{NP} \right) + \frac{\pi D^2}{4} q_b$$

Equation 3:12 External force equilibrium for a pile embedded in a homogeneous soil

Identifying the pile bearing capacity, given by:

$$Q_{ult} = \pi D L q_{s0} + \frac{\pi D^2}{4} q_b$$

Equation 3:13 Pile bearing capacity for a pile within a homogeneous soil

and isolating the asymptotic null point depth yields:

$$z_{NP} = \frac{Q_{ult} - P}{2\pi D q_{s0}}$$

Equation 3:14 Asymptotic position of the null point for a pile embedded in a homogeneous soil

From this, one can see how the applied load P influences the asymptotic position of the null point.

3.4.2 Pile embedded within a layered soil

Considering a layered soil requires using an assumption-validation method in order to find the null point asymptotic depth. Indeed, the integral in *Equation 3:11* needs to be divided into two parts and one has to know in which layer this division occurs. Therefore, the method proposed for a layered soil with N layers is to guess that the null point is in the i^{th} layer of soil, then estimate z_{NP} based on this guess, and finally verify if this guess holds. If it does not hold, then pass to the $i+1^{\text{th}}$ layer and repeat until the guess is verified (Figure 3:23).

Let l_k be the depth of the bottom of the k^{th} layer, $l_0 = 0$ is the soil surface, and q_{sk} the ultimate shaft friction of the k^{th} layer, being constant throughout it. Therefore, the equilibrium of forces above and below the null point that is guessed to be in the i^{th} layer yields:

$$P + \sum_{k=1}^{i-1} \pi D \left(l_k - l_{k-1} \right) q_{sk} + \pi D q_{si} \left(z_{NP} - l_{i-1} \right) = \pi D q_{si} \left(l_i - z_{NP} \right) + \sum_{k=i+1}^{N} \pi D \left(l_k - l_{k-1} \right) q_{sk} + \frac{\pi D^2}{4} q_b$$

Equation 3:15 Equilibrium of external forces applied to a pile embedded in a layered soil

Rearranging Equation 3:15 gives:

$$z_{NP} = \frac{1}{2\pi D q_{si}} \left[\frac{\pi D^2}{4} q_b + \sum_{k=i+1}^{N} \pi D \left(l_k - l_{k-1} \right) q_{sk} + \pi D \left(l_{i+1} + l_i \right) q_{si} - P - \sum_{k=1}^{i-1} \pi D \left(l_k - l_{k-1} \right) q_{sk} \right]$$

Equation 3:16 Position of the null point for a pile in a layered soil

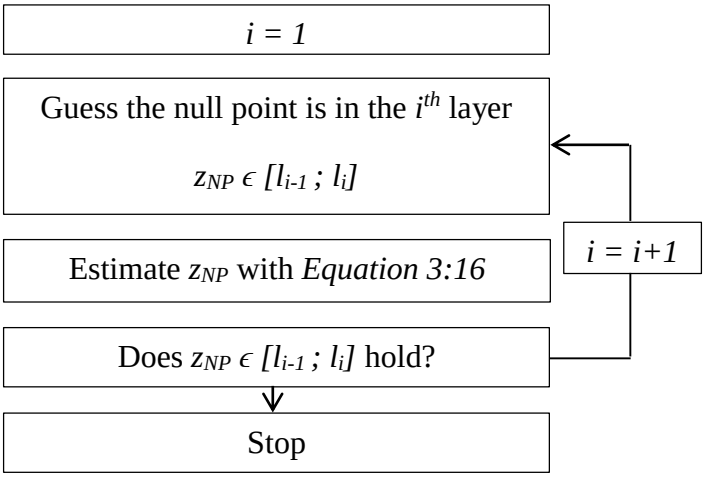

Figure 3:23 Algorithm used to determine the asymptotic location of the null point in a layered soil

3.4.3 Conclusions

This algorithm was tested and compared with the results of Thermo-Pile as it is based on the same assumptions, by imposing a virtually infinite temperature increase to the piles. Results were consistent with the asymptotic positions estimated with the present method. The extension of this method to ultimate bearing capacities depending on depth is achieved by more complex integrations as the ultimate bearing capacities will be a function of depth (e.g. Lang and Huder (1978)). In practice, the mobilisation of ultimate end bearing and ultimate shaft friction might rarely occur and under extreme temperature variations in very long piles in very stiff soils with brutal stress-strain response.

3.5 Piled beams with energy piles – Thermo-Piled-Beam

Interactions between energy piles through the rigidity of the supported structure can lead to significant variations in the behaviour of the foundation. Indeed, heating or cooling a whole piled foundation induces group movements that reduce the pile-structure-pile interactions by minimising the differential settlements. Conversely, heating only a part of a piled foundation leads to greater differential movements between the heated piles and the isothermal ones, inducing greater interactions (Dupray et al., 2014).

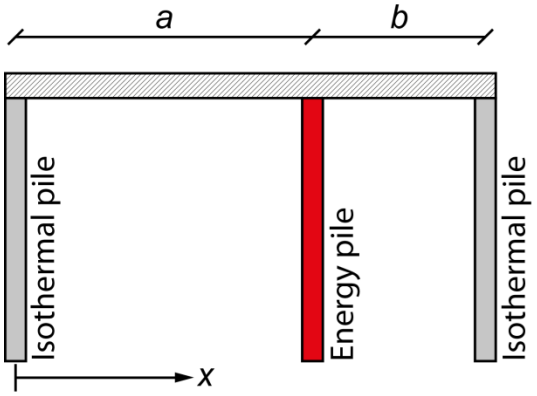

Figure 3:24 Schematic of the pile beam with two isothermal piles at the ends and one energy pile in between

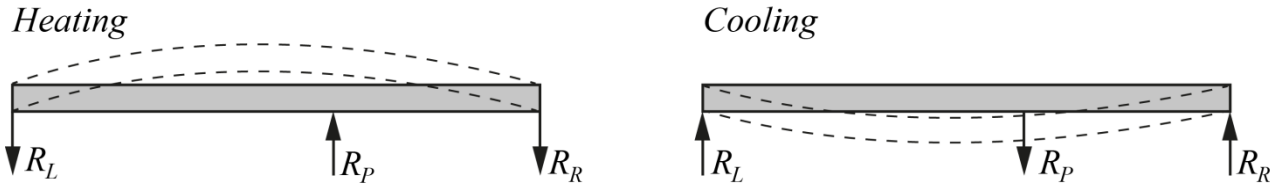

Figure 3:25 Actions and reactions at the pile heads

In situ measurements have shown that a major component of these interactions is the raft. Laloui et al. (1999; 2003) have shown that the degree of freedom of the test pile at EPFL decreased from 0.8 to 0.6 after the construction of the base floor, whereas it only decreased from 0.6 to 0.5 after the construction of the 4 building floors. As a result, understanding the impact of rafts and beams on the behaviour of the piles is an important component of their design because differential settlements should be minimised.

3.5.1 General method

The present section presents a method to investigate elementary piled beams with energy piles. This method couples Thermo-Pile with the Euler-Bernoulli beam model (Bauchau and Craig, 2009). Indeed, applications of energy piles with foundation beams have been reported for example by Diot (2012) in France. The energy piles are represented as punctual forces acting on the beam, and the isothermal piles are represented by inelastic supports. The reaction of the beam to the pile head movements is modelled with head stiffness K_h in Thermo-Pile (Knellwolf et al., 2011). The bearing of the soil on the raft is neglected at first, which remains conservative. The method is only described for isostatic cases that can be simply represented by two static piles at the beam ends and with one energy pile in between (Figure 3:24).

The energy pile expands or contracts under temperature variations. As a result, its head heaves or settles, inducing a reaction of the beam that is transmitted to the isothermal piles. Let R_P, R_L and R_R be the actions applied to the beam at the energy pile, left pile and right pile, respectively. At first, we consider that no mechanical load is initially applied to the beam so that before any thermal load, $P_P = P_L = P_R = 0$. If a load was applied to the beam (punctual or distributed), its distribution to the piles should be according to the beam static prior to any temperature variation. Then, the beam distributes the action R_P (due to the expansion of the energy pile) to the left and right piles according to its static equilibrium (Figure 3:25), given by:

$$\left.\begin{aligned} R_P - R_L - R_R &= 0 \\ a.R_L - b.R_R &= 0 \end{aligned}\right\} \Rightarrow \begin{cases} R_L = \dfrac{a}{L_b} R_P \\ R_R = \dfrac{b}{L_b} R_P \end{cases}$$

Equation 3:17 Static equilibrium of the simply supported beam

where a and b define the position of the energy pile below the beam (Figure 3:24) and L_b ($=a+b$) is the beam length. Therefore, an iterative process is required to solve the problem. The present approach is based on the following sequence:

- Initialisation is achieved by assuming the two isothermal piles to be fixed supports; their head heaves, v_L and v_R, are set to 0. The static of the pile then leads to a relationship linking the beam deflection v_P at the energy pile top to the force magnitude:

$$R_P = \frac{3E_b I_{Gz} L_b}{a^2 b^2} v_P = -P_P = K_h v_P$$

Equation 3:18 Reaction induced by the beam stiffness at the pile top

where I_{Gz} is the quadratic moment of the beam and E_b is the beam Young's modulus. As a result, the static of the beam leads to an initial head stiffness given by:

$$K_h = \frac{3E_b I_{Gz} L_b}{a^2 b^2}$$

Equation 3:19 Initial pile head stiffness as a function of the beam characteristics

- A first analysis is conducted with Thermo-Pile on the energy pile using the value of K_h found in Equation 3:19. This analysis provides the head displacement v_P of the energy pile. From this, a first action R_P applied to the pile is estimated with Equation 3:18. This force is then distributed to the left and right piles with Equation 3:17.

- Two analyses are conducted with Thermo-Pile under isothermal conditions for the left and right piles with the actions previously determined. Those analyses provide two new head displacements of the isothermal piles, v_L and v_R.

- The head displacements at the isothermal piles are used to estimate a new value of K_h. This step is achieved by determining the new set of integration constants used to estimate the deflection profile of the beam (see Equation 3:26). The new effective displacement v_P is then estimated with the new constants. From this, a new value for the head stiffness is found by dividing the action R_P by the new value of v_P.

Steps 2 to 4 are then repeated until convergence is reached. A schematic of the algorithm is given in Figure 3:27.

Determination of the integration constants

Step 4 is detailed in the following paragraph. The method employed is based on the Euler-Bernoulli beam theory, and we consider a simply supported beam with a punctual load, which is given here as an example. The static equilibrium of the beam yields:

$$R_A = \frac{b}{L_b} P \text{ and } R_B = \frac{a}{L_b} P$$

Equation 3:20 Transmitted reactions to the isothermal piles through the beam

where R_A and R_B are the support reactions at points A and B, respectively (see Figure 3:26). The relationship between the curvature of the beam and the bending moment M_{fz} assuming small deflections leads to:

$$EI_{Gz}v'' = M_{fz}(X)$$

Equation 3:21 Moment equilibrium along the beam

where v is the beam deflection and X the longitudinal coordinate along the beam from A ($X = 0$) to B ($X = L_b$). For a cross-section between A and C (Figure 3:26), the bending moment is:

$$M_{fz1}(X) = R_A X = \frac{b}{L_b} PX$$

Equation 3:22 Moment equilibrium along the beam at the left side of the energy pile

Similarly, for a cross-section between C and B (Figure 3:26), the bending moment is:

$$M_{fz2}(X) = R_B(L_b - X) = \frac{aP}{L_b}(L_b - X)$$

Equation 3:23 Moment equilibrium along the beam at the right side of the energy pile

Combining Equation 3:22 and Equation 3:23 with Equation 3:21 and integrating two times yields:

$$E_b I_{Gz} v_1(X) = \frac{bP}{6L_b} X^3 + C_1 X + C_2$$

$$E_b I_{Gz} v_2(X) = \frac{aP}{6L_b}(L_b - X)^3 + C_3 X + C_4$$

Equation 3:24 Profiles of beam deflexion

where C_1, C_2, C_3 and C_4 are the constants of integration.

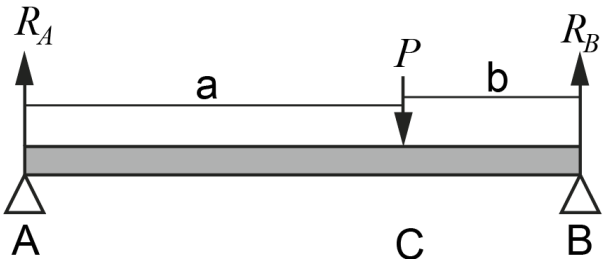

Figure 3:26 Scheme of a generic simply supported isostatic beam

Finally, the boundary conditions of the problem are:

$$\begin{aligned} v_1(X=0) &= v_L \\ v_2(X=L_b) &= v_R \\ v_1(X=a) &= v_2(X=a) \\ v_1'(X=a) &= v_2'(X=a) \end{aligned}$$

Equation 3:25 Boundary conditions applied to the piled beam

Inserting these boundary conditions in Equation 3:24 yields the system:

$$\begin{bmatrix} 0 & 1 & 0 & 0 \\ 0 & 0 & L_b & 1 \\ a & 1 & -a & -1 \\ 1 & 0 & -1 & 0 \end{bmatrix} \begin{bmatrix} C_1 \\ C_2 \\ C_3 \\ C_4 \end{bmatrix} = \begin{bmatrix} E_b I_{Gz} v_L \\ E_b I_{Gz} v_R \\ \dfrac{ab\left(b^2-a^2\right)}{6L_b} P \\ -\dfrac{ab}{2} P \end{bmatrix}$$

Equation 3:26 Matrix system of the piled-beam configuration

where the unknown vector is formed by the four constants of integration.

3.5.2 Example of simulation

A simple example is investigated in this section. The 5 m long beam used in the study is assumed to have a cross section with sides such that the quadratic moment of the beam cross section is equal to 0.1 m^4. The Young's modulus of the concrete in the beam is equal to 20 GPa. The piles have identical geometries with a diameter of 0.5 m and a length of 10 m. They are embedded in the same homogeneous soil, which is represented by its Menard coefficient E_M, equal to 60 MPa, and its ultimate shaft friction and base compression q_s and q_b, equal to 200 kPa and 4500 kPa, respectively. The energy pile is 1 m away from the left pile, and an extreme temperature variation of +60 °C is applied. The results of the simulation are given in Figure 3:28.

The maximum deflexion of the beam is not observed right at the energy pile (Figure 3:28a) because of the beam rigidity and fixities at both ends. The profiles of the axial stress (Figure 3:28b) and axial displacement (Figure 3:28c) show that the heated pile undergoes compression, while the isothermal piles experience tension, the left pile being more affected because it is closer to the energy pile. Finally, the profile of deflexion along the beam shows some differential displacements between the three piles, up to 1 mm between the heated pile and the right pile.

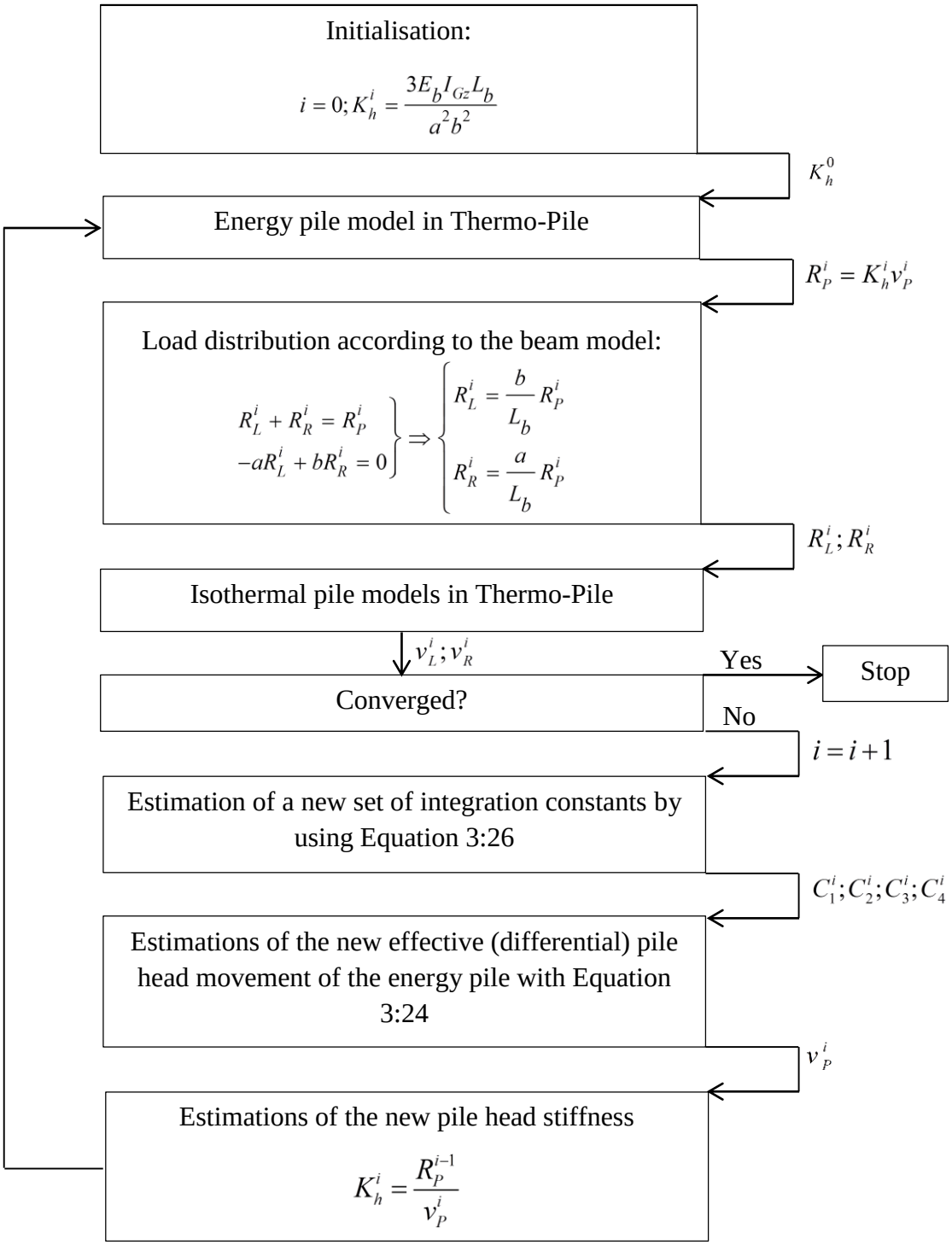

Figure 3:27 Flow chart for the Thermo-Piled-Beam method

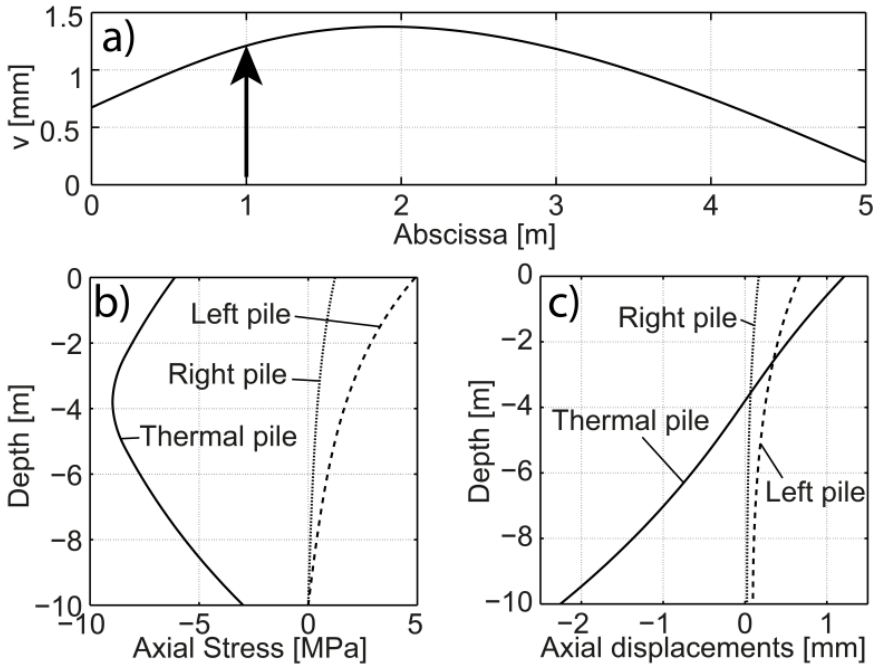

Figure 3:28 Result of the example with (a) the deformed profile of the beam, (b) the profiles of the axial stress and (c) the axial displacements in the piles.

3.5.3 Conclusions

The simple algorithm employed in Thermo-Pile offers great opportunities to develop more complex tools by coupling it with other models such as the Euler-Bernoulli model for beams. An example of coupling was given to study elementary piled beams with energy piles. This method, based on an iterative process, is easy to implement and allows real operational design compared to complex finite element methods. The validation of the method should be achieved using either in situ data or centrifuge test results.

3.6 On accounting for radial thermal strains of energy piles using *p-y* curves

As a pile is heated, it expands axially and radially. Axial displacements may vary the mobilised shaft friction as reported experimentally (Laloui et al., 2003; Bourne-Webb et al., 2009) whilst radial strains may vary the ultimate shaft friction at the soil-pile interface. Indeed, pile radial expansion upon heating may increase the contact stress at the soil-pile interface provided that pore water pressure does not vary too much (see Chapter 4). Conversely, radial contraction may induce a decrease in contact stress between the pile and the soil, reducing the ultimate shaft friction accordingly. Experimental evidences showing the impact of radial thermal strains were reported by Rosenberg and McCartney (McCartney and Rosenberg, 2011). Centrifuge load tests were achieved on scaled pile models at different temperatures. Measurements showed that the hotter the pile, the greater the ultimate load. Different design tools have been developed for the design of such piles based on the load-transfer approach (Knellwolf et al., 2011; Ouyang et al., 2011). However, these approaches only consider axial deformations and do not account for thermally induced radial strains. Ouyang et al. (2011) suggested the importance of radial strains while back-analysing the Lambeth college test pile.

The present section proposes a method to account for thermally induced radial strains based on the Winkler method using "*p-y*" curves developed for laterally loaded piles (e.g. (Matlock, 1970; Reese et al., 1974)). The advantage of using such lateral load transfer curves is that they can be experimentally determined (e.g. (Nguyen Pham, 2008)) and cyclic aspect have already been developed (Heidari et al., 2014). The horizontal equilibrium of the soil-pile interface is derived by equalizing the internal thermal stress within the concrete with the soil response to the pile shaft lateral displacement. This equilibrium provides a variation in the contact stress between the pile and the soil. The *t-z* curves used to estimate the axial response of the pile are then modified accordingly.

First, considerations about the mobilizable radial expansion coefficient are discussed as well as the impact of axial constraints on it. Then, the method to derive the equilibrium at the soil-pile interface is presented. Finally, the method adopted for modifying the *t-z* curves according to the equilibrium found at the soil-pile interface.

3.6.1 Mobilizable thermal expansion coefficient

The mobilizable thermal expansion coefficients are linked to the maximum (i.e. free) axial or radial strains observable in a pile. Former approaches based on the load-transfer methods (Knellwolf et al., 2011; Ouyang et al., 2011) only consider axial strains, inherently assuming that radial strains are free to develop. However, blocking these strains may lead to a greater mobilizable axial thermal expansion, up to $(1+\nu)/(1-\nu)$ times the linear thermal expansion coefficient, where ν is the Poisson's ratio, that is to say an increase between 20 and 50 % for concrete (i.e. ν is between 0.1 and 0.2). Indeed, considering the axisymmetric of the pile as well as its thermoelastic behaviour, one may write that:

$$\varepsilon_{ax} = \frac{\sigma_{ax}}{E_c} - \frac{2\nu}{E_c}\sigma_{rad} - \beta_c^T \Delta T$$
$$\varepsilon_{rad} = \frac{\sigma_{rad}}{E_c} - \frac{\nu}{E_c}\left(\sigma_{rad} + \sigma_{ax}\right) - \beta_c^T \Delta T$$

Equation 3:27 Thermoelastic constitutive law for axisymmetric configurations

where ε_{ax} and ε_{rad} are the axial and radial strains, σ_{ax} and σ_{rad} are the axial and radial stresses, E and ν are the Young's modulus and Poisson's ratio of the concrete, β_c^T is the linear expansion coefficient of the concrete and ΔT is the temperature variation.

To determine the maximum mobilizable thermal expansion coefficient on the axial direction, one may set the radial strains and axial stresses equal to zero:

$$\sigma_{ax} = 0$$
$$\varepsilon_{rad} = 0$$

Equation 3:28 Boundary conditions with blocked radial strains and free axial strains

Solving Equation 3:27 with the boundary conditions given by Equation 3:28 yields:

$$\varepsilon_{ax} = -\frac{1+\nu}{1-\nu}\beta_c^T \Delta T$$
$$\sigma_{rad} = \frac{E}{1-\nu}\beta_c^T \Delta T$$

Equation 3:29 Axial strain and radial stress developed for blocked radial strains and free axial strains.

Therefore, the maximum mobilizable axial thermal expansion $\beta_{ax}{}^T$ is:

$$\beta_{ax}^T = \frac{1+\nu}{1-\nu}\beta_c^T$$

Equation 3:30 Apparent axial thermal expansion with blocked radial strains and free axial strains

Similarly, determining the maximum mobilizable radial thermal expansion $\beta_{rad}{}^T$ requires:

$$\varepsilon_{ax} = 0$$
$$\sigma_{rad} = 0$$

Equation 3:31 Boundary conditions with blocked axial strains and free radial strains

This leads to:

$$\beta_{rad}^T = (1+\nu)\beta_c^T$$

Equation 3:32 Apparent radial thermal expansion with free radial strains and blocked axial strains

In both cases, the maximum mobilizable thermal expansion is greater than the linear thermal expansion as constraints on the strains increase the stress level in the pile. Considering a Poisson's ratio of 0.2 leads to variations in the axial thermal expansion up to 50 % (Equation 3:30).The role of the maximum mobilizable thermal expansion coefficient is highlighted in Section 3.6.2 where the method used to estimate the equilibrium at the soil-pile interface is presented.

In conclusion, the maximum mobilizable thermal expansion coefficients (i.e. axial and radial) may depend on the restraints acting on the pile as axial and radial strains may not be totally free neither fully blocked. However, it is possible to bracket these quantities between the linear thermal expansion coefficients α and values given in Equation 3:30 for the axial expansion coefficient and in Equation 3:32 for the radial expansion coefficient.

3.6.2 Estimating the radial thermomechanical equilibrium at the soil-pile interface

Pile diameter may shrink or dilate as the pile is cooled or heated. As a result, the soil-pile interface may move and the contact stress between the pile shaft and the soil may vary accordingly, impacting the *t-z* (i.e. vertical) load-transfer curves. It is therefore important to accurately determine the variation in contact (i.e. normal to the pile shaft) stress. This is achieved by equalizing the thermally induced horizontal stress $\sigma_{rad,th}$ in the pile to the soil response $p_y(y)$ where y is the displacement of the soil-pile interface.

Similarly to the thermal effects partitioning described by Laloui et al. (2003) for axial thermal effects, radial thermal effects can be divided into observed thermal strains $\varepsilon_{rad,obs}$ and radial thermal stresses $\sigma_{rad,th}$. The relation between these two quantities is:

$$\varepsilon_{rad,free} = \varepsilon_{rad,obs} + \varepsilon_{rad,blo}$$
$$\sigma_{rad,th} = E_c \varepsilon_{rad,blo}$$

Equation 3:33 Thermal effects partitioning

where $\varepsilon_{rad,free}$ represents the free thermal strain in the radial direction and E_c is the concrete Young's modulus.

The equilibrium of the soil-pile interface, after a temperature variation, is given by:

$$\sigma_{rad,th} = p_y(y)$$

Equation 3:34 Horizontal equilibrium of the soil-pile interface

where y is the horizontal displacement of the soil-pile interface given by:

$$y = \frac{D}{2}\varepsilon_{rad,obs}$$

Equation 3:35 Radial thermal displacement

where D is the pile diameter. As a result, the equilibrium of the pile is given as a function of the soil-pile displacement by:

$$p(y) + \frac{2E_c}{D} y = E_c \varepsilon_{rad,free}$$

Equation 3:36 Developed horizontal equilibrium of the soil-pile interface

Equation 3:36 can be inverted depending on the *p*-function. However, the dichotomy method is used to converge toward the equilibrium in order to have a method that is independent from the *p*-function. Two cases can be identified: heating and cooling. The algorithm for the heating is as follows (see Figure 3:30):

- The observed and blocked strains, $\varepsilon_{rad,obs}$ and $\varepsilon_{rad,blo}$, are initialised at half of the free strain $\varepsilon_{rad,free}$
- The internal thermal stress $\sigma_{rad,th}$ and soil reaction $p_y(y)$ are estimated based on the observed radial strain
- Internal thermal stress and soil reaction are compared:
    - If the soil reaction is greater than the internal stress of the pile, then the displacement of the soil-pile interface is too important. Therefore, the new domain of possible value of observed strain is between 0 and half of the free thermal strain
    - If the soil reaction is lower than the internal stress of the pile, then the displacement of the soil-pile is too small. Therefore, the new domain of possible value of observed strain is between half of the free thermal strain and the free thermal strain

- The observed strain for the next step of iteration is given the value at the middle of the new domain of possible value and steps 2 to 4 are repeated until convergence

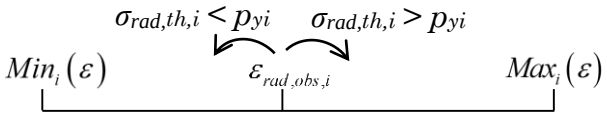

Figure 3:29 Schematic representation of the algorithm used to find the equilibrium at the soil-pile interface

This algorithm allows for using experimentally determined curves or any suitable fitted model and the convergence is linear. The convergence criterion is a simple comparison between the internal thermal stress and reaction of the soil.

The cooling phase induces shrinkage of the pile diameter which reduced the contact stress at the soil-pile interface. This radial shrinkage is assumed not to be constrained so that no iterative procedure is required. The thermal strain is directly taken equal to the free thermal strain. The corresponding soil response is estimated using the *p*-function. The unloading branch of the *p*-function providing negative value of contact stress means that the contact has been lost. Therefore, the contact stress is set to zero.

3.6.3 Evolution of the ultimate shaft friction

P-y curves are useful to represent the soil-pile interface mechanical equilibrium. They link the pile deflection (i.e. radial displacement) to the horizontal reaction of the soil. Reese et al. (Reese et al., 1974) proposed a semi-empirical *p-y* function determined based on the Mustang Island tests. Then, Murchison and O'Neill (Murchison and O'Neill, 1984) compared this semi-empirical function with other simpler functions based on the same experiment. They found that hyperbolic functions were more suitable for *p-y* curves. The present utilisation of *p-y* curves gets rid of the limitation linked to the dependence of the initial stiffness of the soil to the pile diameter as the internal efforts induced by temperature variations can be assumed isotropic within the horizontal plane and remain normal to the pile shaft. Also, the problem of considering a rigid or flexible pile (e.g. (Poulos and Hull, 1989)) is not to be considered as no external lateral load is applied. Brodbaek et al. (Brodbaek et al., 2009) provide an extensive review of the *p-y* functions. Menard pressuremeters with displacement probes may be useful to get *in situ p-y* curves from Menard pressuremeter tests (Nguyen Pham, 2008).

Depending on the model of axial load-transfer curve (i.e. *t-z* curve), evolution with the horizontal contact stress at the soil-pile interface varies. An example is provided on the load-transfer curve for shaft friction as proposed by Franck and Zhao. This curve is defined using three linear parts with different slopes. The first part is linear elastic with a slope K_s. The second part is elastoplastic with a slope equal to $K_s/5$. The last part is perfectly plastic with ultimate value q_s.

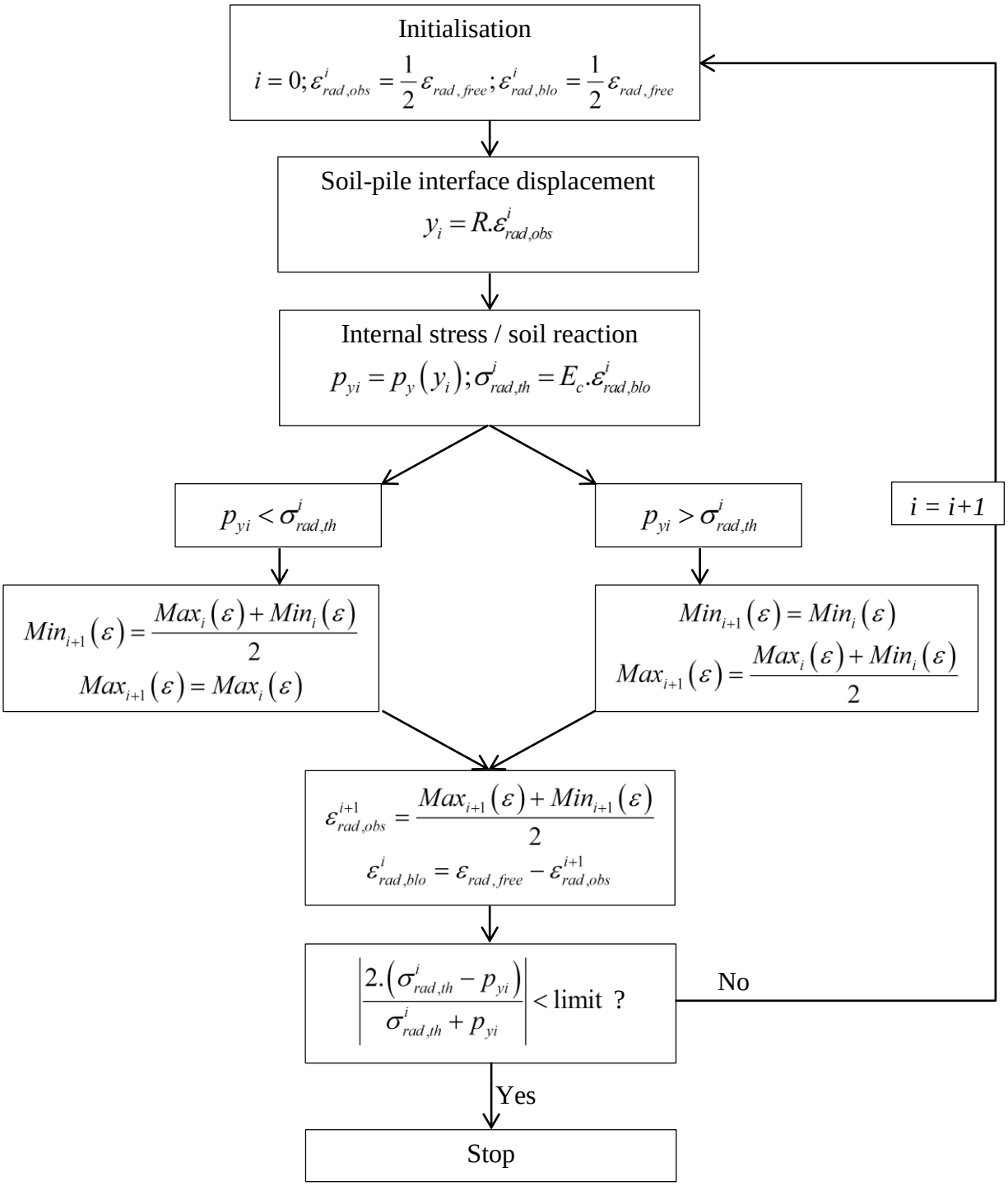

Figure 3:30 Flow chart of the algorithm used to determine the contact stress at the soil-pile interface

Assuming, at first, that the radial strains remain within the domain where the Ménard pressure coefficient is measured leads to constant slopes of the axial load-transfer curves as given by Franck and Zhao. Therefore, the only parameter varying is the ultimate shaft friction q_s, which depends linearly on the horizontal effective contact stress according to (Lang and Huder, 1978):

$$q_s = c' + k_\sigma \sigma_v' \tan\delta$$

Equation 3:37 Ultimate shaft friction as a function of the vertical effective stress

where *c'* is the effective cohesion of the soil, *k* is the earth pressure coefficient and δ is the friction angle of the soil. However, the horizontal stress in the present study may not only depend on the vertical stress and the earth coefficient but also on the horizontal expansions and contractions of the soil and the pile. We therefore modify *Equation 3:37* into a more explicit equation as:

$$q_s = c' + \sigma_h' \tan\delta$$

Equation 3:38 Ultimate shaft friction as a function of the horizontal effective stress

where σ'_h is the effective stress normal to the soil-pile interface. Therefore, q_s depends on the evolution of the effective stress normal to the pile shaft, *Equation 3:37* being used to determine the initial state of the soil.

At first, one may assume that *c'* and δ do not depend on temperature. Therefore, one may write that:

$$q_s(T) = c' + \sigma_h'(T) \tan\delta$$
$$dq_s = d\sigma_h' \tan\delta$$

Equation 3:39 Variation in ultimate shaft friction as a function of the variation in horizontal stress

where *T* is the temperature. Evolution of σ'_h with temperature may be derived according to the algorithm presented in Figure 3:30.

3.6.4 Conclusions

The impact on axial and radial constrains on the mobilizable thermal expansion coefficient was discussed and shown to be significant when one direction is blocked. Therefore, a method to account for radial thermal strains was proposed on the basis of *p-y* curves. The modification of the *t-z* curves according to radial strains was not fully developed as it would require experimental evidences that were not gathered during this thesis.

3.7 Concluding remarks

Evolution of mobilised bearing capacities under non cyclic temperature variations where investigated using an energy pile design tool called Thermo-Pile. Two major *in situ* tests – the EPFL and Lambeth College test piles – as well as three idealized cases were analysed using the load-transfer method. It was shown that dividing the pile into two parts delimited by the null point eases the analyses. Indeed, under heating the upper part of the pile heaves, which induces a relief in the mobilised shaft friction and an increase in head reaction, while the lower part of it settles, inducing an increase in mobilised shaft friction as well as an increase in pile tip compression. When cooling, the upper part of the pile settles and the lower part of it heaves as a result of thermal contraction, along with the induced variations in mobilised shaft friction, head reaction and pile tip compression. It was shown that the geotechnical design of energy piles using such tools is mainly

linked to serviceability concern, that is to say limiting differential pile settlements. However, other processes should be accounted for. A simple way to estimate the asymptotic position of the null point along energy piles was proposed. The significance of cyclic mechanisms was evidenced by the discussion about the back analysis of the Lambeth College test pile carried out by Knellwolf et al. (2011). Thermo-Pile software was coupled with the Euler-Bernoulli beam model to highlight the pile to pile interactions through beam or raft bending. A discussion about the mobilizable axial thermal expansion showed the importance of radial thermal strains on the axial response of energy piles. Finally, such operational design may also account for cyclic degradation of the soil-pile interface and models are available to tackle such an issue (Suryatriyastuti et al., 2014).

3.8 Acknowledgements

The authors want to thank Marc Randolph (University of West Australia) and Kenichi Soga (Cambridge University, UK) for the fruitful discussions about this work. Financial support of EOS Holding through the GRETEL II project is much appreciated.

Chapter 4 Effect of Thermally Induced Pore Water Pressure Build on Long Term Serviceability of Energy Piles

4.1 Introduction

The first energy test pile built on the EPFL (Swiss Federal Institute of Technology Lausanne) campus in Lausanne (Switzerland) was subjected to non-cyclic temperature increases (Laloui et al., 2003). This first *in situ* experiment provided great insight in the mechanisms involved in the thermomechanical response of an energy pile. It was found that heating the pile induces thermal strains and stresses within the pile, depending on the restrains acting on it which are the shaft friction, the base reaction and the head interactions with the supported structure. During the tests and under temperature variations of about 20-25 °C, the pile load was almost doubled as a consequence of pile head heave. Indeed, the thermal expansion of the pile induces a heave of the pile head that pushed against the raft and supported structure which induces a reaction that is added to the initial pile load (Mimouni and Laloui, 2014). However, the thermomechanical response of the pile remained elastic. Furthermore, this site was not equipped with a heat pump so that active cooling of the pile was not possible. Later, Bourne-Webb et al. (2009) installed an energy pile dedicated to testing at the Lambeth College (London, UK). This pile was not included within a real foundation but solicited with a jack mounted on a beam maintained with reaction piles. The test pile was linked to a heat sink pile through a heat pump so that active heating and cooling were both possible. The mechanical load applied to the pile was chosen to get a factor of safety of 2.5 (Ouyang et al., 2011) and it was found that the boundary condition at the pile head was of constant load type (Bourne-Webb et al., 2009). The thermal solicitation consisted in a cooling phase (-19 °C relatively to natural ground temperature) followed by a heating phase (+10 °C relatively to natural ground temperature). Different mechanisms involved in the variations of mobilised bearing shaft friction were identified. Amatya et al. (2012) published a summary of these different *in situ* tests and showed how the different types of pile can be affected by temperature variations. Average maximum change in axial stress within the test piles due to temperature variation is approximately 150 kPa/°C.

Laloui et al. (2006) back analysed the tests carried out on the EPFL test pile using finite elements method. Analyses showed very good agreement with *in situ* measurements, evidencing that the design of the pile was large enough to remain within the elastic domain of load-transfer, which was later confirmed by Mimouni and Laloui (2014) who estimated that the factor of safety of this particular test pile was around 13. Knellwolf et al. (2011) modelled different heating and cooling phases operated on the EPFL and Lambeth College test piles in order to validate a design tool based on finite differences, called Thermo-Pile, using the load-transfer method. Again, the thermoelastic response of the EPFL pile was evidenced. Some inconsistencies were found while modelling the Lambeth College test pile because Knellwolf et al. (2011) considered that heating and cooling phases were two separate sequences while it was obviously a thermal cycle that could not be dissociated. Ouyang et al. (2011) back analysed the test carried out at the Lambeth College using the load-transfer method with unloading path and found better agreements with the *in situ* measurements. But discrepancy was still observed between the measured and modelled pile head displacements. This was attributed to the thermal radial strains that were not accounted for in the conventional load-transfer method. This phenomena was further investigated by McCartney and Rosenberg (2011) who investigated the impact heat exchanges on load-settlement curves of piles using scaled pile models in centrifuge tests. Different temperature changes were applied to the pile

model before the loading sequence was executed. The study showed that thermally induced radial strains can substantially increase (during heating) or reduce (during cooling) the ultimate load that a pile can carry. Mimouni and Laloui (2014) further developed the study of monotonic temperature variations by back analysing the tests piles of the EPFL and Lambeth College, with the same load-transfer method as Knellwolf et al. (2011), and estimated the range of variation of mobilised bearing capacities for temperature variations between -10 °C and +60 °C, relatively to a natural ground temperature of 11 °C. This study showed that the EPFL test pile had enormous margin of safety while the Lambeth College test pile exhibited limited margin of safety. However, it was shown that thermally induced displacements are unlikely to induce excessive settlements when ignoring radial strains and thermo-hydro-mechanical couplings.

If monotonic processes are now well documented, thermal cyclic effects are still weakly understood. Indeed, the lifetime of energy piles is the same as of the supported structure, that is to say around 40-50 years, at least. Therefore, a pile will be subjected to, at least, 40 cycles of thermal expansion-contraction. Suryatriyastuti et al. (2013) used a cyclic degradation model for the soil shaft friction in order to investigate the cyclic response of a single energy pile under free head or fully restrained head conditions, using finite differences. When the head was free, a factor of safety of 3 was adopted (i.e. the applied mechanical load was equal to one third of the ultimate load determined for a settlement of 10 % of the pile diameter). After 24 heating and cooling cycles between +10 °C and -10 °C, the free head condition leads to an additional settlement of 3 mm at the pile head while the blocked head condition leads to a reduction of head load of -4 % (heating) to -25 % (cooling). Thermal degradation of the interface due to thermal consolidation was investigated by Di Donna et al. (Di Donna et al., 2013) using an Advanced Constitutive Model for Environmental Geomechanics with Temperature effects (ACMEG-T) (Laloui and François, 2009). Finally, The service loads of the piles were based on the Eurocode 7 (European Committee for Standardization, 2004). The model employed was considering thermal consolidation of the soil that thermally induces – under cyclic thermal loading – a reduction in horizontal effective stress, directly impacting the ultimate shaft friction around the pile. As a result, the lost friction is transferred to the pile base leading to additional settlements. Therefore, the cyclic analyses that have been carried out until now have been considering one single condition at the pile head and have analysed the impact of thermal cycles. However, engineering practice would require wider investigations to understand how the thermal cycles affect the piles at different loads to be able to draw an optimum design based on both thermal and mechanical loads for different in situ conditions. Furthermore, the conservativeness of the in use design standards needs to be addressed regarding the long term effects of heating and cooling cycles.

Therefore, the present study proposes investigations about the influence of soil type on the long term serviceability of energy piles. The study is carried out using finite element methods and considering Thermo-Hydro-Mechanical (THM) couplings. One single pile is modelled as a pile trial. The methods adopted in the present study are presented in Section 4.2. The loading sequences and investigated values of soil permeability as well as the general strategy adopted for the present simulations are detailed in Section 4.2.1. The THM formulation with the diffusive and constitutive models is presented in Section 4.2.2. The numerical setup with the mesh, associated boundary conditions and physical parameters used to represent the soil, the pile and the pore water are given

in Section 4.2.3. Analyses and interpretations of the results are given in Section4.3. First, the evolutions of pore water pressure and temperature with the thermal cycles are analysed in Section 4.3.1. Section 4.3.2 presents the results of the load test under fully drained conditions which provides pile characteristic loads. Then, Sections 4.3.3, 4.3.4 and 4.3.5 regroup the analyses under drained conditions with permeabilities of $k_w = 10^{-14}$ m^2, $k_w = 10^{-16}$ m^2 and $k_w = 10^{-18}$ m^2, respectively. Section 4.4 provides discussion about the conservativeness of the design approaches proposed by the Eurocode 7, based on the simulation results. Using the load-settlement curve previously obtained, the different design approaches based on pile load test are evaluated and results are compared to the long term behaviour observed with the simulations.

4.2 Method

4.2.1 General method

The aim of this study is to investigate the long term effects of thermal cycles on pile foundations. A single pile is modelled under different loads. Different soil permeabilities were tested to capture the impact of soil type on the long term accumulation of settlements.

First, the load-settlement curve is determined under fully drained conditions in order to estimate the range of mechanical load reasonably applicable to the test pile. Definitions of ultimate and service limits are multiple and may vary according to local regulations (Bengt, 1980). The present study uses the European standard EN 1997 (European Committee for Standardization, 2004) provided by the European Committee for Standardization. Despite the fact that national annexes could vary the different factors involved in the design process, the present study uses the recommended values provided in the annexe A.7 of the EN 1997.

From the obtained load-settlement curve, different load conditions were identified to be tested with thermal cycles in order to have a representative panel of conditions. For each of these loads, the analysis consisted in two phases: 1/ mechanical load applied under fully drained conditions which provides same initial states for any type of soil, and 2/ thermal cycles executed over 40 years.

Values of permeability were selected to represent impervious silts and very fine sands ($k_w = 10^{-16}$ m^2) and impervious unweathered clays ($k_w = 10^{-18}$ m^2) (Bear and Cheng, 2010) where seasonal heat storage can be important for the sustainability of the heat production (Mimouni et al., 2013). Fully drained conditions ($k_w = infinity$) were also investigated to be used as reference in which no pore water pressure builds up under temperature variations.

The heating and cooling phases applied to the pile consist in a cyclic variation in heat flux absorbed by the pile elements, according to a triangular signal as presented in Figure 4:1. This method does obviously not represent the complexity of the heat exchanges occurring between the absorber pipes and the concrete within an energy pile but fairly represents the global temperature variations observed within the pile, which is sufficient for the present study. The heating and cooling cycles were designed to be symmetrical in order to balance the amount of heat injected and extracted.

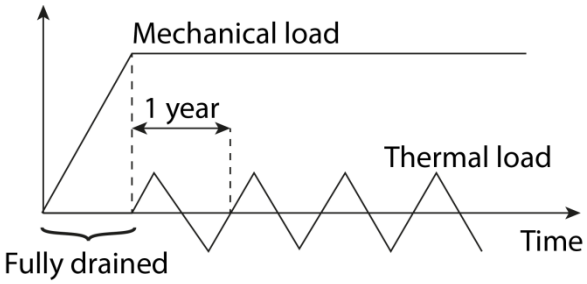

Figure 4:1 Generic load paths for mechanical and thermal loads

As a result, and with the adopted boundary conditions (adiabatic walls), no deviation of the mean temperature of the ground (11 °C) is observed on the long term (see Section 4.3.1). As a result, no long term settlement or heave could be attributed to the long term deviation of the mean temperature of the soil which eases the analyses. Indeed, permanent decrease (resp. increase) in the mean temperature of the soil would have induced permanent contraction (resp. expansion) of the soil massif and pile and consequently long term settlement (resp. heave).

Results of the simulations were analysed in terms of long term accumulation of settlements (i.e. long term serviceability) and transferred load from shaft friction to base compression. The load-transfer mechanisms occurring at the soil-pile interface were also analysed.

The lowest limit of the pile serviceability is defined as the lowest level that the pile head could reach during the thermal cycles. For piles that showed stabilization within the simulated period (i.e. 40 years), the lowest limit is simply the lowest settlement reached during the simulation. For those which did not show stabilization within the 40 simulated years, a function with an exponential decay was fitted on the cyclic minimums as suggested by Pasten and Santamarina (Pasten and Santamarina, 2014):

$$s(N) = s_{inf} + (s_{mech} - s_{inf}) \exp(-\xi_c N_c)$$

Equation 4:1 Model used to fit the long term accumulation of pile settlements

where N_c is the number of cycles, s_{inf} and s_{mech} are the asymptotic and mechanical settlements and ξ_c is a fitting parameter. Settlements are taken as positive downward but they represent a downward, i.e. negative, displacement.

4.2.2 THM formulation

4.2.2.1 Coupled diffusive model

Because saturated conditions are considered in the present study, diffusive phenomena are only linked to water and heat transport. The compositional approach as implemented by Collin et al. (Collin et al., 2002) in the software *Lagamine* is used to describe the porous media.

Water flow

Advective and convective flows are neglected in the present study because of the low permeabilities considered. Phase changes are also neglected based on the reached temperature levels (i.e. from -

1 °C to + 21 °C). However, water is treated as a compressible fluid that expands or contracts under soil deformations or temperature variations. As a result, the water mass conservation is written as:

$$\frac{\partial}{\partial t}\left(\rho_w n\right) + \mathrm{div}\left(\rho_w \mathbf{q_w}\right) - Q_w = 0$$

Equation 4:2 Water mass conservation

where ρ_w is the bulk density of water, n is the porosity, Q_w represents any volumetric source or sink of water and $\mathbf{q_w}$ is the macroscopic velocity of water which is governed by the Darcy's law for porous media:

$$\mathbf{q_w} = -\frac{k_w.k_{r,w}}{\mu_w}\left[\mathbf{grad}\left(p_w\right) + \rho_w g.\mathbf{grad}\left(y\right)\right]$$

Equation 4:3 Darcy's law

Where y is the vertical coordinate, k_w is the intrinsic permeability of the porous media, p_w is the water pressure and μ_w is the dynamic viscosity of water. The relative permeability $k_{r,w}$ is equal to unity because only saturated conditions are considered.

The dynamic viscosity of water is assumed to be temperature dependent according to a linear relationship with a coefficient $\alpha_{\mu w}{}^T$:

$$\mu_w = \mu_{w0}\left[1 + \alpha_{\mu_w}^T\left(T - T_0\right)\right]$$

Equation 4:4 Evolution of water dynamic viscosity with temperature

where μ_{w0} is the dynamic viscosity of water at the temperature T_0. The water is assumed to be a compressible and dilatant fluid whose density varies according to pressure and temperature:

$$\rho_w = \rho_{w0}\left[1 + \frac{p_w - p_{w0}}{\chi_w} - \beta_w^T\left(T - T_0\right)\right]$$

Equation 4:5 Evolution of water density with temperature and pressure

where ρ_{w0} is the density of water at the temperature T_0 and under the pressure p_{w0}, χ_w is the water compressibility and $\beta^T{}_w$ is the thermal expansion coefficient of water.

Heat diffusion

As stated in the previous section, convective flow and phase changes are neglected. Therefore, only conductive heat transport is considered and the heat balance equation is the heat equation (Equation 2:1) in which the total system enthalpy is given as the sum of the enthalpies contained in each phase (here water and solid matrix):

$$S_T = \left[\left(1-n\right)\rho_s c_s + n\rho_w c_w\right]\left(T - T_0\right)$$

Equation 4:6 Total enthalpy of a multiphasic material

where ρ_s is the bulk density of soil grains, and c_s and c_w are the specific heat capacities of the soil grains and water, respectively. Heat conduction is assumed to be isotropic and is governed by the Fourier's law:

$$\mathbf{q_T} = -\left[\left(1-n\right)\lambda_s + n\lambda_w\right]\mathbf{grad}\left(T\right)$$

Equation 4:7 Fourier's law

where λ_s and λ_w are the thermal conductivities of the soil grains and water, respectively. The set of equations presented above evidences the thermo-hydraulic couplings involved in the study.

4.2.2.2 Coupled mechanical constitutive model

Stress-strain framework

The behaviours of the soil and pile are assumed to be governed by the Terzaghi's effective stress tensor **σ'**:

$$\boldsymbol{\sigma}' = \boldsymbol{\sigma} - p_w\mathbf{I}$$

Equation 4:8 Effective stress

where **σ** is the total stress tensor and **I** the identity matrix. The effective stress introduces a hydro-mechanical coupling in the constitutive modelling. The Lagrangian approach is used with the small strain theory. An important thermo-mechanical coupling is represented by the thermal expansion and contraction of the porous media. As a result, the total strain tensor increment *d***ε** can be divided into three terms:

$$d\boldsymbol{\varepsilon} = \mathbf{E}^{-1}d\boldsymbol{\sigma}' + \beta_L^T\mathbf{I}dT + d\boldsymbol{\varepsilon}^{\mathbf{p}}$$

Equation 4:9 Thermoelastic constitutive law

where the elastic tensor **E** depends on the Young's modulus *E* and Poisson's coefficient *v*, β^T_L is the linear thermal expansion of the porous media, $d\boldsymbol{\varepsilon}^{\mathbf{p}}$ is the plastic strain tensor increment, *dT* is the temperature increment and *d***σ'** is the effective stress tensor increment. The thermoelastic response of the pile is obtained from Equation 4:9 by removing the plastic strain tensor increment.

Plastic formulation

The failure surface used to represent the elastoplastic response of the soil is assumed to be of Mohr-Coulomb type as it is a simple perfectly plastic model which is useful to observe soil-pile interface failure due to pore water pressure variations only. Indeed, other advanced models may include complex mechanisms which would also interfere in the long term behaviour of the soil-pile interface and analyses would be less focused on pore water pressure. Because the present study does

not address a specific soil, soil hardening was ignored in order to remain conservative. Indeed, keeping the yield surface unchanged from the beginning provides an upper limit of plastic accumulation. Furthermore, the hardening is not expected to be much significant during the thermal cycles compared to during the mechanical load. The failure surface is given by:

$$f = \frac{I_{\boldsymbol{\sigma}}}{3}\sin\phi' + II_{\sigma'}\cos\beta_{Lode} - \frac{II_{\sigma'}}{\sqrt{3}}\sin\beta_{Lode}\sin\phi' - c'\cos\phi' = 0$$

Equation 4:10 Mohr-Coulomb yield surface for the adopted model

where ϕ' is the friction angle, c' the cohesion of the material and the stresses and stress invariants are:

$$\sigma'_{ij} = \sigma_{ij} - \frac{I_{\boldsymbol{\sigma}}}{3}\delta_{ij}; I_{\boldsymbol{\sigma}} = \sigma_{ii}; II_{\sigma'} = \sqrt{\frac{1}{2}\sigma'_{ij}\,\sigma'_{ij}}; III_{\sigma'} = \frac{1}{3}\sigma'_{ij}\,\sigma'_{jk}\,\sigma'_{ki}$$

Equation 4:11 Stress invariants

and β_{Lode} is the Lode angle defined as:

$$\beta_{Lode} = -\frac{1}{3}\sin^{-1}\left(\frac{3\sqrt{3}}{2}\frac{III_{\sigma'}}{II_{\sigma'}{}^{3}}\right)$$

Equation 4:12 Lode angle

4.2.3 Numerical setup

4.2.3.1 Mesh and boundary conditions

The configuration was chosen as axisymmetric because of the geometry of the problem. Therefore, the mesh is two-dimensional in the depth-radius plane. The modelled pile is 20 m long and 1 m in diameter. The computational domain is 55 m long and 40 m high. The mesh is composed by 1931 nodes defining 711 quadrilateral and triangular elements. Triangular elements were used to join fine to coarse layers of quadrilateral elements. The low number of nodes therefore reduced the CPU time. However, the mesh was refined close to the pile to correctly capture heat flow and interface strains. As suggested by Potts and Zdravkovic (Potts and Zdravkovic, 2001), a thin layer of elements with a maximum aspect ratio of 5 was inserted between the soil and the pile and was given the same properties as the soil (Figure 4:2).

Horizontal displacements are prohibited along the axis of symmetry (left vertical boundary), left vertical boundary and bottom boundary. Vertical displacements are only prohibited along the bottom boundary. The axis of symmetry is assumed adiabatic and impervious for symmetry reasons. The bottom boundary is also assumed impervious and adiabatic as it is far enough from the pile from thermal and hydraulic standpoints. The right vertical boundary is assumed adiabatic because of its distance to the pile and a hydrostatic profile of water pressure with a water table at the soil surface is prescribed along it. The top boundary is assumed impervious and adiabatic.

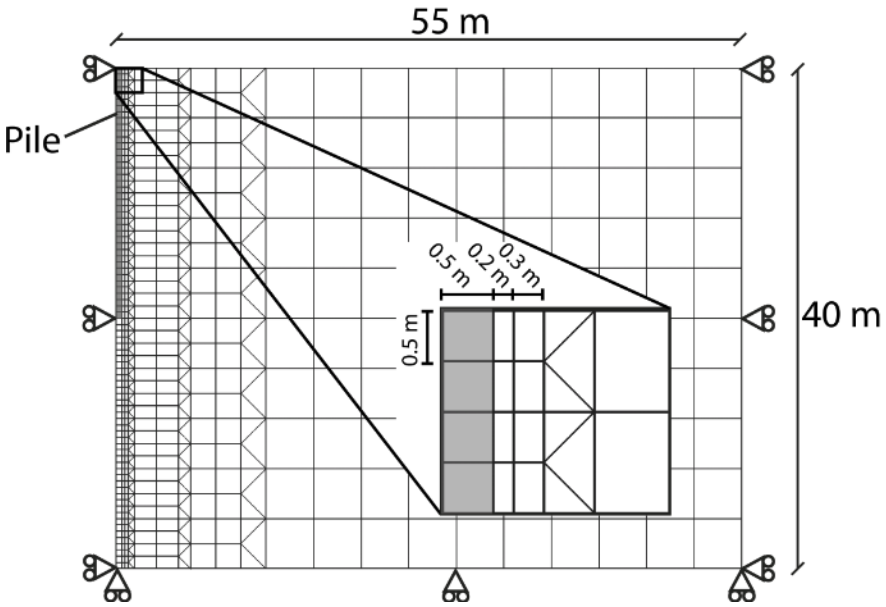

Figure 4:2 Mesh and boundary conditions of the analyses

Specifying an adiabatic soil surface is arguable and the consequences of this are still under discussion (Bordas Freitas et al., 2013). The main motivation of using an adiabatic soil surface along with balanced heat loads is to conserve a closed energy balance during the heating and cooling cycles in order to maintain the mean temperature of the ground and avoid long term thermal contraction or expansion of the whole soil mass which could interfere with the mechanical settlements of the pile.

The heating and cooling cycles consist in a symmetric, triangular and periodic function (Figure 4:1) varying between + 75 W/m^2 and – 75 W/m^2. These variations lead to temperature variations around +/- 10 °C in the pile, the natural temperature of the ground being equal to 11 °C – a typical value at European latitudes.

4.2.3.2 Material physical properties

The mechanical, thermal and hydraulic properties of the soil, pile and water are presented in Table 4:2 and Table 4:1, respectively. The thermoelastic response of the pile is characterised by a Young's modulus of 2x10^7 Pa and a Poisson's coefficient of 0.2. The soil is modelled with a friction angle of 20 °, cohesion of 10 kPa and no dilatancy. The Young's modulus of the soil is 200 times lower than that of the concrete pile and its Poisson's coefficient is equal to 0.3. Linear thermal expansion of the soil and concrete pile are chosen equal to 1.0 x10^{-5} °C^{-1}. The permeability of the concrete is fixed equal to 10^{-14} m^2.

Table 4:1 Physical properties of water

Physical property	Water
Thermal conductivity λ_w (W/m/K)	0.6
Specific heat capacity c_w (J/K/kg)	4186
Density ρ_w (kg/m^3)	1000
Thermal expansion β^T_w (K^{-1})	2.0 x10^{-4}
Compressibility coefficient χ_w (Pa^{-1})	4.54 x10^{-10}
Dynamic viscosity at 284 K μ_{w0} (Pa s)	0.001

Table 4:2 Mechanical, thermal and hydraulic properties of the soil and the pile

Physical property	Soil	Pile
Young's modulus E (Pa)	1.0×10^5	2.0×10^7
Poisson's coefficient v	0.3	0.2
Grain density ρ (kg/m^3)	2700	2700
Friction angle ϕ' (°)	20	-
Effective cohesion c' (kPa)	10	-
Dilatancy (°)	0	-
Grain thermal conductivity λ (W/m/K)	2.4	1.7
Specific heat capacity c (J/K/kg)	930	880
Porosity n	0.4	0.12
Linear thermal expansion β^T (K^{-1})	1.0×10^{-5}	1.0×10^{-5}
Permeability k_w (m^2)	∞ /10^{-16}/10^{-18}	10^{-14}

4.3 Analyses

First, evolutions of temperature and pore water pressure at the soil-pile interface are analysed. The load-settlement curve of the pile is then presented under fully drained conditions. From this analysis, ultimate load is defined. Results of simulations are organized according to the value of permeability that is used. First, analyses under fully drained condition are detailed and interpreted. Next, the analyses with $k_w = 10^{-16}$ m^2 are presented as well as the impact of the decreasing permeability. Finally, the extreme case with $k_w = 10^{-18}$ m^2 is detailed and the effects of such a low permeability are analysed.

4.3.1 Preliminary analyses of pore water pressure and temperature variations

This section is devoted to the preliminary analyses of the evolutions of pore water pressure and temperature. It is necessary to quantify the role of permeability in the pore water pressure. Temperature variations within the pile range between – 10 °C and + 10 °C over a year and around a natural temperature of 11 °C, which is reasonable based on *in situ* data reported from the Dock Midfield (Pahud and Hubbuch, 2007). These variations do not depend on the permeability as saturated conditions are considered (Figure 4:3a). Conversely, the evolution of pore water pressure strongly depends on the permeability. During the thermal cycles, no pore water pressure is generated under fully drained conditions while variations of +/- 4 kPa are observed with a permeability of 10^{-16} m^2 and of +/- 40 kPa with a permeability of 10^{-18} m^2 (Figure 4:3b).

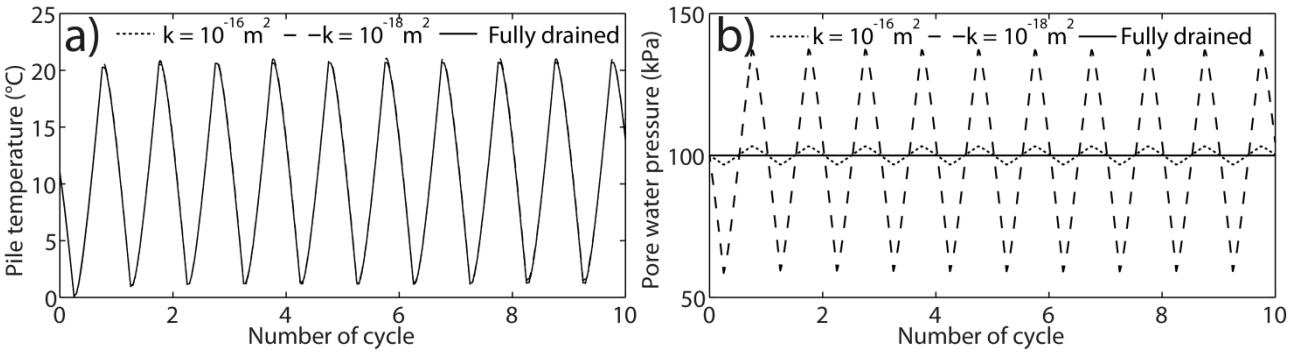

Figure 4:3 Time series of (a) temperature in the middle of the pile (x = 0 m,y = -10 m) and (b) pore water pressure at the soil-pile interface (x = 0.5 m, y = -10 m)

In conclusion, thermal loading is identical for the different analyses whereas pore water pressures show very different evolutions as a function of permeability.

4.3.2 Pile load-settlement curve under fully drained conditions

The load-settlement curve associated with the pile and the soil was obtained under fully drained conditions. This analysis was achieved controlling the load applied to the pile and recording the settlement because it is easier to control the applied load and follow the nodal settlements. This analysis indicates that the settlement at the ultimate limit state, defined as 10 % of the pile diameter according to the EN 1997, is reached for a load of about 5.11 MN (Figure 4:4). Therefore, the analyses carried out in the present study do not consider loads greater than 4.0 MN (Table 4:3) as this would be out of the scope of design practice based on static load tests (European Committee for Standardization, 2004).

Table 4:3 Settlements for the loads used in the long term analyses

Load (MN)	0	1	2	2.5	3	3.5	4
Settlement s_{mech}(mm)	0	1.21	2.66	3.57	4.62	7.84	20.66

4.3.3 Fully drained condition and permeability $k=10^{-14}$ m^2

4.3.3.1 Pile serviceability and resistances

Under fully drained conditions, accumulation of settlements starts for a mechanical load between 2.5 MN and 3.0 MN (Figure 4:5a). For loads lower than or equal to 2.5 MN, very little accumulation is observed (not visible without zooming on individual cycles) whose magnitude remains negligible compared to the reversible cycles. For loads greater than or equal to 3.0 MN, gradual accumulation of settlements is observed. This accumulation tends to vanish with the increasing number of thermal cycles and the greater the load, the longer the stabilization (Figure 4:5a). The increase in settlement was quantified as a percentage of the mechanical load and results are given in Table 4:4.

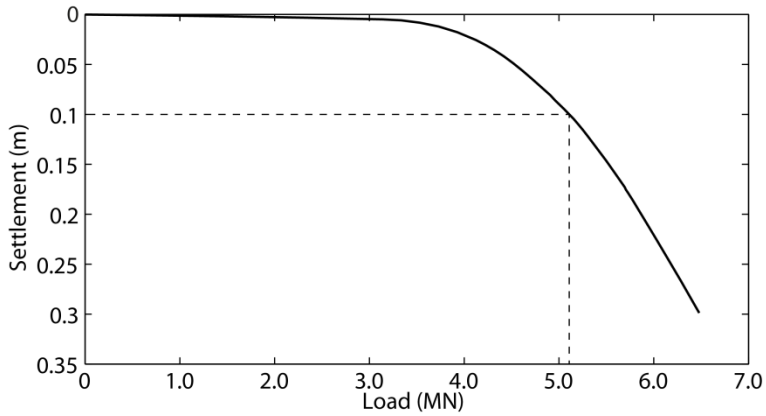

Figure 4:4 Load-displacement curve under fully drained conditions with the 10 % limit settlement indicated and the corresponding ultimate limit state load

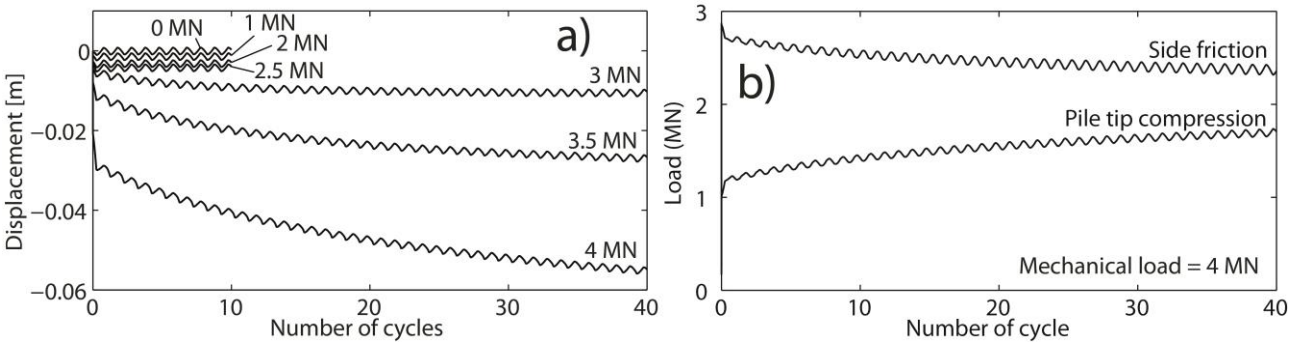

Figure 4:5 Evolutions of (a) pile settlements and (b) bearing forces under a load of 4 MN and with fully drained conditions

Because the mean temperature of the ground is maintained (see Section 4.3.1and Figure 4:3a), the long term accumulations of settlement are only linked to the mechanical transfer of load from the shaft friction to the base compression. As a result, for loads lower or equal to 2.5 MN, no load is transferred from shaft friction to base compression whereas, for greater loads, transfers whose magnitudes increase with increasing load happen. Example of a transfer from shaft friction to base compression is given in Figure 4:5b for a pile load of 4 MN.

Table 4:4 Evolution of mobilised resistances and settlements according to the mechanical load under fully drained conditions

Mechanical load (MN)	Base compression before → after cycling (MN)	Part of transferred load relative to the total load	Lowest settlement s_{inf} (m)	Variation compared to mechanical settlement
0.00	~ 0	~ 0 %	0.001	-
1.00			0.0023	90 %
2.00			0.004	50 %
2.50			0.0051	43 %
3.0	0.281 → 0.700	14 %	0.0114	147 %
3.50	0.537 → 0.725	18 %	0.0285	264 %
4.00	1.005 → 1.195	17 %	0.0603	192 %

The amount of transferred load from shaft friction to base compression remains between 15-20 % of the total carried load, which induces increase in settlements from 150 % to 260 % relatively to the settlement under mechanical load only (Table 4:4). The lowest settlements observed when there is no load transfer from shaft friction to base compression correspond to the minimum settlement experienced during the reversible cycles.

4.3.3.2 Analyses of the load transfer mechanisms

Under fully drained conditions, the variations in effective stress are only due to thermal expansion or contraction of the pile and the soil. As a result, the impact of radial strains can be clearly identified by analysing the load-transfer mechanisms which are described based on observations made at the soil-pile interface and 1.9 m below the pile top.

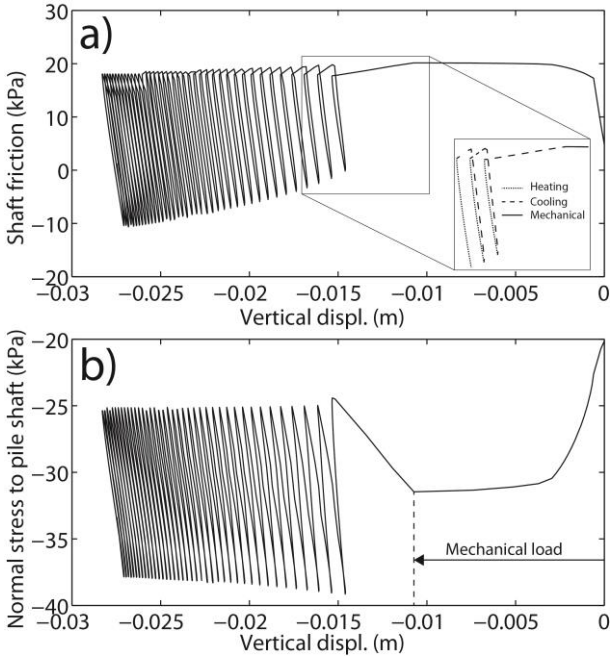

Figure 4:6 Evolutions of (a) the effective stress normal to the pile shaft and (b) the mobilised shaft friction with vertical displacements at 1.9 m below the pile top, above the null point, and with a mechanical load of 4 MN under fully drained conditions

This depth is located above the null point (i.e. the steady point around which the pile expands or contracts thermally) as cooling induces settlement and heating induces heave (Figure 4:6). For the analysed example (P = 4 MN) and at this depth, the ultimate (i.e. maximum) shaft friction is mobilised under mechanical load (Figure 4:6a, Figure 4:6c). Then, the first cooling phase induces further settlement as well as a decrease in shaft friction (Figure 4:6a, Figure 4:6c) which is counterintuitive as further settlement should mobilise more friction or at least remain at the ultimate value. But, the thermal contractions of the pile and the soil that are induced by the cooling lead to a drop in the effective stress normal to the pile shaft (Figure 4:6b, Figure 4:6d). As a result, the ultimate shaft friction decreases. Therefore, the settlement during the first cooling occurs at at the ultimate state of the soil-pile interface while the ultimate value of shaft friction decreases because of the thermal contraction of the soil and pile. The following heating induces a heave and therefore an unloading of the shaft friction. During this phase, the effective stress normal to the pile shaft increases (Figure 4:6b, Figure 4:6d) because of thermal dilation of the pile and soil, which increases the ultimate shaft friction. Then, the second cooling induces settlement with the consequent reloading of shaft friction. This reloading can be divided into two parts (Figure 4:6a, Figure 4:6c): a first part in which the mobilised shaft friction increases with settlements and a second part in which the mobilised shaft friction decreases with settlements. The first part corresponds to a conventional reloading in shaft friction while the second part occurs at the ultimate state (i.e. when the ultimate shaft friction is mobilised). Because this process occurs during a cooling phase, the ultimate shaft friction continuously decreases until the next heating because of thermal contraction of the pile and soil. The transition between these two parts corresponds to the moment when the decreasing ultimate shaft friction meets the increasing mobilised shaft friction. Therefore, two mechanisms are converging during cooling phases: 1/ the reloading mechanism which increases the mobilised shaft friction towards its ultimate value and 2/ the thermal contractions of the soil and the pile which

decrease this ultimate shaft friction. As a result, from the start of the cooling phase to the moment when the mobilised shaft friction equals the ultimate friction, a positive slope is observed. Then, once the ultimate state is reached, the shaft friction remains equal to the ultimate shaft friction which decreases because of the decrease in effective stress normal the pile shaft.

For points below the null point, temperature increase would induce settlement while increasing the ultimate shaft friction and cooling would induce heave and subsequence unloading while decreasing the ultimate shaft friction. However, this is not visible on the present case as the null point remains very close to the pile tip and therefore, the whole pile either heaves or settles.

4.3.4 Case with permeability $k=10^{-16}$ m^2

Variations in pore water pressure due to temperature variations of +/- 10 °C over a year and under drained conditions with a permeability $k_w = 10^{-16}$ m^2 are around +/- 4 kPa (Figure 4:3b). Therefore, two mechanisms whose consequences are opposed are in competition: when temperature increases, thermal expansions of the soil and the pile tend to increase the contact effective stress at the pile-soil interface – and consequently the ultimate shaft friction, as observed under fully drained conditions – whereas water thermal expansion tends to reduce it, and vice versa when cooling.

4.3.4.1 Pile serviceability and resistances

The long term behaviour is similar to the one observed under fully drained conditions with little but relevant differences. Observed long term settlements have the same magnitude of those observed under fully drained conditions and are even slightly less important. This could be explained by the fact that, during heating, pore water pressure induces a decrease in contact stress at the soil-pile interface, facilitating the pile head heave. Conversely, during cooling, the pore water pressure decreases and the contact stress at the soil-pile interface increases. This limits the pile contraction and consequently the pile head settlement. Similarly to the results under fully drained conditions, long term settlements start developing for loads greater than or equal to 2.5 MN (Figure 4:7a). The long term accumulation of settlements is, again, linked to the load transfer from shaft friction to base compression. The portion of total load transferred along the cycles remains around 15 %, slightly lower than under fully drained conditions because of the above mentioned reasons, which causes further settlements equal to 120-160 % of the mechanical settlements (Table 4:5).

Table 4:5 Evolution of load transfer from shaft friction to base compression according to the mechanical load with a permeability $k_w = 10^{-16}$ m^2

Mechanical load (MN)	Base compression before → after cycling (MN)	Percentage of load transferred	Lowest settlement s_{inf} (m)	Variation compared to mechanical settlement
0.00	~ 0	~ 0 %	0.0010	-
1.00			0.0023	90 %
2.00			0.0040	50 %
2.50			0.0050	40 %
3.00	0.281→0.650	12 %	0.0102	121 %
4.00	1.005→1.610	15 %	0.0552	167 %

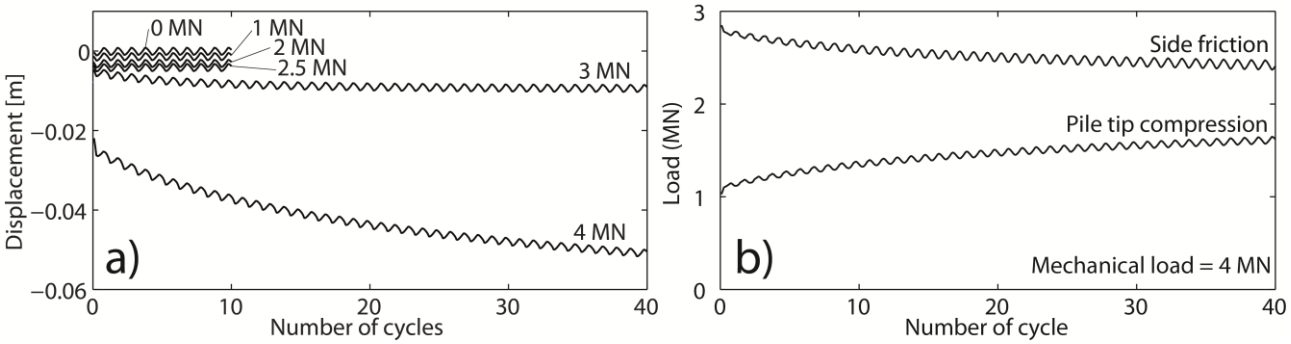

Figure 4:7 Evolutions of (a) pile settlements and (b) bearing forces under a load of 4 MN with the number of thermal cycles in a soil with permeability $k_w = 10^{-16}$ m²

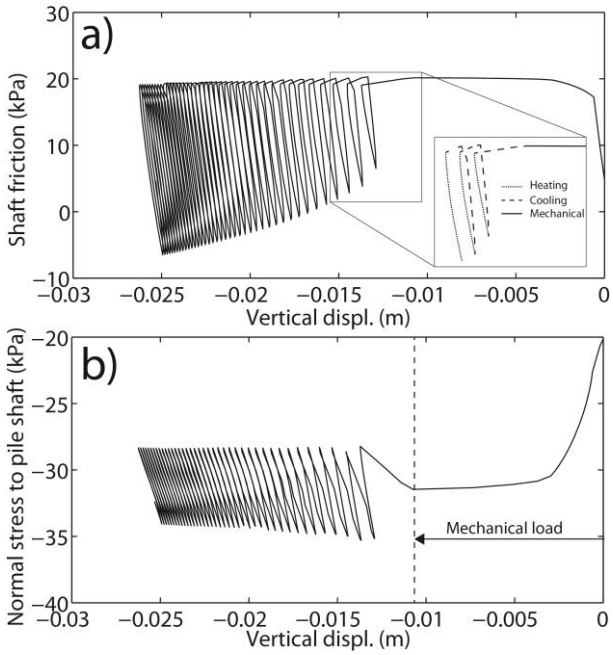

Figure 4:8 Evolutions of (a) shaft friction and (b) effective stress normal to the pile shaft according to vertical displacements at 1.9 m below the pile top, with a load of 4 MN and a permeability $k_w = 10^{-16}$ m²

4.3.4.2 Analysis of the load-transfer mechanisms

Observations of shaft friction and effective stress normal to the pile shaft 1.9 m below the pile top and with a load of 4 MN are presented in Figure 4:8. Settlements are observed during cooling while heating induces heaves. Therefore, this point is located above the null point. The evolution of the contact effective stress follows trends attributed to the thermal expansions of the concrete and soil: the contact effective stress decreases during cooling and increases during heating (Figure 4:8a). However, comparing Figure 4:8b with Figure 4:6b shows that the thermally induced variations in pore water pressure reduce the variations in effective stress normal to the pile shaft. As a result, negative skin friction can even be mobilized during the heating phases because of the "eased" axial thermal deformations (Figure 4:8a).

4.3.5 Case with permeability $k_w = 10^{-18}$ m²

4.3.5.1 Pile serviceability and resistances

The long term serviceability of the pile with a soil permeability $k_w = 10^{-18}$ m² is similar to the two previous cases for loads lower than or equal to 2.5 MN. However, for greater loads, a sudden settlement occurs at the end of the first heating phase (Figure 4:9a) which is accompanied with a sudden transfer from shaft friction to base compression (Figure 4:9b). This settlement happens with such a magnitude that the following cycles are - almost – reversible; suggesting that enough load was transferred to the pile tip compression to prevent further accumulation of settlement.

The amount of transferred load from shaft friction is equal to 15 % while the pile settlement increased by 168 %, values which are similar to the previous cases. This suggests that the permeability $k_w = 10^{-18}$ m² induces long term effects similar to the previous cases but within one single cycle.

Table 4:6 Evolution of load transfer from shaft friction to base compression according to the mechanical load with a permeability $k_w = 10^{-18}$ m²

Mechanical load (MN)	Base compression before → after cycling (MN)	Percentage of load transferred	Lowest settlement s_{inf} (m)	Variation compared to mechanical settlement
0.00	~ 0	~ 0 %	0.0009	-
1.00			0.0022	82 %
2.00			0.0038	43 %
2.50			0.0048	34 %
3.00	0.281 → 0.720	15 %	0.0124	168 %

4.3.5.2 Analysis of the load-transfer mechanisms

Load-transfer mechanisms linked to shaft friction are identified in Figure 4:10 for a point located 14.9 m below the pile top and with a pile load of 3 MN. Because cooling induces settlement and heating induces heave, the point is located above the null point. During the first cooling, further settlement mobilises more shaft friction with a greater trend as pore water pressure decreases (Figure 4:3) and effective contact stress at the soil-pile interface increases (Figure 4:10b).

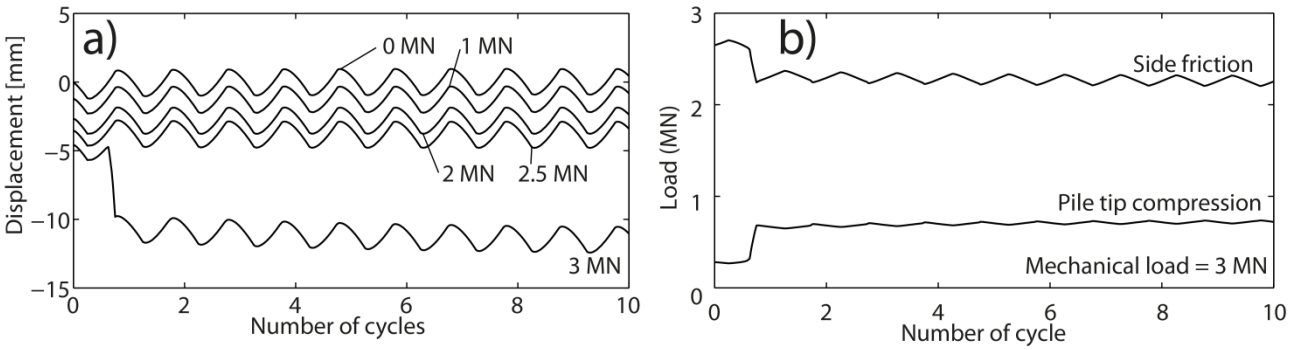

Figure 4:9 Evolutions of (a) pile settlements and (b) bearing forces under a load of 3 MN with the number of thermal cycle within a soil with permeability $k_w = 10^{-18}$ m²

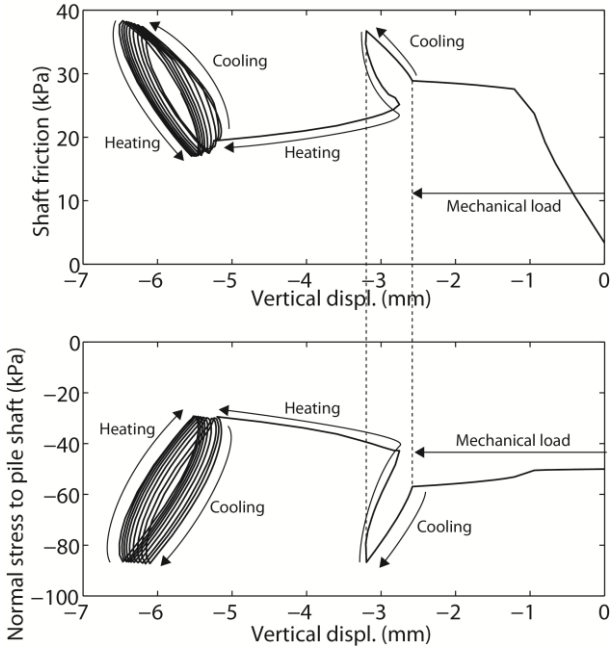

Figure 4:10 Evolutions of (a) shaft friction and (b) effective stress normal to the pile shaft according to pile displacements at 4.9 m below the pile top under a load of 3 MN and with a permeability $k_w = 10^{-18}$ m²

As a result, the thermomechanical response of the pile is driven by pore water pressure variations rather than soil and concrete thermal expansions like for the previous cases. At the beginning of the first heating, an unloading is observed (Figure 4:10a) as well as a significant drop in contact stress due to pore water thermal expansion (Figure 4:10b). When the contact effective stress – and consequently the bearing capacity in friction – becomes too small, the pile starts sliding and load that was previously supported through shaft friction is transferred to the pile base through further compression and therefore pile settlement. The magnitude of this transfer is such that the consecutive thermal cycles are almost reversible (Figure 4:10).

4.4 Assessment of the conservativeness of design approaches based on load-settlement curves

The present discussion assesses the conservative character of the design approaches based on static load tests on pile foundations proposed by the Eurocode 7 (European Committee for Standardization, 2004). The global method is as follows:1/ carry the load tests and gather the results, then 2/ estimate the ultimate compression resistances for each test and deduce the design resistances and finally 3/ make sure that the settlement induced by the design load does not exceed the serviceability limit of the project. Therefore, the approaches proposed by the Eurocode 7 remain conservative when no long term accumulation is observed after mechanical loading. Therefore, the aim of this section is to evaluate if the proposed approaches still remain conservative when including thermal cycles. Indeed, if the serviceability limit is lower than the settlement corresponding to the design resistance but greater than the long term settlement as observed in the present simulations, then the design does not remain conservative. This is illustrated in Figure 4:11 where two load-settlement curves are plotted: the conventional load test curve shows mechanical

settlements as a function of the applied load while the second curve represents the long term settlements (i.e. after heating and cooling cycles) as a function of the applied load.

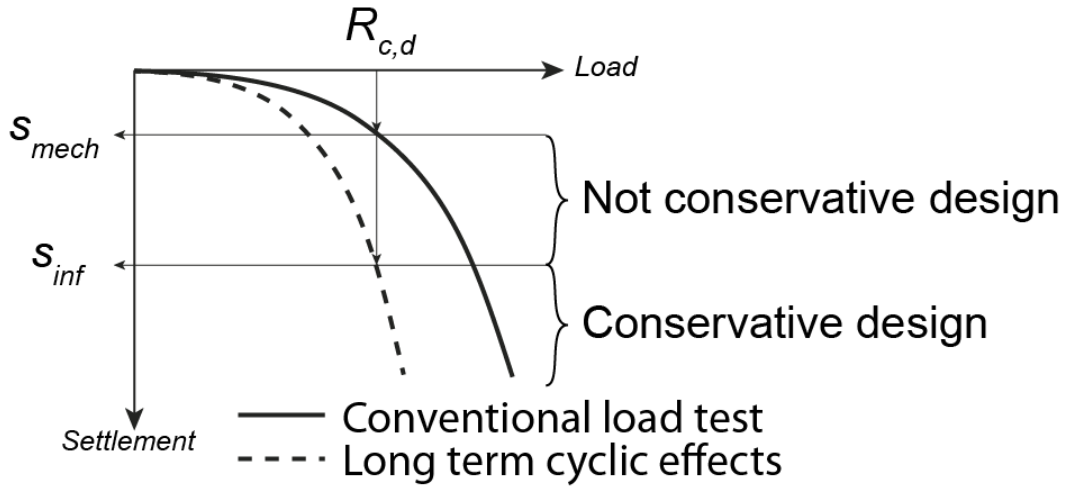

Figure 4:11 Schematic of serviceability verification after design as specified by the Eurocode 7 and "not conservative design" domain associated with long term settlements wherein the Eurocode 7 does not ensure that serviceability limits are respected

If the serviceability limit is within the "not conservative design" area, then the serviceability is not ensured whereas if the serviceability limit is within the "conservative design" area, then the design ensures the serviceability. An example of design based on the present study is derived afterwards to illustrate this statement.

4.4.1 Estimating the design resistances based on the EN 7

According to the Eurocode 7 (European Committee for Standardization, 2004), when the load-settlement curve shows continuous curvature, the measured ultimate compressive resistance $R_{c,m}$ can be defined as the load inducing a settlement equal to 10 % of the pile diameter. From this resistance, the characteristic value $R_{c,k}$ of the ultimate compressive resistance can be estimated as:

$$R_{c,k} = \min\left\{\frac{\left(R_{c,m}\right)_{mean}}{\xi_1}; \frac{\left(R_{c,m}\right)_{\min}}{\xi_2}\right\}$$

Equation 4:13 Characteristic value of pile ultimate bearing resistance based on load tests

where ξ_1 and ξ_2 are correlation factors which may vary according to national annexes. The values used in the present study come from the annexe A.9 provided with the Eurocode 7. Based on the single load test simulated, $\xi_1 = \xi_2 = 1.4$. When the foundation and supported structure are rigid enough so that loads can be redistributed across the foundation, the correlation factors can be divided by 1.1 to take advantage of this. As a result, the characteristic compressive resistance is given by:

$$R_{c,k} = \frac{R_{c,m}}{1.4} \text{ (soft) or } R_{c,k} = 1.1\frac{R_{c,m}}{1.4} \text{ (rigid)}$$

Equation 4:14 Characteristic value of pile ultimate bearing resistance based on a single load test

Finally, the design resistance $R_{c,d}$ is given by:

$$R_{c,d} = \frac{R_{c,k}}{\gamma_t}$$

Equation 4:15 Pile design resistance

where γ_t is the partial factor for the total resistance of the pile. This factor can vary according to national annexes but the values considered in the present study are those of the annexes A.6 for driven piles, A.7 for bored piles and A.8 for Continuous Flight Auger (CFA) piles provided with the Eurocode 7 (European Committee for Standardization, 2004). The different design resistances for the three types of piles (driven, bored or CFA) are presented in Table 4:7.

Table 4:7 Values of design resistance $R_{c,d}$ according to the different design approaches. Values are given in MN and are classified as follows: bored pile / driven pile / CFA pile.

	Design approach 1		Design approach 2	Design approach 3
	Combination 1	Combination 2		
with LR*	3.5 / 4.0 / 3.6	2.7 / 3.1 / 2.9	3.6 / 3.6 / 3.6	4.0 / 4.0 / 4.0
without LR*	3.2 / 3.6 / 3.3	2.4 / 2.8 / 2.6	3.3 / 3.3 / 3.3	3.6 / 3.6 / 3.6

The estimated design loads were then compared to the results of the analyses and conclusions about the serviceability were drawn.

4.4.2 Comparing the EN7 design resistances to the limit loads under which long term accumulation of settlements is observed

For the temperature variations investigated (i.e. +/- 10 °C), no accumulation is observed for loads lower than or equal to 2.5 MN. Design resistances in the design approach 1 are given by the combination 2 as it is the one providing the lowest resistances. Therefore, considering that no redistribution of load is possible (which is the simulation conditions with a pile constant load), the design approach 1 is at the limit (design resistances between 2.4 and 2.8 MN, see Table 4:7) and should remain relatively conservative. But considering that load redistribution can occur within the foundation allows for greater design resistances: long term accumulation of settlements may occur as the design resistances given by the EN7 are greater than 2.5 MN. Conversely, design resistances based on design approaches 2 and 3 are, with or without load redistribution, greater than 2.5 MN. Thus, long term accumulations of settlements that could exceed the serviceability limits provided by the project are to be expected for designs based on these approaches. The present analyses have estimated that under the stated conditions, these long term accumulations range from 120 % to 260 % of the mechanical settlement which is significant.

Obviously, different temperature variations of the pile may lead to different long term behaviours and the presented results should not be considered as representative for all service conditions that energy piles could undergo. But the relatively reasonable ranges in temperature , between -10 °C and +10 °C (Pahud and Hubbuch, 2007), show that conventional design methods may miss some information about the long term behaviour during heating and cooling cycles because serviceability limits may not be respected on the long term while being fulfilled for a conventional (isothermal) design.

Comparisons between the design resistances considering load redistribution with the results of the present simulations should be nuanced as the boundary condition applied at the pile top is of load control type which obviously corresponds to inability to redistribute loads across the foundation. The ability to transfer loads from one pile to another within a piled foundation should reduce the long term accumulations of settlement for the relieved piles but could increase it for the piles towards which the load is transferred. Therefore, maintaining conventional piles within pile foundations that allow load redistribution could reduce this effect as the isothermal piles would carry the transferred loads from the thermal piles without undergoing thermal cycles. Finally, particular attention should be given to saturated impervious soil layers that may significantly lose friction capacity when heated and the a priori design could ignore them as far as this does not lead to significant pile overdesigns.

4.5 Conclusions

The long term behaviour of a single energy pile was investigated for conventional temperature variations of +/-10 °C over 40 years and for different soil permeabilities. The fully drained condition was used as reference where the load-transfer mechanisms are driven by the thermal expansions of the soil and pile. Two values of permeabilities, $k_w = 10^{-16}$ m^2 and $k_w = 10^{-18}$ m^2 were then tested in order to understand the impact of pore water pressure variations on the long term behaviour of the energy pile.

Under fully drained conditions, the behaviour of the pile is only driven by the thermal expansion of the soil and concrete. As a result, the shaft bearing capacity, i.e. the ultimate shaft friction, decreases during cooling and increases during heating. Thus, load is gradually transferred from shaft friction to base compression during the cooling phases with the associated irreversible settlements when the pile load is greater than 2.5 MN.

Pore water pressure variations of +/- 4 kPa were observed at the soil-pile interface with a permeability $k_w = 10^{-16}$ m^2. Despite these variations, the evolution of the soil-pile contact effective stress follows trends due to thermal expansion of the soil and concrete, similar to the case under fully drained conditions. However, differences were observed as the pore water pressure variations enhance the thermal expansion of the pile during heating by decreasing the soil-pile contact effective stress and thus the soil resistance to pile expansion. Conversely during cooling, the water thermally shrinks, increasing the soil-pile contact effective stress and constraining more the pile contraction.

Finally, variations of +/-40 kPa in pore water pressure observed at the soil-pile interface with a permeability $k_w = 10^{-18}$ m^2 drive the load-transfer mechanisms. Indeed, during heating, the decrease in contact effective stress due to pore water thermal expansion exceeds the increase in contact stress due to thermal expansion of the soil and concrete. As a result, the bearing force in shaft friction decreases and, depending on the pile load, the exceeding shaft friction that is not supported anymore is transferred to the pile tip through further settlement. This transfer is rather sudden as it occurs at the end of the first heating phase and that the subsequence cycles are almost irreversible.

Long term accumulations of settlement were found similar in all cases despite the identified load-transfer mechanisms are different, between 150 and 260 % of the mechanical settlement. The amount of load transferred from shaft friction to tip compression remains around 15 % of the pile load.

Finally, the design approaches based on static load test as proposed by the Eurocode 7 were evaluated. It was found that some design approaches may not guaranty the long term serviceability of pile foundations submitted to cyclic temperature variations as design resistances may exceed the loads for which no long term settlement is observed.

Chapter 5 On Using Tunnel Anchors and Bolts as Heat Exchangers with the Ground

5.1 Introduction

The introduction of this thesis has evidence that the heating and cooling of buildings represent an important part of the daily energy consumption in developed and developing countries as well as that geothermal energy represents a significant heat source for which there is a ready supply on Earth (Axelsson, 2010). However, the sustainability of the heat production must be addressed as noted by Axelsson (2010) because even if the shallow geothermal energy is renewable, its sustainability depends on how we use it (Rybach and Eugster, 2010). Various production methods such as simple constant production remaining below design limits, or intermittent high-level operations can be considered sustainable, provided that these methods are correctly designed based on both the production device and the heat source (Franco and Vaccaro, 2012).

The use of geothermal energy at shallow depth was first developed with ground source heat pumps coupled with geothermal loops or aquifers (Sanner, 2001). But relatively recent developments of energy geostructures suggested that using the thermal properties of concrete foundations, i.e. piles, diaphragm walls, concrete slabs, increases the efficiency of the heat exchange between the ground and the GHE (Brandl, 2006; Pasquier and Marcotte, 2012). The concept of energy geostructures was also identified for use in urban tunnel structures, using tunnel linings, geosynthetics or anchors. This could provide additional renewable heat sources to the neighbouring infrastructures (Brandl, 2006; Adam, 2008a). Nicholson et al. (2013) also underlined that producing heat from the tunnels would help extracting the heat generated by train breaks or road traffic.

Several solutions adapted for urban tunnels have already been examined on site – mainly in Austria – and numerically. Thermoactive lining segments (Franzius and Pralle, 2011) have been fabricated with absorber pipes included within the lining elements, and installed on a 54-m long portion of the Jenbach tunnel. The activated portion is located 27 m below the soil surface, has a diameter of 12 m. It was chosen that the heat pump would deliver 43 kW out of the 80 kW of the peak demand at -16 °C, which represents a heat extraction rate from the ground of 15 kW (SFP ~ 3) (Frodl et al., 2010). This required a 54-m long portion of tunnel made of 189 special 0.5-m thick lining elements (Figure 5:1). Nicholson et al. (2013) modelled a tunnel section using thermoactive lining elements using thermohydromechanical finite element analyses and thermally induced stresses remains relatively low, i.e. less than 10 % variation. They also tested the impact of a train fire and found that since the absorber pipes are installed close to the tunnel extrados, the fire induced temperature increase does not threatens their integrity despite at the element connections which could not be protected. Thermoactive geotextile deployed between the primary and secondary linings have been tested on a portion of the Lainzer tunnel in Vienna, Austria (Adam and Markiewicz, 2009). Portions of geotextile were equipped with 2 U-loops (see Figure 5:2) off site so that *in situ* installation was not delayed too much. On site work consisted in connecting the geotextile portions to the collection line. Diaphragm walls of cut and cover tunnels were equipped with absorber pipes either tightened within the reinforcing cage of the walls as in Vienna (Austria) where Brandl (2006) listed nearly 38’000 m^2 of thermally activated diaphragm wall in 2006, or on the outer face of the walls as in the United-Kingdom (Amis and Robinson, 2010). Invert slabs and floor slabs were also equipped with absorber pipes when the U2 metro line of Vienna (Austria) was extended. Prototype rock bolts were also developed and tested in an embankment in Vienna, Austria (Figure 5:4). These were self-

drilling anchor bolts whose hollow bore, dedicated to flushing or grouting, was equipped with coaxial geothermal probes, the external part of which acted as the bolt (Adam, 2008b). The heat exchanger anchors (in the broad sense) were numerically investigated by Adam and Markiewicz (2009). This concept could be extended to grouted anchors (e.g., Store-Norfors bolts) or strand anchors provided that there is enough space for the absorber pipes to be installed in the anchor borehole. The former type of anchor, grouted in mortar, lends itself well to the installation of absorber pipes as its mechanical performances are hardly sensitive to the actual diameter of the anchor borehole. Mechanical anchors and resin rock bolts are made of rebars that are sealed at the bottom of the anchor borehole. They therefore require boreholes with a diameter adjusted to the anchor mechanism (30 mm to 50 mm), which may not allow the installation of absorber pipes.

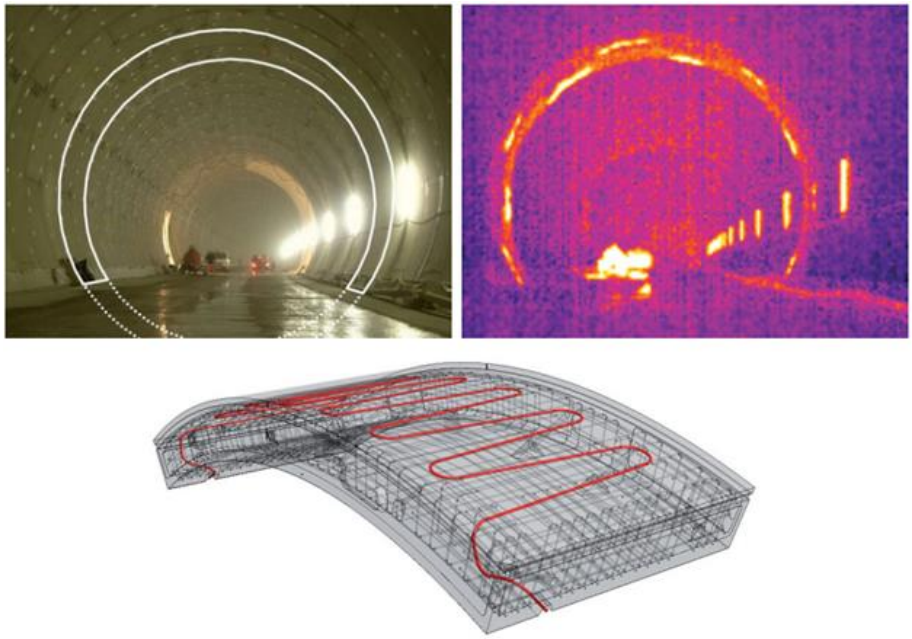

Figure 5:1 Visible and infrared pictures of the thermoactive portion in the Jenbach tunnel (Austria), and 3-D model of the thermoactive lining elements, from (Frodl et al., 2010)

Figure 5:2 Portion of the Lainzer tunnel (Austria) equipped with thermoactive geosynthetics, from(Adam and Markiewicz, 2009)

Figure 5:3 Picture of a diaphragm wall reinforcing cage equipped with absorber pipes in Vienna ,Austria (left), from (Brandl, 2006), and thermoactive floor slab (middle) and tunnel invert (right), from (Adam and Markiewicz, 2009)

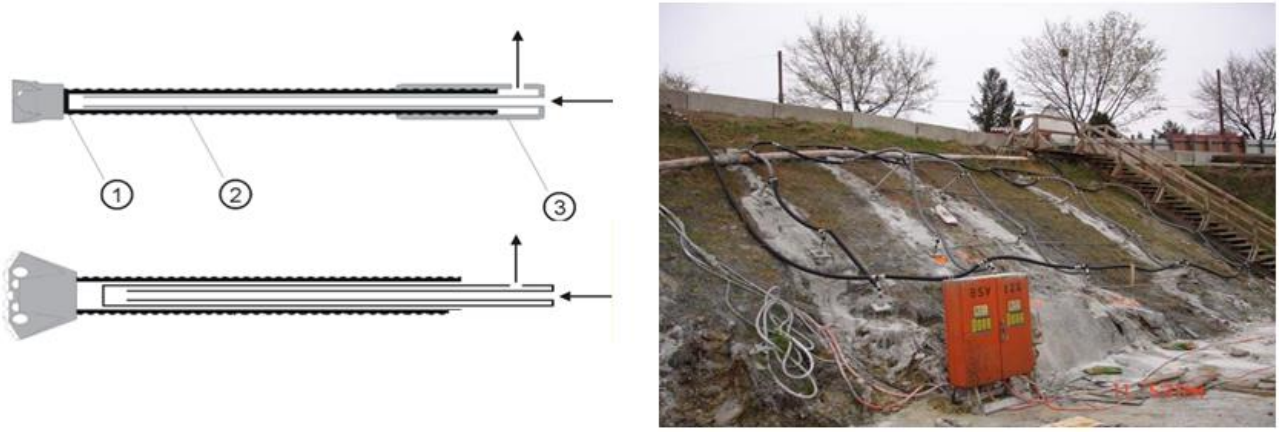

Figure 5:4 Scheme of the heat exchanger anchors (left) and picture of the test site in Vienna, Austria (left), from (Adam, 2008b).

Therefore, the present study addresses the potential of using ground anchors of a cut and cover tunnel and bolts of a bored tunnel as heat exchangers with the ground. No particular anchor technology is identified, as the purpose of the study is to provide a first insight in the concept before developing technical solutions for real implementation.

The method of investigation is first presented. The geometries of the cut and cover tunnel and bored tunnel are detailed as well as the tested ground conditions and heat production methods. The mathematical formulation of the thermohydromechanical approach is then given. Finally, a model to estimate the price of the produced energy is proposed in order to include the economic factor within the comparisons.

The second section is divided into two similar parts, one related to the cut and cover tunnel and the other to the bored tunnel. The numerical analyses are presented with the meshes, boundary conditions and numerical strategies for each of the tunnels. Results of the finite element analyses are then discussed and compared.

Finally, estimated amounts of produced energy through the tunnels are compared to the productivity of energy piles, another type of energy geostructures that has now been used for 30 years, in order to support the concept.

5.2 Method of investigation

This section first provides information about the two urban tunnels whose geothermal potentials linked to the use of anchors as heat exchangers with the ground were quantified. Next, the different production methods as well as the conditions under which these potentials were evaluated are presented and discussed. Then, the mathematical formulation of the thermohydromechanical analyses is given. Finally, an energy budget of the global system allowed building a quantitative model for the price of the produced heat.

5.2.1 Two different types of urban tunnels

5.2.1.1 The cut-and-cover tunnel

The cut-and-cover tunnel modelled for the study was built following the top-bottom method: diaphragm walls are first installed on each side of the future excavation which is then executed; the tunnel body is installed within the excavation and the remaining space is backfilled. Ground anchors are required to maintain the diaphragm walls from the excavation phase until the cut is backfilled. They are installed at the desired depths as the excavation progresses. The modelled excavation is 14-m wide and 9-m deep in order to contain a 10-m wide and 7-m high tunnel.

The diaphragm walls are 16-m deep and 0.5-m thick. The backfill material is the same as the excavated ground. The design of the ground anchors was achieved using Rido software for a silty soil and with a longitudinal (along the tunnel axis) spacing of 3 m. The final design consists in eight 20-m-long ground anchors per cross section whose inclination is 20 ° below the horizontal. The construction method of cut-and-cover tunnels implies that the anchors remain relatively close to the soil surface. As a result, they can undergo unsaturated conditions and the thermal influence of the soil surface subjected to the temperature variations can have a significant impact on the heat production efficiency. Mechanical implications of the heat production on the cut-and-cover tunnel were not quantified because the initial state of the soil (i.e. stresses and strains) strongly depends on the tunnel location and the overlying structures.

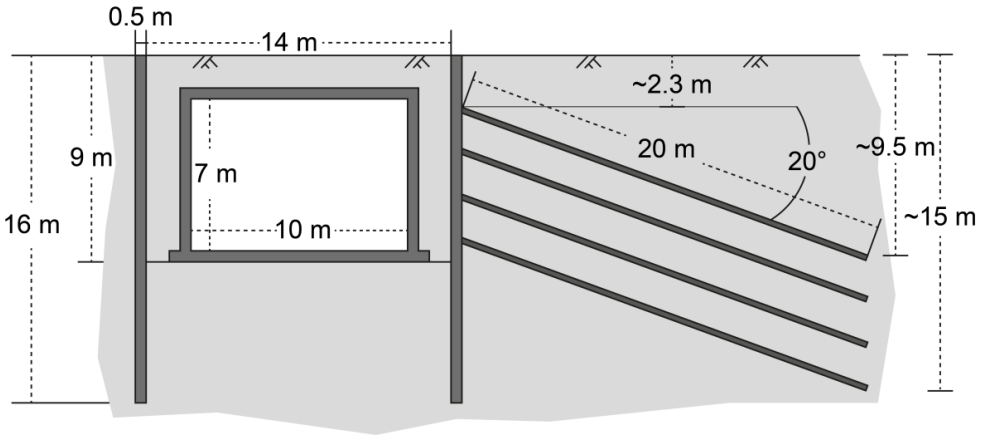

Figure 5:5 Scheme of the cut-and-cover tunnel

5.2.1.2 The bored tunnel

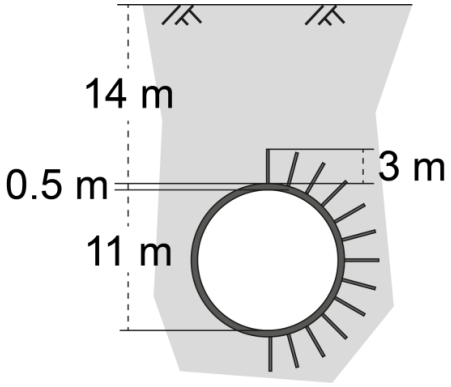

Figure 5:6 Scheme of the bored tunnel

The investigated bored tunnel is based on the St-Laurent M2 metro tube in Lausanne (Switzerland). The tunnel has a diameter of 11 m and is shielded with a 0.5-m thick concrete lining. The tunnel ceiling is located 24 m below the soil surface and the ground around the excavation is maintained with twenty four 3-m long bolts each 1.5 m along the tunnel axis.

Because of the depth at which the tunnel is installed, we assumed that the soil remains saturated and that the thermal influence of the soil surface is negligible. Furthermore, the mechanical implications of temperature variations in the ground may become significant due to the confinement induced by the surrounding ground. They are therefore quantified within the thermoelastic framework assuming that plastic mechanisms may develop during the excavation phase, prior to geothermal exploitation of the tunnel.

5.2.2 Production methods and ground conditions

5.2.2.1 Pure heat production and seasonal heat storage

In practice, the design of the heat exchanging system would be based on building heat demand. However, because no particular demand was targeted, the adopted strategy is to increase heat production until the ground temperature drops below a given threshold in between the anchors or bolts. This threshold is set to roughly 273 K (i.e. 0 °C) in order to prevent frost heave and induced damages to surface structures as well as the freezing of buried water pipes that could break them.

The thermal loads applied to the ground anchors and bolts are based on air temperature because the colder the climate the greater the heating demand. Data taken from Meteoswiss weather station of Pully-Lausanne (Switzerland) were found to be fairly representative for the Swiss climate. Indeed, different simulations were achieved using air temperature data from other Swiss cities (i.e. Zürich and Lugano) and no significant impact on ground temperature profiles was found. The statistics used were obtained over a 30-years long period of time. The curve used in the present study was obtained by averaging these 30 curves month by month.

Adapting the heat production/storage on air temperature data allows building a better scenario than using step functions. Indeed, heating systems installed in the buildings generally use a temperature gauge to monitor the outside air temperature. Thus, thresholds delimit the domain when heating or cooling is required.

The shape of the thermal loads applied to the ground anchors or bolts were therefore designed as mirror-like curves relatively to the air temperature. Two different heat flux multipliers were defined:

- Ce, which stands for "Cycle with extraction", represents a cycle where only heat production is considered, letting the ground at thermal rest during hot spells
- Cei, which stands for "Cycle with extraction and injection", represents seasonal heat storage. Cei,i stands for a Cei cycle beginning by heat injection and Cei,e for a Cei cycle starting with heat extraction.

Thermal loads applied to the cut-and-cover and bored tunnels have the same shapes as given by the heat flux multipliers Ce and Cei, only their amplitudes vary. These amplitudes were determined by optimising seasonal heat storage (i.e. the Cei cycle) under the most favourable conditions which are in a saturated silty soil. The optimum amplitude P_{T0} fulfilling the 273-K temperature threshold is 4 W/m for the cut-and-cover tunnel and 16 W/m for the bored tunnel. Subsequent optimisations are achieved by reducing the amplitude of the heat extraction (positive heat flux multiplier) only, keeping the amplitude during heat injection equal to P_{T0} for seasonal heat storage or 0 for pure heat production.

5.2.2.2 Investigated soils

Because significant groundwater could compromise the seasonal heat storage that is investigated in the present study, only the soil properties that are relevant to impermeable (NP) to slightly permeable (SP) soils were retained. The physical properties of the soils were selected based on extensive studies (Farouki, 1986; Schaap et al., 2001; Bear and Cheng, 2010) to represent the typical characteristics of silt and clay for SP and NP soils, respectively, which are representative for two extremes in soil classification (Figure 5:8).

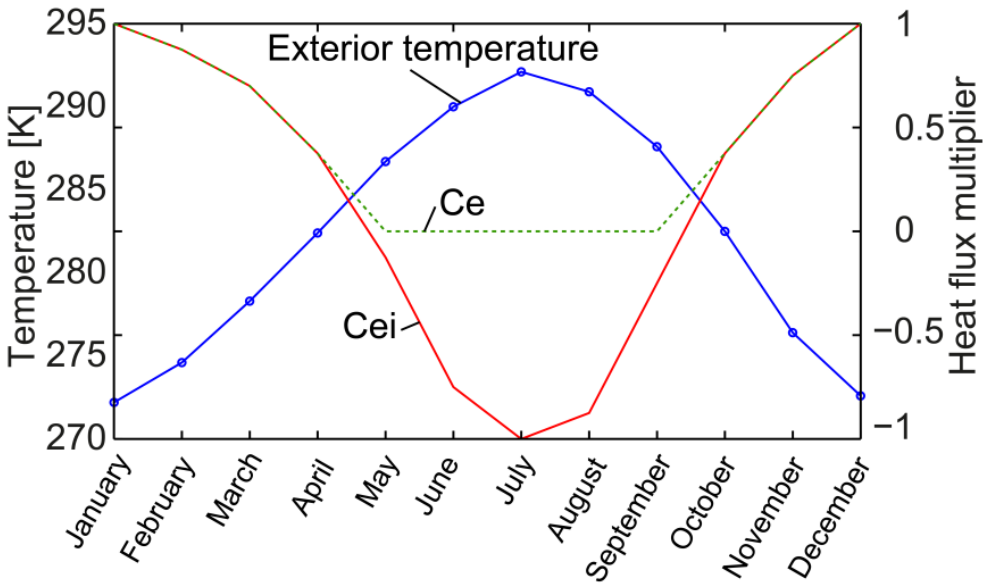

Figure 5:7 Mean monthly temperatures (blue, solid dotted line) and thermal loads for pure heat production Ce (green, dotted line) and for seasonal storage Cei (red, solid line)

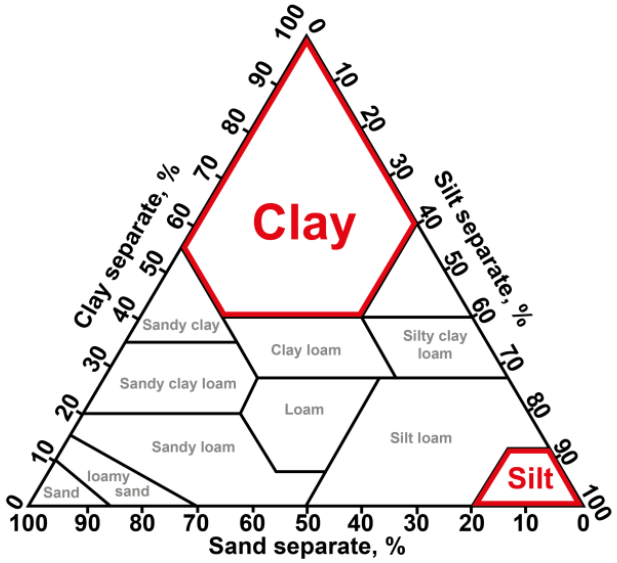

Figure 5:8 USDA soil texture classifications

5.2.3 Mathematical formulations

5.2.3.1 Groundwater seepage and water content

The fluid flow through the porous media is modelled using the Darcy's law and the soil water content follows the van Genuchten model. The mathematical formulations of these two phenomena are given in this section.

Water mass balance equation

Since neither evaporation nor condensation is considered in the present study, the mass balance of water is:

$$\frac{\partial}{\partial t}\left(n\rho_w S_w\right) + div\left(\rho_w \boldsymbol{q_w}\right) = 0$$

Equation 5:1 Water mass balance

where n is the soil porosity, S_w is the degree of saturation, ρ_w is the water density and $\boldsymbol{q_w}$ is the Darcy's velocity. The water density ρ_w depends on water pressure p_w and temperature T according to:

$$\rho_w = \rho_{w0}\left(1 + \frac{p_w - p_{w0}}{\chi_w} - \beta_w\left(T - T_0\right)\right)$$

Equation 5:2Evolution of water density with temperature and pressure

where χ_w is the water compressibility, β_w is the water thermal expansion and ρ_{w0}, p_{w0} and T_0 are reference values.

Fluid flow through a porous media

The air pressure is set constant and equal to 1 atm everywhere unsaturated conditions are encountered. As a result, there is no air flow within the domain. The water flow within porous media is described using the Darcy's law:

$$\boldsymbol{q_w} = -\frac{k_{r,w}k_w}{\mu_w}\left[\nabla p_w + \rho_w g \nabla y\right]$$

Equation 5:3 Darcy's law

where p_w *is* the pore water pressure, y is the vertical coordinate, k_w, $k_{r,w}$ and μ_w are the intrinsic and relative kinematic permeability coefficients and the water viscosity, respectively.

Table 5:1 Water dynamic viscosity

Fluid	Dynamic viscosity μ_{w0} (in Pa s)	Dynamic viscosity coefficient $\alpha_{\mu w}^{T}$ (K^{-1})
Water	0.0013	0.011

The water dynamic viscosity μ_w (in Pa.s) describes the shear developed in water when it is put in movement. It is assumed linearly dependent on temperature (reference temperature T_0 = 273 K) according to the linear coefficients $\alpha_{\mu_w}^{T}$ given in Table 5:1:

$$\mu_w(T) = \mu_{w0}\left(1 + \alpha_{\mu_w}^{T}\left(T - T_0\right)\right)$$

Equation 5:4 Evolution of the dynamic viscosity with temperature

Water flow also depends on the intrinsic permeability k_w (in m^2) and the relative permeability $k_{r,w}$ (without unit). The intrinsic permeability is representative for solid matrix wherein the fluid flows. Adopted values for clay and silty soils are given in Table 5:2. Relative permeability $k_{r,w}$ is used to take into account the reduction of the space utilized to build the flow of the water according to the degree of saturation of water in the soil matrix. Indeed, water will have less space to flow when the water saturation of the soil matrix is reduced and therefore its relative permeability will be reduced. Thus, the water relative permeability lies between 1 (for a saturated material) and 0 (for a dry material). The final permeability of the soil matrix is then given by the product of the intrinsic permeability k_w and the relative permeability $k_{r,w}$. Nevertheless, the relative permeability of water was set constant and equal to 1 for the present study, giving an upper bound of water flow.

Table 5:2 Intrinsic permeabilities of the investigated materials (Bear and Cheng, 2010)

Soil	Intrinsic permeability k_w (in m^2)
Clay	10^{-15}
Silt	10^{-13}

Because no forced water flow is imposed in the present study, flow can only be triggered by porosity variation or thermal expansion of water. In one hand, deformations of the soil lead to variations in porosity, increasing or decreasing the space where water is contained and creating

pressure gradients. On the other hand, thermal expansion coefficient of water β^{T}_{w} is taken equal to $3.4.10^{-4}$ K^{-1} while air expansion is neglected (e.g. any variation of air pressure is assumed to diffuse rapidly). Furthermore, soil thermal expansion is taken equal to 10^{-5} K^{-1}. Thus, as water expands or contracts more than the soil matrix, pressure gradients are generated when local temperature varies (water compressibility coefficient is equal to $1/\chi_w = 4.54\ 10^{-10}$ Pa^{-1}).

Saturation of the soil

Pores in soils are generally filled by air and/or water. When pores are filled only with water, the soil is fully saturated. When both air and water are present, the soil experiences unsaturated conditions under which the degree of freedom of the soil can be linked to the matrix suction h_w thanks to water retention curves. The model chosen in the present study is the van Genuchten model (van Genuchten, 1980) that describes the degree of saturation S_w of a soil according to the suction h_w ($=p_w$-p_a) thanks to four parameters: m and Π that are defining the shape of the curve and $S_{w,res}$ and $S_{w,max}$ that are the residual and maximum degrees of saturation, respectively. Everywhere the water pressure is greater than the air pressure, the degree of saturation is set to 1; elsewhere, it is given by Equation 5:5 where h_w is the suction and Π is the air entry, i.e. the pressure for which the soil starts desaturating. The adopted model neglects the possibly hysteretic behaviour of water retention in some soils.

$$S_w(h_w) = S_{w,res} + \left(S_{w,max} - S_{w,res}\right)\left[1 + \left(\frac{|h_w|}{\Pi}\right)^{\frac{1}{1-m}}\right]^{-m}$$

Equation 5:5 van Genuchten model for soil degree of saturation

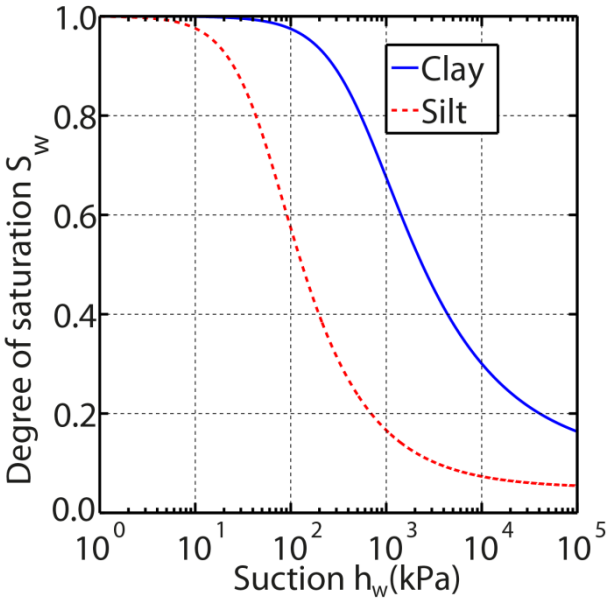

Figure 5:9 Representative water retention curves for clay and silt soils with the parameters listed in Table 5:3

Values of the different parameters used to represent the different soils are listed in Table 5:3. Those were chosen to be representative (Fredlung and Xing, 1994). Thus, the air entry value Π of clay is taken 10 times greater than for the silt and its residual degree of saturation $S_{w,res}$ is 2 times greater than for the silt. The water content is specified thanks to a water pressure profile that is in equilibrium with gravity (i.e. constant slope of $\rho_w.g$) and the water table depth is represented by the altitude where $p_a = p_w$.

Table 5:3 Van Genuchten parameters (Fredlung and Xing, 1994)

Soil	m	Π (kPa)	$S_{w,max}$	$S_{w,res}$
Clay	1/3	500	1	0.1
Silt	7/17	50	1	0.05

5.2.3.2 Heat transport

Heat balance

Heat propagation in soils involves conduction, radiation and convection for the most important part of heat transport. Phase changes and ion exchanges can also take place but in unfrozen soils, the main heat transfer remains conduction as convection requires large fluid movements to occur (Hermansson et al., 2009). Therefore, the heat balance is given by:

$$\frac{\partial S_T}{\partial t} + div\left(\boldsymbol{q_T}\right) = Q_T$$

Equation 5:6 Heat balance considering only heat conduction

where $\boldsymbol{q_T}$ is the heat flux density, Q_T represents any volumetric heat source or sink and S_T is the system enthalpy:

$$S_T = \rho c\left(T - T_0\right)$$

where ρc is the bulk heat capacity of the soil.

Heat transport

The heat flux density is given by the Fourier's law:

$$\boldsymbol{q_T} = -\lambda\, \boldsymbol{grad}\left(T\right)$$

Equation 5:7 Fourier's law

where λ is the bulk thermal conductivity of the soil. Soils being multiphasic materials, bulk properties have to be defined from the individual properties of each constituent (i.e. air, water, solid) according to their proportions. We chose to use volumetric proportions for the thermal conductivity and mass proportions for heat capacity, using the soil porosity n and degree of saturation S_w:

$$\lambda = (1-n)\lambda_s + nS_w\lambda_w + n(1-S_w)\lambda_a$$

Equation 5:8 Bulk thermal conductivity

where λ_s, λ_w and λ_a are the thermal conductivities of the soil grains, liquid water and air, respectively.

$$\rho c = (1-n)\rho_s c_s + nS_w\rho_w c_w + n(1-S_w)\rho_a c_a$$

Equation 5:9 Bulk heat capacity

where ρ_s, c_s, ρ_w, c_w, ρ_a and c_a are the densities and specific heat capacities of the soil grains, liquid water and air, respectively. Individual thermal properties used for the study are given in Table 5:4.

Table 5:4 Individual thermal properties of the different constituents of the investigated soils (Anstett et al., 2005). Properties of concrete, silt and clay are the grain properties.

	Thermal conductivity λ (W m^{-1} K^{-1})	Specific heat capacity c (J kg^{-1} K^{-1})	Density ρ (kg m^{-3})
Clay	2.42	732	2700
Silt	3.43	419	2700
Concrete	1.7	880	2500
Water	0.57	4186	1000
Air	0 (negligible)	1000	1.18

5.2.3.3 Mechanical behaviour

Mechanical implications of the heat production through anchors were only estimated for the bored tunnel as justified in Section 5.2.1.

Momentum conservation

The porous medium equilibrium is given by:

$$div(\boldsymbol{\sigma}) + \boldsymbol{b} = 0$$

Equation 5:10 Global solid equilibrium

where $\boldsymbol{b}$ is the body force vector (i.e. the gravity) and $\boldsymbol{\sigma}$ is the total (Cauchy) stress tensor. The behaviour of porous media is assumed to be governed by the effective stress tensor $\boldsymbol{\sigma'}$ given by:

$$\boldsymbol{\sigma'} = \boldsymbol{\sigma} - p_w\boldsymbol{I}$$

Equation 5:11 Effective stress tensor

The strain tensor in this Lagrangian approach is defined by:

$$\boldsymbol{\varepsilon} = \frac{1}{2}\left(\boldsymbol{L} + \boldsymbol{L}^T\right)$$

Equation 5:12 Lagrangian strain tensor

where ***L*** is the gradient of the displacement vector (***u***) (Charlier et al., 2001).

Constitutive law

Soil and concrete are considered isotropic and their mechanical behaviours are assumed thermoelastic. Therefore, the constitutive law relating the strain tensor to the effective stress tensor is given by:

$$\boldsymbol{\varepsilon} = \boldsymbol{E}^{-1}\left(\boldsymbol{\sigma}' - \nu\left[tr\left(\boldsymbol{\sigma}'\right).\boldsymbol{I} - \boldsymbol{\sigma}'\right]\right) + \left(\beta_L^T \Delta T\right)\boldsymbol{I}$$

Equation 5:13 Thermoelastic constitutive law

where ***E***, ν and β_L^T are the elastic modulus tensor, Poisson's ratio and linear thermal expansion coefficient of the porous medium, respectively. These properties are given in Table 5:5.

Table 5:5 Mechanical properties (Kovari and Tisa, 1998; Bear and Cheng, 2010)

	Elastic modulus E (MPa)	Poisson's ratio ν	Porosity n	Thermal expansion coefficient β^T ($°C^{-1}$)
Clay	30	0.3	0.55	10^{-5}
Silt	30	0.3	0.45	10^{-5}
Concrete	30'000	0.2	0.2/0*	10^{-5}

* *the porosity of the concrete was set to 0 for the bored tunnel analyses in order to have an impervious lining*

5.2.4 Estimating the produced energy price

Energy fluxes of the heating and cooling system can be represented schematically in a Sankey diagram (Figure 5:10) which regroups the ground and ground heat exchangers on the left side of the diagram and the building on the right side of it. We built a quantitative model based on this representation. We consider direct storage (i.e. the heat pump is bypassed during hot spells).

Let E_f be the total electricity consumption of the system during one cycle (i.e. one year), which is the electricity consumed by the heat pump E_{hp} plus the electricity used for running the pumps E_i during hot spells (i.e. when cooling is required) for direct storage (i.e. free cooling):

$$E_f = E_{hp} + E_i$$

Equation 5:14 Total electricity consumption of the geothermal system

The cost of running one cycle is therefore estimated by multiplying the consumed electricity E_f by its price P_{elec}, considering that the heat extracted from the ground is "free". The final gain is represented by the outcome in heat from the heat pump, H_f, which is a function of the Seasonal Factor of Performance (SFP) and the extracted heat H_e:

$$H_f = \frac{SFP}{SFP - 1} H_e$$

Equation 5:15 Final produced heat

Complementarily, the required energy to process the extracted heat H_e with the heat pump, E_{hp}, is given by:

$$E_{hp} = \left(\frac{1}{SFP - 1} \right) H_e$$

Equation 5:16 Electricity consumed by the heat pump

Let assume that the energy used to operate the pumps during direct storage, E_i, is proportional to the stored heat H_i according to a coefficient C_{pump} depending on the pump efficiency and hydraulic head losses in the system:

$$E_i = C_{pump} H_i$$

Equation 5:17 Injected heat during direct storage

Thus, the total consumed energy E_f can be expressed as a function of H_e, H_i and the SFP:

$$E_f = \left(\frac{1}{SFP - 1} \right) H_e + C_{pump} H_i$$

Equation 5:18 Final consumed electricity

Neglecting losses at the different production levels, we can simply estimate the cost of the produced heat, P_h, from the cost (P_{elec}) and amount (E_f) of the consumed energy (i.e. electricity) and amount of produced energy H_f:

$$P_h = \frac{E_f P_{elec}}{H_f} = \frac{\left[\left(\frac{1}{SFP - 1} \right) H_e + C_{pump} H_i \right]}{\left(\frac{SFP}{SFP - 1} \right) H_e} P_{elec}$$

Equation 5:19 Brut price of the produced heat without loss

Note that if storage during hot spells is not considered, the price of the produced heat reduces to:

$$P_h = \frac{P_{elec}}{SFP}$$

Equation 5:20 Brut price of the produced heat without loss and without storage

The finite element analyses have been used to estimate the amounts of energy H_i and H_e that could be stored into and extracted from the ground under various conditions. More accurate analyses may require accounting for individual efficiencies of each component of the system. In the present study, this is quantified as an increase in amounts of extracted and injected heat as well as consumed electricity for the same final amount of produced heat H_f.

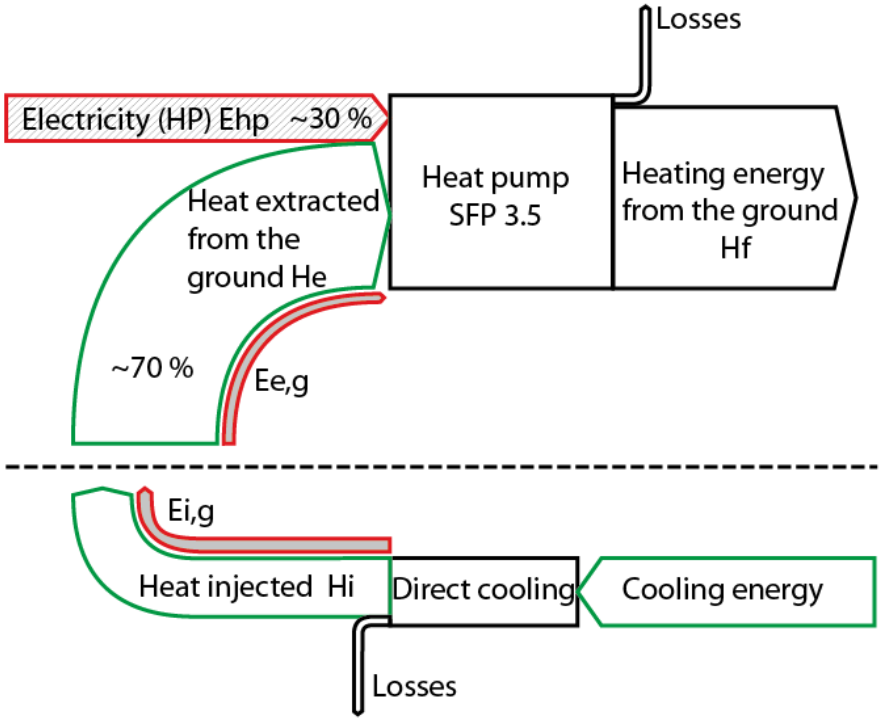

Figure 5:10 Sankey diagram of energies for the heating/free cooling scenario.

The first heat loss is related to the heat exchanger placed between the ground and the heat pump. An efficiency coefficient, $\eta_{e,g}$ which is between 0 and 1, can be used to change the extracted heat H_e into $H_e/\eta_{e,g}$. Indeed, in order to get H_e at the heat pump inlet, we need to harvest slightly more heat from the ground ($H_e/\eta_{e,g}$) to include the transport losses. Similarly, injection efficiency can be used to change H_i into $H_i/\eta_{i,g}$ and the pump efficiency η_P can be used to account for the efficiency of the pumps to convert electricity to mechanical work, changing E_i into E_i/η_P. The price of the produced heat therefore becomes:

$$P_h = \frac{E_f P_{elec}}{H_f} = \frac{\left[\left(\frac{1}{SFP-1}\right)\frac{H_e}{\eta_e} + \frac{C_{pump}}{\eta_P}\frac{H_i}{\eta_i}\right]}{\left(\frac{SFP}{SFP-1}\right)H_e} P_{elec}$$

Equation 5:21 Brut price of the produced heat considering system losses

It is interesting to note that injecting heat always increases the final price of the produced heat which means that other criteria different from the brut price has to be taken into account. Indeed, this estimation does not fit any building energy demand or any power demand. Thus, injecting heat or not into the ground cannot be only based on the final brut price of the produced heat but also on the global energy demand. In order to fully close the analysis of the prices, one may choose another energy source that would compensate the reduced productivity of systems not considering heat storage compared to the one using direct storage. For this purpose, we defined an equivalent price that represents the price of a constant amount of energy either coming only from the geothermal resource or completed with another energy source (fuel oil, gas or electricity):

$$P_{eq} = \left(1 - \frac{H_e(Cei) - H_e(Ce)}{H_e(Cei)}\right) P_h + \left(\frac{H_e(Cei) - H_e(Ce)}{H_e(Cei)}\right) \frac{P_{fill}}{\eta_{fill}}$$

Equation 5:22 Net price of the produced heat considering a given demand

where P_{fill} is the price of the energy used to fill the gap between the amounts of heat produced considering heat storage (H_e(Cei)) and not considering it (H_e(Ce)), and η_{fill} is the efficiency of the conversion of this filling energy into heat. For sake of simplicity in the analyses, we take η_{fill} equal to unity. We considered the following filling energies with the price levels of 2012 (Heizen Mit Öl, 2012):

- Fuel oil, whose price is taken equal to 9.25 cts/kWh
- Gas, whose price is taken equal to 9.53 cts/kWh
- Type VI electricity whose price is taken equal to 15.24 cts/kWh

The proposed quantitative model will be used to compare the final prices of the produced heat by the investigated solutions. Note that this model does not include the initial investment for such a system.

5.3 Numerical analyses

This section presents in details the numerical analyses with the setups, mesh and adopted numerical strategies for each tunnel. We used the finite element code *Lagamine* (Charlier, 1987; Charlier et al., 2001; Collin et al., 2002; Collin, 2003).

5.3.1 The cut-and-cover tunnel

5.3.1.1 Numerical strategy

The seasonal temperature variation induced by the soil-atmosphere interactions in the shallow ground (5-10 m) is accounted for as the ground anchors remain relatively close to the soil surface. As a result, the numerical analyses require an initialization phase during which the ground thermally equilibrates with the atmosphere. The impact of seasonal temperature variations of the atmosphere is modelled as a prescribed temperature variation at the soil surface, based on temperature measurements (see Figure 5:7). Despite the soil skin temperature is not exactly the same as the one from the weather data (i.e. taken 2 m above the ground), it has been shown that it is still a fair approximation (Jin et al., 1997). The initialization phase represents 30 years and the thermal equilibrium was monitored looking at time variations of temperature across the entire domain. Ground anchors were activated once the initialization was finished and the analyses were carried out over 10 more years.

Two different soils were investigated as described in Section 5.2.2.2 as well as three modes of heat production (Section 5.2.2.1). In addition, the soils have been allowed to experience unsaturated conditions: fully saturated with a water table at the soil surface and unsaturated with a water table 20 m below the soil surface which induces a suction of 200 kPa at the soil surface considering that the pore water pressure profile remains in equilibrium with the gravity (rough assumption). As a

result, clay may not really experience unsaturated conditions under this condition while the silt will have a degree of saturation lower than 40 % (Figure 5:9). Therefore, a total of 9 thermohydraulic finite element analyses were carried out for the cut and cover tunnel, the mechanical part being ignored (Section 5.2.1.1). The names of the analyses are given in Table 5:6

Table 5:6 Analyses carried out for the cut and cover tunnel

		Saturated	Unsaturated
Clay (NP)	Ce cycle	NP–Ce–0 m	No
	Cei,i cycle	NP–Cei,i–0 m	No
	Cei,e cycle	NP–Cei,e–0 m	No
Silt (SP)	Ce cycle	SP–Ce–0 m	SP–Ce–20 m
	Cei,i cycle	SP–Cei,i–0 m	SP–Cei,i–20 m
	Cei,e cycle	SP–Cei,e–0 m	SP–Cei,e–20 m

5.3.1.2 Mesh and boundary conditions of the analyses

The mesh and different components of the numerical setup of the analyses are presented in Figure 5:11. The domain is built around a plane of symmetry that is the left vertical boundary. The mesh was refined in the area surrounding the anchors and is made of 4988 nodes, which define 1722 8-nodes plane quadrilateral elements. A 2-dimensional model was chosen because the spacing of the anchors is shorter in the modelling plane (2 m) than in the longitudinal dimension (3 m along the tunnel axis). Therefore, the temperature reductions among the anchors are greater in the modelling plane, and the temperature criterion that is used remains conservative. Obviously, longitudinal heat flow will accumulate in the out-of-plane anchor, but the heat exchange will mostly occur with the far-field ground, i.e., in the plane that contains the tunnel cross-section. As a result, the 2-D model used in the present study represents anchor layers as thin sheets in the third-dimension (i.e. along the tunnel axis) instead of individual rods spread every 3 m along the tunnel axis. The present analyses therefore provide a lower bound of heat production.

The boundary conditions that were applied to the domain limits are presented in Figure 5:11. The temperature at the top boundary of the domain was imposed and varied with time according to the yearly seasonal temperature variations shown in Figure 5:7 in order to account for the thermal interactions between the atmosphere and the soil surface. During cold periods, the soil surface is cooler than the ground, and a heat flux is established from the ground toward the atmosphere. Conversely, during hot periods, the soil surface is warmer than the ground, and a heat flux develops from the atmosphere toward the ground. The left vertical boundary was assumed to be adiabatic because it is the plane of symmetry. The walls of the tunnel were also assumed to be adiabatic. This assumption is a limitation of the present analysis, but it determines a lower bound of the extractible amount from the ground. Indeed, heat is generally produced within the tunnels from traffic activity (i.e. most significant for trains but also for cars) which implies that the tunnel walls act as a heat source helping the sustainability of the system for heating (Nicholson et al., 2013).

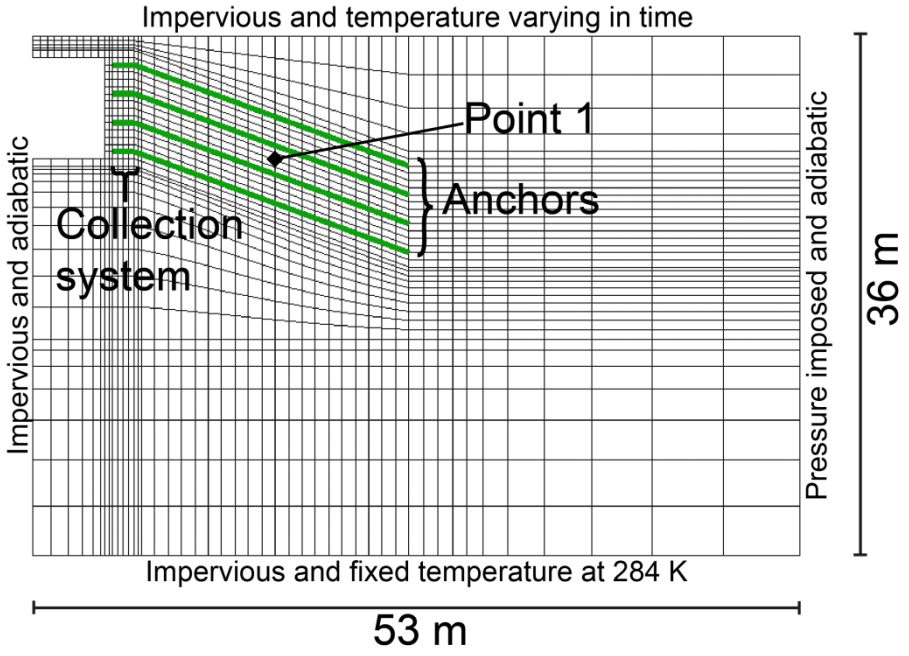

Figure 5:11 Mesh and boundary conditions used for the finite element analyses of the cut and cover tunnel

A more refined analysis would require *in situ* data that may strongly depend on the tunnel geometry and technology (ventilation, tunnel length, etc.). The horizontal far field was represented at the right side of the domain with an adiabatic condition to account for the influence of the seasonal thermal wave because the time-dependent variation of the far field would have been removed by imposing a constant temperature profile. The bottom of the domain was maintained at 284 K, the mean yearly air temperature. Finally, a heat flux is imposed along the anchors as a linear power in W/m (see Section 5.2.2.1). The top and the bottom boundaries as well as the symmetry plane and the tunnel walls are impervious, whereas the vertical right boundary has an imposed hydrostatic pressure profile.

5.3.1.3 Results

Optimisation of heat production

Optimisation of the heat production was achieved looking at the time series of temperature recorded at point 1 (see Figure 5:11) and shown in Figure 5:12. The differences between the Cei,i cycle, which starts with heat injection, and the Cei,e cycle, which begins with heat extraction, vanish after 5 cycles of production. In an optimised configuration, the mean temperature drop is more important when no heat is injected during the hot periods. However, the yearly variations of temperature increase by two to three times when seasonal heat storage is considered. This causes a phenomenon that is observed in the SP–Cei,e–20 m analysis (Figure 5:12), where the 273 K temperature threshold is not fulfilled only during the first year. It happens because the natural temperature level of the ground does not provide sufficient energy to prevent freezing the soil during the first extraction, although it does after the first injection.

The optimisation accuracy is 5 %, meaning that extracting 5 % more heat than in the optimised cycles leads to temperature variations that fall below the 273 K temperature threshold.

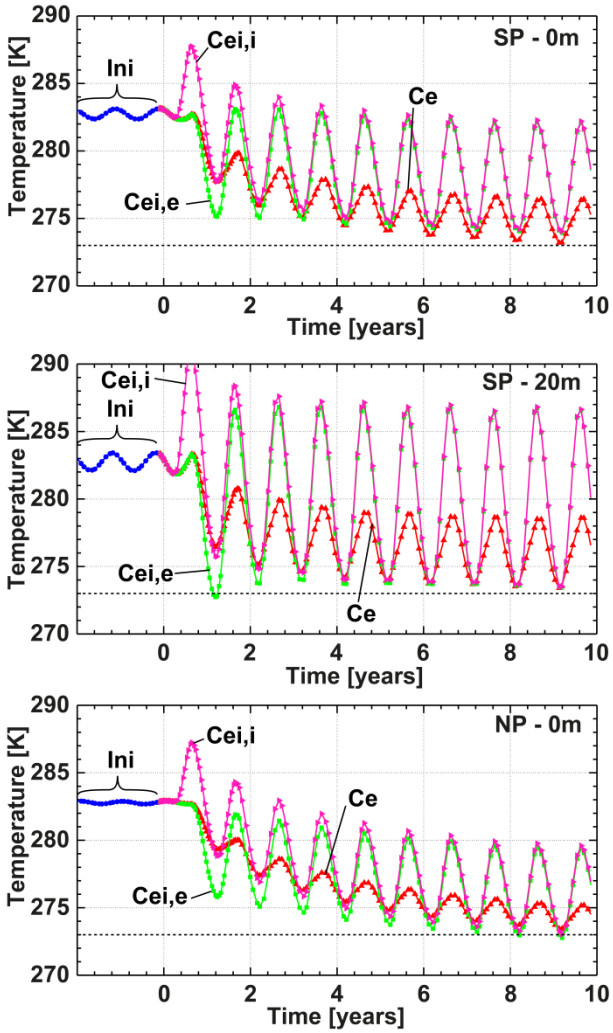

Figure 5:12 Time series of temperature recorded at point 1, in between the ground anchors, and used for the optimisation of heat production on the cut and cover tunnel (SP=silt and NP=clay)

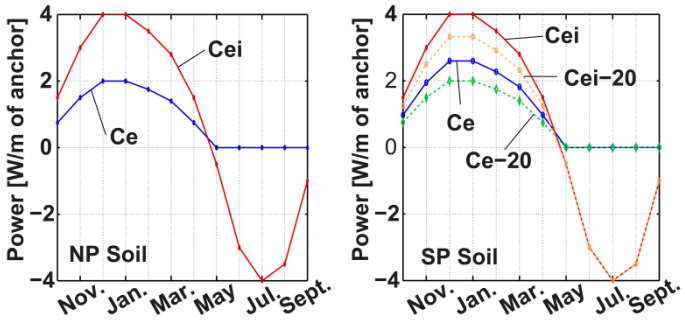

Figure 5:13 Optimised cycles for the cut and cover tunnel in the clay (left) and silt (right)

The optimised cycles for the silt and clay under saturated and unsaturated conditions are presented in Figure 5:13. The main parameter that affects the heat production in the clay is the seasonal heat storage. The relatively weak retention potential of the silt induces significant variations of its water content when the water table varies. Thus, its thermal properties are affected and the heat production efficiency is reduced when the soil is unsaturated (Figure 5:13).

Table 5:7 *Values of extracted and injected heat for different configurations and bounds of the corresponding heat production and injection cycles.*

Cases	*He* (kWh/y/ml)	*Hi* (kWh/y/ml)	*Heat extraction and injection bounds (W/m)*
SP - Ce - 0 m	9.63	0	0 – 2.6
SP - Ce - 20 m	7.41	0	0 – 2
SP - Cei - 0 m	14.46	8.41	-4 – 4
SP - Cei - 20 m	12.02	8.41	-4 – 3.33
NP - Ce - 0 m	7.41	0	0 – 2
NP - Cei - 0 m	14.46	8.41	-4 – 4

Lowering the water table from 0 m to -20 m in the silt reduces the production by 23 % when no seasonal heat storage is achieved and by 17 % with seasonal heat storage (Table 5:7). However, for both the silt and clay, seasonal heat storage leads to greater production. The different amounts of extracted (*He*) and injected (*Hi*) heat per year and per meter of anchor are listed in Table 5:7. These amounts are determined by integrating the optimised cycles over the time length of the hot (for H_i) and cold (for H_e) spells. Being given that there are 8 ground anchors per tunnel cross section, the produced heat per year and per meter of tunnel ranges between 0.6 and 1.2 MWh.

Efficiency of heat storage

The efficiency of seasonal heat storage, η_{inj}, is estimated by comparing the gain in produced heat to the injected heat ($H_i(Cei)$) for a given configuration. The gain in produced heat is represented by the difference in produced heat between the Cei cycle ($H_e(Cei)$) and the Ce cycle ($H_e(Ce)$). Therefore, the efficiency of seasonal heat storage is given by:

$$\eta_{inj} = \frac{H_e(Cei) - H_e(Ce)}{H_i(Cei)}$$

Equation 5:23 Heat storage efficiency

The values of this efficiency are listed in Table 5:8.

Table 5:8 *Efficiencies of the seasonal heat storage for the cut and cover tunnel (SP=silt and NP=clay)*

	SP - 20 m	SP - 0 m	NP - 0 m
η_{inj}	55 %	57 %	84 %

Only half of the injected heat is retrieved during the extraction in the silt, whereas almost 84 % is retrieved in the clay. The desaturation of the silt has little effect on the retrieved heat (Table 5:8). The differences in efficiency are due to the temperature variations that are greater in the silt than in the clay. This is due to the differences in thermal diffusivity between the two soils. Indeed, the thermal diffusivity D_T is relevant for the heat transport: the greater the thermal diffusivity, the better the heat transmission (Hermansson et al., 2009). For example, under fully saturated conditions, the thermal diffusivities of the clay and silt are 4.4 x 10^{-7} m^2/s and 8.5 x 10^{-7} m^2/s, respectively. Therefore, temperature variations observed in the silt (SP) can exceed the natural temperature level

when the water table is at -20 m (Figure 5:13). Thus, a heat flux is established from the heat storage to the surrounding ground, which induces greater heat losses. Conversely, the low temperature levels in the clay minimise the losses and are favourable to establish a heat flux from the ground towards the anchors.

Estimating the price of the produced heat

The quantitative model for the price of the produced heat described in Section 5.2.4 was used to roughly estimate the cost of the heat produced through the cut and cover tunnel. We arbitrarily assumed that C_{pump} = 0.15. The price of the electricity, P_{elec} used to feed the heat pump and the pumps of the system as reported by the Swiss Federal Office of Energy (OFEN) for the year 2011 was 16.2 cts/kWh. The SFP of the heat pump was assumed equal to 3.5.

The estimations were achieved with and without considering losses and when considering them, every efficiency coefficient was set to 0.95. The estimated prices of the produced heat range from 5 to 7cts/kWh (see Figure 9:4) which is competitive compared to the prices reported by the Swiss Federal Office of Energy (OFEN, 2012) and the Heizen Mit Öl (Heizen Mit Öl, 2012) which range between 9 and 16 cts/kWh (see Section 5.2.4). However, this model does not include the relatively high initial investments linked to this type of system. Equivalent prices considering filling energies instead of heat storage range from 6 to 10 cts/kWh, which remains relatively higher than the prices obtained with the seasonal heat storage.

5.3.2 The bored tunnel

5.3.2.1 Numerical strategy

Modelling of the tunnel excavation

The tunnel excavation was first modelled in order to obtain a representative initial stress state of the ground and tunnel lining. This was achieved using the convergence-confinement method (Panet, 1995) as the mesh already comprised the tunnel excavation. Initially, nodal forces balancing the earth pressure were applied along the inner face of the lining and the lining elements were given the properties of the surrounding soil. Then, nodal forces were reduced to 30 % of their initial values before the lining was activated by giving the lining element concrete properties. Finally, the nodal forces were reduced to zero. The amount of relieved excavation forces prior to the lining installation was chosen so that axial stress within the lining reaches 1-2 MPa.

The method employed to model the lining installation remains simple and may deviate from the conventional methods because the finite element code *Lagamine* used in the present study was developed for soft rocks and soils with specific focus on nuclear waste storage and reservoir subsidence (Collin, 2003). Hence, tunnelling oriented elements (e.g. anchors elements, shield elements, joints...) were not available. However, the advantage of using the *Lagamine* finite element code is that it accounts for thermo-hydro-mechanical couplings that are the main focus of the present study.

The first phase of the excavation is carried out in a period of time of approximately 6 days, corresponding to a relatively high tunnel front advancement rate of 1.35 x 10^{-6} s^{-1} (Callari, 2004)

but consistent with the fact that the inner face of the excavation is assumed impervious. The second unloading phase of the excavation, after the lining is activated, is carried out on 52 more days so that the consolidation process around the lining develops. Heating and cooling cycles are then applied to the bolts. As stated above, the mechanical role of bolts was not modelled but the thermal loads through them are modelled using linear heat absorbing elements.

Being given the relatively high unloading rate (Callari, 2004) during the phase prior to lining installation and the low permeability of the considered soils (Table 5:2), the excavation perimeter is assumed to be impervious and it was chosen that it would not act as a drain. Therefore, the porosity of the lining concrete was set to zero because considering a waterproof tunnel which is not acting as a drain gives a higher bound of the stress levels developed around the lining (Lee and Nam, 2001).

5.3.2.2 Mesh and boundary conditions of the analyses

The domain is built around a vertical plane of symmetry (i.e. the vertical left boundary). The mesh is refined in the area surrounding the bolts and is made of 5385 nodes defining 1867 8-nodes plane quadrilateral elements among which 192 are arranged in 4 concentric layers to represent the tunnel lining. The justification of using a 2-D model are similar to the ones provided for the cut and cover tunnel configuration (see Section 5.3.1.2).

Linear heat flux is imposed along the bolts according to the heat production method that is investigated (Figure 5:7). Vertical displacements are prohibited on the bottom boundary and horizontal displacements are blocked along the vertical boundaries except along the tunnel lining. The boundary conditions applied to the domain limits are presented in Figure 5:14. Temperature is fixed to the average yearly air temperature of 11 °C (284 K) all around the domain except along the left vertical boundary which is adiabatic for symmetry reasons.

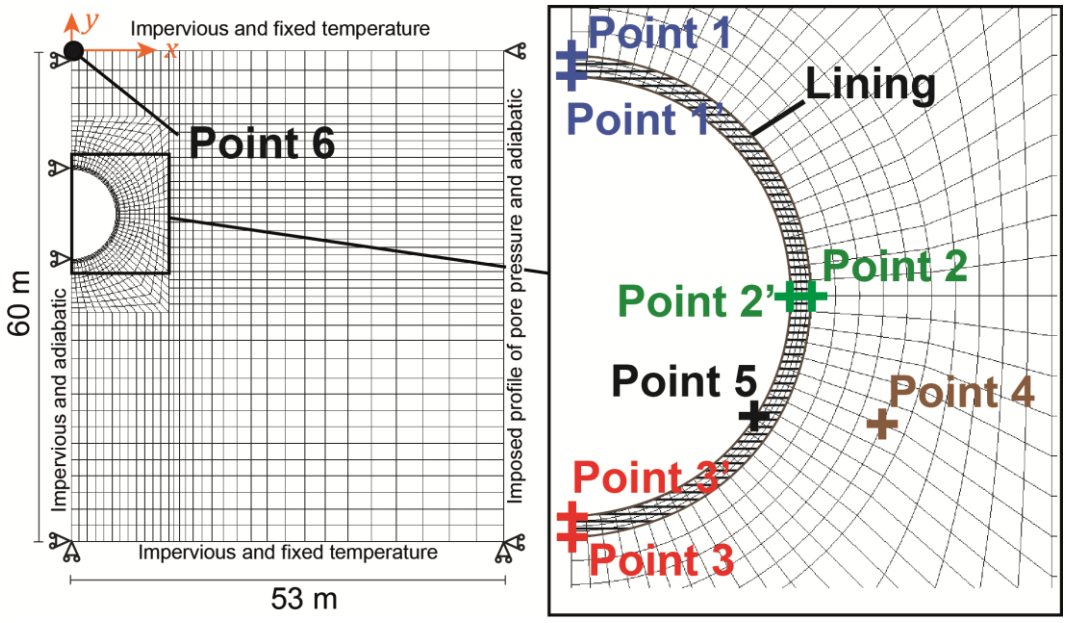

Figure 5:14 Mesh and boundary conditions of the bored tunnel analyses

The temperature at the tunnel intrados is assumed to be constant and equal to 11 °C which is a rough assumption but remains conservative as hot tunnels may be hotter and would act as a heat source. Therefore, this condition gives a lower bound of heat production capacity. A hydrostatic profile of pore water pressure, corresponding to a water table at the soil surface, is imposed on the right vertical boundary.

5.3.2.3 Results

The results of the numerical analyses are presented in this section. First, the excavation is analysed. Then, the thermal behaviour and its thermomechanical response are detailed. Finally, the price of the produced energy is quantified using the model proposed in Section 5.2.4.

The excavation

Vertical displacements observed along vertical profiles at x = 0 m (i.e. along the symmetry axis) and at x = 7 m (i.e. 1 m away from the lining) are presented in Figure 5:15. The part above the tunnel settles while the part below it heaves. Those displacements are attenuated as the profile is farther from the tunnel axis. The major part of the vertical displacements occurs prior to the lining construction. The retaining role of the lining is clearly evident in Figure 5:16 and Figure 5:17. Then, convergence stops and axial stress accumulates within the lining after its construction.

The unloading carried out in the confinement-convergence method induces a consolidation process in the soil. The efforts within the unloaded area are first transmitted to the pore fluid which is less compressible than the soil matrix and creates pressure gradient. Thus, water flows from the unloaded area towards areas where the pore water pressure is lower, transmitting the efforts to the soil matrix. As seen in Section 5.2.3.1, this process is driven by the Darcy's equation that links the fluid flow to the observed hydraulic gradient through the permeability coefficient. Equation 5:3 clearly evidences that the greater the permeability, the greater the flow, being given a hydraulic gradient. Therefore, the consolidation process is slightly faster in the silt than in the clay. Therefore, more effort is transmitted to the silt than to the clay under the same excavation rate. Furthermore, silt and clay are given the same mechanical properties (Table 5:5). Consequently, the vertical displacements observed during the excavation in silt are slightly greater than the ones observed in clay (Figure 5:16). The axial stresses developed within the tunnel lining were estimated as the average at each location (tunnel crown, middle or invert) between the intrados and extrados values (points 1 and 1', 2 and 2' and 3 and 3', see Figure 5:14). The compression reached at the end of the excavation ranges from 1 to 2 MPa.

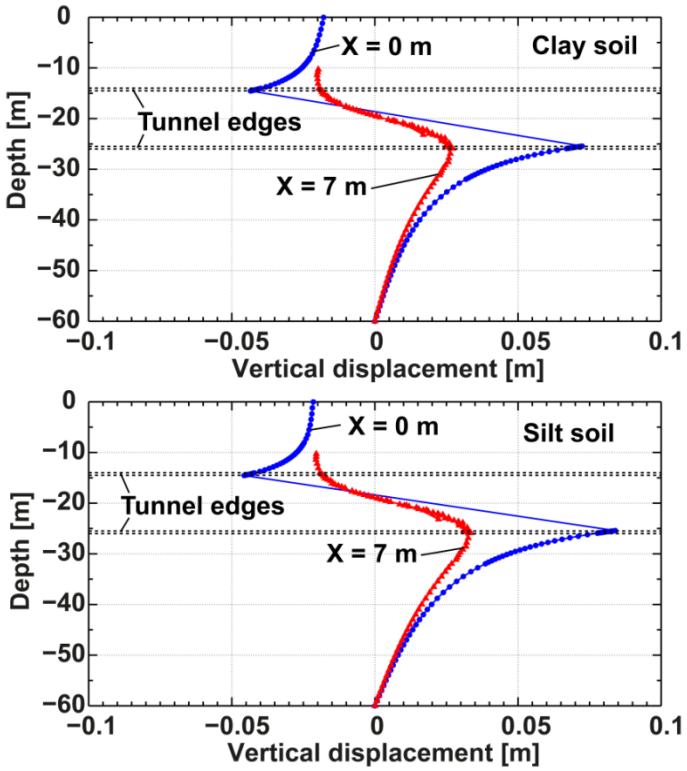

Figure 5:15 Profiles of vertical displacement at the end of the excavation along x=0 m and x=7 m for clay (top) and silt (bottom)

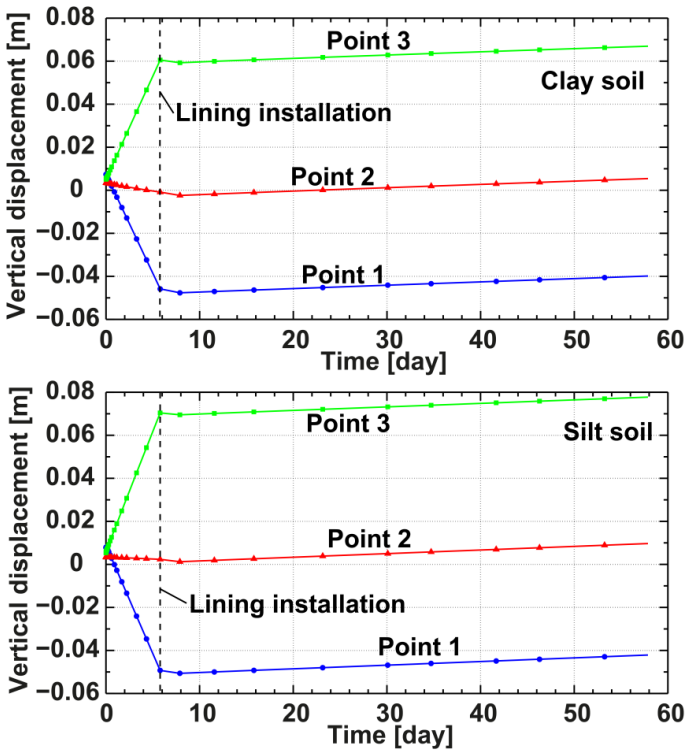

Figure 5:16 Evolution of the vertical displacement at the tunnel crown (point 1), tunnel middle (point 2) and tunnel invert (point 3) for clay (top) and silt (bottom)

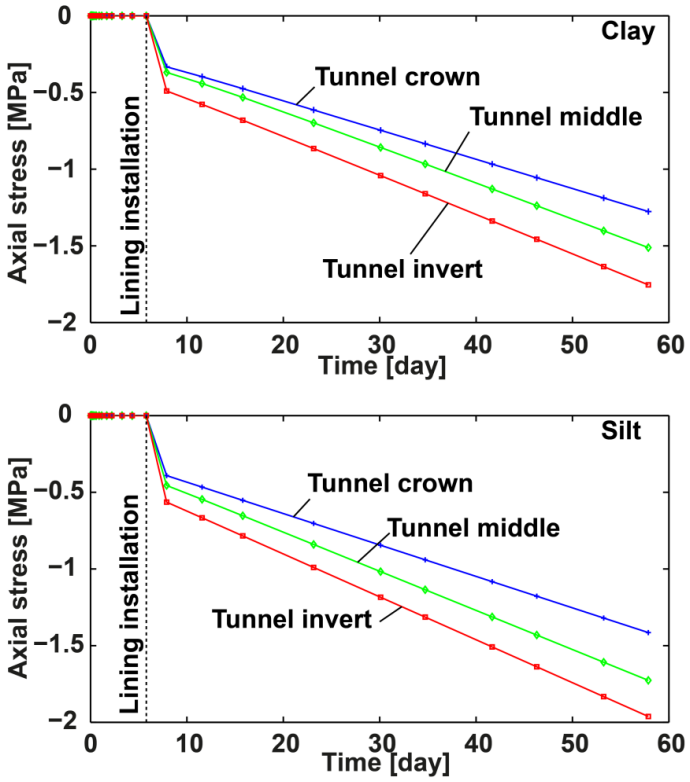

Figure 5:17 Axial stress development within the tunnel lining during the nodal force reduction for clay (top) and silt (bottom)

Thermal behaviour

Energies (extracted and injected) were estimated by integrating the optimized cycles over time. In the most efficient configuration (i.e., silt with Cei cycle), heat production (H_e) reaches 57.86 kWh per year per metre of anchor for an injection (H_i) of 33.62 kWh per year per metre of anchor. The production in the clay (NP) is slightly lower with 54.92 kWh per year per metre of anchors for the same injection. The production is obviously reduced when no heat injection is considered, reaching only 45.94 kWh per year per metre of anchor in the silt and 38.68 kWh per year per metre of anchor in the clay (Table 5:9). However, only saturated conditions were considered so that only the thermal properties of the soil affect the natural heat reload. Therefore, the thermal properties of the silt are more favourable to a significant natural heat recharge than the thermal properties of the clay.

Table 5:9 *Values of extracted and injected heat for the different configurations as well as the bounds of the corresponding heat production and extraction cycles.*

Cases	*He* (kWh/y/ml)	*Hi* (kWh/y/ml)	*Heat extraction and injection bounds (W/m)*
SP – Ce	45.94	0	0 / 12.4
SP – Cei	57.86	33.62	-16 / 16
NP – Ce	38.68	0	0 / 10.45
NP – Cei	54.92	33.65	-16 / 15.2

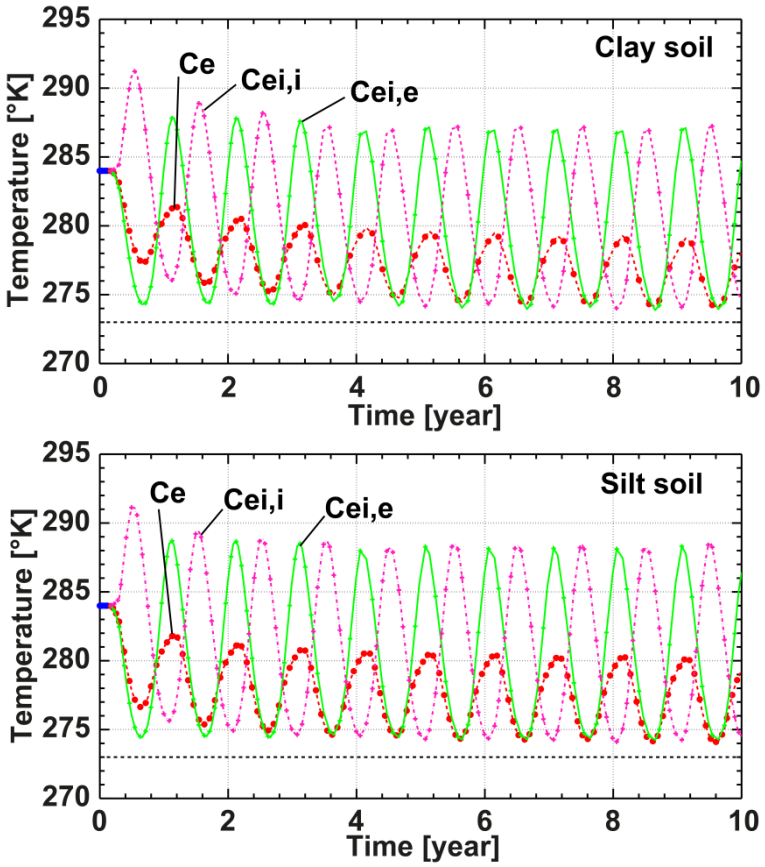

Figure 5:18 Time series of temperature at point 4, right in between the bolts (see Figure 5:14)

The efficiency of heat storage η_{inj} was estimated using Equation 5:23. It never exceeds 50 %, with 48.5 % of retrieved energy from the injection in the clay and only 35 % in the silt (Table 5:10). In conclusion, heat injection does not appear to be necessary with the bored tunnel and seasonal heat storage might not be efficient at the investigated levels. This result is mainly attributed to the geometry of the heat exchangers, which are short in length but distributed around the circular excavation. This defines a 3 m thick ring around the tunnel body, which benefits from a good heat reload coming from all the surrounding soil. Finally, the differences between Cei cycles starting with injection (i.e., Cei,i) and extraction (i.e., Cei,e) vanish after a couple of years without impacting heat production levels (Figure 5:18).

Table 5:10 Efficiency of heat storage through the bored tunnel

	Silt	Clay
η_{inj}	35 %	48.5 %

Thermomechanical response of the lining

The evolution of the axial stress (i.e. in the orthoradial direction within the cross-section of the tunnel) in the lining is monitored to quantify the impact of heat production on the tunnel body. Observations are made at the tunnel crown (points 1 and 1'), middle (points 2 and 2') and invert (points 3 and 3') along the intrados and extrados of the lining (see Figure 5:14).

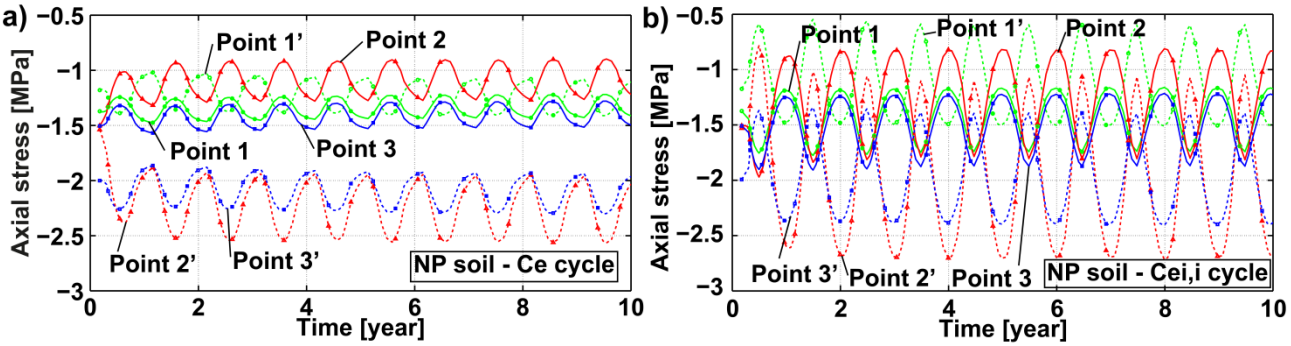

Figure 5:19 Cyclic evolution of axial stress along the intrados and extrados of the lining in the clay (NP)(a) with and (b) without heat injection.

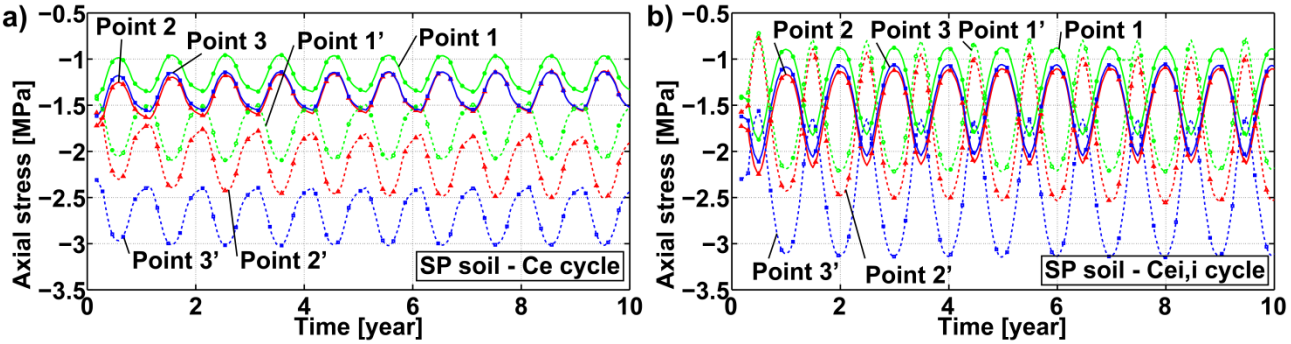

Figure 5:20. Cyclic evolution of axial stress along the intrados and extrados of the lining in the silt (SP) (a) with and (b) without heat injection.

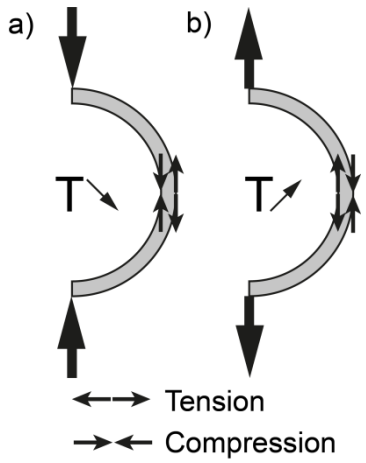

Figure 5:21. Schematic of the lining thermal loads when the temperature of the ground (a) decreases and (b) increases.

The time series of axial stress (Figure 5:19 and Figure 5:20) show that the tunnel intrados experiences further compression while the axial stress on the extrados is relieved when the ground temperature decreases. This results in an increase in the load applied to the lining (Figure 5:21a). Conversely, the axial stress decreases along the intrados and increases along the extrados when the ground temperature increases (i.e., during heat storage), which results in a decrease in the load applied to the lining (Figure 5:21b).

The variations in axial stress reach approximately 0.6 MPa when the ground is at rest during hot spells and increases up to 1.5 MPa when heat is injected. Therefore, heat injection has a significant impact on the stress levels in the lining as they are almost three times greater when considering seasonal heat storage. Thermo-elastic deformations of the tunnel lining during heat production are discussed hereafter. Variations in the vertical diameter of the tunnel are investigated, and horizontal strains are monitored to quantify the serviceability of an invert slab. Variations in the vertical diameter are estimated based on the vertical displacements of points 1, 1', 3 and 3' (see Figure 5:14). The lining is sufficiently rigid – compared to the soil – such that radial displacements along the intrados and extrados of the lining are the same (Figure 5:22 and Figure 5:23).

When no injection is considered, the diameter of the tunnel only undergoes contraction (Figure 5:22a and Figure 5:23a). This contraction varies cyclically between 0.13 mm and 0.8 mm in the silt and between 0.8 mm and 1.4 mm in the clay. When heat is injected during hot periods, the amplitude of the diameter variations is more important, and expansion can even be observed in the silt (Figure 5:22b). In this case, cyclic variations in vertical diameter range from -0.4 mm to +0.2 mm in the silt and from -0.8 mm to 0 mm (i.e., no expansion) in the clay. The general decreasing trends observed in Figure 5:22 are attributed to the long term decrease in ground temperature which induces a long term thermoelastic contraction of the ground.

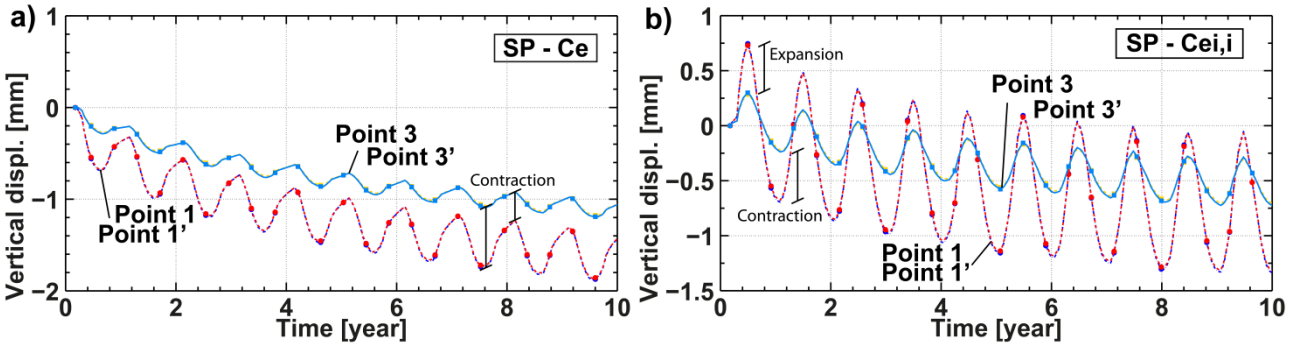

Figure 5:22. Vertical displacements at the tunnel ceiling and invert in the silt (SP) (a) without and (b) with heat injection.

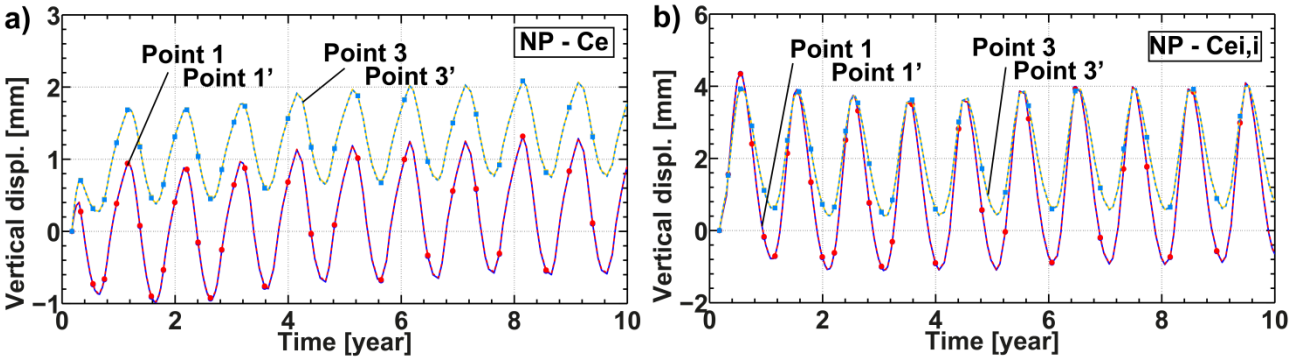

Figure 5:23. Vertical displacements at the tunnel ceiling and invert in the clay (NP) (a) without and (b) with heat injection.

Serviceability of an invert slab is also investigated by monitoring horizontal displacements at point 5 (Figure 5:14), which represents the level of the invert slab top. Amplitudes of the horizontal displacements in the clay are between 0.02 mm and 0.03 mm when heat is not injected and between 0.05 mm and 0.06 mm when heat is injected during hot periods. This is more significant the silt, where the amplitude of horizontal displacements at point 5 is between 0.06 mm and 0.07 mm when no heat is injected and between 0.16 mm and 0.17 mm when heat is injected.

In conclusion, the mechanical implications of seasonal heat storage are relatively significant while its thermal efficiency is moderate.

Estimating the price of the produced heat

Estimations of the price of the produced heat using the quantitative model proposed in Section 5.2.4 lead to values between 5 and 7 cts/kW. Details of the estimates are given in Figure 9:5.

5.4 Discussion

This section compares the heat production of the investigated heat exchanger tunnel anchors and bolts with the production from geothermal piles, which have been used in some major constructions in Switzerland (Anstett et al., 2005) and worldwide. The Swiss Society of Engineers and Architects provides orders of magnitudes of heat extraction that range from 25 W/m to 50 W/m, which corresponds to 50 kWh to 100 kWh per year per meter of pile (Anstett et al., 2005). The linear heat rate that is applied to the anchors (i.e., 4 W/m) may seem small compared to the production of the energy pile, but this quantity is discussed, considering the anchor diameters (100-200 mm) in comparison to the pile foundations (500-1000 mm) and the spacing between the heat exchanger structures. The anchors may be relatively close to each other (1-3 m), whereas the pile foundations are typically separated by at least 3 times the pile diameter and are generally more spaced, which reduces the thermal interactions.

Nevertheless, from an energy standpoint, the piles and the tunnel anchors/bolts should also be compared considering the volumes of soil that they mobilise as well as the absorber-pipe network. Indeed, piles are generally concentrated below a building, whereas the tunnel structures are deployed along longer distances. Two main examples from (Anstett et al., 2005) are compared to capacity-equivalent tunnel structures.

The first example is the Dock Midfield of the Zürich airport (Zürich, Switzerland), which is 500 m long and 30 m wide. The foundation consists of 350 piles among which 306 are geothermal piles. The average active length of the geothermal piles is 26.8 m which represents approximately 660’000 m^3 of soil for an extraction rate of 49 W/m. Thus, the installed capacity of the geothermal piles is approximately 402 kW (Anstett et al., 2005). The capacity-equivalent tunnels based on the configuration used in the present study would be between 1.7 and 3 km long for the cut and cover tunnel, which would activate a volume between 381’000 and 672’000 m^3, and between 500 and 800 m for the bored tunnel, which would activate a volume between 70’000 and 113’000 m^3 of soil.

The second example is the school building complex “Vers-l’Eglise” in Fully (Valais, Switzerland), which has approximately twenty classrooms. This building is approximately 50-m-long and is

founded on 118 driven piles, 41 of which were thermally activated along 23.2 m in average with an extraction rate of 50 W/m in the heating mode. Thus, the extraction capacity of the installation is approximately 45.6 kW, and the piles activate 30'000 m^3 of soil (Anstett et al., 2005). The capacity-equivalent cut and cover tunnel length would be 214 and 427 m and would activate 48'000 and 96'000 m^3 of soil, while the capacity equivalent bored tunnel would be 60 to 91 m, activating a volume of soil between 8'480 and 12'865 m^3.

Therefore, geothermal piles and thermo-active ground anchors reach comparable volumes of soil for a given capacity while the bored tunnel requires much less space because of its increased capacity. However, tunnel structures require longer horizontal dimensions along which losses could be significant and the application of thermoactive tunnels will require that consumers are close to the tunnels (i.e. in an urban or suburban configuration).

5.5 Conclusions

The potential of using ground anchors or bolts as heat exchangers with the ground was estimated. Different configurations were investigated because the dimensions and geometry of the supporting structures vary significantly according to the tunnel type. Few but long anchors are used to support the diaphragm walls during the construction of the cut and cover tunnel while numerous short bolts are distributed all around the bored tunnel lining. Furthermore, different soil conditions were tested since the different tunnels reach different depths. The influence of the soil surface was taken into account for the cut and cover tunnel due to the proximity of the anchors but because no significant ground confinement is expected at this depth, the mechanical implications of heat production were not investigated. Conversely, the bored tunnel reaches greater depths. It was thus assumed to be far enough from the soil surface to neglect the soil-atmosphere thermal interactions. But the stress levels reached deeper in the ground were taken into account as significant confinement on the lining is expected. Finally, different types of heat production methods were investigated in order to estimate the pros and cons of seasonal heat storage. One method considers heat production only, letting the soil at thermal rest during hot spells, while the two others are considering seasonal heat storage, one starting with heat injection and the other one with heat extraction.

It is found that storing heat is economically interesting with the cut and cover tunnel but not so much with the bored tunnel being given the lower heat injection efficiency. Indeed, the configuration of the ground anchors in the cut and cover tunnel is such that they cannot beneficiate from a good natural heat recharge. The ground anchors are long and on top of each other so that the volume wherein they are embedded is important while the perimeter of this volume, which is relevant for the natural heat reload potential, is reduced. Conversely, the bolts of the bored tunnel are shorter but are more numerous and distributed all around the tunnel perimeter so that the impacted volume is still important but beneficiate from an increased surface of exchange with the rest of the soil. This provides a better natural heat recharge. Indeed, if the bolts were longer, the impacted volume would increase while the surface through which the heat recharge occurs would be, in proportion, reduced, therefore lowering the production of the system.

Estimations of produced heat range from 0.6 to 1.2 GWh per year and per kilometer of tunnel for the cut and cover tunnel, and from 2.8 to 4.2 GWh per year and per kilometer of tunnel for the

bored tunnel. The volume of soil impacted by the heat production remains within the vicinity of the ground anchors or bolts and does not go beyond 10 m away from them. Finally, starting with heat injection or heat extraction only affects the first 3 to 5 years of the exploitation. Nevertheless, it is recommended to start by injecting heat in order to prevent freezing the soil during the first year of exploitation, or to adapt the first extraction phase when starting with it.

Mechanical implications of heat production were quantified for the bored tunnel, assuming that the soil and tunnel structure behaved thermoelastically. Depending on the production method, variations in axial stress within the lining, along the intrados and extrados range, from 0.5 MPa – when considering heat extraction only – to 1.5 MPa – when considering heat injection. Corresponding vertical and horizontal displacements were quantified and variations in vertical diameter ranged from 0 to 1.5 mm. These diameter variations are also observed in the horizontal direction and remain around 0.1 mm close to the top of the invert slab. Shear stress within the lining is not significantly amplified by the heat exploitation. Soils having greater permeability will diffuse faster the pressure variations of water induced by temperature variations so that the mechanical implications will be reduced. Vertical displacements at the soil surface, above the tunnel crown, are not negligible as they can reach amplitudes of 1 cm in clay and when heat storage is achieved.

In conclusion, it was shown that using ground anchors or bolts as heat exchangers with the soil is thermally efficient and that it can provide great amount of heat for GSHP systems. However, mechanical implications must be taken into account from a design standpoint. Experiments are needed to confirm the results that have been obtained in this study. Managing the efficiency of both systems with regard to thermal losses has been shown to be an important factor in the economic aspect of these systems, with bored tunnels showing as a better candidate and a better starting point to develop heat exchanger anchors/bolts on an industrial scale.

5.6 Acknowledgements

The author is particularly thankful to Sophie Minon who started this study and realized the meshes of the tunnels, and to Dr. Fabrice Dupray who was strongly involved along the entire project.

Section 3: Experimental investigations of energy piles

Chapter 6 Estimating the Soil Thermal Diffusivity with Interference Analyses

6.1 Introduction

The proper design of closed-loop GSHPs requires a good knowledge of the *in situ* soil conditions, which can be classified in two main categories. The first one corresponds to soils in which a significant natural underground water flow exists. In this case, the soil conditions are not favourable for seasonal heat storage, as the injected heat would be advected away from the GHEs, but are favourable for providing a heat source with a rather stable temperature all year long. The second category corresponds to soils in which no significant underground water flow is observed. In this case, seasonal heat storage is recommended to ensure the sustainability of the heat source. The present paper focuses on the second category of soil conditions, in which no natural underground water flow is observed.

The thermal inertia of the ground is of great importance in ensuring the sustainability of the heat storage as well as the efficiency of the GSHP system. The sensitivity of GSHP systems to design and applied loads was evidenced by Garber et al. (2013). Furthermore, the use of foundation structures as heat exchangers with the ground leads to shorter and more closely spaced GHEs which makes the thermal inertia of the ground even more important.

Under the stated ground conditions, the main heat transport process is heat conduction (Hermansson et al., 2009), which is characterised by the thermal conductivity, thermal diffusivity and/or heat capacity of the ground. Therefore, great efforts have been applied to determine these characteristics. Farouki (1986) separates the methods to estimate the thermal properties of soils into two categories: those based on steady-state analyses and those based on transient analyses.

The steady-state analysis methods are mainly used to determine the thermal conductivity of soils once a heat flux is established either through a sample, i.e. using a guarded hot plate (Materials, 1963) or a cylindrical arrangement (Kersten, 1949), or *in situ*, i.e. using the sphere method (Mochlinski, 1964) or a heat meter (Scott, 1964).

Transient methods provide information about the thermal inertia of the soil, i.e., its thermal diffusivity. Forbes et al. (1849) analysed the propagation of temperature waves in soil using transient one-dimensional (vertical) heat transport analyses. Hoekstra et al. (1973) estimated the thermal diffusivity of cylindrical soil samples by applying sinusoidal temperature signals to the sides of the samples and measuring the temperature variations at the centres. Shannon and Wells (1947) used a thermal shock procedure (i.e., a sudden change in temperature that is maintained) to estimate the thermal diffusivity of a cylindrical sample.

However, these different methods do not provide estimates at an operational scale for GHEs that reach depths between 10 m and 100 m. Samples barely represent real *in situ* conditions, and *in situ* techniques such as the dual-probe pulse method (Bristow et al., 1993) (that is also used for laboratory testing) and time series analyses of 1-D vertical heat conduction data (Hinkel, 1997) only permit investigation of the thermal diffusivity of soils within the first few meters below the surface. Indeed, the former technique is limited by the size of the probes (Bristow et al., 1993), while the latter is limited by the relatively shallow depths, not exceeding 3–5 m, within which the temperature varies annually (Williams and Gold, 1976).

Thermal response tests (TRTs) have been developed based on the infinite line source model (Eskilson, 1987) to estimate the bulk thermal conductivity of a soil mass in which a geothermal borehole is installed (Mattsson et al., 2008). However, the thermal inertia of soils has not yet been investigated on such a scale, even though the bulk thermal diffusivity of soils is becoming more important as shorter and more concentrated GHEs, i.e. energy geostructures (Laloui and Di Donna, 2013), are increasingly being used.

Therefore, this study investigates the potential of using a periodic pumping test that was originally designed to determine the *in situ* hydraulic properties of soils (Renner and Messar, 2006) to estimate the bulk thermal diffusivity of a soil mass on a borehole scale. This estimation was accomplished using an experimental scaled model of a geothermal borehole. The mathematical basis of the method, including the derivation of the equations involved and the graphical inversion used to retrieve thermal diffusivity values from the experimental data based on interference analyses, is presented in Section 6.2. The scaled model used in the present study is described in Section 6.3, as well as the data processing method. Finally, the results obtained based on source–thermocouple and thermocouple–thermocouple interference analyses are presented in Section 6.4. Section 6.5 discusses the applicability of this method on a real scale, based on the scaled model results.

6.2 Testing methodology

Determining the physical (hydraulic or thermal) properties of soils under a periodic steady regime is achieved by comparing an input signal to a recorded signal at a given distance from the source. Comparisons are achieved by means of phase shift and attenuation analyses. The phase shift represents a certain delay between the source and the recorded signal and is related to the inertia of the system. Attenuation is also observed between the amplitude of the source signal and the monitored response. This attenuation is characteristic of storage and/or dissipative effects between the source and the measuring point. This type of analysis is called interference analysis because comparisons are achieved between two different points (Renner and Messar, 2006).

6.2.1 Mathematical basis

Heat transport within soils can be achieved through many different processes (Brandl, 2006) but thermal conduction is the main process occurring in soils in which water advection is negligible (Hermansson et al., 2009). This process is governed by the so-called heat equation (Equation 2:1).

Because the present study focuses on determining the bulk thermal properties of a soil under a periodic steady regime imposed through an "injection well" (Renner and Messar, 2006), the geometry of the source is axisymmetric, and one may want to transpose Equation 2:1 into cylindrical coordinates. Furthermore, if the soil is assumed to be isotropic from a thermal standpoint and it is assumed that no volumetric heat sources or sinks are present, it becomes:

$$\frac{\partial T}{\partial t} = D_T \left\{ \frac{\partial^2 T}{\partial r^2} + \frac{1}{r} \frac{\partial T}{\partial r} \right\}$$

Equation 6:1 Heat equation in cylindrical coordinate system

where r is the distance to the source axis and D_T is the bulk thermal diffusivity of the soil, defined as:

$$D_T = \frac{\lambda}{\rho c}$$

Equation 6:2 Thermal diffusivity

The temperature anomaly applied to the soil at the soil–GHE interface (i.e., at $r = r_i$) is a sinusoidal variation that is assumed to be homogeneous along the GHE wall. Therefore, the applied temperature anomaly can be modelled with a complex form, expressed as:

$$\theta(r = r_i, t) = \theta_i(t) = \theta_0 \exp(j\omega t)$$
$$\theta(r = r_i, t) = \mathrm{Re}\{\theta_0 \exp(j\omega t)\}$$

Equation 6:3 Complex representation of the sinusoidal temperature anomaly at the borehole wall

where $\omega=2\pi/\tau$ is the signal pulsation, τ is the period of the source signal and θ_0 its amplitude. Inserting the following temperature anomaly equation:

$$\theta(r,t) = T(r,t) - T_g$$

Equation 6:4 Temperature anomaly

where T_g is the undisturbed field temperature, into Equation 6:1 yields the following equation:

$$\frac{\partial \theta}{\partial t} = D_T \left\{ \frac{\partial^2 \theta}{\partial r^2} + \frac{1}{r} \frac{\partial \theta}{\partial r} \right\}$$

Equation 6:5 Heat equation in cylindrical coordinates satisfied by the temperature anomaly in the soil

Spreading the space and time variables and searching for a solution with the same pulsation as the source signal (Equation 6:3) yields the following equations:

$$\theta(r,t) = \theta_r(r) \exp(j\omega t)$$
$$\theta(r,t) = \mathrm{Re}\{\theta(r,t)\}$$

Equation 6:6 Complex representation of the temperature anomaly in the soil

Combining Equation 6:5 with Equation 6:6 yields the following equation:

$$r^2 \frac{\partial^2 \theta_r(r)}{\partial r^2} + r \frac{\partial \theta_r(r)}{\partial r} - \left(r \sqrt{\frac{j\omega}{D_T}} \right)^2 \theta_r(r) = 0$$

Equation 6:7 Bessel equation satisfied by the temperature anomaly in the soil

which is a modified Bessel equation of 0th order whose solution is given by a linear combination of the modified Bessel functions of 0th order I_0 and K_0:

$$\theta_r(r) = A.I_0(\varsigma r) + B.K_0(\varsigma r)$$

Equation 6:8 Temperature anomaly satisfying Equation 6:7

where $\varsigma = \sqrt{j\omega D_T^{-1}}$. From this general solution, two types of analyses can be developed, depending on the type of boundary conditions that are applied. Considering a fixed temperature at a given distance R from the source (the Dirichlet condition) yields the following equation:

$$\theta(r,t) = \frac{I_{0R}.K_0(\varsigma r) - K_{0R}.I_0(\varsigma r)}{I_{0R}.K_{0r_i} - K_{0R}.I_{0r_i}}\theta_i(t)$$

Equation 6:9 Temperature anomaly using the boundary condition of Dirichlet type

where $I_{0R} = I_0(\varsigma R)$, $I_{0r_i} = I_0(\varsigma r_i)$, $K_{0R} = K_0(\varsigma R)$ and $K_{0r_i} = K_0(\varsigma r_i)$ are constants. Considering an adiabatic wall at a distance R from the source (the Neumann condition) yields the following equation:

$$\theta(r,t) = \frac{K_{1R}.I_0(\varsigma r) + I_{1R}.K_0(\varsigma r)}{K_{1R}.I_{0r_i} + I_{1R}.K_{0r_i}}\theta_i(t)$$

Equation 6:10 Temperature anomaly using the boundary condition of Neumann type

where I_1 and K_1 are the modified Bessel functions of the 1st kind and $K_{1R} = K_1(\varsigma R)$ and $I_{1R} = I_1(\varsigma R)$ are constants. However, in both cases, letting R approach infinity (i.e., the far-field condition) yields the following equation:

$$\theta(r,t) = \frac{K_0(\varsigma r)}{K_0(\varsigma r_i)}\theta_i(t)$$

Equation 6:11 Temperature anomaly with boundary condition at infinity

Based on Equation 6:11, one can define an amplitude attenuation δ_{TT} and a phase shift φ_{TT} between the source and a point (at r) as follows:

$$\delta_{TT} = \left|\frac{\theta(r,t)}{\theta_i(t)}\right| = \left|\frac{K_0(\varsigma r)}{K_0(\varsigma r_i)}\right| \qquad \varphi_{TT} = \arg\left\{\frac{\theta(r,t)}{\theta_i(t)}\right\} = \arg\left\{\frac{K_0(\varsigma r)}{K_0(\varsigma r_i)}\right\}$$

Equation 6:12 Definition of the signal attenuation and phase shift

6.2.2 Graphical inversion of attenuation and phase shift

In practice, the amplitude attenuation δ_{TT} and phase shift φ_{TT} are experimentally determined from temperature time series recorded at the source and at a distance r. A graphical inversion is then used to derive the thermal diffusivity D_T because Equation 6:12 is not reversible. To accomplish this inversion, Equation 6:12 is rewritten as follows:

$$\delta_{TT}\left(X_{DT}\right)=\left|\frac{K_0\left(N_r\sqrt{j}\left[\sqrt{\frac{\omega}{D_T}}r_i\right]\right)}{K_0\left(\sqrt{j}\left[\sqrt{\frac{\omega}{D_T}}r_i\right]\right)}\right|=\left|\frac{K_0\left(N_r\sqrt{j}X_{DT}\right)}{K_0\left(\sqrt{j}X_{DT}\right)}\right| \qquad \varphi_{TT}\left(X_{DT}\right)=\arg\left\{\frac{K_0\left(N_r\sqrt{j}X_{DT}\right)}{K_0\left(\sqrt{j}X_{DT}\right)}\right\}$$

Equation 6:13 Graphical inversion principle

where $N_r = r/r_i$. Curves $\delta_{TT}(X_{DT})$ and $\varphi_{TT}(X_{DT})$ are then used to estimate values of X_{DT} corresponding to the observed amplitude attenuation and phase shift (Figure 6:1) and consequently values of thermal diffusivity D_T, using the following equation:

$$X_{DT}=\sqrt{\frac{\omega}{D_T}}r_i \Rightarrow D_T=\frac{2\pi}{\tau}\left(\frac{r_i}{X_{DT}}\right)^2$$

Equation 6:14 Retrieving the thermal diffusivity from graphical inversion

6.3 Scaled model experimental setup

The pumping test method was investigated on a scaled model of borehole in which the soil homogeneity and the positions of the temperature sensors are much easier to control than *in situ*. Furthermore, the scaled model is logistically simpler, less expensive and makes it possible to have several sensors embedded in the soil around the heat source to better evaluate the potential of the method. The main features of this method are the application of a sine-like temperature signal at the heat source that mimics seasonal operations of a ground heat exchanger and the recording of the temperature anomaly in the ground at a given distance from the source.

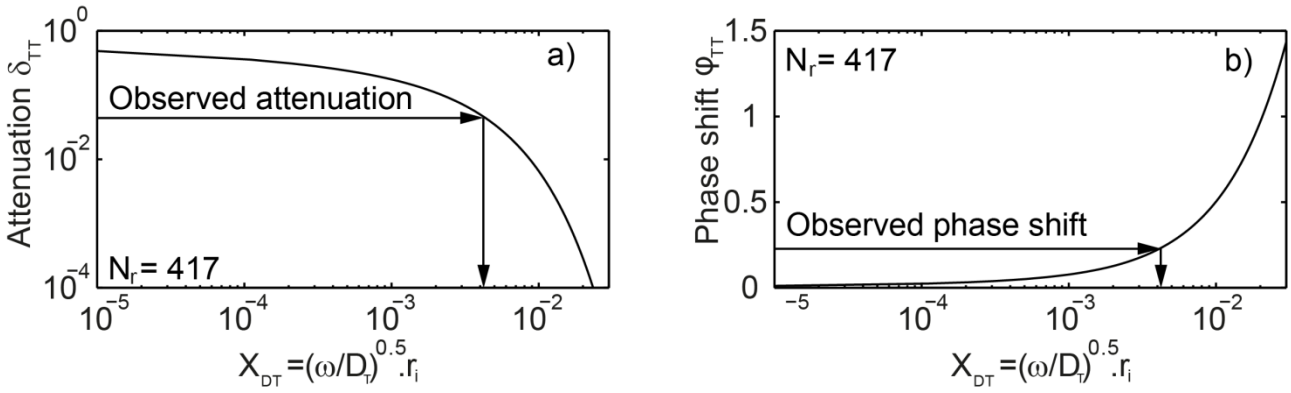

Figure 6:1 Illustration of the graphical inversion of Equation 6:13 with the amplitude attenuation and phase shift, redrawn from (Renner and Messar, 2006)

The thermal diffusivity can then be estimated by comparing the time lag and the attenuation in amplitude between the source signal and the signals measured in the ground.

6.3.1 Scaled model

A scaled model of borehole heat exchanger was developed at laboratory scale (Figure 6:2 and Figure 6:3). The absorber pipes consist of two collocated U-shaped loops made of copper. The equivalent diameter of the borehole is 0.01 m. The buried length of the U-loops is 0.6 m. These pipes are buried within a cylindrical tank whose inner diameter is 0.31 m. The tank wall is made of steel and is 0.04 m thick. A top cap is used to apply a vertical load to the filling material. Two apertures (one at the base of the tank and the other in the top cap) were managed to allow water drainage resulting from the consolidation of the filling material that was installed in slightly saturated conditions. The aperture in the top cap also allowed connecting the scaled borehole to the heater/chiller. Holes in the tank wall, 20 cm above the tank bottom, were used to install the thermocouples around the scaled borehole. The filling material is Bioley silt. This material was tested in detail by Péron et al. (2009). The tank was filled layer by layer up to a level of 0.6 m.

The heater/chiller device is a temperature controlled tank equipped with a pump delivering a flow rate of 5.4 L/min. The heating is provided by electrical heaters. The cooling is provided using a cryostat immersed in the tank. This cryostat had a constant cooling rate so that when the temperature of the heat-carrier fluid dropped below the cooling temperature limit, heaters were activated.

The heat-carrier fluid used in the absorber pipes was a mixture of water and glycol. Although no negative temperature was investigated in this study, the glycol prevented any ice to form around the cryostat which would have reduced its cooling rate.

The construction of the laboratory test was as follows:

- The porous stone was placed on top of the bottom hole of the tank
- The absorber pipes were installed and maintained vertically on top of the porous stone
- The tank was filled layer by layer up to the level of 0.2 m. Although no compaction was achieved between the installations of two layers, particular attention was given to avoid air pockets along the sidewalls and around the absorber pipes. The filling material was levelled by hand. Therefore, the thermal contact between the silt and the absorber pipes might be better than in full-scale practice.
- Thermocouples were placed on top of the silt at the desired distance from the absorber pipes.
- The tank was filled layer by layer up to 0.6 m
- The top cap was placed on top of the tank. An O-ring was used to seal the top cap – tank contact. The top cap was then loaded with 100 kg and its settlements were monitored using a mechanical comparator. The scaled model was ready to use when the measured settlements stabilized.

Heating and cooling cycles were produced by alternating the temperature limit of the temperature controlled tank between T_0+15 °C and T_0-15 °C, where T_0 is the ambient temperature of the

laboratory, maintained at approximately 23 °C. The period adopted was 24 hrs, so the temperature limit was changed every 12 hrs. The test described here was conducted over 3.5 cycles.

Six thermocouples were deployed around the absorber pipes. Two additional thermocouples were installed right at the inlet and outlet of the absorber pipes to monitor the temperature of the inflow and outflow of heat-carrier fluid. This allowed measuring the quantity of heat effectively transmitted to the ground. Because of the consolidation occurring after the installation of the thermocouples, these might have slightly moved downward, slightly increasing their distance to the absorber pipes. However, this was not quantified and therefore assumed to be negligible for these analyses.

Facing thermocouples were installed at the same distances from the absorber pipes so that data for three different distances to the source axis were obtained (Figure 6:2): 7.5 cm (T2 and T5), 10 cm (T1 and T4) and 12.5 cm (T3 and T6).

6.3.2 Data processing

The temperature limit was reached more rapidly during heating than during cooling. As a result, a plateau was observed during heating, whereas the limit during cooling was only reached in the first cooling phase (Figure 6:4). This dissymmetry arose from the fact that the heater and the cryostat that were used did not have the same capacities.

The raw data obtained from the test consisted of eight time series of temperature from each of the eight thermocouples. The measurements were synchronised and taken every minute. A running average algorithm was used to smooth the noisy raw data, except the temperature data for the absorber pipes. This running average algorithm involved averaging values over 20 time steps which represent 20 min, centred on the value being smoothed.

The temperature of the heat-carrier fluid was not smoothed because doing so would have erased the sharp transition between heating and cooling and would have induced error in the determination of the phase shift. Indeed, the phase shift was estimated as the time required by the sharp change in the heating-cooling curve to propagate from the source to the monitoring points (Figure 6:4). The temperature of the heat source (i.e. the absorber pipes) was approximated as the mean of the temperatures at the inlets and outlets of the absorber pipes.

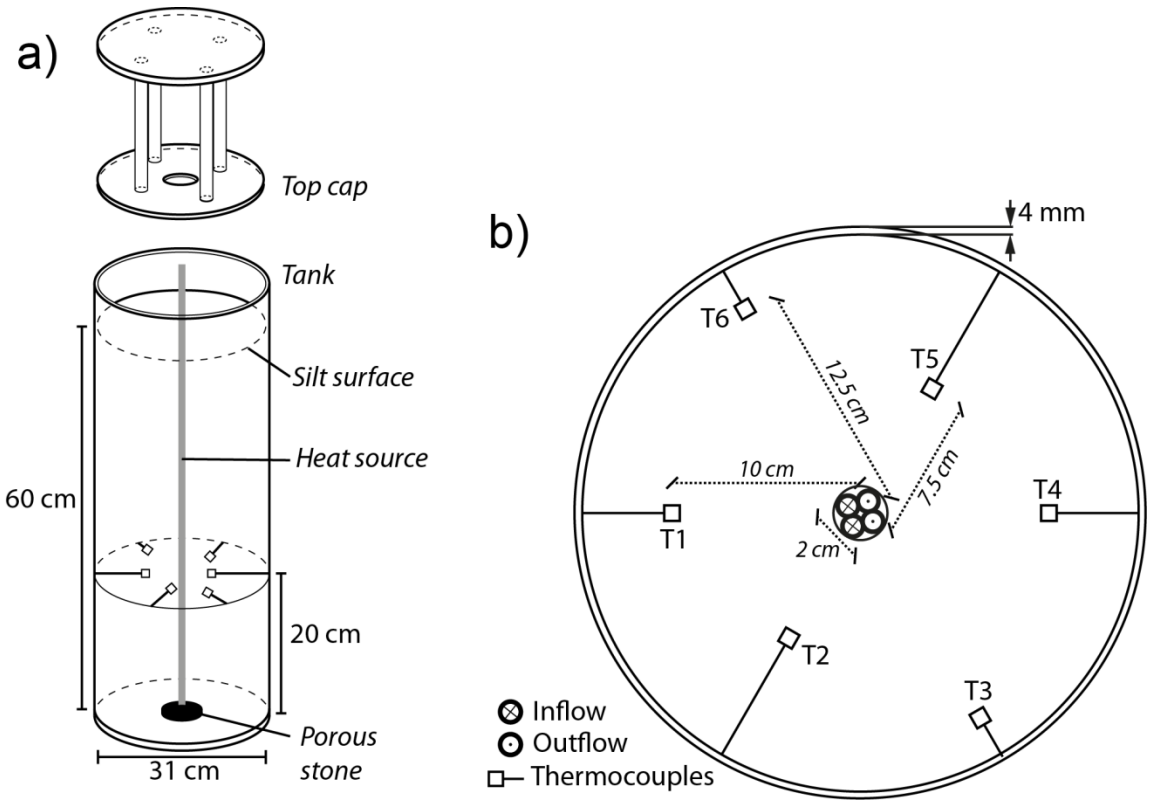

Figure 6:2 (a) 3D schematic of the scaled model tank and (b) cross section of the setup showing the thermocouples and absorber pipes

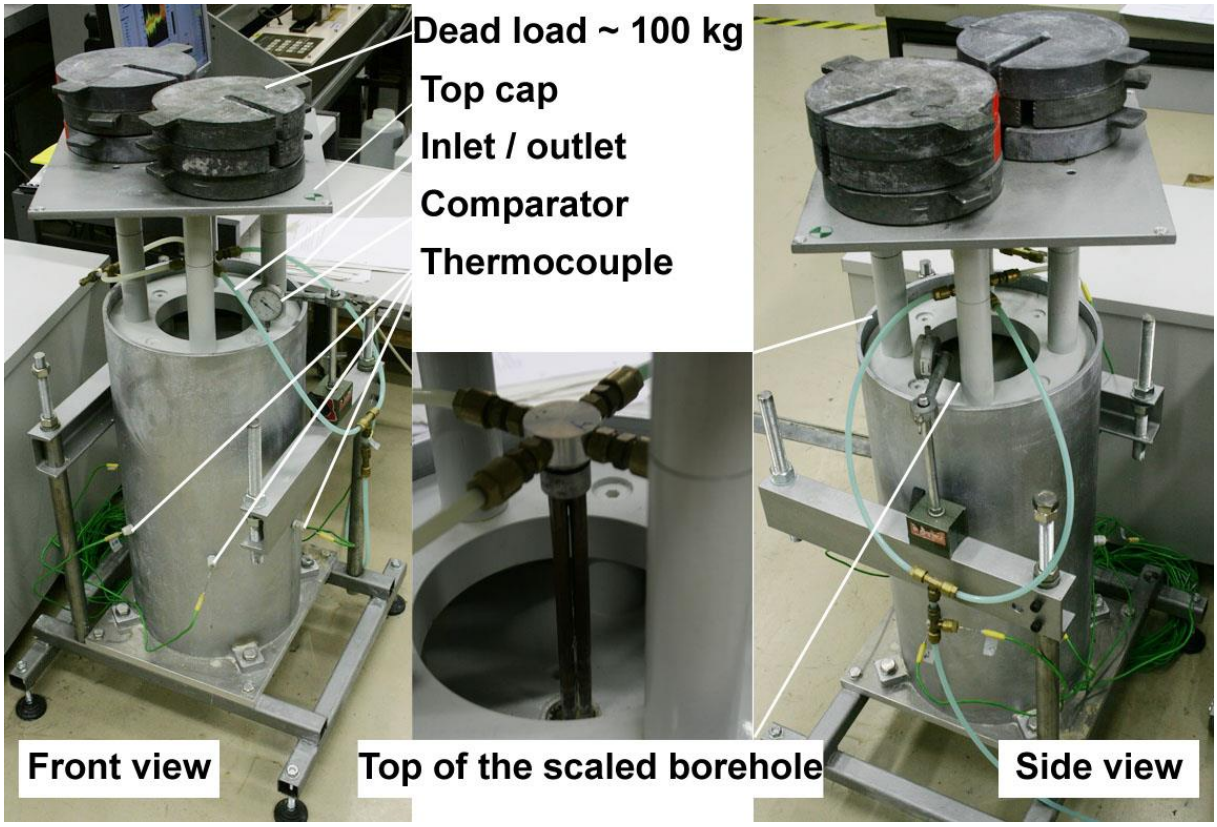

Figure 6:3 Pictures of the experimental setup

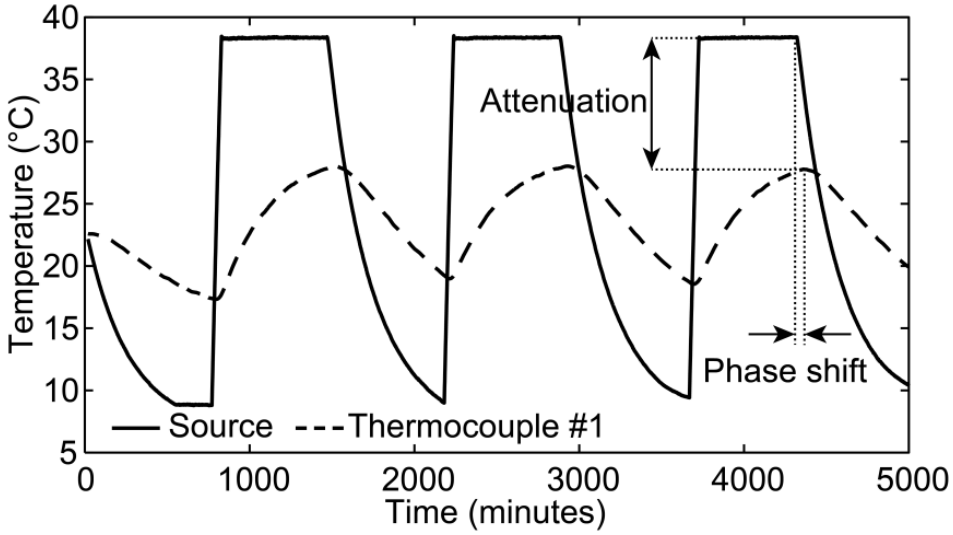

Figure 6:4 Example of source–thermocouple analysis, here between the source and thermocouple T1

An analysis of the spectral density of energy obtained from a fast Fourier transform of the time series was conducted to verify and retrieve the pulsation of the source and to ensure that this pulsation was not affected while propagating through the silt (Figure 6:5). The peak energy density was found to occur at a frequency of $10^{-4.952}$ Hz for each thermocouple, which corresponds to a period of 1.04 d. Therefore, the applied period was 24 hrs, as expected.

The amplitude attenuation was estimated for the last heating phase as the ratio between the amplitude of the response and the amplitude of the source (Figure 6:4). The amplitude attenuation was estimated in this manner for each of the six thermocouples installed in the tank.

Two types of interference analysis were carried out. The first type is based on the comparisons between the source and the thermocouples and is called source–thermocouple interference analysis. The second type is based on the comparisons between the thermocouples and is called thermocouple–thermocouple interference analysis.

The time lag between the thermocouples in the thermocouple–thermocouple interference analysis was estimated using cross correlation by finding the maximum of the normalised cross covariance function based on the two thermocouple signals. However, determination of the time lag was more challenging for source–thermocouple interference analyses. Indeed, the presence of the plateau during the heating phase in the source signal would have overestimated the lag because cross correlation maximises the common area between the two curves instead of aligning the sharp transitions from heating to cooling which physically corresponds to the maximum temperature observed at the thermocouples (Figure 6:4). Therefore, in the source–thermocouple interference analyses, the time lag was estimated manually from the smoothed curves for the thermocouples, and a large margin of error, ± 10 time steps (i.e., ± 10 min) was assumed for the estimates. The phase shift was estimated as the lag between the last transition from heating to cooling at the source and the last positive peak observed at the thermocouple (Figure 6:4).

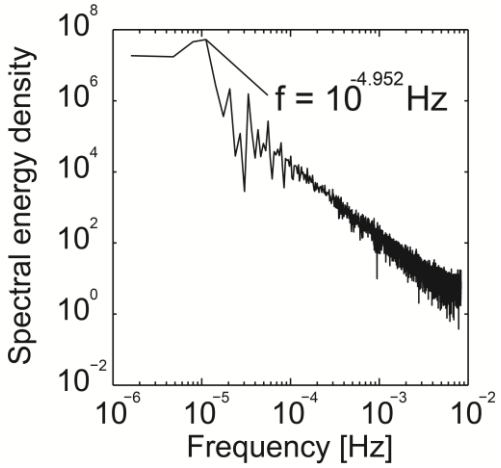

Figure 6:5 Spectral density of energy of thermocouple T1

6.4 Analyses

The analyses are divided into source–thermocouple interference analyses and thermocouple–thermocouple interference analyses.

6.4.1 Source-thermocouple interference analyses

The source–thermocouple interference analysis involves comparing the signal from the source with the responses measured by the different thermocouples.

Observed phase shifts and attenuations for the different thermocouples are presented in Table 6:1. Curves of phase shift and attenuation, as illustrated in Figure 6:5, were produced for a source radius equal to 1 cm—the radius of the heat exchanger borehole—and values of N_r ($= r/r_i$) for each thermocouple. In total, three sets of curves were used (one set per distance to the source for three different distances to the source; see Section 6.3). Four values of thermal diffusivity were derived per thermocouple: one from the amplitude attenuation ($D_{T,\delta}$) and three from the phase shift: one from the measured phase shift value ($D_{T,\varphi}$) and two from the phase shift bounded by the error ($D_{T,\varphi-10}$ and $D_{T,\varphi+10}$). These values were estimated only for assumed conditions of no heat flux at infinity, using Equation 6:11, and no heat flux at the tank radius, using Equation 6:10. The Dirichlet-type condition did not permit retrieval of any value of thermal diffusivity because the observed attenuations were greater than those allowed by Equation 6:12 and Equation 6:9. This was attributed to the plateaux that were observed when heating, during which energy was injected while the source temperature (i.e. the mean between inlet and outlet temperatures) remained constant. The temperature increases that are thus observed in the silt are higher than those that would be observed if the source signal was really sinusoidal.

Table 6:1 Phase shift and attenuation from interference analyses between the source and the thermocouples

Sensor	1	2	3	4	5	6
φ_{TT} (cycles)	-0.1745	-0.1309	-0.3185	-0.2269	-0.1309	-0.3185
δ_{TT}	0.3205	0.3694	0.2626	0.3006	0.3656	0.2752

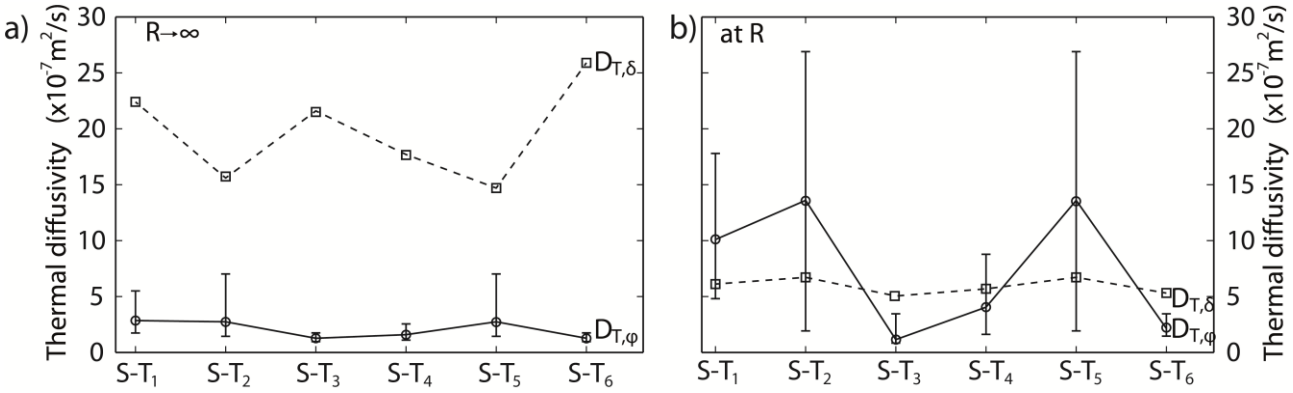

Figure 6:6 Thermal diffusivity based on phased shift ($D_{T,\varphi}$ – solid lines) and attenuation ($D_{T,\delta}$ – dashed lines) with the far field condition of (a) no heat flux at infinity and (b) at the tank wall for the source-thermocouple analyses

The results based on the lag between the source and the thermocouples with no heat flux at infinity yield a mean thermal diffusivity of 2.08×10^{-7} m^2/s, bounded by 1.27×10^{-7} m^2/s and 4.26×10^{-7} m^2/s (Figure 6:6a). The results based on the attenuation are likely to overestimate the retrieved thermal diffusivity because of the source signal shape, as detailed previously, and in this case yielded values one order of magnitude higher, with a mean value of 1.97×10^{-6} m^2/s (Figure 6:6a). The results using the condition of no heat flux at the tank wall yielded mean estimates of 7.62×10^{-7} m^2/s and 5.94×10^{-7} m^2/s, based on the phase shift and attenuation, respectively (Figure 6:6b).

6.4.2 Thermocouple-thermocouple interference analyses

Thermocouple–thermocouple interference analyses were carried out by comparing the thermocouples with each other. Both attenuation and phase shift were analysed for the different pairs of thermocouples used. For a given pair, one thermocouple had to be identified as the source and the other as the monitoring point. For each pair of thermocouples, the thermocouple closer to the heat source was taken to be the new source, producing a source radius equal to the distance between this thermocouple and the tank axis. The other thermocouple (farther from the heat source) was then taken as the monitoring point. Only boundary conditions of the Neumann type were considered, for the reason discussed in the previous section.

Observed phase shift and attenuation between the thermocouple are presented in Table 6:2 and Table 6:3, respectively, where the first column and raw represent the thermocouple number as shown in Figure 6:2b. The phase shift can be positive or negative, as the values in Table 6:2 represent the lag between the thermocouple reported in the first column and the thermocouple reported in the first raw. Obviously, thermocouples have no delay with respect to themselves, which explains the diagonals of zeroes. Amplitude attenuation (Table 6:3) can be greater than 1. For example, if the signal at thermocouple 1 has an amplitude equal to 0.8672 times the amplitude at thermocouple 2, then thermocouple 2 has an amplitude equal to 1/0.8672 = 1.1531 times the amplitude at thermocouple 1. Obviously, comparing thermocouples to themselves yields no attenuation, so these ratios are equal to 1.

Table 6:2 Phase shift between the different thermocouples. The phase shift is given as the lag in number of cycles between the thermocouple of the first column and the thermocouple in the first row. A positive lag represents a delay

	1	2	3	4	5	6
1	0	0.092	-0.079	0	0.092	-0.061
2	-0.092	0	-0.249	-0.127	0	-0.227
3	0.079	0.249	0	0.048	0.244	0
4	0	0.127	-0.048	0	0.127	-0.031
5	-0.092	0	-0.244	-0.127	0	-0.227
6	0.061	0.227	0	0.031	0.227	0

Table 6:3 Attenuations between the thermocouples. Values can be greater than 1 because thermocouples in the first column are compared to thermocouples in the first row

	1	2	3	4	5	6
1	1	0.8672	1.2177	1.0642	0.876	1.1615
2	1.1531	1	1.4042	1.2272	1.0101	1.3393
3	0.8212	0.7121	1	0.8739	0.7194	0.9538
4	0.9397	0.8149	1.1443	1	0.8231	1.0914
5	1.1416	0.99	1.3901	1.2149	1	1.3259
6	0.861	0.7466	1.0485	0.9163	0.7542	1

Nevertheless, interference analyses were carried out considering only positive phase shifts and attenuations lower than 1, which is consistent with selecting the thermocouple closer to the tank axis as the source and the thermocouple farther from the tank axis as the monitoring point. Because cross correlation was used to estimate the phase shift, no margin of error was associated with the phase shift values, in contrast to the assumption of a margin of error for the manual time lag estimates described for the source-thermocouple interference analyses. Even if little attenuation is observed (Table 6:3) between thermocouples that are at the same distance from the tank axis (the pairs T1–T4, T2–T5 and T3–T6), this was ignored and the attenuation was set to 1 for the rest of the analyses. This can come from the location of the thermocouples, either on one side of the other of the absorber pipes. The thermocouples on the hotter side (T1, T2 and T3), where the heat carrier fluid goes downward, therefore experience slightly greater temperature increase than the ones placed on the colder side (T4, T5 and T6) where the fluid goes upward (Zeng et al., 2003) (Figure 6:2b). Figure 6:7 gathers the results of the thermocouple-thermocouple interference analyses for the conditions of no heat flux at infinity ($R \rightarrow \infty$) and at the tank wall (R). The results are presented as boxplots. The dashed line in the box represents the median of the value set, the box edges are the 25^{th} and 75^{th} percentiles and the whiskers extend to extreme data not considered as outliers. The individual points are outliers. Despite these are plotted as outliers in the boxplots, they were included in the estimation of the mean values presented in Table 6:4. Individual values of estimated diffusivities are given in Section 9.4. The estimates based on the phase shift yield mean thermal diffusivities of 1.24×10^{-7} m^2/s for the condition of no heat flux at infinity and 1.45×10^{-7} m^2/s for the condition of no heat flux at the tank wall. The estimates based on attenuation yield mean thermal diffusivities of 1.18×10^{-5} m^2/s for the condition of no heat flux at infinity and 2.39×10^{-7} m^2/s for the condition of no heat flux at the tank wall.

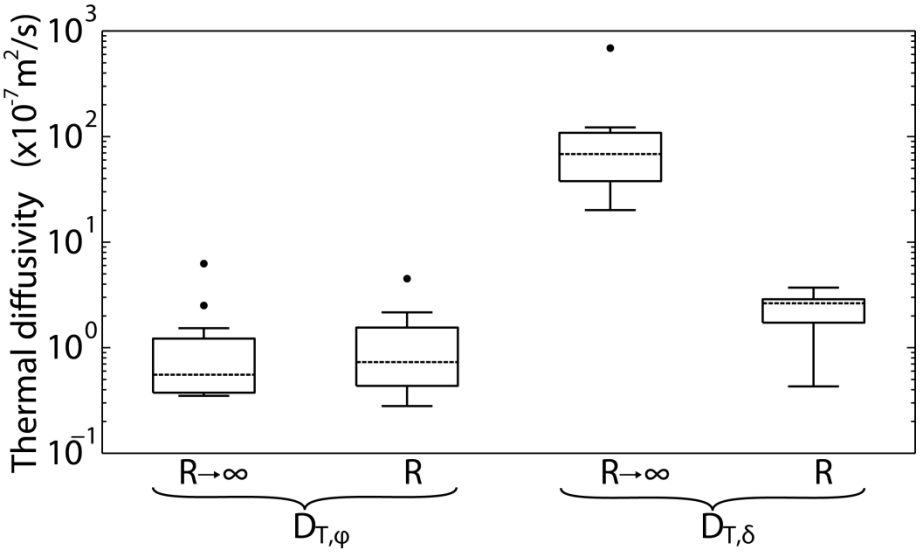

Figure 6:7 Results of the interference analyses between thermocouples based on phase shift ($D_{T,\varphi}$) and attenuation ($D_{T,\delta}$) with no heat flux at infinity ($R \rightarrow \infty$) and at the thank wall (R)

6.5 Discussion

Estimates based on the attenuation of the source signal across the soil mass are more scattered because of the deviation of the source signal from a real sine wave (Table 6:4). The results therefore show that the phase shift analysis does not really require a perfect shape of the source signal, though the shape of the source signal does have a significant impact on the attenuation analysis. Based on the phase shift only, the estimated thermal diffusivity of the silt was found to be, on average, 3.1×10^{-7} m^2/s, whereas the estimated value based on the attenuation was higher: 3.65×10^{-6} m^2/s.

Table 6:4 Summary of the mean values of thermal diffusivity retrieved by the different analysis approaches

	Source–Thermocouple NHF* at $R \rightarrow \infty$	Source–Thermocouple NHF* at R_{wall}	Thermocouple–Thermocouple NHF* at $R \rightarrow \infty$	Thermocouple–Thermocouple NHF* at R_{wall}
$D_{T,\varphi}$ (m^2/s)	2.08×10^{-7}	7.62×10^{-7}	1.24×10^{-7}	1.45×10^{-7}
$D_{T,\delta}$ (m^2/s)	1.97×10^{-6}	5.94×10^{-7}	1.18×10^{-5}	2.39×10^{-7}

* NHF: no heat flux

Al Nakshabandi and Kohnke (1965) estimated the thermal diffusivity of a silt using Equation 6:2 by measuring the bulk density and thermal conductivity of samples and assuming an average specific heat value of 0.199 cal/g/°C (i.e. 833 J/kg/K) which are "averages of data obtained in the literature". The thermal conductivity was measured using a thermal probe at different soil moisture contents. The estimates of thermal diffusivity obtained by these researchers range from 1.5×10^{-7} m^2/s to 7.0×10^{-7} m^2/s for moisture contents going from 0 % to 35 % (i.e. dry to saturated). Wolfe and Thieme (1964) measured the thermal conductivity and specific heat capacity of samples of silt at various temperatures in nearly saturated conditions (i.e. moisture content between 17 % and 22 %). The thermal conductivity was measured using a cylindrical configuration (Farouki, 1986). Within

the temperature range considered in the present study, Wolfe and Thieme estimated a thermal conductivity of approximately 0.5 BTU/ft/h/°F (0.865 W/m/K) and a specific heat of approximately 0.3–0.4 BTU/lb/°F (1656–1674 J/kg/K). Combining of these measurements with a soil grain density of 2700 kg/m^3 leads to values of thermal diffusivity of approximately 3.0x10^{-7} m^2/s (Equation 6:2). Therefore, the estimates obtained from the phase shift seem to be more consistent with the values reported in the literature, while the estimates from attenuation are, as expected, greater.

However, deploying this test procedure at full scale would be challenging for different reasons. First, the accurate deployment of the temperature sensor at a given distance from the absorber pipes requires perfectly parallel drilling which is limited on long boreholes. Sensitivity of the method to the source-thermocouple distance was tested for the thermocouples T2 and T5 at a radius of 7.5 cm. Thermal diffusivities were estimated using inversion curves as in Figure 6:1 for distances of 6.5 cm, 7.5 cm and 8.5 cm, allowing an error of 1 cm corresponding to 13 % and considering no flux at infinity.

Results are (Figure 6:8):

- Based on phase shift, thermal diffusivity is bounded between 1.75 x10^{-7} m^2/s and 3.48 x10^{-7} m^2/s
- Based on attenuation, thermal diffusivity is bounded between 1.15 x10^{-6} m^2/s and 5.78 x10^{-6} m^2/s. These results should be tempered as they were shown not to be consistent because of the source signal shape deviating from a sine.

Therefore, the technique is sensitive to the location of the monitoring points. Second, deploying this technique at full-scale will be more time consuming than with the scaled model and would involve the installation of temperature sensors in boreholes. Because TRTs do not require thermal cycles, they are not totally compatible with the tested method. However, the heat source is the same for a TRT and for a pumping test (i.e. a geothermal borehole). Therefore, the TRT test could represent the first heating of a series of cycles that would be used for the pumping test. Typical time span of a TRT is one week (Mattsson et al., 2008) so that should represent a half cycle. Then, considering that 3 cycles are required to reach the periodic steady regime, a total time span of 6 weeks should be required to carry this test at full-scale, which is significant, but consistent with the experience of Renner and Messar (2006). Indeed, because hydraulic diffusivity is 6 to 7 orders of magnitudes higher than thermal diffusivity, much more time is required for the thermal test.

A clear signal (i.e. with significant amplitude) at the monitoring points is required to obtain good estimates of phase shift and attenuation. The accuracy of commercial thermistors or thermocouples designed for underground installations is roughly 0.1 °C while amplitude of heat source temperature increase during a TRT is between 10-20 °C. Therefore, the monitoring points should not be too far from the source to avoid important attenuation, and in the same time should not be too close to the source as the thermal impact of the filling material of the installation borehole would induce greater bias. Figure 6:9 was drawn to estimate the optimal source-sensor distance based on order of magnitudes. It represents the quadratic evolution of the characteristic pulse time according to the characteristic dimension (i.e. source-monitoring point distance). The curves are based on the dimensionless heat equation that yields:

$$D_T \approx \frac{L^2}{\tau} \Leftrightarrow \tau \approx \frac{L^2}{D_T}$$

Equation 6:15 Order of magnitudes: thermal diffusivity and characteristic time and length of heat conduction

where L and τ are the characteristic length (i.e. radius) and time (i.e. heat source period) on which heat conduction occurs. Therefore, the two bounding curves presented in Figure 6:9 are parabolas using $D_T = 10^{-7}$ m^2/s and $D_T = 10^{-6}$ m^2/s.

A signal period of one day is shown to generate good signals at the monitoring points for the scale of the scaled model used in this study (i.e. source-sensor distance of approximately 10 cm). Using a signal period of one week at the heat source for the full-scale application leads to a favourable source-sensor distance between 0.2 m and 0.8 m. However, the portion of borehole filling material is significant for low distances as the borehole diameters are generally between 0.1 m and 0.2 m (Pahud and Matthey, 2001). Therefore, a reasonable range of source-sensor distance is between 0.5 m to 0.8 m, wherein the portion of borehole filling material varies between 10 % and 20 %. The bias introduced by the thermal influence of the filling material could be accounted for as its thermal properties are known but no particular solution is provided herein.

The vertical inhomogeneity should also be assessed for the deployment at full-scale. Indeed, several temperature sensors should be installed along the monitoring borehole when different soil layers can be found. When local stratigraphy is well documented, at least one temperature sensor should be placed in each of the identified soil layer.

Furthermore, provided the relatively low cost of thermistors or thermocouples compared to the cost of a borehole should encourage installing at least 5 to 10 temperature sensors.

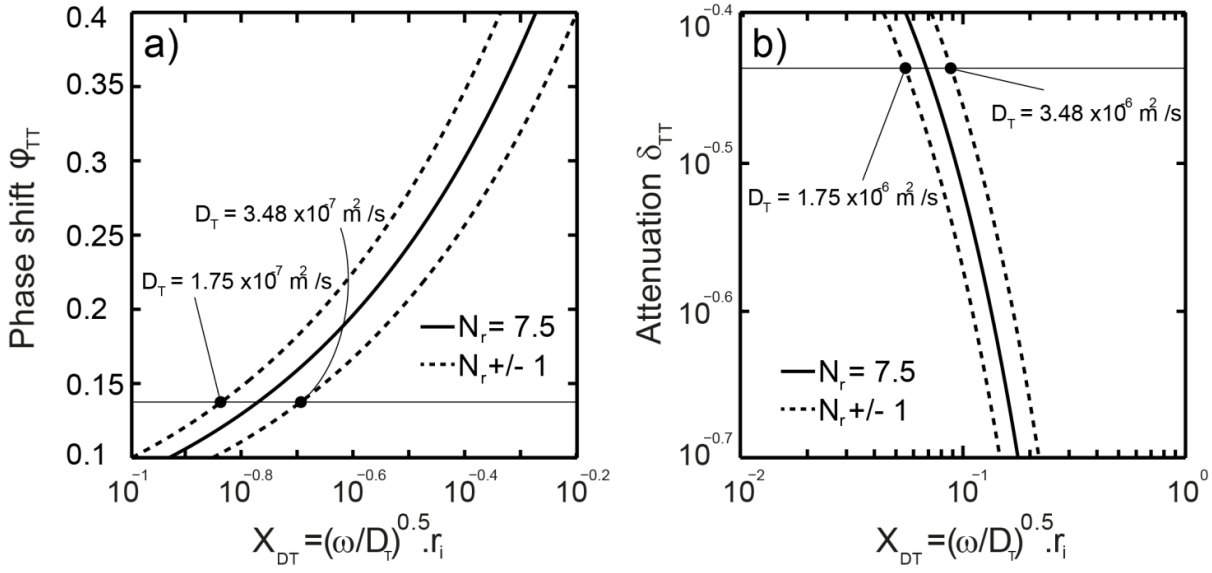

Figure 6:8 Curves used for graphical inversion of Equation 6:13 for the thermocouples T2 and T5 (solid lines) and curves with and error of +/- 13 % (dashed lines). Horizontal lines represent the observed phase shift and attenuation as reported in Table 6:1

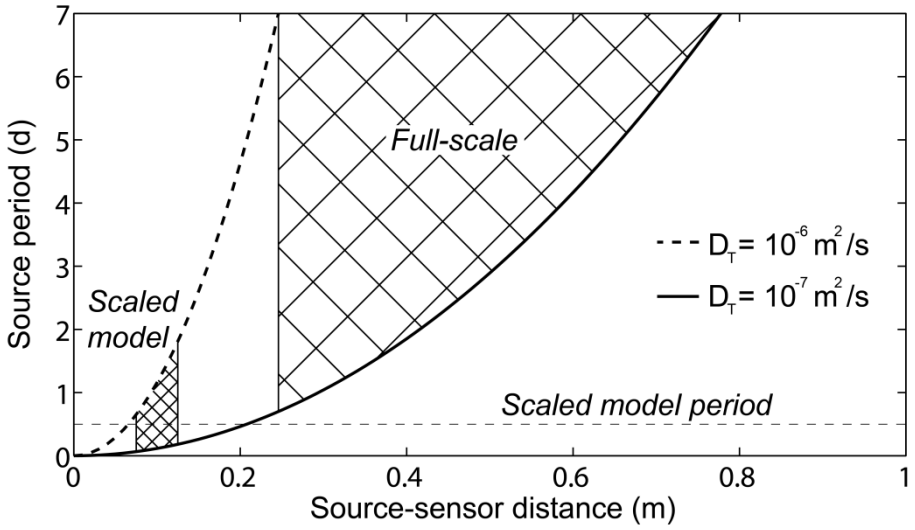

Figure 6:9 Relationship between time and space scales for heat conduction in soils with thermal diffusivities between 10^{-7} m^2/s and 10^{-6} m^2/s

Despite some extra installation requirements and a longer testing time if deployed on a larger scale, this test would be of great value in the design of thermal foundations that reach depths of approximately 10–30 m and have narrow spacing between the heat exchanger structures. Indeed, seasonal operations could dramatically affect the sustainability of the system if the inertia of the ground were not taken into account properly in the design phase.

Finally, Renner and Messar (2006), suggest that using different periods of input signal may allow investigating the intrinsic period dependence of the soil thermal properties as both daily and yearly operations may have a significant impact on ground heat exchangers.

6.6 Conclusions

A method based on periodic pumping tests was evaluated using a scaled model of a geothermal borehole for the purpose of *in situ* estimation of the bulk thermal diffusivity of a soil. The potential of this method is demonstrated on the scaled boreholes. The thermal diffusivity estimates based on the phase shift exhibit good agreement between each other and with estimates found in the literature. Analyses based on the attenuation of the source signal should not be considered if the source signal deviates too much from a sine-like signal. The limitations of deploying the presented method at full-scale were discussed. A time period of 4 to 6 weeks should be required to reach a periodic steady regime over 2-3 heating/cooling cycles of two weeks each. The heat source-sensor distance is found to be an important parameter as the portion of filling material between the source and the temperature sensor may significantly influence the finally retrieved thermal diffusivity. Therefore, this portion should be kept as minimal as possible. Finally, the sensitivity of the method to the accurate localization of the sensor was investigated based on the results of the scaled model. An error of 13 % in the heat source-sensor distance leads to an error of 50 % in the final estimates based on phase shift analyses. Furthermore, vertical stratigraphy of the ground must be accounted for by deploying several temperature sensors along the monitoring borehole.

In conclusion, the method potential was clearly evidenced on the scaled model but several limitations remain to be overcome for the full-scale deployment.

6.7 Acknowledgements

The author would like to particularly thank M. Lingxi Lei from the Ecole des Ponts Paris Tech (Paris, France) who was in charge of the construction of the scaled model and experimental part, i.e. data acquisition, of the present work during his Bachelor thesis.

Chapter 7 Full-Scale *In Situ* Testing of a Group of Energy Piles

7.1 Introduction

Energy piles are the most widely-used energy geostructures around the world. Bourne-Webb (2013) did a review of the existing studies which evidenced that there have mainly been thermal performance studies assessing the potential of heat production and storage through these foundation structures. Few studies were carried out on the mechanical implications of the heat exchanges between the pile and the ground despite it seems to be one issue faced when designing such structures. All the tests carried out to characterise the thermomechanical response of energy piles considered a single pile either under a building, and therefore experiencing real service conditions but somehow extreme, or aside from buildings for testing purposes only. The first test pile was built on the EPFL campus in Lausanne (Switzerland) and was of end-bearing type, resting on a strong sandstone bedrock (Laloui et al., 2003). It was below a real building funded on top of 100 static piles but was the only thermoactive pile so that the constraints acting on it were maximised. This test allowed observing the thermomechanical response of such ground heat exchanger at full-scale. The particularity of this test was that different response tests were achieved along the construction stages so that the evolution of the pile top constraints was quantified and analysed. This test provided great insight in the thermomechanical response of a single pile below a raft subjected to heating but was largely overdesigned to prevent possible damages during the tests. Later, Bourne-Webb et al. (2009) tested a pile apart from any building but loaded with a jack mounted on a beam maintained by anchor piles. Thermal loading was achieved using a heat pump and a heat sink pile so that active heating and cooling were possible. The pile top condition was of constant load type so no head constraint other than the pile load was applied. The test pile was of floating pile type, that is to say embedded within clay without significant pile tip resistance. The examined test was a sequence of cooling (-19 °C) and then heating (+10 °C). Murphy et al. (2012) investigated the thermal and thermomechanical responses of two energy piles coupled with geothermal boreholes below the Denver Housing Authority Senior Living Facility in Denver, Colorado. The piles were 13-15 m long and 1.1 m in diameter, and they are embedded within a layered soil made of fill (~ 3 m), sand and gravel (~ 4.6 m) and claystone. Three loops were installed per pile, and were subjected to real service conditions. Temperature inside the absorber pipes ranged between 8 and 25 °C depending on the season. It was found that operational conditions would not lead to excessive thermal strains and stresses. Later, Murphy et al. (2014b) investigated response of a piled beam foundation with 8 energy piles supporting a small single storey building. Despite the 8 piles (0.61 m in diameter and 15.2 m long) were thermally activated, only 3 were instrumented. The local stratigraphy would have allowed a slab-on-grade foundation but using the piles also provided the heat source. Therefore, the soil can be considered as relatively stiffer than in the previous field tests. In situ heating test used temperature increase up to 21-22 °C which induced concrete thermal expansion between 20 and 150 με, thermal stresses from 1 to 5 MPa and pile displacement up to 1.5 mm. Therefore, tests carried out during previous field investigations focused on single pile responses. However, mechanical interactions between the piles may occur when only a part of the foundation is thermally activated, which is generally the case (Anstett et al., 2005). As a result, differential settlements between the heat exchanger piles and the conventional ones could develop and induce potential damages to the supported structure. Sangseom et al. (2014) numerically

investigated the thermomechanical responses of energy pile groups with different layouts but deplored the lack of experimental data to validate their models.

We therefore propose to carry *in situ* experiments to quantify the magnitude of interactions that could develop within a thermoactive foundation based on a group of 4 test piles below a water retention tank.

The sensors used on the experimental site as well as the data processing methods are first presented. Next, the experimental site is detailed with the local stratigraphy, the pile characteristics and the pile heating system. Then, the thermomechanical responses of the piles during three different tests are analysed and compared. The thermal aspects with the retrieving of the thermal conductivity of the soil and heat propagation in the ground are discussed. Finally, we provide a thorough discussion about the determination of the thermomechanical response of the piles according to axial and radial strains observed along the piles. This discussion suggests that using 2 dimensional analyses is better than only considering axial thermal strains.

7.2 Monitoring the thermomechanical response of energy piles

7.2.1 Estimating strains and measuring temperature along the piles

Measuring strains in the test piles is achieved using two types of sensors: optical fibers and strain gauges. Optical fibers provide accurate strain measurements but require more logistics (i.e. a large dedicated reading unit plus a computer to operate it) while strain gauges provide reliable measurements of strain and temperature with a light and compact reading unit.

The systems used on the EPFL campus to measure strains in the group of test piles are:

- The SOFO system of optical fiber from SMARTEC^{TM} / ROCTEST^{TM}. This system is based on the comparison of a signal travelling along a reference fiber and a measuring fiber. The reference fiber is long enough so that it is never put under tension. As a result, strains on the reference fiber are only caused by temperature variations. The system is therefore auto-corrected in temperature since the reference fiber is under the same conditions as the measuring fiber (Glišić and Simon, 2000; Inaudi et al., 2000; Lloret et al., 2000). The system directly provides information on the fiber elongation and therefore does not need further data treatment.
- Vibrating wire strain gauges – model EM-5 from ROCTEST^{TM} – are used to measure strains. Because the tests are carried out in non-isothermal conditions, a part of the vibrating wire strain is due to temperature changes. Therefore, a 3kΩ thermistor is included in each strain gauge for temperature correction. The gauge outputs – using the MB-3TL reading unit from ROCTEST^{TM} – are the resonant frequency of the vibrating wire and its temperature. Therefore, data processing is required.

These two types of sensor were deployed along the pile axes, attached to the reinforcing cages. Since optical fibers are delivered with anchors already mounted on the sensor body, tie wires or plastic ties were used to attach them along the rebars of the reinforcing cages (Figure 7:1). However, these must be attached with an initial tension to avoid having loose fibers after the

mechanical compression of the piles. Strain gauges were attached to frames prior to their installation on the reinforcing cages with a wire attached perpendicular to the gauge axes, which avoids measuring the axial strain of the frame. The frames were designed to fit exactly in between the rebars of the reinforcing cages. Next, the frames were attached to the reinforcing cages with wire ties (Figure 7:2); this saved a substantial amount of time on site and provided a reliable attachment of the sensors.

Data processing for the strain gauges is based on the vibrating wire theory. The actual resonant frequency of a wire is compared to a reference value which provides information about its strain ε. Indeed, the resonant frequency F of a wire under tension is given by:

$$F = \frac{1}{2L_{wire}}\sqrt{\frac{f_{wire}}{\upsilon_{wire}}}$$

Equation 7:1 Resonant frequency of a vibrating wire

where L_{wire} is the wire length, f_{wire} is the wire tension and υ_w is the wire linear density. The wire tension can be related to its strain ε through its Young's modulus E_{wire} and cross section A_{wire} by:

$$f_{wire} = A_{wire}E_{wire}\varepsilon$$

Equation 7:2 Wire tension

Therefore, the wire strain can be directly linked to the square of its resonant frequency through a linear relationship as provided by the gauge supplier:

$$\varepsilon = \frac{K}{1000}F^2$$

Equation 7:3 Strain as a function of resonant frequency

where K is a constant depending on the instrument characteristics. Because the experiments are carried out under non-isothermal conditions, thermal expansion or contraction of the wire must be accounted for. Any increase in the temperature of the wire induces expansion and consequently reduces its tension. Therefore, the observed variation in wire tension with the reading unit, $\Delta f_{wire,obs}$, is lower than the mechanically-induced one, $\Delta f_{wire,mech}$, and can be written as:

$$\Delta f_{wire,obs} = \Delta f_{wire,mech} + \Delta f_{wire,th}$$

Equation 7:4 Tension partitioning between mechanical and thermal effects

where $\Delta f_{wire,th}$ is the variation in wire tension due to thermal expansion of the wire. As a result, the "real" strain measured by the gauge is:

$$\Delta\varepsilon = \frac{K}{1000}\left(F_1^2 - F_0^2\right) + \beta_{wire}^{T}\left(T_1 - T_0\right)$$

Equation 7:5 Strain from the vibration wire strain gauges

where β^{T}_{wire} is the linear thermal expansion coefficient of the wire (11.5 με/°C, given by the constructor), F_0, F_1, T_0 and T_1 are the resonant frequencies and temperatures at initial and current states, respectively. The vibrating wire reading unit, model MB-3TL from ROCTEST™, provides measurements of the resonant frequency within an accuracy of +/- 0.5% F.S. (Full-Scale). On the other hand, the accuracy of the optical fibers is 0.2% F.S. The uncertainty in strain gauge reading is +/- 0.05 Hz for the frequency and +/- 0.05°C for the temperature. As a result, the uncertainty in the strain measurement, $\delta\varepsilon$, is given by:

$$\delta\varepsilon = \left|\frac{\partial\varepsilon}{\partial F}\right|\delta F + \left|\frac{\partial\varepsilon}{\partial T}\right|\delta T = \frac{K}{500}\delta F + \beta^{T}_{wire}\delta T$$

Equation 7:6 Strain reading accuracy

with $\delta T = \delta F = 0.05$. For a recorded frequency of 1200 Hz (the maximum for strain gauges), the resolution of the measurement is roughly 1 με (K~4).

7.2.2 Estimating pile tip load

Pile tip compression is measured using TPC – Total Pressure Cell – from ROCTEST™. The cells installed on the *in situ* sites at EPFL are coupled with vibrating wire transducers, whose principle is the same as for strain gauges and a 3kΩ thermistor is used for temperature correction.

The cells were attached to a cross that was welded at the base of the reinforcing cages (Figure 7:3). However, the installation of this type of cell is challenging when intended for pile tip monitoring.

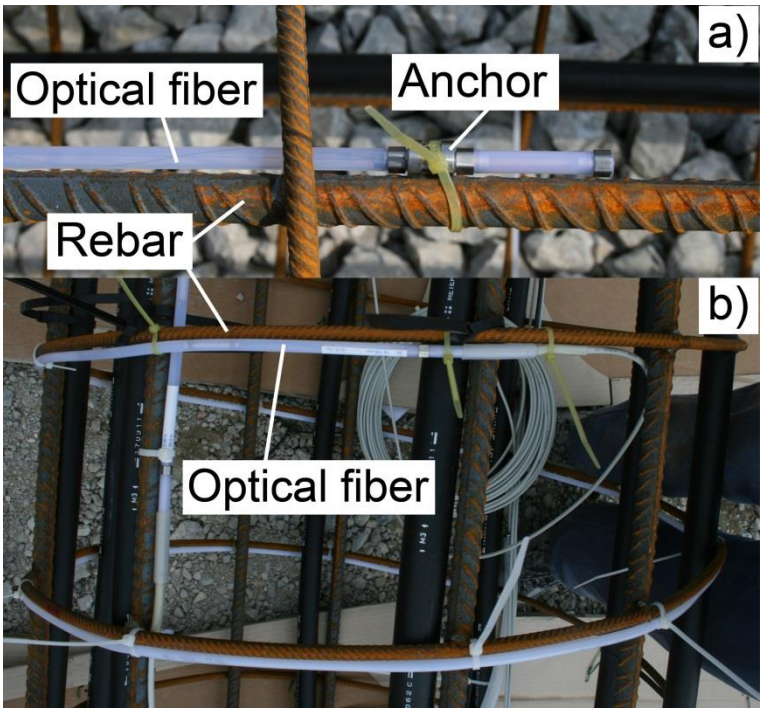

Figure 7:1 Pictures of optical fibers attached to the reinforcing cages of the piles. One fiber (a) is attached along the pile axis to measure axial strains and the other (b) is attached along a reinforcing hoop to monitor radial strains

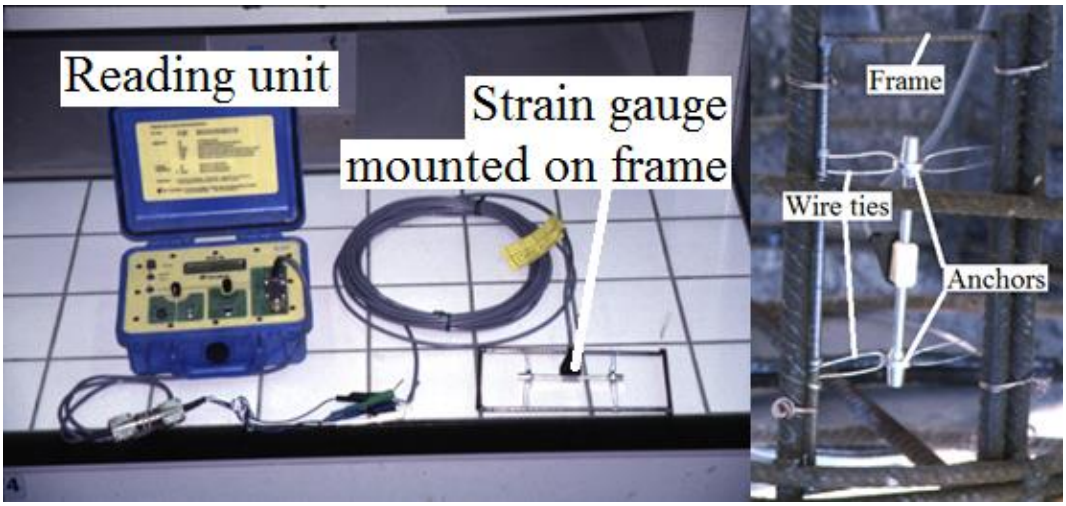

Figure 7:2 Pictures of a strain gauge (here an old C-110 model from SMARTEC^{TM}) mounted on a steel frame and connected to the reading unit (left) and a close-up of the same strain gauge mounted on the reinforcing cage (right)

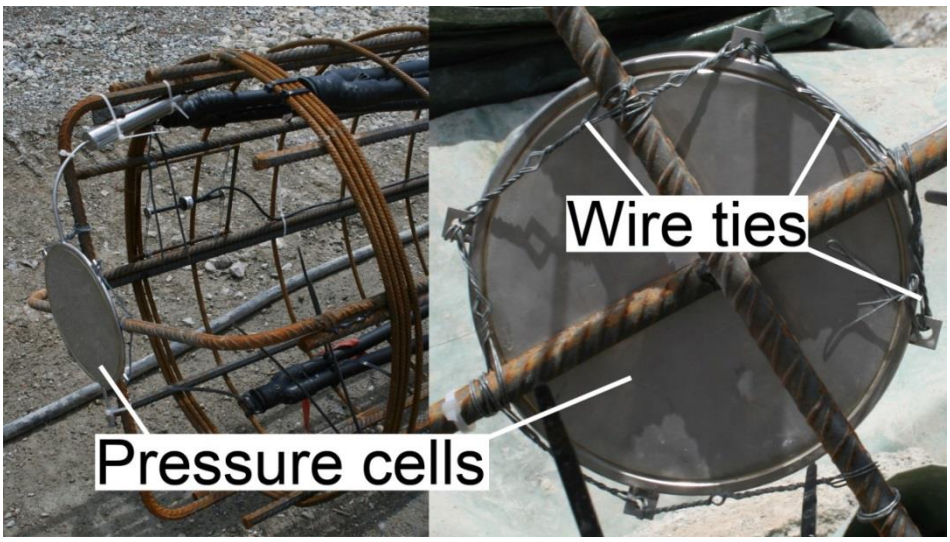

Figure 7:3 Pressure cells attached at the base of reinforcing cages

Indeed, shrinkage of the concrete might degrade the contact between the cell and the surrounding concrete. Pressurisation tubes are available to inflate the cell when concrete shrinkage is deemed to be important but having such a tube along the whole pile axis can present several additional challenges. Furthermore, pre-casting the cells within a mass of concrete and then inflating them before installing the block at the tip of the reinforcing cages would have been time consuming and a good contact between the pre-casted block and poured concrete is not ensured. The solution adopted to overcome these difficulties was to poor some concrete into the bottom of the boreholes using a tremie pipe and to push the reinforcing cages, with the cells attached to their bases, into the fresh concrete. This method also helped avoiding segregation of the concrete and was successful as significant variations were recorded during tests. Calibration sheets were available from the cell manufacturer and were used to estimate absolute cell loads.

7.2.3 Deriving profiles of thermal load and degree of freedom from measurements, and pile radial strains from radial optical fibers

7.2.3.1 Axial degree of freedom and thermal load

The experimental outputs from the tests carried out on the full-scale test group are the observed axial strains, temperatures and pile tip compressions. From these measurements, one can derive thermal stresses and loads using the degree of freedom of the pile. This concept is based on the fact that the potential free thermal strain, $\Delta\varepsilon_{ax,free}$, given by:

$$\Delta\varepsilon_{ax,\,free} = \beta_c^T \Delta T$$

Equation 7:7 Free thermal strain

where β_c^T is the concrete axial thermal expansion (taken equal to 10^{-5} °C^{-1}) and ΔT is the measured temperature variation, is split into effectively observed strain ($\Delta\varepsilon_{ax,obs}$), which is directly measured, and blocked thermal strain ($\Delta\varepsilon_{ax,blo}$). These quantities are linked together by:

$$\Delta\varepsilon_{ax,\,free} = \Delta\varepsilon_{ax,obs} + \Delta\varepsilon_{ax,blo}$$

Equation 7:8 Thermal strains partitioning

The degree of freedom, n, is then defined as the observed strain divided by the free thermal strain, which yields:

$$n = \frac{\Delta\varepsilon_{ax,obs}}{\Delta\varepsilon_{ax,\,free}}$$

Equation 7:9 Pile degree of freedom

Practically, the degree of freedom is determined using linear regressions on the ΔT-$\Delta\varepsilon_{ax,obs}$ curves (Figure 7:4). A thorough discussion of this method is given in Section 7.6.1.

The blocked thermal strain is therefore turned into thermal stress using:

$$\sigma_{ax,th} = E_c\left(\Delta\varepsilon_{ax,\,free} - \Delta\varepsilon_{ax,obs}\right) = E_c\left(1-n\right)\Delta\varepsilon_{ax,\,free}$$

Equation 7:10 Pile thermal internal stress

where E_c is the concrete pile Young's modulus, determined using compression tests on concrete samples (see Table 7:2). The Young's modulus of each tested pile (i.e. piles #1, #2 and #3) was taken equal to the average of the measurements while the Young's modulus of pile #4 was taken equal to the mean of all the measurements. Finally, the thermal load is derived from the thermal stress using the pile cross section (900 mm diameter).

The maximum pile displacement is estimated by integrating the strain profile along the pile considering that the pile null point is at the pile tip. The average pile temperature is estimated as the mean temperature of the thermoactive part of the pile (i.e. along the lower 24 m).

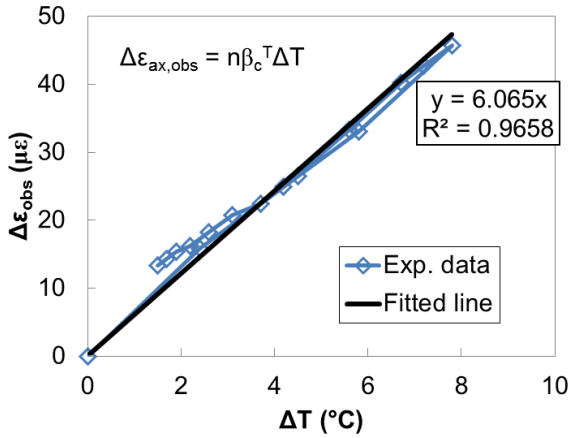

Figure 7:4 Practical determination of the degree of freedom

7.2.3.2 Radial strains

Radial strains are estimated from the lengthening of 3 m long optical fibers deployed along the reinforcing cage perimeter of pile #1, whose diameter is 0.76 m. Therefore, the optical fibers are longer than the perimeter of the reinforcing cage and some correction is required to retrieve the pile radial expansion. Let l_{OF} be the optical fiber length (i.e. 3 m), dl_{OF} be the measured optical fiber lengthening, R_{RC} be the reinforcing cage radius, dR_{RC} the pile radius variation, l_{RC} the reinforcing cage perimeter and and dl_{RC} its variation. Assuming that the optical fiber strain is homogenous yields:

$$dl_{RC} = \frac{2\pi R_{RC}}{l_{OF}} dl_{OF}$$

Equation 7:11 Variation in reinforcing cage perimeter

As a result, the variation in reinforcing cage radius is:

$$dR_{RC} = \frac{dl_{RC}}{2\pi} = \frac{R_{RC}}{l_{OF}} dl_{OF}$$

Equation 7:12 Variation in reinforcing cage radius

Finally, assuming that radial strains are homogeneous in the pile, the variation in pile radius, dR_{Pile}, is given by:

$$dR_{Pile} = \frac{R_{Pile}}{R_{RC}} dR_{RC} = \frac{R_{Pile}}{l_{OF}} dl_{OF}$$

Equation 7:13 Variation in pile diameter

where R_{Pile} is the pile radius (= 0.45 m). Equation 7:13 was used to derive the radial strains of the pile from optical fiber measurements.

7.2.4 Monitoring of the soil

Soil displacements are monitored using two BOR-EX borehole extensometers from ROCTEST^{TM}. These were designed to be used with three rebar anchors at different depths (15 m, 12 m and 5 m). The three anchors are linked to a reference plate by stainless steel rods coated with PVC pipes. The borehole extensometers were installed in boreholes with a diameter of 160 mm and then backfilled with an 80/20 cement-bentonite mixture (Mikkelsen, 2002).The Young's modulus (E_g), strength and density of the backfill were estimated using compression tests on cylindrical samples (32 mm high and 16 mm in diameter) after 28 days of curing: E_g = 2780 MPa, $\sigma_{c,g}$ = 7 MPa and ρ_g = 1535 kg/m^3. Reference plates were grouted into the concrete raft. Automatic reading heads were installed with vibrating wire transducers so that the measurements are achieved using the same reading unit as for the strain gauges and load cells. Piezometers – model PWS with stainless steel filter from ROCTEST^{TM} – were installed within two dedicated 160 mm diameter boreholes. Two piezometers were installed in each borehole: one just on top of the stiff bottom moraine at a depth of 15 m and the other one about half way to the surface. For the installation, a PVC screen pipe was first inserted into the borehole to maintain its shaft and the temporary casing was removed.

Then, piezometers were installed within sand layers sealed with compactonite (a highly expansive clay material). Each piezometer is equipped with a vibrating wire transducer and therefore a thermistor for temperature correction. Thermistors – TH-T model from ROCTEST^{TM} – were also deployed in between the piezometers to complete the temperature profiles within the ground. Piezometers came along with calibration sheets which allow the determination of absolute pore water pressure (see Appendix 9.5.3).

7.3 Full-scale *in situ* group test

7.3.1 Description of the test site

The local stratigraphy in which the test piles are installed was deduced from contour lines of moraine and sandstone (Figure 7:6 a, b and c). Top alluvial layers were positioned based on the stratigraphy determined by Laloui et al. (Laloui et al., 2003) the test sites being very close (200 m).The resulting stratigraphy is given in Table 7:1.

Figure 7:5 Reading head of a borehole extensometer embedded within the raft (left) and the PWS piezometer from ROCTEST^{TM} (right)

Table 7:1 Stratigraphy of the test site

Above sea level (m)	Type	Thickness
392.2 (pile top) – 390.0	Very soft alluvial clay (A1)	2.2 m
390.0 – 384.5	Very soft alluvial clay (A2)	5.5 m
384.5 – 376.5	Loose sandy gravelly moraine (B)	8.0 m
376.5 – 373.0	Stiff bottom moraine (C)	3.5 m
373.0 – 364.2 (pile tip)	Sandstone (D)	8.8 m

7.3.2 Pile characteristics

The test site is located below the water retention tank of the Swiss Tech Convention Center of EPFL in Lausanne (Switzerland) that collects rainfalls from the center roof. This tank, whose floor slab is 0.9 m thick, is supported by 20 piles among which 4 are equipped with absorber pipes as well as strain, temperature and load sensors whose details were given in the previous section. The four test piles are bored piles, cast on site. A temporary casing was installed prior to the boring operation in order to maintain the borehole shaft through weak soil layers. This casing crossed the moraine and alluvial layers and rested on the sandstone bedrock. The drilling was achieved using an auger through the alluvial and moraine layers and a drilling bucket through the sandstone. The test piles are 28 m long and have a diameter of 0.9 m. The reinforcing cages of the piles have a diameter of 0.76 m, allowing a concrete cover of the pipes of approximately 7 cm. They are made of 10 vertical rebars with a diameter of 18 mm and maintained by 9 mm diameter reinforcing hoops spaced every 0.2 m along the pile axis. The other piles supporting the water retention tank are Fundex piles.

Samples of concrete used for the test piles were collected during the pouring operations for piles #1, #2 and #3 (2 samples per pile). The elastic modulus E, compressive strength σ_c and density ρ of the concrete were estimated after 28 days of curing from compression tests on the cylindrical samples (16 mm in diameter and 32 mm high). The average elastic modulus was found to be 26.3 GPa for an average compressive strength of 44.9 MPa and density of 2450 kg/m^3 (Table 7:2).

Table 7:2 Results of compression tests on concrete samples. Two samples (a and b) were taken from each of the piles #1, #2 and #3

Sample	1a	1b	2a	2b	3a	3b
E_c (GPa)	28	27.1	26	21.1	23.3	32.4
σ_c (MPa)	41.0	40.5	44.7	30.3	57.9	55.2
ρ_c (kg/m^3)	2440	2460	2450	2460	2450	2450

The absorber pipes (i.e. loops inside the piles and junction pipes) are made of polyethylene (PE 100) with an outer diameter of 32 mm and a wall thickness of 2.9 mm. Loops are connected using narrow 180° elbows (used for geothermal boreholes) as the pile diameter does not allow bending the PE 100 pipes, and are attached inside the reinforcing cages of the piles with large plastic ties in order to avoid damages when installing the cage into the borehole. The final circuit is made of four 24 m high U-loops, representing a total of 192 m of absorber pipe per pile.

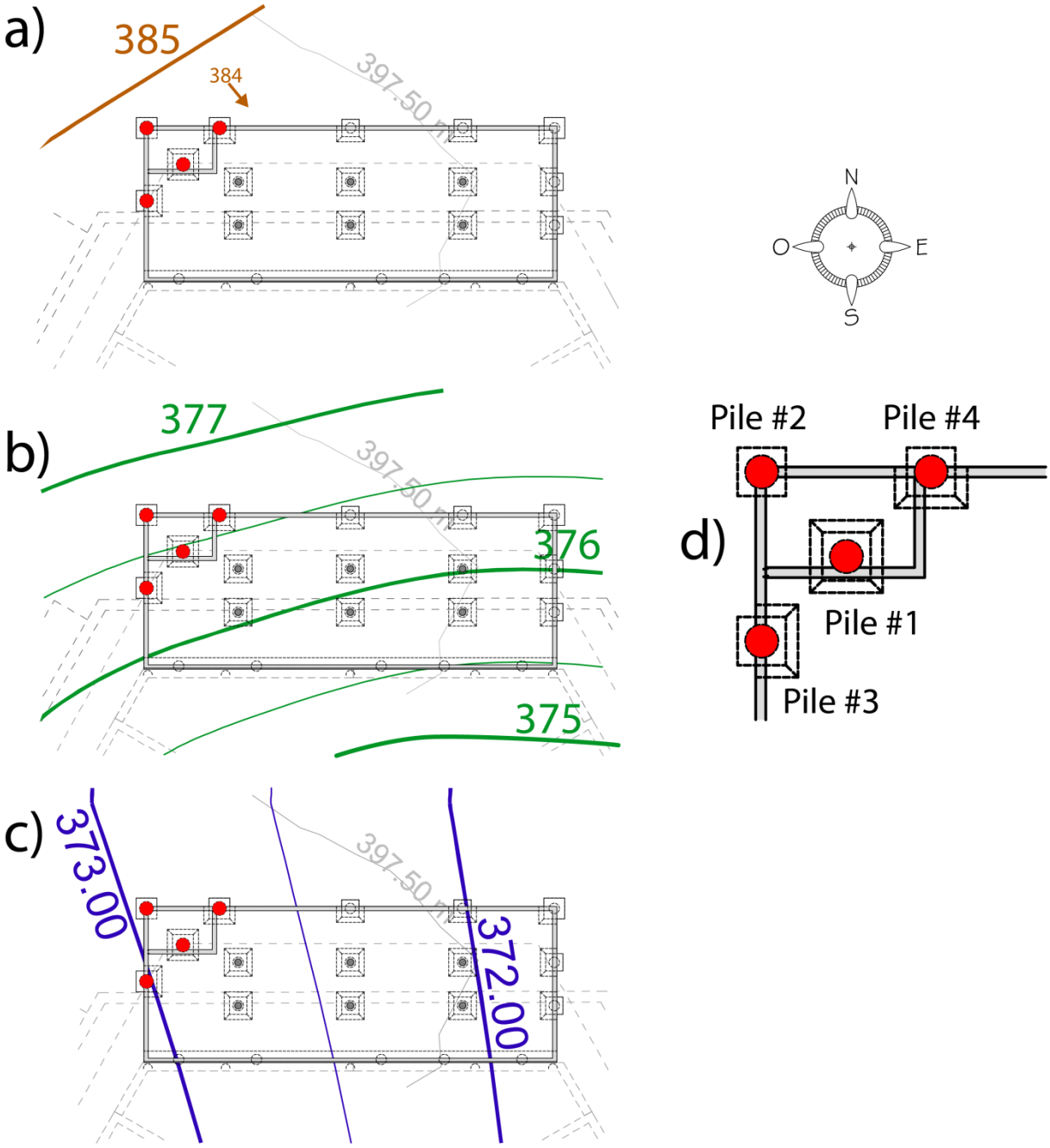

Figure 7:6 Contour lines of (a) moraine, (b) bottom moraine and (c) sandstone, and (d) close up on the energy test piles

The top of the loops is installed 4 m below the pile top and the inlet and outlet portions are thermally insulated with foam in order to prevent thermal interactions with the overlying water retention tank which collects hot water during summer and cold water during winter (Figure 7:7).

Each test pile is equipped with 17 strain gauges, 14 optical fibers and a load cells at the pile tip (level -28 m). 3 strain gauges are deployed in each pile head (level 0 m) in order to monitor potential rotations during interactions through raft bending and the rest is installed every 2 meters along the pile axis. Optical fibers are 1 m long and are also installed every 2 m.

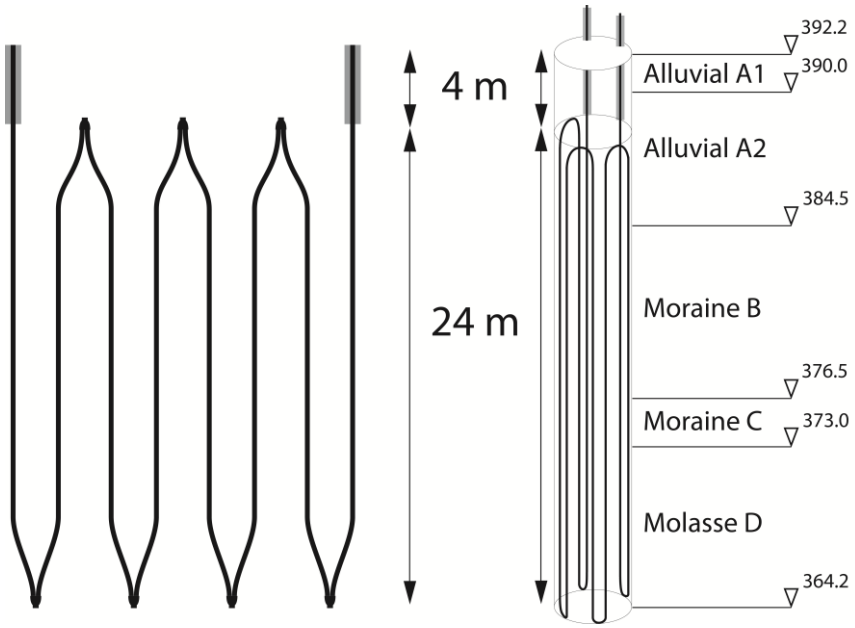

Figure 7:7 Absorber pipes (left) and pile with the local stratigraphy (right)

7.3.3 Heating system (mini-module)

7.3.3.1 General overview

The mini-module (Figure 7:8) used to heat the piles during the tests was developed at the EPFL by the Laboratory of Soil Mechanics (Mattsson et al., 2008). It fits within a flight suitcase (0.3 m x 0.6 m x 0.7 m) and contains 2 heating elements that allow injecting a heat rate between 0 and 9 kW with an increment of 1 kW. The heating element switches (3) are made of 3 switches of 1 kW and 3 of 2 kW. A pump is used to fill the tubes and get the system pressure up to 3 bars. Two valves prevent leakage from the filling pump (9). A pressure valve (6) prevents the system to be over pressurised. The circulation pump (8) provides three different flow rates but the one used during the tests is of 21 L/min. The general control panel is used to switch the pumps and heaters ON and OFF. The circulation pump is inhibited when the system pressure is below 1 bar and the heating elements are inhibited when the circulation pump is OFF. The modem and the data logger are connected to a 12 V battery (4).

The data logger monitors the variable used during a thermal response test, that is to say:

- Inside and outside temperatures from the suitcase
- Inlet and outlet fluid temperatures
- Inlet and outlet fluid pressures
- Flow rate
- Electrical consumption of the module (from which the heat rate is estimated)

7.3.3.2 Connecting the mini-module to the absorber pipes

In order to limit the problems linked to humidity inside the module, it must be kept closed as often as possible. First of all, the general electrical switch (2) should be on position OFF to prevent troubles if water is projected into the module. Next, the absorber pipes are prepared for connection (Figure 7:9): their ends are cleaned up, slightly roughen using sandpaper and coated with silicone grease.

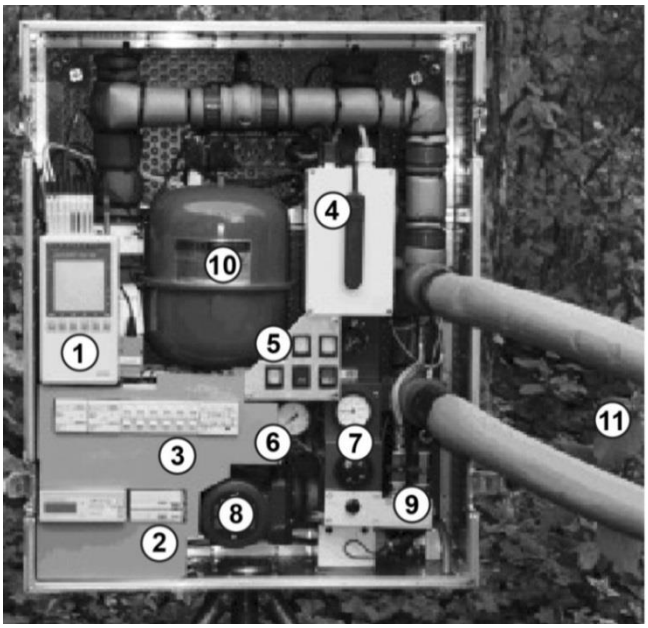

1. Data logger
2. General electrical switch
3. Heating element switches
4. 12 V generator and modem antenna
5. General control panel
6. Pressure regulator valve
7. Aquastat
8. Circulation pump
9. Filling pump and valves
10. Expansion vessel
11. Inlet and outlet pipes

Figure 7:8 Details of the mini-module main control and operation features, picture from (Mattsson et al., 2008)

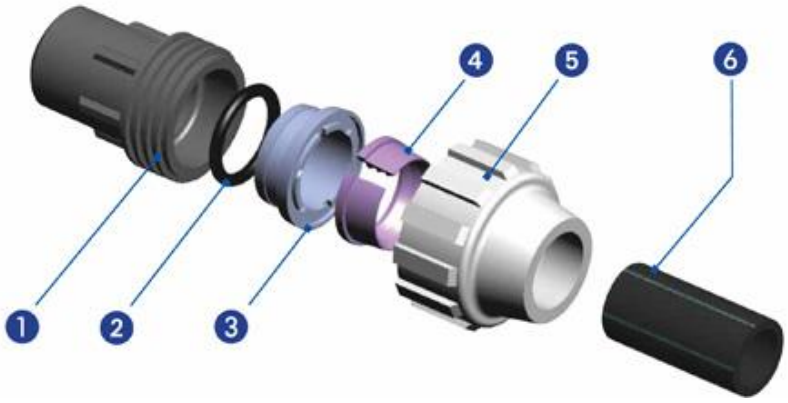

Figure 7:9 Connection between the mini-module and the absorber pipes: (1) connection body, (2) O-ring, (3) contact ring, (4) toothed ring, (5) nut and (6) PE absorber pipe, picture from anjou-connectique.com

Then, the nut and the toothed ring are installed on the absorber pipe which is inserted into the connection body through the contact ring. Finally, the nut is screwed with the toothed ring on the connection body. Leakage at this level is checked when pressurising the module.

7.3.3.3 Pressurising the mini-module

Once connected to the absorber pipes, the system needs to be pressurised in order to expel the trapped air in the connection pipes and the module. For this, filling and emptying pipes are installed into a tank filled with water (at least 20 L). At first, filling and emptying valves are opened and the purge is closed. The general electrical switch is switched ON as well as the filling pump. This operation removes the major part of the air trapped within the pipes and module. Once no air bubble is observed within the water tank, the emptying valve is closed to increase the pressure in the system up to 2 bars (pressuremeter (6)) and the circulation pump is intermittently switched ON and OFF to drive the air through the expansion vessel and purge. Finally, the purge is intermittently

opened to expel the trapped air. This operation is repeated until no air comes out from the purge. Then, the system pressure is increased up to 3 bars, the filling pump switched OFF and the filling valve closed. The system is finally ready even though some leakage may be seen at the pressure regulator valve. Those are not dramatic and the module pressure should stabilise around 2.4-2.5 bars during heating. During cooling, the water will thermally contract and the pressure within the system may drop down to 1.5-1.6 bars (see Figure 9:10).

7.3.3.4 Running a thermal response test on a pile

Thermal response tests on piles follow similar procedures as tests on geothermal boreholes. The natural ground temperature is first estimated by circulating the heat carrier fluid through the absorber pipes without heat rate. This phase roughly takes half a day or one night.

The second phase of the test is the heating. First, the desired heat rate is selected on the heating element switches (3) and the heaters are switched ON with the general control panel (5). A short delay (few seconds) before heaters start functioning may be observed when using 2 kW switches. The applied heat rate can be checked with the consumption panel close the general electrical switch (2) or with the data logger (see Figure 9:10).

The last phase consists in ending the test and disconnecting the mini-module. First, the data logger is stopped. Then the heaters and the circulation pump are switched OFF with the corresponding button on the general control panel (5). Finally, the module is shut OFF. The module is emptied through the emptying valve using the dedicated tubes. When done, the absorber pipes are disconnected. Finally, all valves are closed for transport.

7.4 Thermomechanical response of a group of energy piles

The group of test piles allows designing different types of test that will provide significant insight into the pile to pile interactions. The first type of test deals with “free head” pile thermomechanical response when no structure is built on top of it. The second type is called “single test” as each pile was individually tested once the tank was built. Finally, we carried out a “group test” heating the four test piles at the same time.

7.4.1 “Free head” thermomechanical response test

This first test provides an initial state of constraints only due to the ground friction and base compression. Since the piles were installed close to each other (max. 4.2 m between the pile axes), this test was carried out only on pile #1 and we assumed that the results are the same for the three others. Furthermore, the construction schedule would not have allowed us to carry out a second test on the other test piles. This test was carried out using a heat rate of 1 kW during the first two days and 2 kW during the last three days as the temperature was not increasing fast enough to complete the test within the given schedule. However, the maximal temperature increase in the pile was only 3.6 °C at the end of the heating phase (Figure 7:10), also because of a power cut.

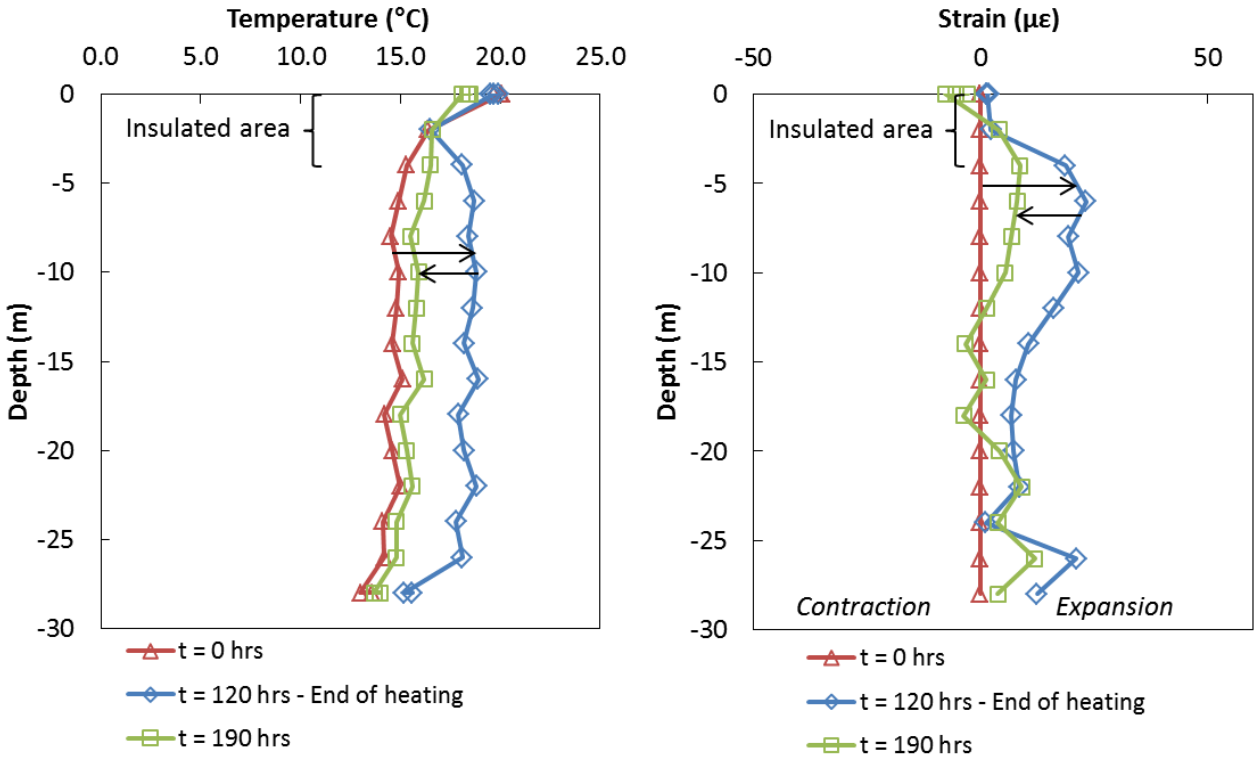

Figure 7:10 Evolution of the temperature (left) and thermal strain (right) profiles along pile #1 during the "free head" test

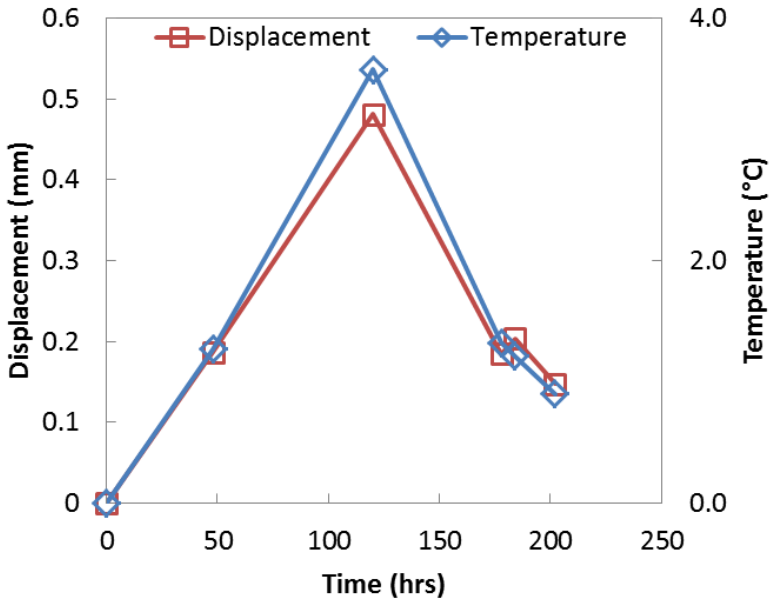

Figure 7:11 Maximum pile #1 top displacements and temperature variation during the "free head" test

Thus, the determined degree of freedom contains some margin of error but this ensured that the pile remained within its elastic domain of response. Maximal thermal expansion of the pile active part reached approximately 30 με for a temperature increase of 3.6 °C, which leaded to the development

of thermal compression up to 560 kN (i.e. 880 kPa, see Figure 7:12). The pile maximum head heave reached 0.48 mm (Figure 7:11).

The thermomechanical response of the pile was quantified using the degree of freedom which contains both the observed thermal strains and the thermal stresses (i.e. the blocked thermal strains). The degree of freedom of the "free head" test shows that a large part of the blocked strains occur within the stiff bottom moraine and sandstone. However, high degree of freedom (up to 0.8) is observed at the pile tip, a phenomenon also experimentally or numerically observed, e.g. Laloui et al. (2006) and Murphy et al. (2014a), and yet not explained. This point is discussed in Section 7.6. The points at the pile top are not representative because the thermal forcing was not coming from the absorber pipes (thermal insulation from 0 to -4 m) but climate factors (bare soil around the piles at this moment of the construction). Therefore, they are not represented on Figure 7:12 nor in Figure 7:13. Based on this degree of freedom profile, one can simply retrieve the observed thermal strains and estimate the thermal stresses as a consequence of blocked thermal stains (see Section 7.2.3). Comparing the directly measured and retrieved strains (i.e. based on the profiles of degree of freedom and temperature) shows how efficient the concept of degree of freedom is for a global thermoelastic characterisation of the pile response (Figure 7:13). However, when non-linearity is observed in the strain-temperature correlation, retrieved values may slightly differ from direct measurements.

Simple numerical analyses were achieved using Thermo-pile software (Knellwolf et al., 2011), developed at the Laboratory of Soil Mechanics of EPFL. The soil parameters were taken from Knellwolf et al. (2011) who back analysed the first test pile built on the EPFL campus for validating the software. The temperature profiles measured *in situ* were used in the analyses as well as the average value of the concrete Young's modulus based on compression tests (Table 7:2). These analyses evidence the fact that the measurements overestimate the average pile temperature because the observed thermal strains are lower than the modelled ones while the analyses consider a homogeneous temperature within pile cross sections (Figure 7:12 and Figure 7:13). This is consistent with the fact that both sensors and absorber pipes were attached to the reinforcing cages, so relatively close to each other. As a result, the estimated thermal loads based on observations are overestimated, which still remains on the safe side of the analyses. In conclusion, this initial test provides important features of the "free head" thermomechanical response of pile #1; response which is then assumed to be the same for the three other test piles since they have the same properties and are very close to each other.

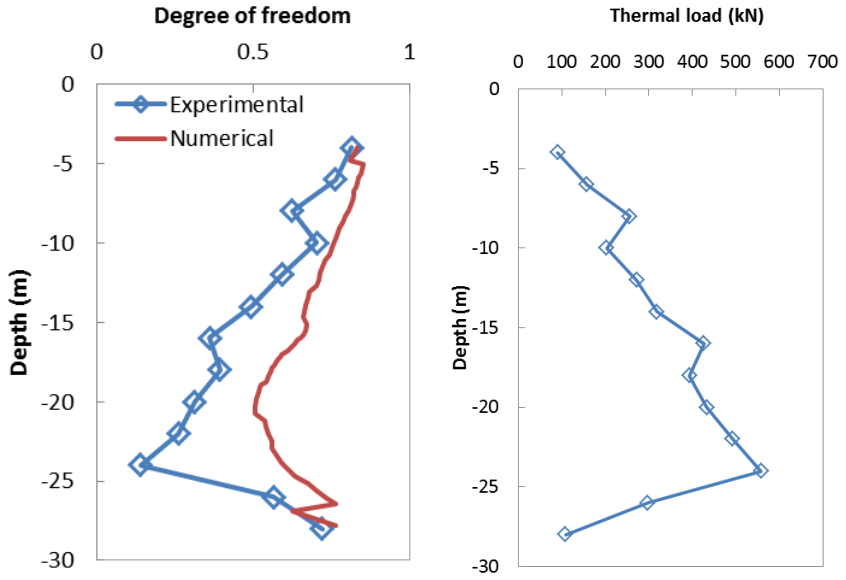

Figure 7:12 (left) "Free head" degree of freedom and (right) profile of internal thermal effort during the "free head" test

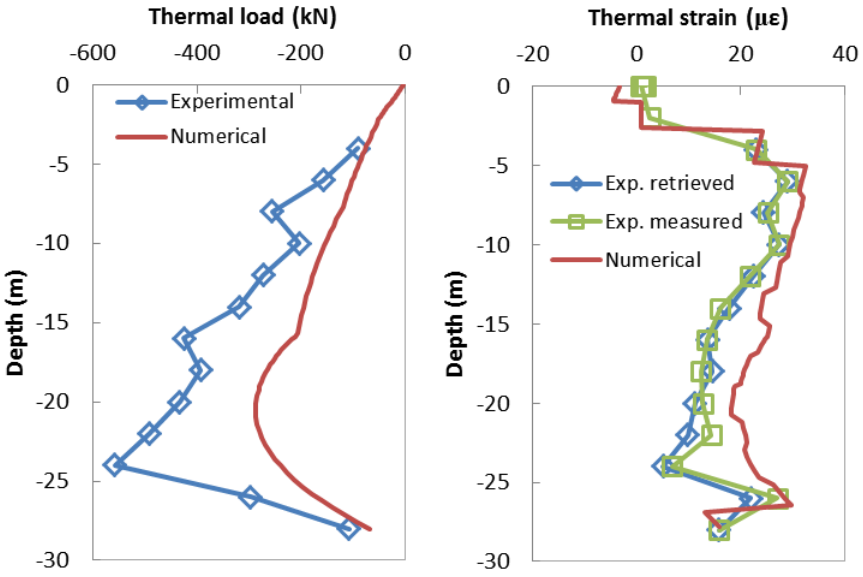

Figure 7:13 (left) Thermal load and (right) thermal strains based on the degree of freedom profile

7.4.2 Single thermomechanical response tests

These tests were carried out after the water retention tank was built. Comparing each individual pile response with the tank on top of it to the "free head" response allows estimating the amount of constraint induced by the tank. These constraints can be divided into the carried load and the pile-to-pile interactions through raft bending. The former is linked to the pile design while the latter is related to the stiffness of the raft. If the raft is soft enough so that no load redistribution is expected within the foundation, then the pile top boundary condition is of constant load type. Otherwise, when the raft is stiff, load redistribution (the overall load carried out by the foundation remaining the same) may occur within the foundation and pile-to-pile interactions are to be expected when using heat exchanger piles.

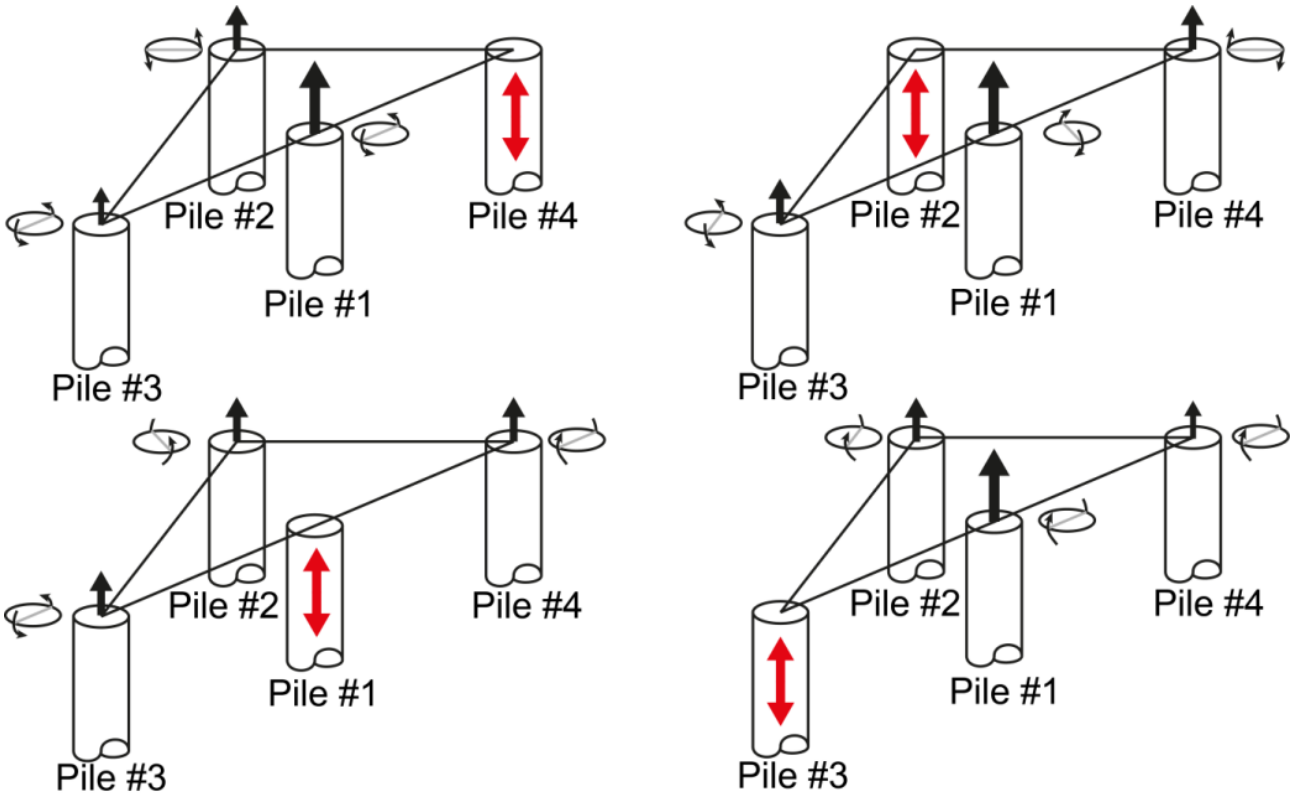

Figure 7:14 Concept of pile to pile interactions through raft bending when one pile is heated at a time. The vertical arrows on top of the piles represent the magnitudes of the interactions; the cross section displayed beside the piles shows the possible induced rotations, the main axis of rotation being represented in grey. The heated pile is expanding

The main aim of this campaign is to evidence and quantify the pile-to-pile interactions of first level (i.e. with directly adjacent piles) and second level by observing how the heated pile pulls on the neighbouring ones. Indeed, the heated pile will expand and then push below the raft. As a result of raft bending, the surrounding piles will then be pulled upward and will experience less compressive stress and strains. Rotations of pile top cross sections may also occur (Figure 7:14). To monitor this phenomenon, we measured full strain and temperature profiles along the heated pile plus the tip compression as well as head strains and tip compression from the three other – not heated – test piles. The reference state is taken just prior starting the heating so that it is easy to observe compression increase and relief.

7.4.2.1 Single test 1: heating pile #1

The test on pile #1 started on July 13th 2013 and lasted 264 hours (i.e. 11 days) among which 168 hrs were dedicated to heating, the rest being used for passive cooling. The heat rate was 3 kW and the flow rate was 21 L/min which induced a maximum temperature increase in the pile of approximately 8.2 °C. The thermally insulated part is clearly visible on the temperature profiles (Figure 7:15) and when the passive cooling phase was stopped after 264 hours of test, a temperature anomaly of about 3.3 °C was still observed. This reduced to 0.6 °C after 1392 hours (58 days) of passive cooling. This illustrates the significant heat capacity of large diameter heat exchanger piles.

During test 1, pile #1 experienced compression within its insulated portion (from 0 to -4 m) because it is trapped between the thermally expanding portion of the pile, which pushed upward, and the raft

on top, which pushed downward because of the surrounding piles. As a result, compressive (negative) strains up to -50 με developed at the top of pile #1 for a pile temperature increase of about 8.3 °C. Along the rest of the pile, expansive (positive) strains were observed with an average value of 20 με (Figure 7:15). Meanwhile, piles #2, #3 and #4 experienced expansive strains at their tops (Figure 7:17) significantly lower than the compression observed at the top of pile #1, between 10 and 25 με. Despite pile #1 is equidistant from each other pile (3 m between pile axes), the impact of its heating seemed to be stronger on pile #4 than on piles #2 and #3. This might come from the enhanced rigidity induced by the walls of the room where sensor cables and measuring instruments are gathered (see Figure 7:6d). When pile #1 cooled, compressive strains that were observed at its top returned to zero, so did the expansive strains observed at the other pile tops. However non-reversible axial strains were observed along the lower portion of pile #1 embedded within the sandstone (Figure 7:15). The induced thermal loads are discussed with the evolution of the degree of freedom in Section 7.4.2.5.

The three strain gauges deployed at the pile tops did not exhibit exactly the same behaviours as some experience more compression or expansion than the others in the same pile. This could come from pile top rotations. Indeed, the strain gauges facing the heated pile may experience greater expansion than the ones on the opposite side of the pile.

The facing positions of theses gauges were not recorded before concrete pouring but we can get an idea of where they are based on the observations considering that:

- Gauges facing the heated pile experience the greater expansion
- Gauges that have similar strain paths have symmetrical positions

Therefore, we can lead these analyses:

- Pile #2: two strain gauges (S2.2 and S2.3) experienced similar and high expansive strains while the third one (S2.1) experienced lower expansive strain, therefore S2.2 and S2.3 are facing pile #1 while S2.1 is on the opposite side of the pile
- Pile #3: one strain gauge (S3.2) experienced high expansive strain while the two others (S3.1 and S3.3) experienced similar but lower expansive strains, therefore S3.2 is facing pile #1 while the two others are not
- Pile #4: the strain gauge S4.1 experienced the greatest expansive strain while the two others had similar strain paths, therefore S4.1 is facing pile #1 and the two others are not

It is not possible to identify where the strain gauges in pile #1 are located from test 1, but this will be achieved using the tests on the three other piles. Compression at the tip of pile #1 increased by about 600 kPa during the heating phase, relieving the compression at the bases of pile #2, #3 and #4 by 15 to 35 kPa. Even if the variations in the isothermal piles are one order of magnitude lower than in the heated pile, good correlation is found for their evolutions during the test (Figure 7:16). The maximum pile head heave was estimated by integrating the strain profile along the pile. It reaches 0.36 mm for a temperature increase of approximately 8.2 °C (Figure 7:18).

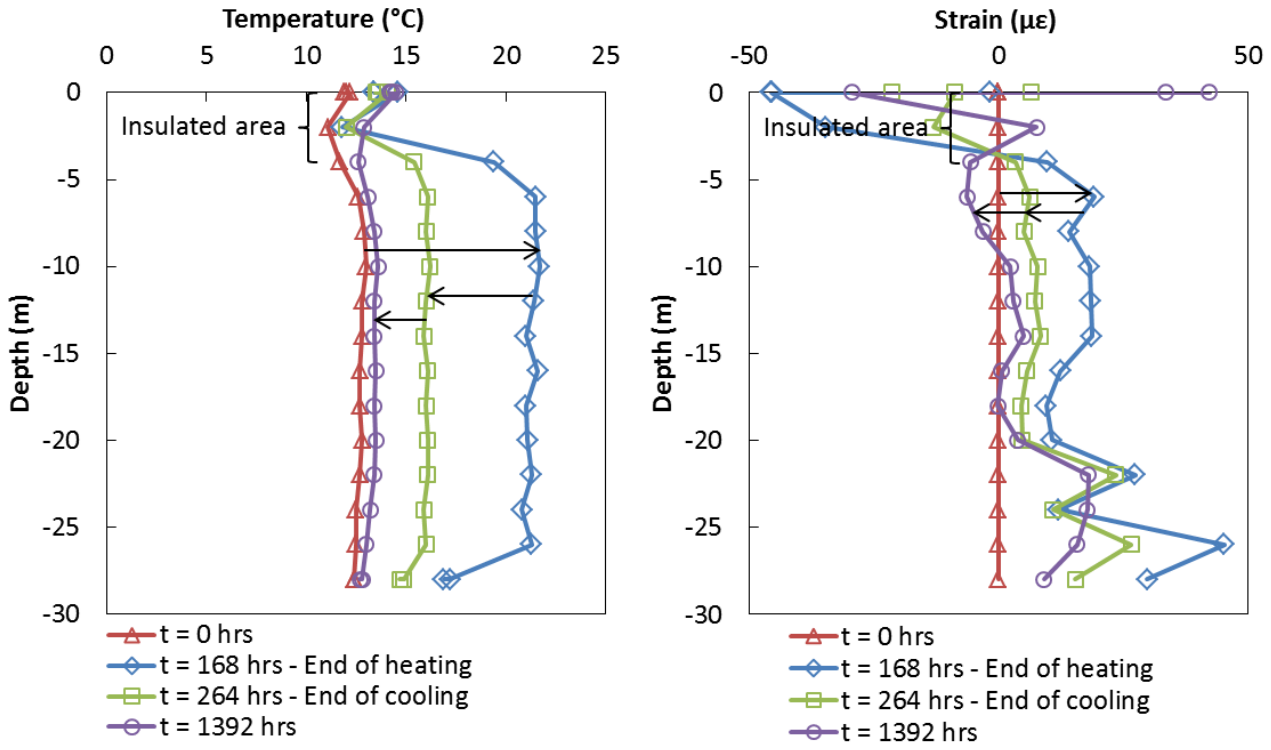

Figure 7:15 Evolution of the temperature (left) and thermal strain (right) profiles along pile #1 during the single test 1

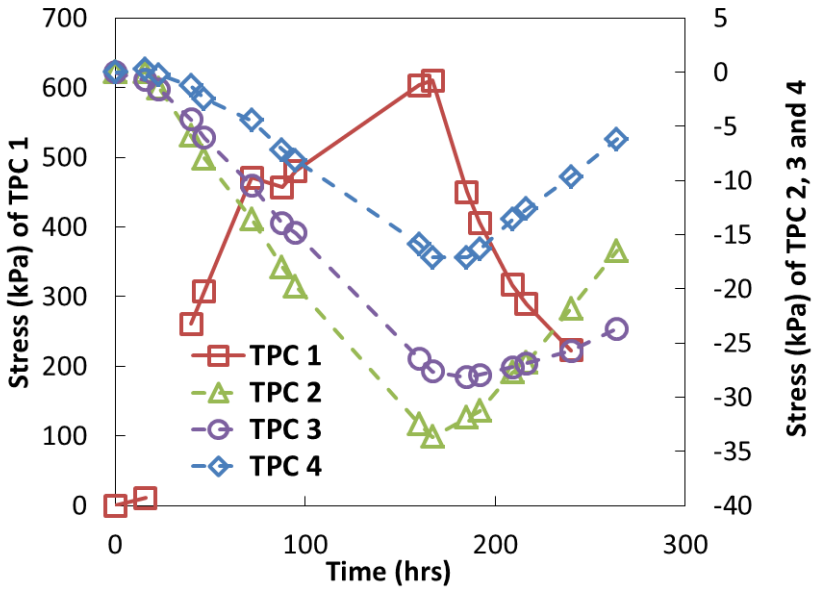

Figure 7:16 Evolutions of pile tip compressions during the single test 1

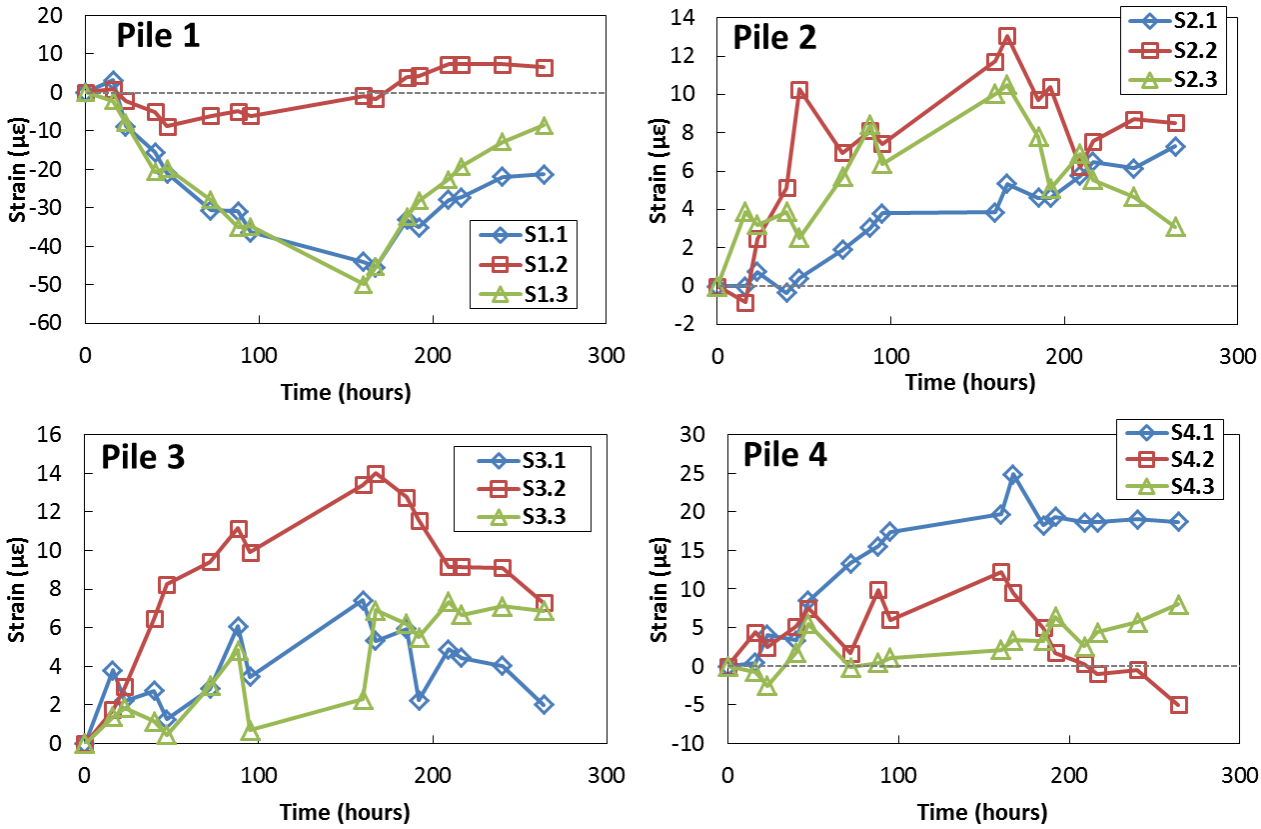

Figure 7:17 Evolutions of pile head strains during the single test 1

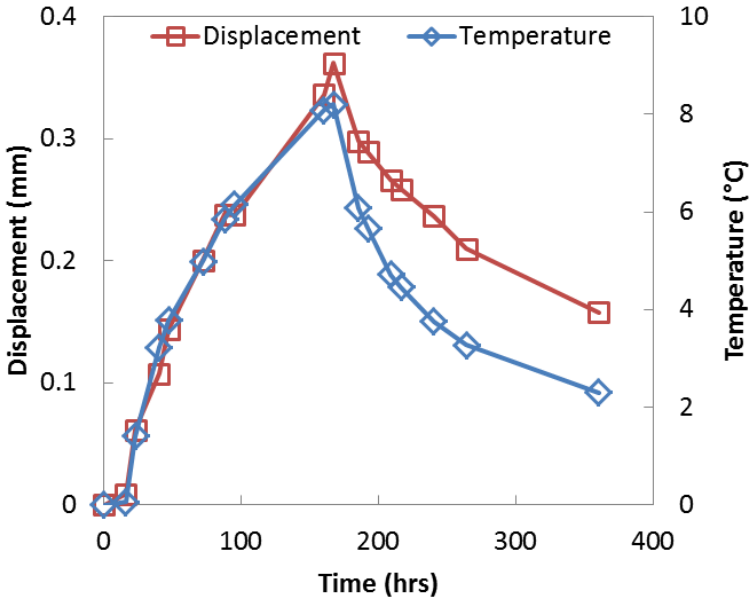

Figure 7:18 Maximum pile #1 top displacements and temperature variation during the single test 1

7.4.2.2 Single test 2: Heating pile #4

Test 2 started on August 2nd 2013 on pile #4. The heating phase lasted 120 hours (i.e. 5 days), with a heat rate of 3 kW and a fluid flow of 21 L/min. This led to a temperature increase of about 6.5 °C.

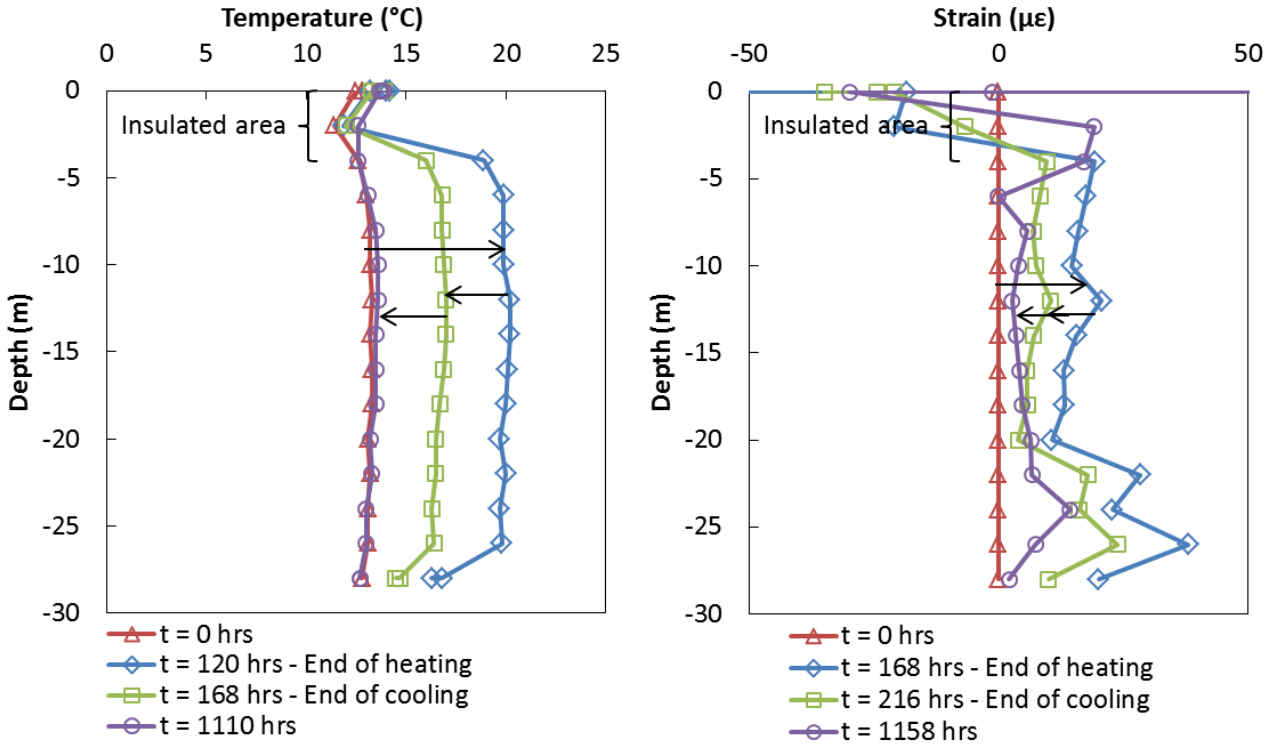

Figure 7:19 Evolution of the temperature (left) and thermal strain (right) profiles along pile #4 during the single test 2

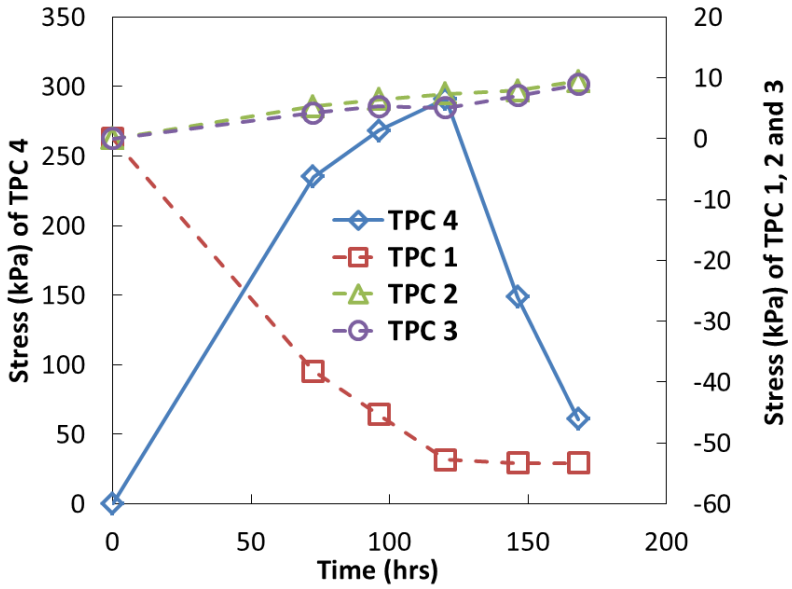

Figure 7:20 Evolutions of pile tip compressions during the single test 2

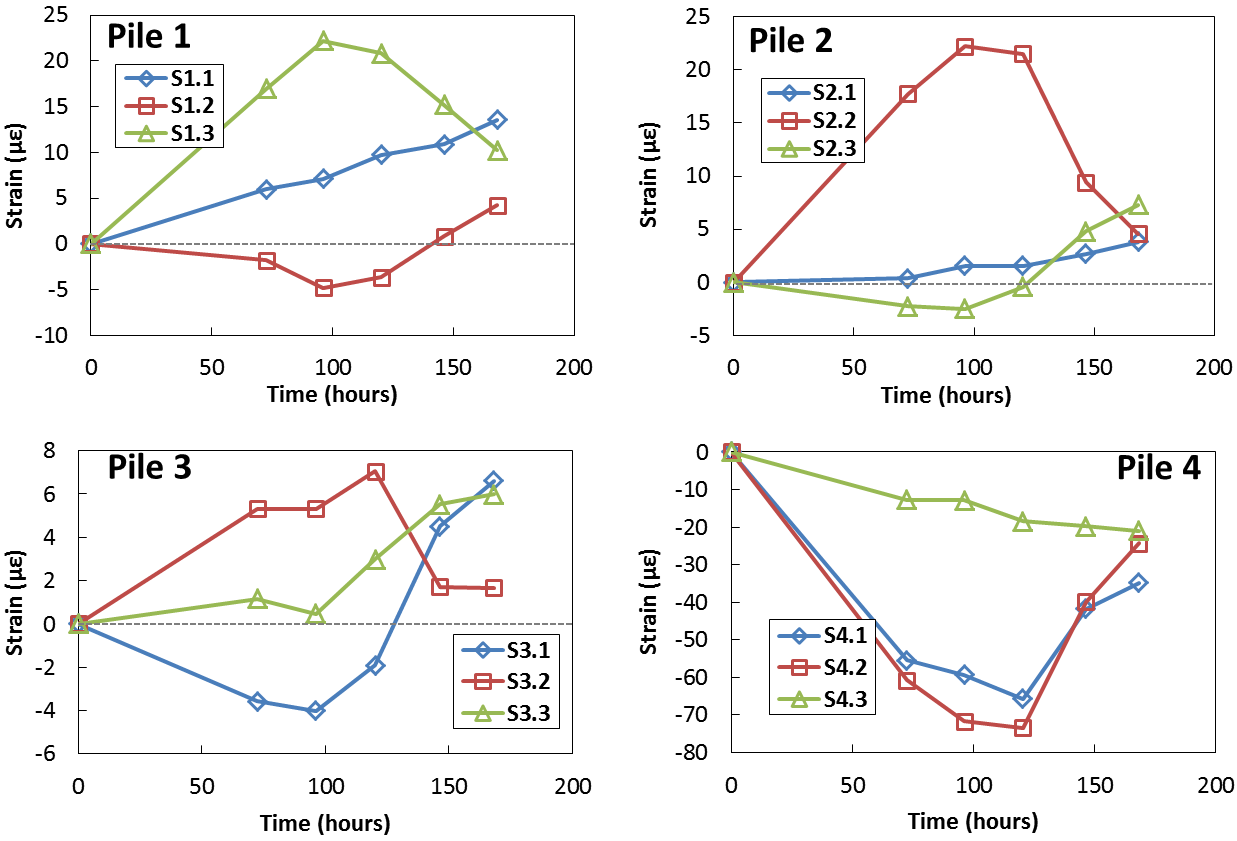

Figure 7:21 Evolution of pile head strains during the single test 2

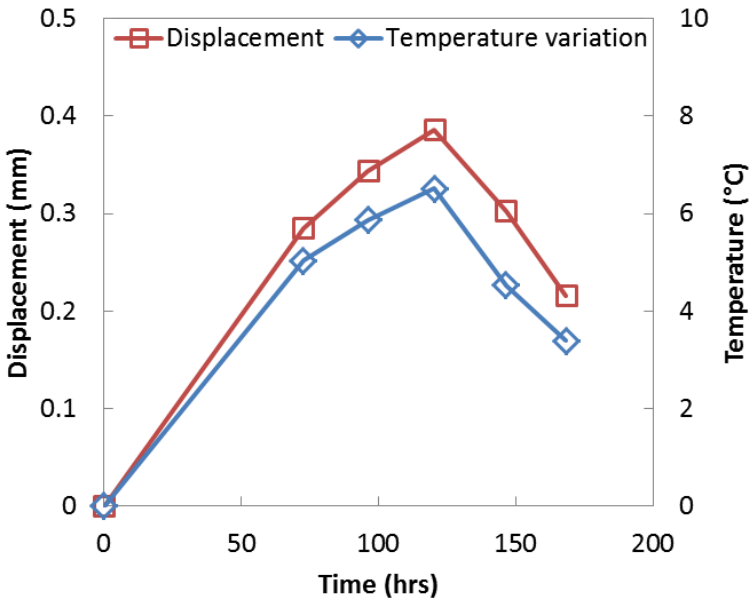

Figure 7:22 Maximum pile #4 top displacements and temperature variation during the single test 2

Expansive strains between 20 and 40 με were observed along the thermoactive part of the pile (Figure 7:19). Again, the heated portion of the pile exhibits a relatively homogeneous temperature except at the pile basis where end effects are significant. Similarly to the previous test, non-

reversible axial strains are observed in the sandstone (Figure 7:16). The maximum pile top heave was around 0.39 mm for a temperature increase of 6.5 °C (Figure 7:22).

This test started just after test 1 was stopped on July 24th 2014. Therefore, the required recovery time for passive cooling was not long enough to allow pile #1 to come back to its initial "isothermal" state. As a result, observations are a coupling between the cooling of pile #1 and the heating of pile #4. This is particularly visible when looking at the evolution of pile tip compression where no direct correlation is observed between the heated pile response and the other piles. The compression at the tip of pile #1 kept decreasing even after the heating of pile #4 was stopped as it was recovering from test 1. Similarly, piles #2 and #3 were regaining their initial pile tip compression even though we can see small variations correlated with the heating of pile #4 (Figure 7:20).

Evolution of the strains at the pile tops was also influenced by the cooling of pile #1: S1.1, S2.1 and S3.3 followed the cooling trend of pile #1 while the other strain gauges showed correlations with the heated pile response. We observe that piles #1, #2 and #3 had one strain gauge experiencing significant expansion, another one little compression while the third one was not really impacted by test 2 and mainly underwent the cooling of pile #1. This could be an evidence of small pile top rotation as the strain gauge facing the heated pile would undergo expansion while the one on the opposite face would undergo compression. The impact of heating pile #4 was more important on first level piles (i.e. piles #1 and #2), with relative expansive strains up to 20-25 με, than on the second level pile #3 with expansive strains up to 6-7 με.

Based on the observations (Figure 7:21), S1.3, S2.2 and S3.2 should be facing pile #4 while S1.2, S2.3 and S3.1 should be on the opposite pile faces. This test therefore allows drawing the positions of the head strain gauges in pile #2.

7.4.2.3 Single test 3: heating pile #3

Test 3 started on September 3rd 2013. The heating of the pile #3 was achieved over 277 hours because of a power cut that occurred between September 6th and 9th. The heat rate used was again 3 kW and the flow rate was 21 L/min. The maximum temperature increase was around 10 °C and induced expansion of the heated portion is between 20 and 60 με (Figure 7:25).

The power cut is clearly identified in time series of pile head strains (Figure 7:23) and base compression (Figure 7:24). The heated pile (pile #3) undergoes compression up to -50 με at its top while the other ones undergo expansion up to 15 με (Figure 7:23). However, responses of the piles are not very clear and good correlations between the observations are difficult to draw. This might be due to the fact that pile #3 is not located below the walls of the service room and therefore has a limited impact as it does not beneficiate from the enhanced rigidity provided by the room walls. However, evolutions of pile base compression are well correlated. It increased by 600 kPa in the heated pile while it was relieved by 10 to 40 kPa in the non-heated piles. Pile #1 exhibited the greatest reaction as it is closer to pile #3. Then, pile #2, which is at an intermediate distance from pile #3, showed lower reaction and was clearly less affected than pile #1. Finally, reaction at the tip of pile #4, which is the farthest away from the heated pile, was almost insignificant. No particular information about the positions of the head strain gauges were gathered using this test because of

the power cut. It was only used as a confirmation of the deductions based on the three other single tests. Maximum pile head heave reached 0.51 mm for a temperature (Figure 7:26).

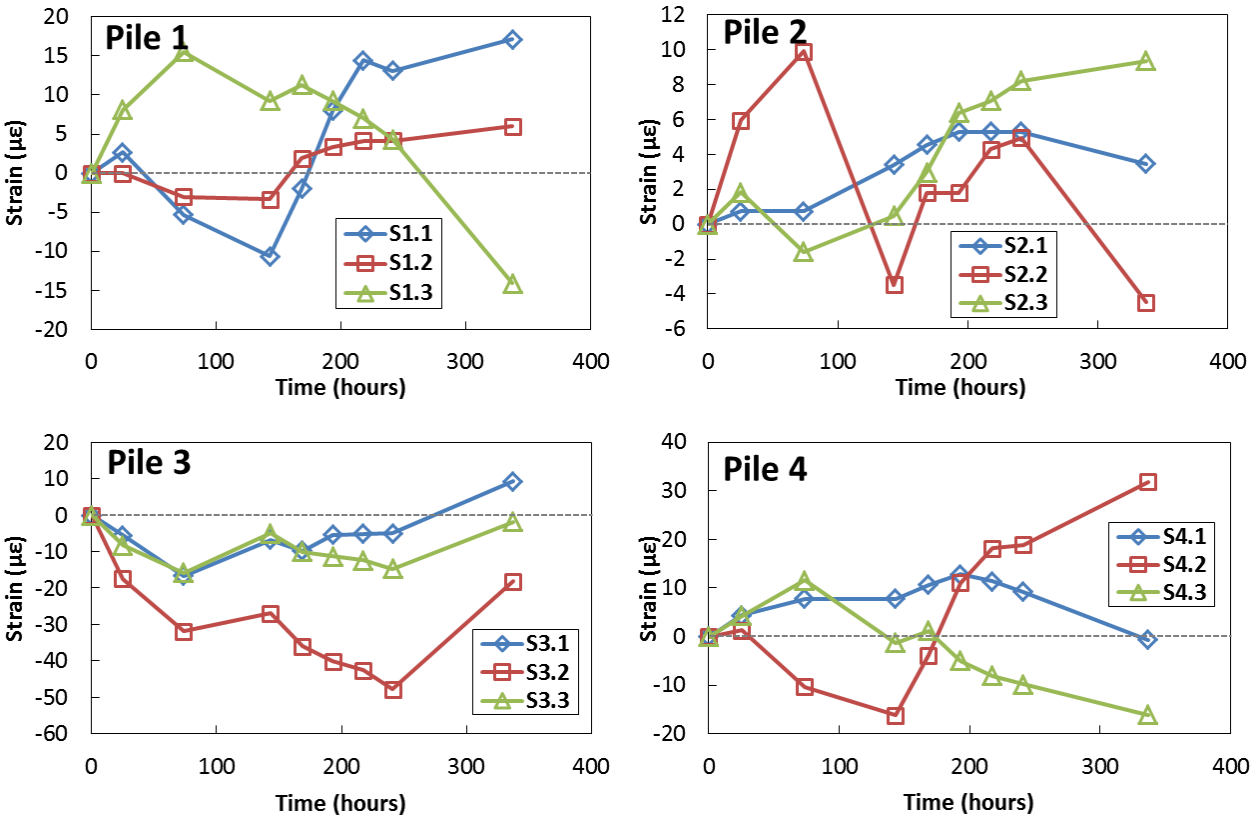

Figure 7:23 Evolution of pile head strains during the single test 3

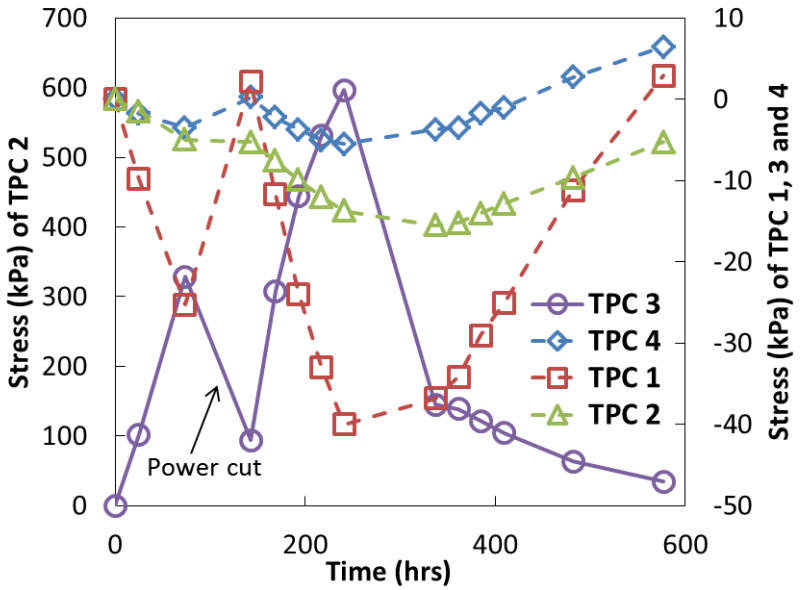

Figure 7:24 Evolutions of pile tip compressions during the single test 3

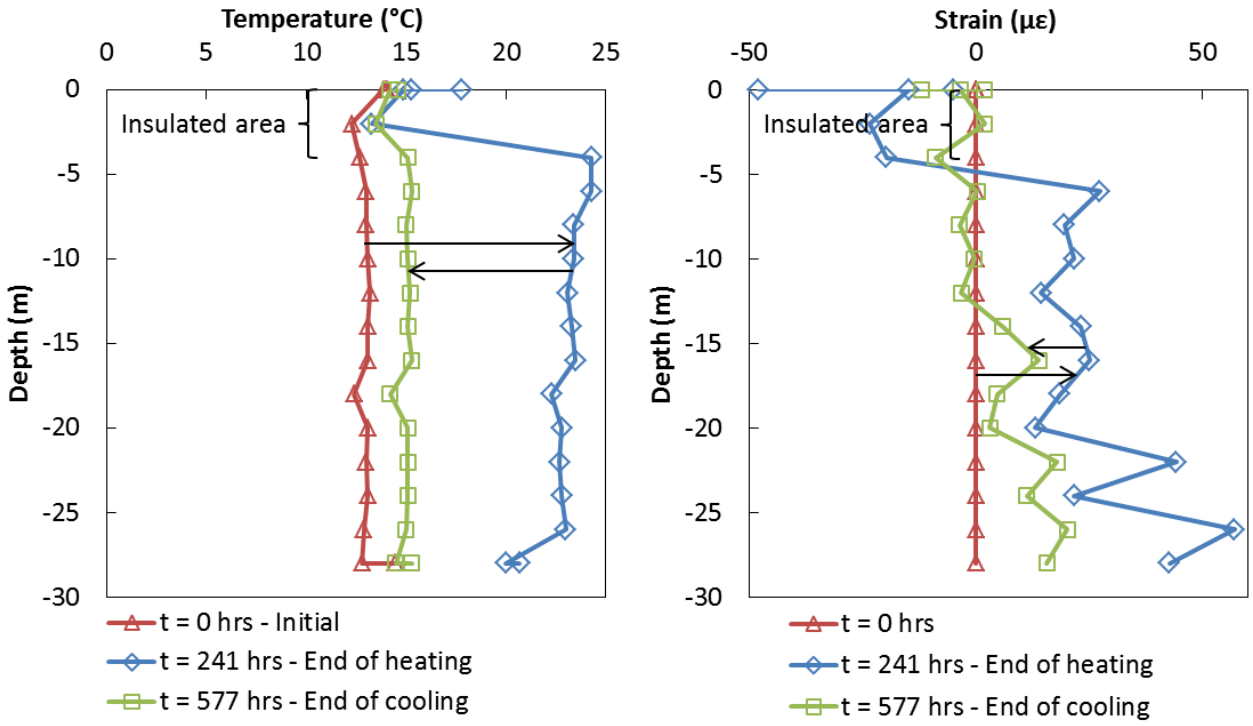

Figure 7:25 Evolution of the temperature (left) and thermal strain (right) profiles along pile #3 during the single test 3

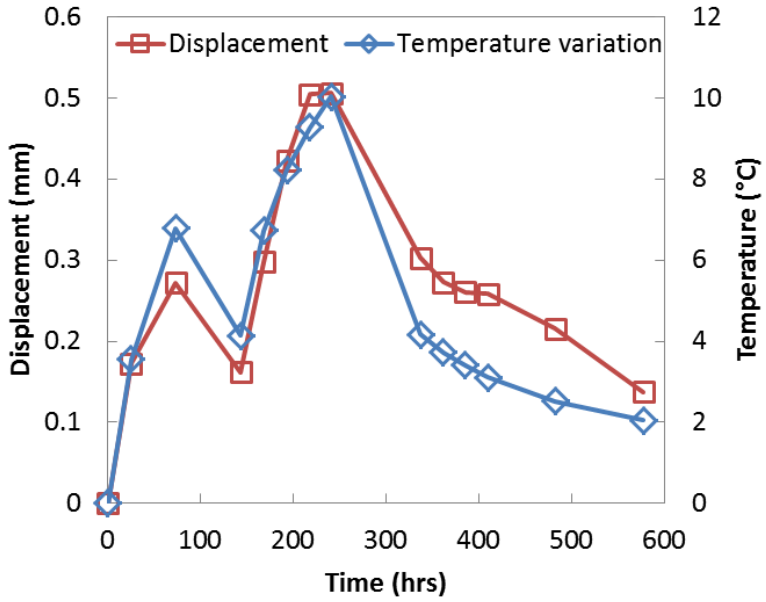

Figure 7:26 Maximum pile #3 top displacements and temperature variation during the single test 3

7.4.2.4 Single test 4: heating pile #2

Test 4 started on May 23rd 2014. The heating of pile #2 lasted 192 hours (i.e. 8 days) with a constant heat rate of 3 kW, which led to a maximum temperature increase of about 9.3 °C. The thermal expansion along the thermoactive part of the pile ranged between 20 and 60 με (Figure 7:27). Compression observed at the heated pile top reached -40 με while expansion at the other pile tops ranged from 5 to 35 με (Figure 7:29). Despite piles #3 and #4 have symmetrical positions

around pile #2, pile #4 reacted more to the heating of pile #2 which suggests that the interactions are enhanced thanks to the room walls as already suggested in Section 7.4.2.1.

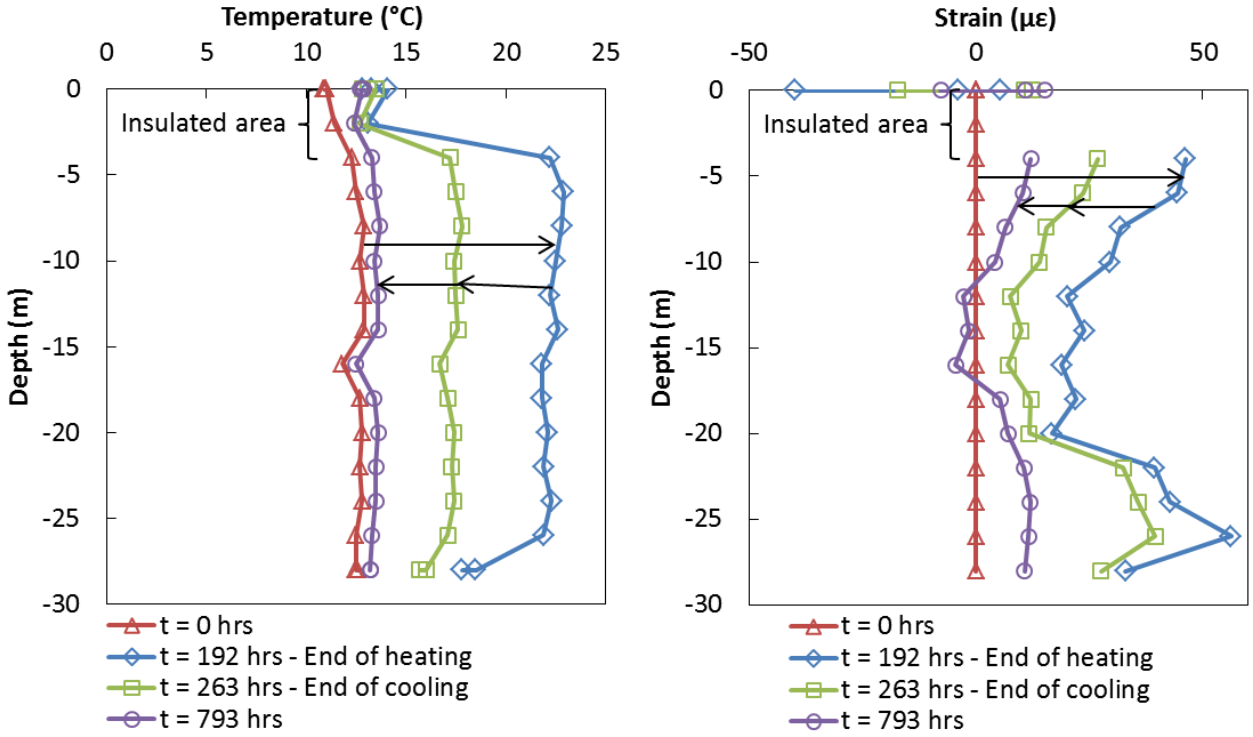

Figure 7:27 Evolution of the temperature (left) and thermal strain (right) profiles along pile #2 during the single test 4

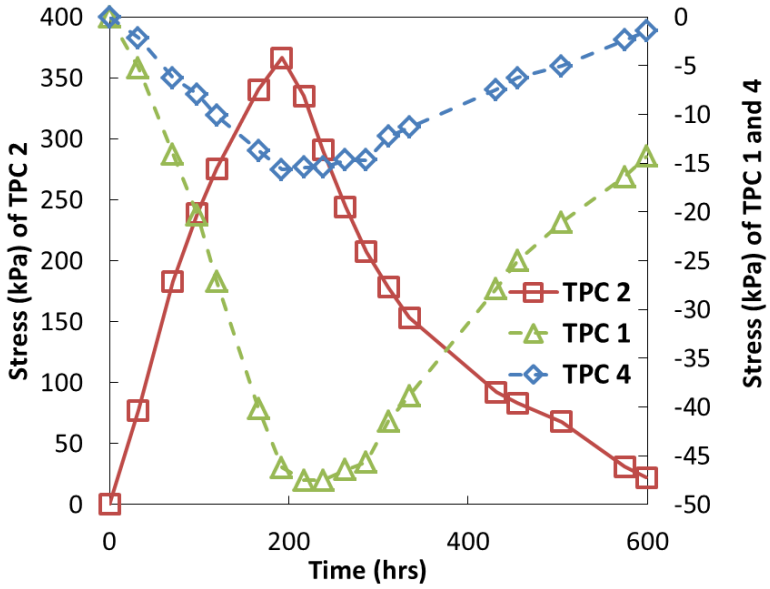

Figure 7:28 Evolutions of pile tip compressions during the single test 4

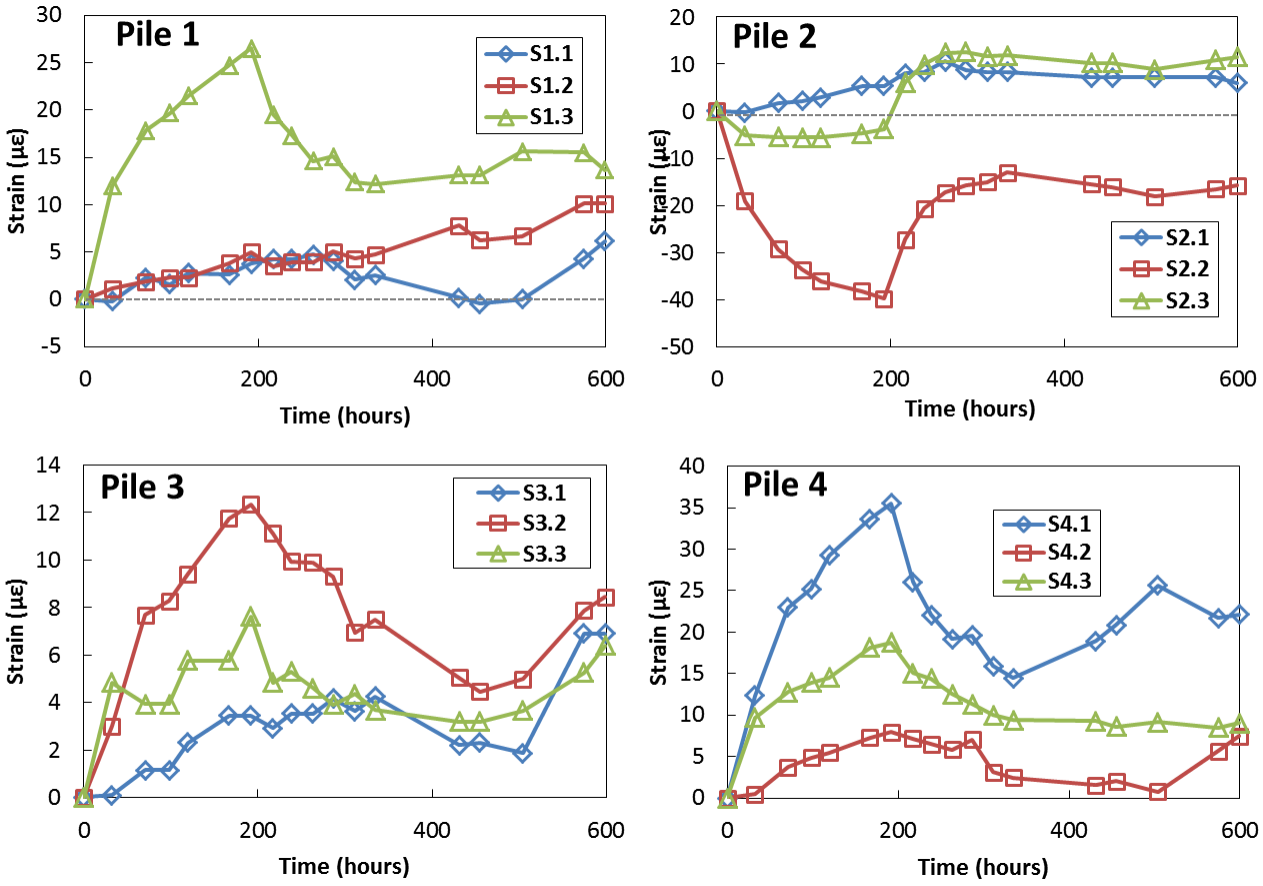

Figure 7:29 Evolution of pile head strains during the single test 4

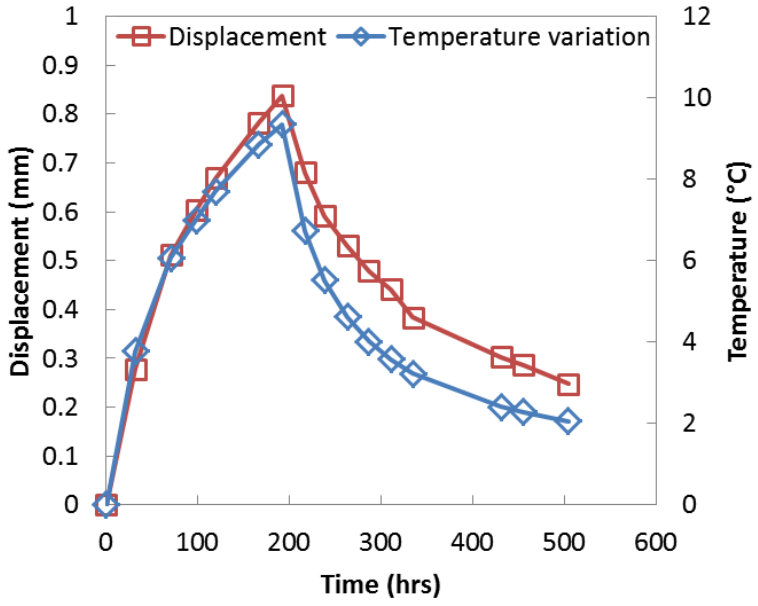

Figure 7:30 Maximum pile #2 top displacements and temperature variation during the single test 4

The load cell at the tip of pile #3 did not show good measurements (i.e. sudden jump in measured frequency) during this test and was therefore not considered in the analyses. Pile tip compression in the heated pile increased by approximately 370 kPa whereas the relief in the closest pile (i.e.

pile #1) reached 50 kPa and 16 kPa in the farthest pile (pile #4). One may expect that pile #3 would exhibit similar or lower response as pile #4 because of the symmetrical position they occupy around pile #2 (Figure 7:28). Maximum pile head heave was estimated to approximately 0.84 mm (Figure 7:30).

This test suggests that S3.2 faces pile #2 and therefore allows concluding on the locations of the strain gauges at the top of pile #3. However, it is not possible to conclude about pile #1 as S1.3 is the most responsive strain gauge in any single test. This test also suggests that S4.1 face pile #2. However, S4.3 exhibits a greater reaction than S4.2 while heating pile #2 while S4.2 has a greater response than S4.3 when heating pile #1. Therefore, S4.3 is closer to pile #2 and S4.2 is closer to pile #1. Similarly, S3.3 shows greater response than S3.1 when heating pile #2 whereas S3.1 shows a greater response than S3.3 when heating pile #1. Therefore, S3.3 is closer to pile #2 and S3.1 is closer to pile #1. The final scheme is given in Appendix 9.5.7.

7.4.2.5 Evolution of the degree of freedom

Profiles obtained with the "single" tests exhibit lower degree of freedom than the "free head" test from 0 to -20 m (D_{II} on Figure 7:31). This shows that the construction of the tank impacts the thermomechanical response of the piles down to the sandstone. Furthermore, differences between the profiles from the "single" tests are observed between 0 and -10 m (D_I on Figure 7:31) which suggests that the pile positions below the raft influence their thermomechanical responses along their first 10 m. This can be attributed to the coupled effects of the carried load and the raft rigidity.

Indeed, pile #2 is located below the corner of the raft which induces less stiff head constraints whereas pile #1 is below the raft and surrounded by other piles which maximises its constraints. Pile #3 and #4 have intermediate positions, below raft edges. However, the intermediate response of pile #4 must be nuanced considering that his degree of freedom might be slightly overestimated as pile #1 was still cooling when test #2 was carried out.

Profiles of thermal load were evaluated along each pile after the tank construction (Figure 7:31). For temperature variations between 6.5 °C and 10.2 °C, maximum thermal loads vary between 1000 and 1550 kN, corresponding to thermal stress rates around 150 kPa/°C. Loads estimated from the load cells at the pile tips are also represented on Figure 7:31 and are in good agreement with the loads based on the pile tip strain gauges.

7.4.3 Group thermomechanical response tests

The group test started on June 25th 2014. It consisted in heating the four piles at the same time in order to observe variations in their thermomechanical response compared to the "single" tests.

Because only 3 heating modules were available to test 4 piles at the same time, we connected two piles in series: piles #2 and #3, the heat carrier fluid going first through pile #3 and then through pile #2. Each pile was heated using a heat rate of 3 kW, the module connected to piles #2 and #3 therefore delivering 6 kW. The heating phase lasted 141.5 hrs (almost 6 days).

During this test, radial strains along pile #1 were monitored using the optical fibers attached along the reinforcing cage perimeter.

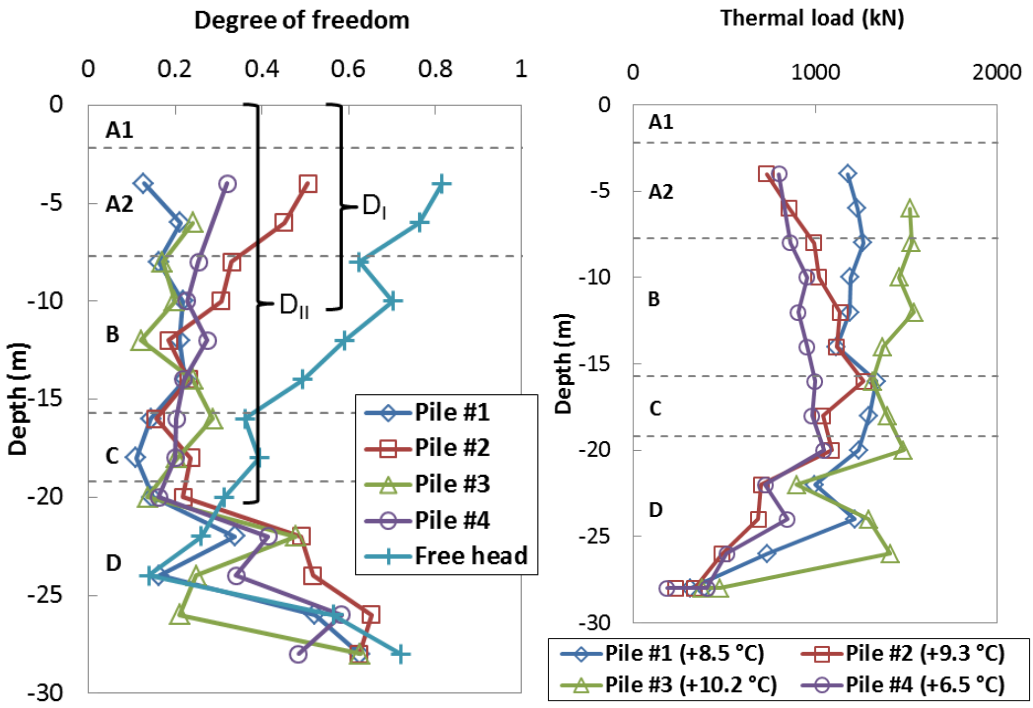

Figure 7:31 (left) Evolution of the degree of freedom from the "free head" condition to single test piles and (right) thermal loads deduced from the profiles of degree of freedom for the maximum temperature variation in the piles during single tests

7.4.3.1 Group test – pile #1

Temperature increase in pile #1 during the group test reached 8.5 °C after 141.5 hrs of heating. This induced expansive strains around 30 με in the soft soil layers (between 0 and -20 m) and around 50 με in the sandstone (Figure 7:33). The maximum pile top heave was 0.88 mm (Figure 7:34). The circulation pump of the module was stopped after 390 hrs of test. At this moment, the pile temperature was still 2-3 °C higher than the natural level observed at the test beginning (Figure 7:33). Even after 408.5 hrs of cooling, the pile temperature anomaly was around 2 °C and significant strains were still observed along the lower part of the pile.

Radial strains were measured using the radial optical fibers (Figure 7:32). Data from those fibers started being recorded one day after the beginning of the test because of the availability of the reading unit. Therefore, the reference for the optical fibers is not the same as for the temperature and axial strains in the pile. As a result, estimated free radial thermal strains which are based on temperature records have not the same reference as the optical fiber measurements. However, the estimated free radial thermal strains were shifted downward (dashed line in *Figure 7:34*) to compare with the measurements. The fiber at the pile top did not show significant reaction as it is not in the thermoactive part while the fiber placed at 1/3rd of the pile (i.e. at -9 m) exhibited a clear response well correlated with the heating-cooling sequence. This shows that radial strains are permitted within the soft soil layers. Conversely, no clear response was observed along the fiber located at 2/3rd of the pile despite it is located within the thermoactive part, suggesting that radial strains were prohibited along the part embedded within the sandstone. As a result, mobilizable axial thermal expansion might be greater along the lower part of the pile as discussed in Chapter 3

Section 6, which can explain the greater axial strains observed there. This is further discussed in Section 7.6.2.

Furthermore, the free thermal radial expansion of the pile at 1/3rd of its length was estimated from the temperature time series recorded at -8 m and -10 m, using a thermal expansion of 10 με/°C. It is compared to the measured radial expansion in Figure 7:32. Despite measurements have not the same initial points, it is clear that radial strains do not occur freely (Figure 7:32). This pile experienced little compression at its top, along the insulated portion; which indicates that its mechanical load might have slightly increased.

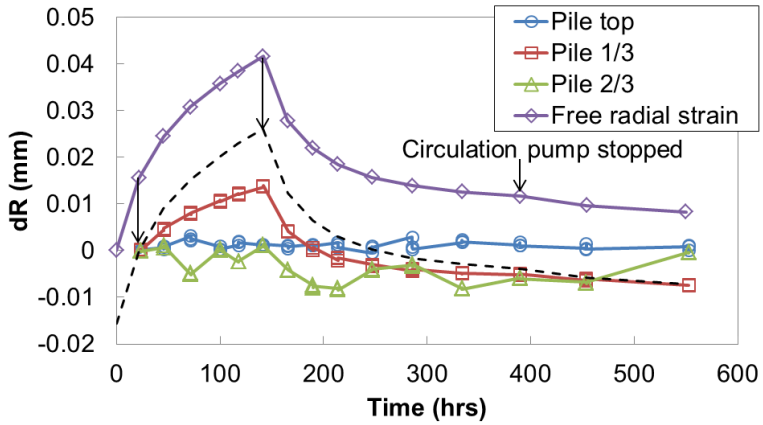

Figure 7:32 Variations in pile radius along pile #1 at the pile top, pile 1/3rd and pile 2/3rd during the group test

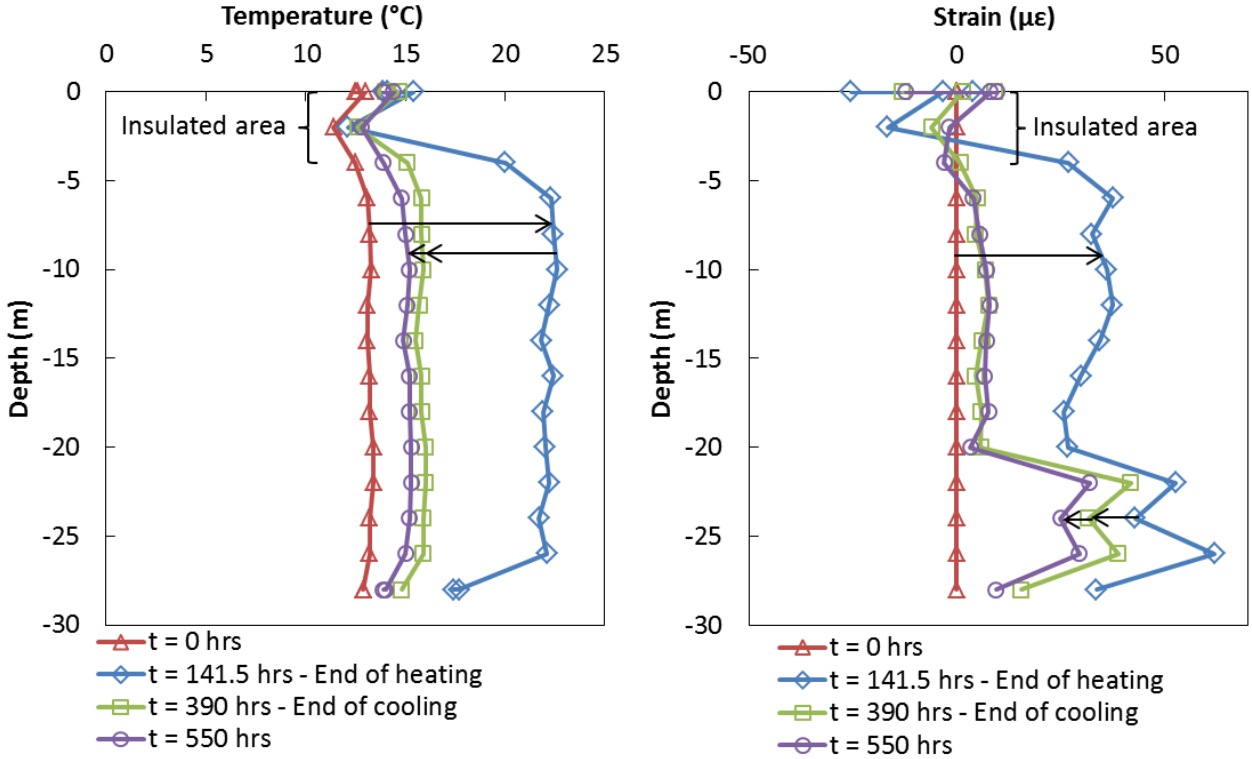

Figure 7:33 Evolution of the temperature (left) and thermal strain (right) profiles along pile #1 during the group test

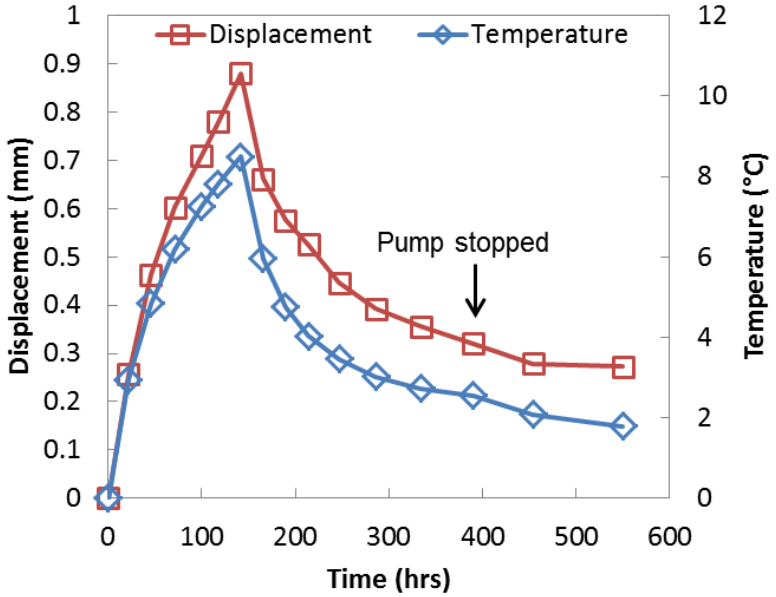

Figure 7:34 Maximum pile #1 top displacements and temperature variation during the group test

7.4.3.2 Group test – pile #2

Pile #2 was connected in series with pile #3 during the group tests, pile #2 being the second pile heated in the circuit. As a result, the temperature increase only reached 7.4 °C at the end of the 141.5 hrs of heating. However, axial strain profiles show that thermal strains along the upper part of the pile were similar to that along the lower part of the pile, slightly lower than 50 με, except at the basis of the stiff bottom moraine.

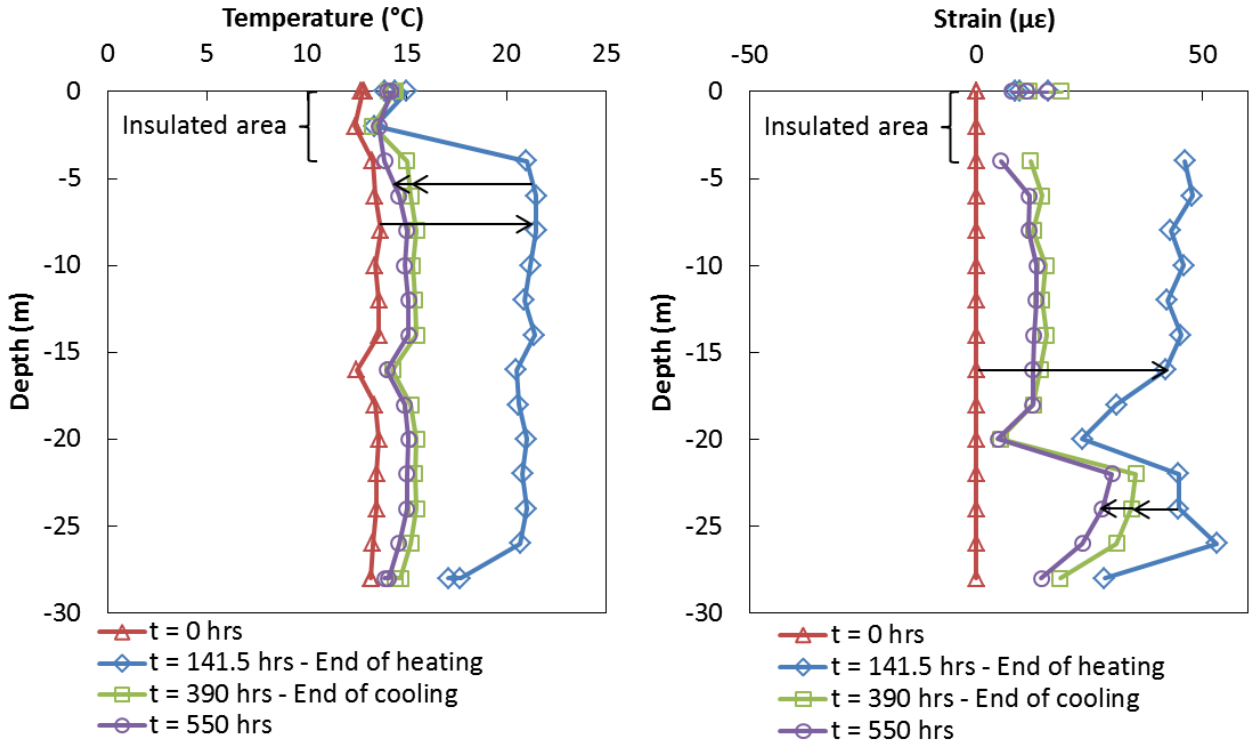

Figure 7:35 Evolution of the temperature (left) and thermal strain (right) profiles along pile #2 during the group test

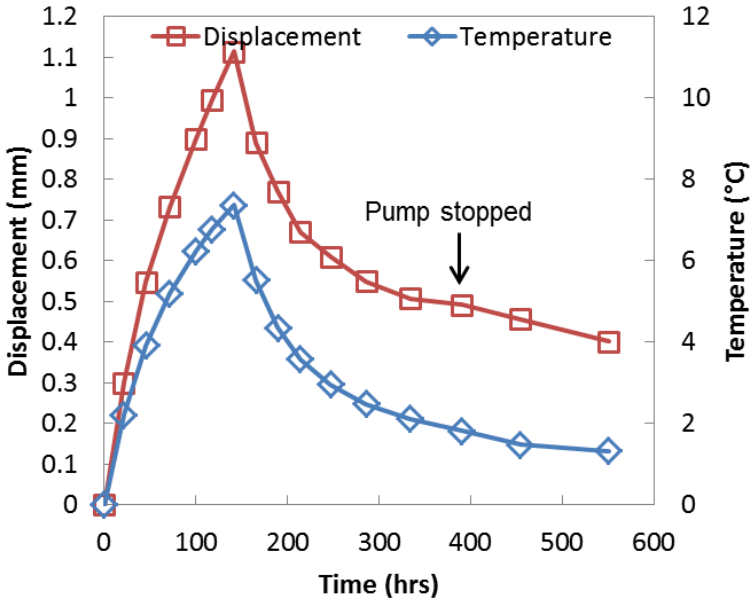

Figure 7:36 Maximum pile #2 top displacements and temperature variation during the group test

The pile experienced expansion at its top which indicates that a part of its mechanical load might have been transferred to the neighbouring piles (Figure 7:35). The pile thermal expansion leaded to a maximum pile top heave of 1.1 mm (Figure 7:36) and an increase in pile tip compression of 775.6 kPa (Figure 7:41).

7.4.3.3 Group test – pile #3

Pile #3 was connected with pile #2 to the same heating module during the group test. It was however the first pile along the circuit and therefore its temperature increased by 9.1 C. Thermal expansion was relatively homogeneous along the portion of the pile embedded within soft soil layers and ranged between 30 and 40 με.

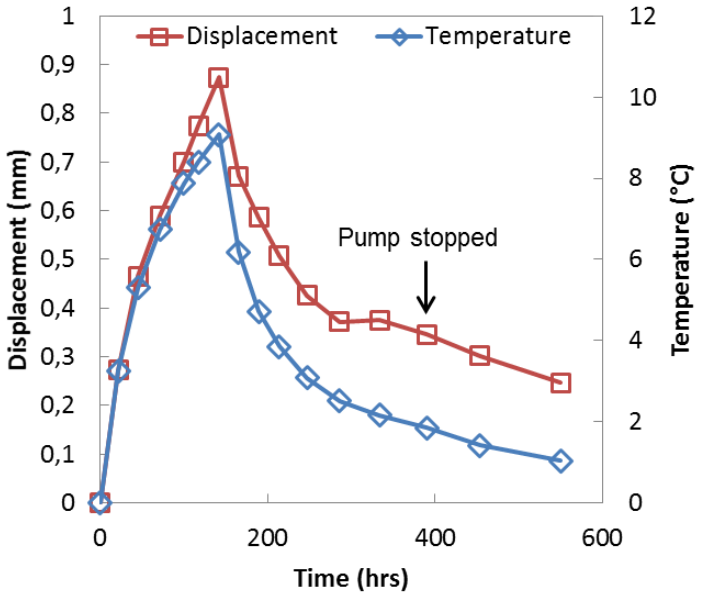

Figure 7:37 Maximum pile #3 top displacements and temperature variation during the group test

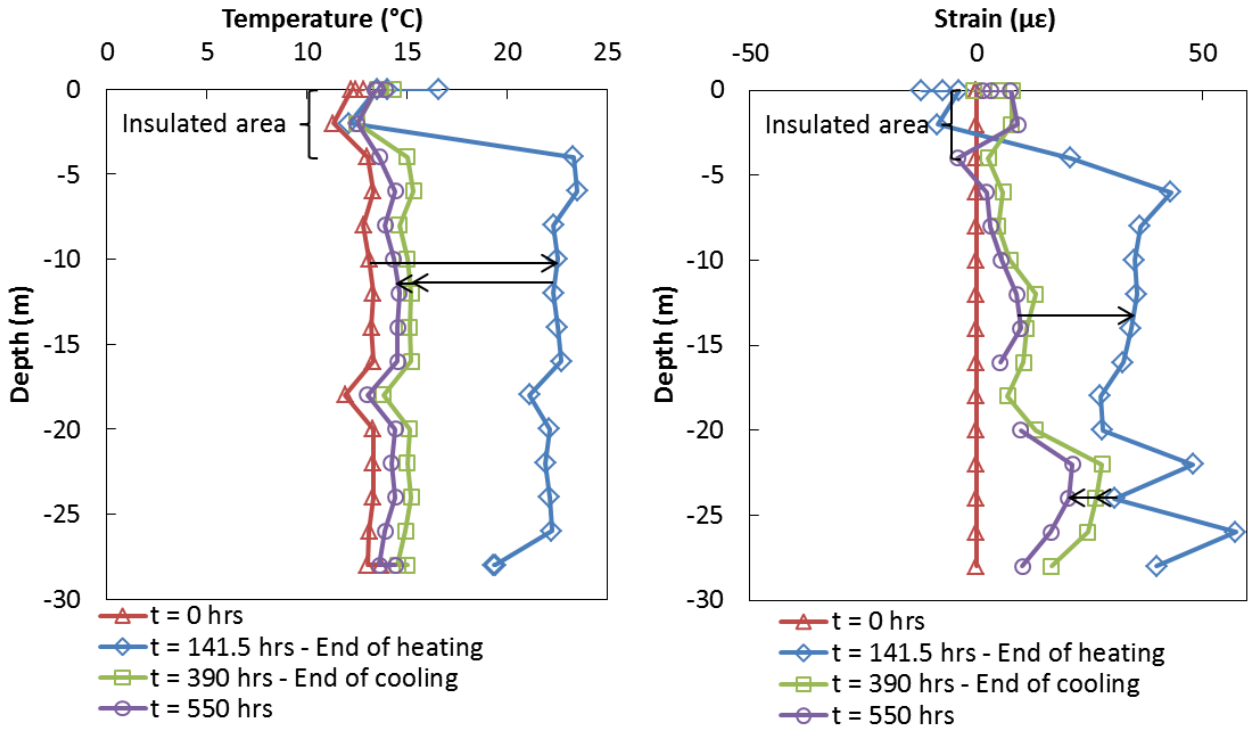

Figure 7:38 Evolution of the temperature (left) and thermal strain (right) profiles along pile #3 during the group test

Thermal expansion up to 50 με was observed within the sandstone. The pile experienced little compression at its top which indicated that its load would have been slightly increased (Figure 7:38). As a result, the maximum pile top heave reached 0.87 mm (Figure 7:37) ant the pile tip compression increased by 517.5 kPa (Figure 7:41).

7.4.3.4 Group test – pile #4

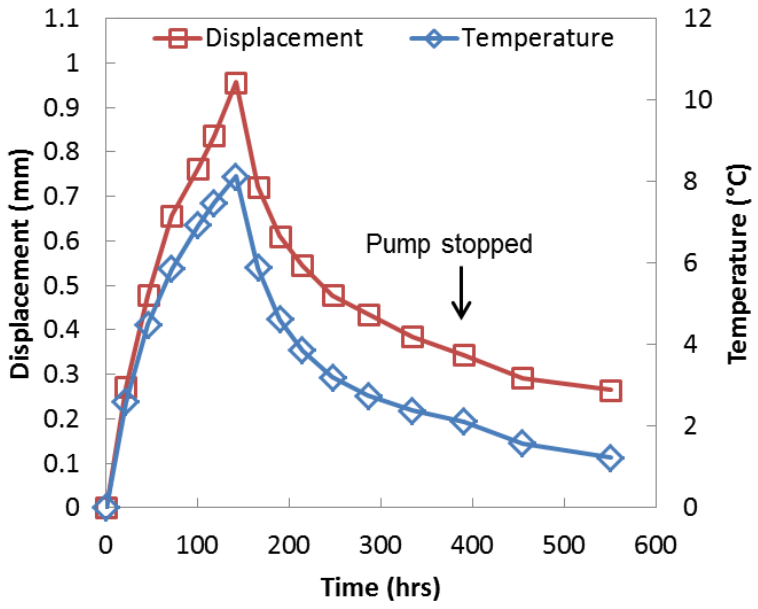

Figure 7:39 Maximum pile #4 top displacements and temperature variation during the group test

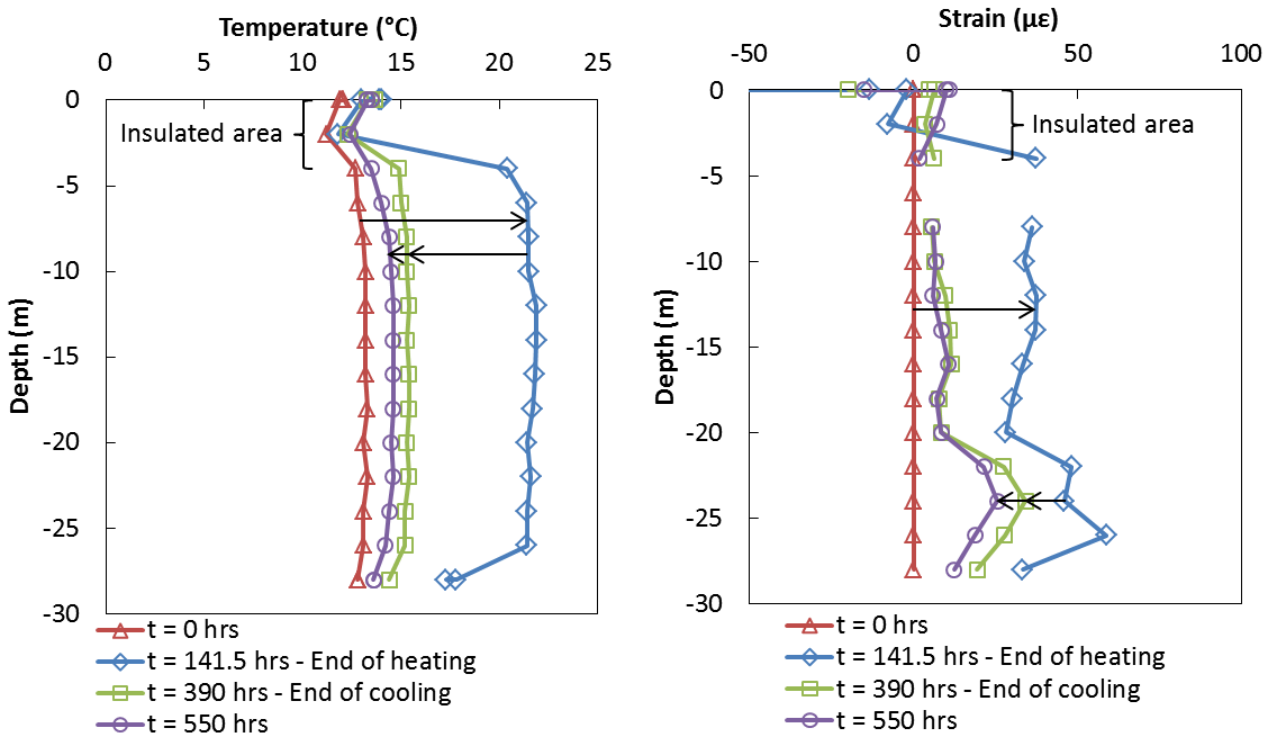

Figure 7:40 Evolution of the temperature (left) and thermal strain (right) profiles along pile #4 during the group test

Pile #4 experienced a temperature increase of 8.1 °C during the group test. This induced expansive strains between 30 and 40 με within the soft soil layers and of 50 με within the sandstone. Light compression was observed at the pile top indicating that its load might have been slightly increased (Figure 7:40). The pile expansion induced a maximum pile top heave of 0.96 mm (Figure 7:39) and a pile tip compression of 321 kPa (Figure 7:41).

7.4.3.5 Pile tip compressions

In order to get rid of the differences in pile temperatures for comparisons, we computed the stress rate as the ratio between the maximum pile tip compression and the maximum temperature increase. This evidences that piles #1 and #3 are the most affected during the group test with tip compression increases greater than 500 kPa, while piles #2 and #4 experienced tip compressions of 254 and 321 kPa, respectively (Figure 7:41).

7.4.3.6 Evolution of the degree of freedom

The profiles of degree of freedom from the "free head" test, the single tests and the group test are compared in Figure 7:42. As reported in Section 7.4.2.5, the construction of the water retention tank on top of the piles restrained the first 20 m of the piles, down to the sandstone bedrock, while the position of the piles below the tank slightly influenced the first 10 m of the piles. Group effects, in contrast, relieve the constraints applied to the piles as the entire group heaves under heating, reducing differential settlements and consequently pile-to-pile interactions.

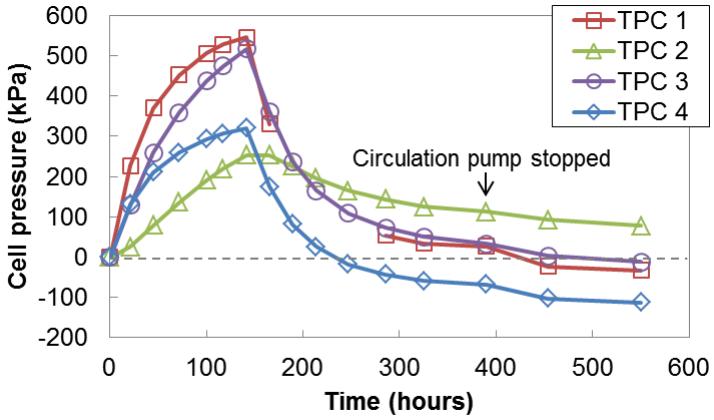

Figure 7:41 Evolution of the pile tip compressions during the group test

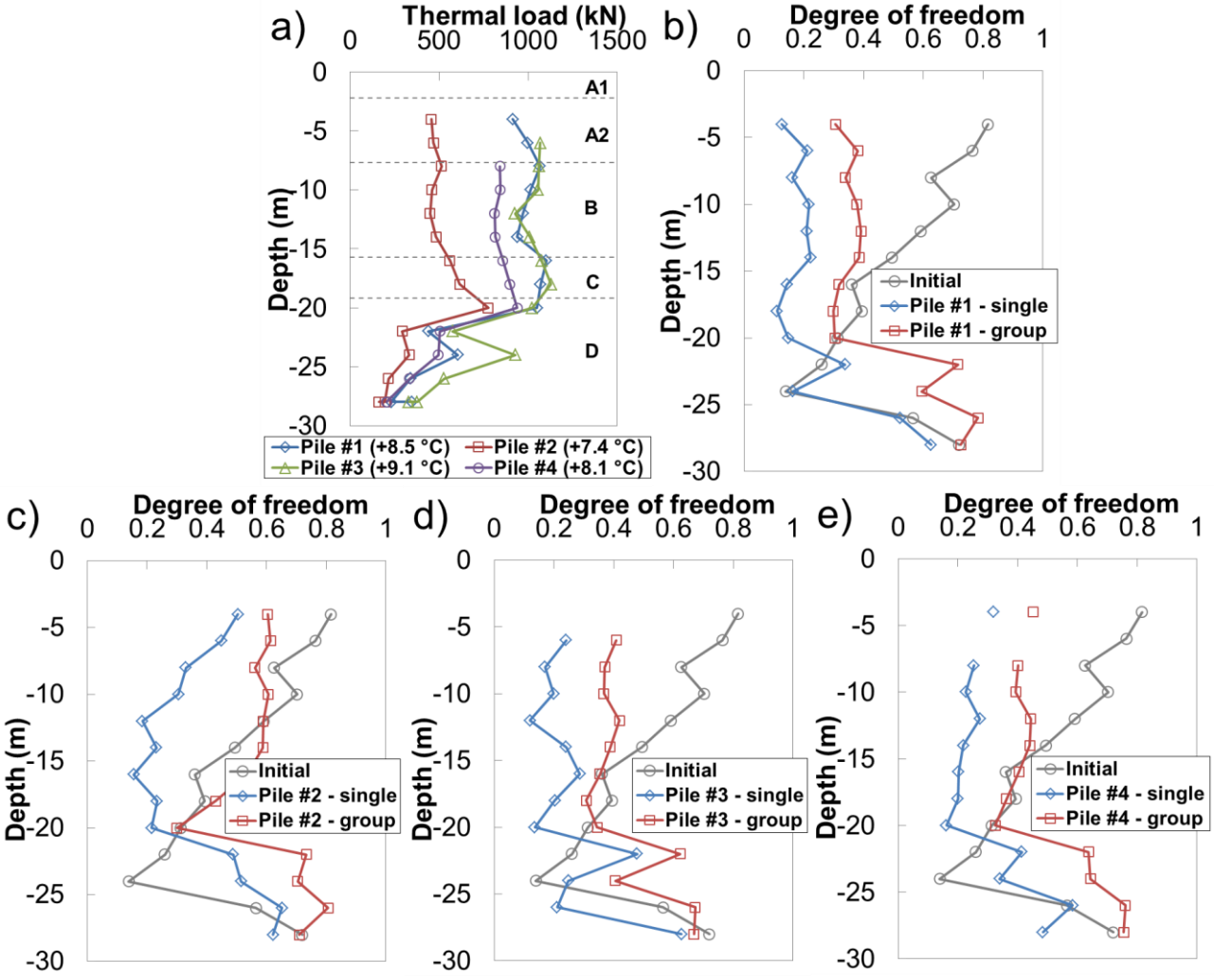

Figure 7:42 (a) Thermal loads during the group test and (b, c, d, e) evolution of the degree of freedom profiles from the free head (initial) configuration to the group heating test

This impact is seen along the entire thermoactive parts of the piles, where the degree of freedom is increased by about 0.2, doubling this quantity. As a result, internal thermal efforts are reduced (Figure 7:42a) while pile top heaves are increased.

7.4.4 Conclusions

Comparing the "free head" test to the single tests have evidenced that the tank construction affects the thermomechanical response of the piles down to -20 m which corresponds to the stiff bottom moraine and sandstone layers. Furthermore, single tests have shown that the position of the pile below the raft influences the thermomechanical response of the piles down to -10 m. Then, the group test allowed observing how group effects relieve the constraints acting on the piles. When heating the entire group, the degree of freedom of the piles was doubled, which increased the absolute pile top heaves but reduced differential settlements, therefore reducing the internal thermal efforts (Table 7:3 and Table 7:4). The impact of group effects is observed along all the piles, from pile top to pile tip which is confirmed by comparing pile tip compressions recorded during single tests and the group test (Table 7:5 and Table 7:6). Strain profiles along the piles show systematic increase in axial strains within the stiff soil layers (i.e. bottom moraine and sandstone) despite temperature profiles evidence a homogenous temperature along the thermoactive parts of the piles. This feature is discussed in Section 7.6.2.

Table 7:3 Maximum displacements at the pile tops and temperature during single tests 1, 2, 3 and 4

	Pile #1	Pile #2	Pile #3	Pile #4
Max. disp. (mm)	0.36	0.84	0.51	0.39
Max. therm. load (kN)	1335.6	1265.5	1543.4	983.1
Max. temp. increase (°C)	8.5	9.3	10	6.5

Table 7:4 Maximum displacements at the pile tops and temperature during the group test

	Pile #1	Pile #2	Pile #3	Pile #4
Max. disp. (mm)	0.88	1.1	0.87	0.96
Max. therm. load (kN)	1100.9	775.6	1128.0	938.1
Max. temp. increase (°C)	8.5	7.4	9.1	8.1

Table 7:5 Maximum pile tip compression during single tests

	Pile #1	Pile #2	Pile #3	Pile #4
Max. tip comp. (kPa)	610	367	597	291
Max. temp. increase (°C)	8.5	9.3	10	6.5
Tip comp. rate (kPa/°C)	71.8	39.5	59.7	44.8

Table 7:6 Maximal pile tip compressions during the group test

	Pile #1	Pile #2	Pile #3	Pile #4
Max. compression (kPa)	546	254	517	321
Max. temp. increase (°C)	8.5	7.4	9.1	8.1
Tip comp. rate (kPa/°C)	64.2	34.3	56.8	39.6

7.5 Thermal response of the pile group

This section is dedicated to the thermal response of the energy piles during the tests. First the measurements from the thermal response test module are analysed and used to estimate the ground thermal diffusivity. Then, the heat propagation into the ground is investigated with the equipped boreholes in between the piles.

7.5.1 Thermal response test

7.5.1.1 Raw test outputs

The procedure adopted for the heating of the piles is similar to conventional thermal response tests on geothermal boreholes. The first phase consists in circulating the heat carrier fluid inside the absorber pipes without any heating for half a day or a night. Then, a constant heat rate is injected (between 1 and 3 kW) for a period of about 7 days (Figure 7:43a). Finally, the heat rate is decreased to zero and passive cooling occurs (Figure 7:43b).

The passive cooling is achieved with the circulation pump ON so that pile temperature remains relatively homogeneous which is better for investigating the thermomechanical responses of the piles. A pressure valve protects the heating module from overpressures. Because the heat carrier fluid expands during heating, there are some discharges/leakages happening resulting in a relatively constant heat carrier fluid pressure (around 2.5 bar) during this phase.

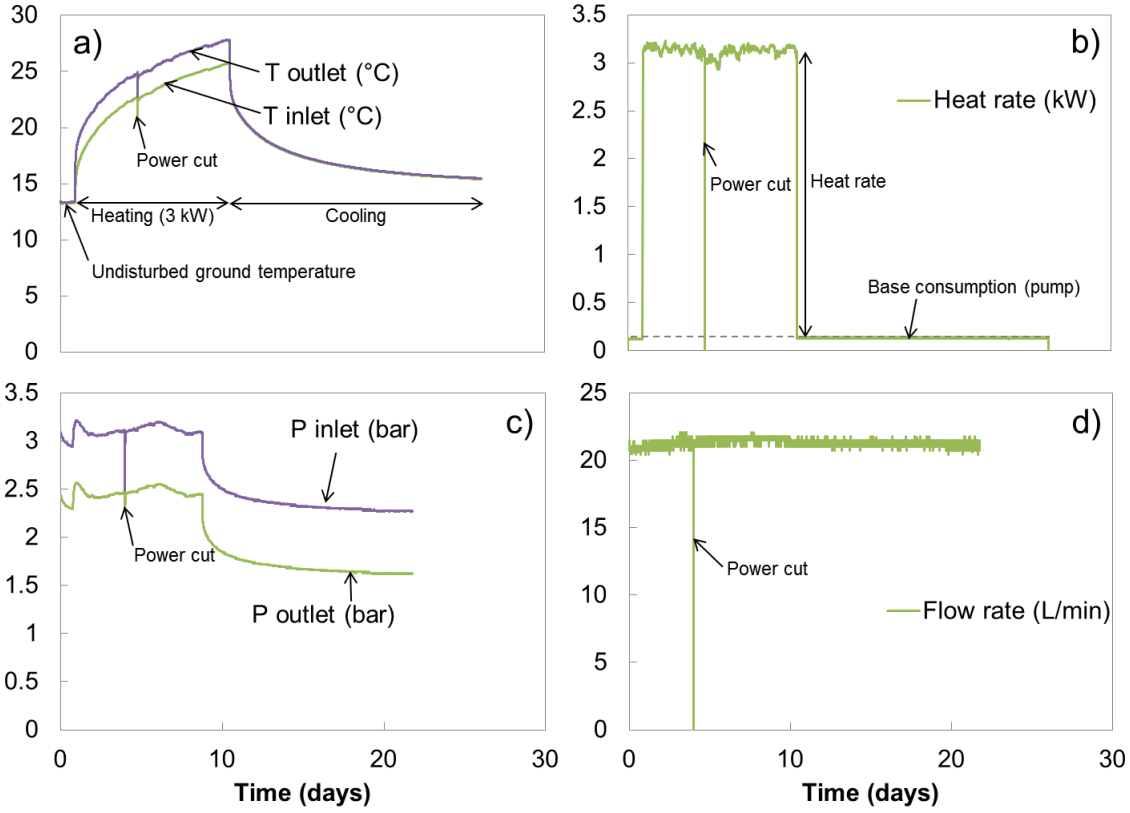

Figure 7:43 Measurements from the mini-module: (a) inlet and outlet temperature, (b) electrical consumption of the module, (c) inlet and outlet pressures and (d) flow rate during the single test on pile #2

Then, the heat carrier fluid pressure decreases during the cooling phase because of thermal contraction and the heat carrier fluid pressure drops down to 1.5 bar Figure 7:43c. The difference between the inlet and outlet pressures is around 1 bar which induces a flow rate of about 21 L/min (Figure 7:43d). The heat rate fluctuates around 3 kW when removing the base consumption linked to the circulation pump.

7.5.1.2 Method of analysis

The present analyses are based on the line source theory. This theory was found to be adequate by Brettman and Amis (2011) who analysed TRTs carried out on auger pressure grouted piles, 300 and 450 mm in diameter and 16.8 m in length, i.e. aspect ratios of 56 and 37, respectively. Furthermore, Hemmingway and Long (2013) found good agreement between the results based on the line source theory and the Geothermal Properties Measurement model which increased the confidence in the applicability of the line source theory to energy piles. However, Bouazza et al. (2013) have compared results from TRTs carried out on a 600 mm diameter piles and using different test durations (9 and 52 days of heating), to TRTs on geothermal boreholes and laboratory tests on samples. They found that the estimated thermal conductivity based on the energy pile tests were higher than the others. Finally, Loveridge et al. (2014a; 2014b) highlighted the weaknesses of the infinite line source model when considering piles with low aspect ratios and proposed a method based on G-functions for the concrete and the ground.

But, despite the attempts to carry out successful analyses of TRTs on energy piles, one may think of how relevant this is. Indeed, carrying TRTs on piles might not be that relevant in practice for two main reasons:

- The piles are designed before they are built so that it is useful to know the thermal conductivity of the ground before pile installation and not after. Cases where TRTs on piles could be achieved are construction sites where pile load tests are carried out, the tested piles being equipped with absorber pipes
- This *in situ* characterisation using energy piles might happen too late for pre-project studies and design which generally utilise representative values or estimates from conventional TRT tests using geothermal boreholes

Finally, energy piles are more likely to undergo intermittent (i.e. hourly to daily) operations (Bonvin and Cordier, 2002) and may mobilise transient thermal conductivity and thermal resistance.

Therefore, TRTs on energy piles should mainly be used to derive a characteristic value representing the energy pile system because an efficient method already exists to determine the thermal conductivity of the ground (i.e. TRTs). This characteristic value could be used for post-construction adjustments and/or checks. The question of costs is not that relevant as the price of a conventional TRT compared to costs considered in projects that can involve energy piles is almost insignificant.

The analysis of TRTs uses Equation 7:14 to first estimate the effective thermal conductivity along the “steady-state” portion of the test which is linearly dependent on the natural logarithm of the time.

$$T_f(t) - T_g = \frac{q_c}{4\pi\lambda_{eff}} \ln(t) + q_c \left[R_b + \frac{1}{4\pi\lambda_{eff}} \left(\ln\left(\frac{4D_T}{r_b^2} \right) - \gamma \right) \right]$$

$$T_f(t) = \frac{T_{in}(t) + T_{out}(t)}{2}$$

Equation 7:14 Line source model describing the evolution of the borehole temperature anomaly in time

where T_{in} and T_{out} are the inlet and outlet temperatures of the ground heat exchanger, q_c is the linear heat rate (in W/m), R_b is the heat exchanger thermal resistance (in K/(W/m)), r_b is the heat exchanger radius, D_T is the soil thermal diffusivity and γ is the Euler constant (= 0.5772).

Loveridge et al. (2014a) suggest to keep the dimensionless testing time τ_0 (Equation 7:15) below 10 in order to limit the impact of end effects while the validity of Equation 7:14 requires at least a dimensionless time equal to 5 to get an error less than 10 % (Hellstrom, 1991).

$$\tau_0 = \frac{D_T}{r_b^2} t$$

Equation 7:15 Dimensionless time for TRT analysis

Therefore, a linear regression is achieved (Figure 7:44) and the effective thermal conductivity is retrieve using Equation 7:16.

$$T_f(t) - T_g = a_\lambda \ln(t) + b_\lambda$$

$$\lambda_{eff} = \frac{q_c}{4\pi a_\lambda}$$

Equation 7:16 Determination of the effective thermal conductivity from TRTs

Then, one can estimate the thermal resistance inverting Equation 7:14 and assuming a soil heat capacity C_{soil}, the thermal diffusivity D_T of the soil being estimated using Equation 7:17. The soil heat capacity is taken equal to 2.5 MJ/K/m^3 in the present analyses (Mattsson et al., 2008).

$$D_T = \frac{\lambda_{eff}}{C}$$

Equation 7:17 Thermal diffusivity determination from TRTs

The line source theory was directly applied ("Not corrected" values in Table 7:8 and Table 7:9) and also accounting for capacitive effects of the pile materials ("Corrected" values in Table 7:8 and Table 7:9) (Pahud, 1999). This concept consists in reducing the heat rate effectively transmitted to the ground through the heat exchanger pile shaft because a part of it is used to increase the pile temperature. The assumption is that despite the pile is not at the same temperature as the heat carrier fluid, its temperature increases with the same rate when the "steady-state" is reached. As a result, we can estimate the stored portion of the injected heat rate.

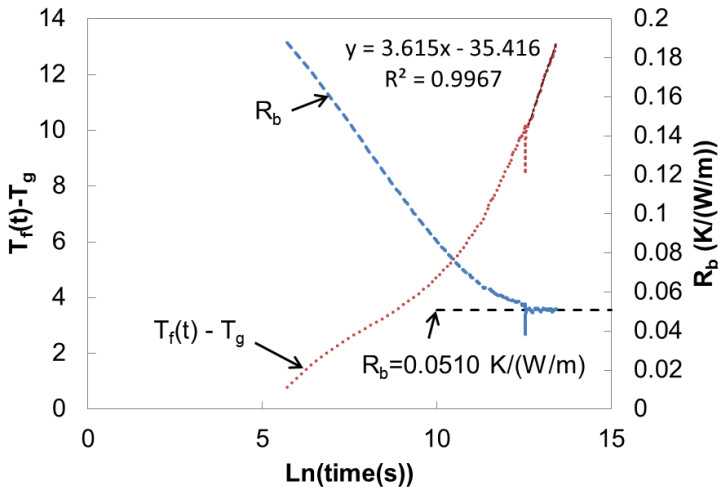

Figure 7:44 Evolution of pile #2 temperature anomaly and thermal resistance during the tests "single pile"

At first, we neglect the contribution of the pipe walls and consider the storage in the heat carrier fluid and pile concrete. The volume of heat carrier fluid inside the pile is assumed to be equal to the inner volume of pipes and the volume of concrete is equal to the volume of the pile cylinder, neglecting the volume of reinforcing cage and absorber pipes. The total heat capacity of the heat exchanger, C_{GHE}, is therefore estimated from (see parameters in Table 7:7):

$$C_{GHE} = V_c \rho_c c_c + V_f \rho_f c_f$$

Equation 7:18 Total ground heat exchanger heat capacity

Table 7:7 Thermal properties of concrete and water

	Specific heat (J/K/kg)	Density (kg/m^3)
Heat carrier fluid (water)	4186	1000
Concrete	2500	880

Next, the rate of temperature increase is determined from the evolution of the mean heat carrier fluid temperature. This is achieved over the same period of time as the one selected for the determination of the effective thermal conductivity. The absorbed heat rate, Q_{abs} (Equation 7:19), is finally subtracted from the injected heat rate before applying the line source model.

$$Q_{abs} = \frac{\Delta T_{AB}}{\Delta t_{AB}} C_{GHE}$$

$$q_c = \frac{Q_{th} - Q_{abs}}{H}$$

Equation 7:19 Correction of the linear heat rate accounting for capacitive effects

where Q_{th} is the heat rate applied by the heating module and H it the heat exchanger depth. Values of estimated effective thermal conductivity and thermal resistance with and without accounting for

capacitive effects are given in Table 7:8 and Table 7:9, respectively. The different graphs used during these analyses, whose an example is given in Figure 7:44, are given in Appendix 9.5.9.

7.5.1.3 Estimated effective thermal conductivities and thermal resistances

The different thermomechanical response tests carried out on the piles were used to investigate the thermal response of the energy piles. The free head test used a heat rate of 1 kW during the first days and then 2 kW. For this test, only the first heating phase with 1 kW was studied. Single tests were carried out using heat rates between 2.7 and 3 kW and the group test used 3 kW on piles #1 and #4 and 6 kW on piles #2 and #3 connected in series. The testing period varied between 55.6 and 197 hrs, mainly driven by the temperature increase observed in the piles for the thermomechanical tests.

Effective thermal conductivity estimates corrected and not corrected for the pile capacitive effects are reported in Table 7:8. Analyses accounting for the pile capacitive effects provide lower thermal conductivities, between 2.16 and 3.06 W/m/K, than not corrected values, between 2.38 and 3.30 W/m/K. The pile thermal resistance is also greater when considering the pile capacitive effects, between 0.0414 and 0.610 K/(W/m), than when not considering them, between 0.0348 and 0.0537 K/(W/m) (Table 7:9). In comparison, Anstett et al. (2005) estimated the thermal resistance of a 100 mm diameter pile with 4 U-loop placed 10 cm away from the pile shaft to about 0.058 K/(W/m), which is consistent with the estimates considering the pile capacitive effects.

Furthermore, the pile aspect ratio is equal to 24/0.9 = 26.7. Therefore, the deviation of the line source model might remain small for a dimensionless times $\tau_0 > 1$ (see Figure 4 in Sass and Lehr (2011)), which corresponds to approximatively 2.34 days of heating (Equation 7:15 using the pile radius of 0.45 m and a soil thermal diffusivity of 10^{-6} m^2/s).

Table 7:8 Estimated effective thermal conductivity from the different tests in W/(m·K)

	Free head	Single tests			Group tests		
		Pile #1	Pile #2	Pile #4	Pile #1	Piles #2/3	Pile #4
Corrected	2.68	2.16	2.51	3.06	2.69	2.87	2.69
Not corrected	3.30	2.38	2.75	3.32	3.06	3.13	2.97
Heating (hrs)	55.6	197	192	115	141.5	141.5	141.5
Heat rate (kW)	1	2.7	3	2.7	3	6	3

Table 7:9 Estimated pile thermal resistance in K/(W/m)

	Free head	Single tests			Group tests		
		Pile #1	Pile #2	Pile #4	Pile #1	Piles #2/3	Pile #4
Corrected	0.0581	0.0414	0.0510	0.0521	0.0570	0.0610	0.0548
Not corrected	0.0422	0.0348	0.0439	0.0460	0.0492	0.0537	0.0471

However, these results were not obtained on tests that lasted enough time to get a dimensionless time $\tau_0 > 5$ (i.e. 12 days assuming a thermal diffusivity of the soil equal to 10^{-6} m^2/s) which is the TRT standard. We therefore decided to run a 24 days long test which satisfies this condition as well as $\tau_0 < 10$ (i.e. 24 days) as suggested by Loveridge et al. (2014a). This test was carried out on pile #3 from July 18th 2014 to August 12th 2014 with a heat rate of 3 kW.

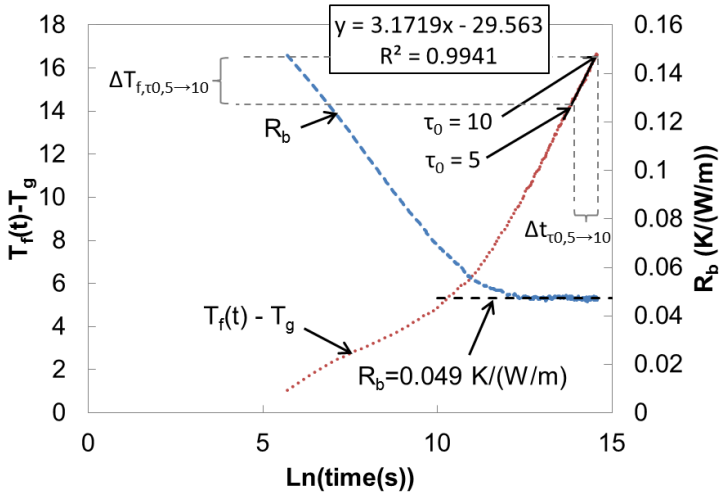

Figure 7:45 Long thermal response test on pile #3

The thermal conductivity estimated using a linear regression between $\tau_0 = 5$ (i.e. 11.7 days) and $\tau_0 = 10$ (i.e. 23.4 days) is equal to 3.06 W/(m·K) considering capacitive effects and 3.14 W/(m·K) without considering them.

The thermal resistance is estimated to 0.049 K/(W/m) considering capacitive effects and 0.048 K/(W/m) without (Figure 7:45). It is therefore interesting to note that estimated properties do not differ a lot considering capacitive effects or not, which may indicate that a steady state is almost reached.

In conclusion, the retrieved bulk thermal conductivity of the ground is around 3.1 W/(m·K) and the thermal resistance of the pile is approximately 0.048 K/(W/m).

7.5.2 Thermohydraulic response of the soil

The thermohydraulic response of the soil around the test piles was monitored during the "free head" test, the group test and the long TRT on pile #3. The observations consisted in measuring the pore water pressure and temperature profiles along the P+T 1 and P+T 2 boreholes. These boreholes are between piles #1 and #2, and piles #2 and #4, respectively (Appendix 9.5.2).

The pore water pressure profiles observed during the "free head" test exhibit a clear deviation from the hydrostatic gradient, suggesting that the drilling operations may have significantly impacted the soft soil layers down to -16 m. However, no thermal effect on pore water pressure was visible during this test (Figure 7:46a) despite temperature increased by approximatively 1.5 °C half a meter away from pile #1 shaft, along P+T 1 (Figure 7:46b). The temperature variation did not reach P+T 2 (Figure 7:46c).

Pore water pressure observed during the group test shows a better agreement with the hydrostatic gradient (Figure 7:47a). A temperature increase up to 3.5-4 °C observed along P+T 1 (Figure 7:47c) induced no significant pore water pressure variation at -9 m and an increase of 4.6 kPa at -16.3 m (Figure 7:47b). Temperature measurements along P+T 2 were not stable during this test and therefore no pore water pressure estimate could be achieved because of poor temperature correction.

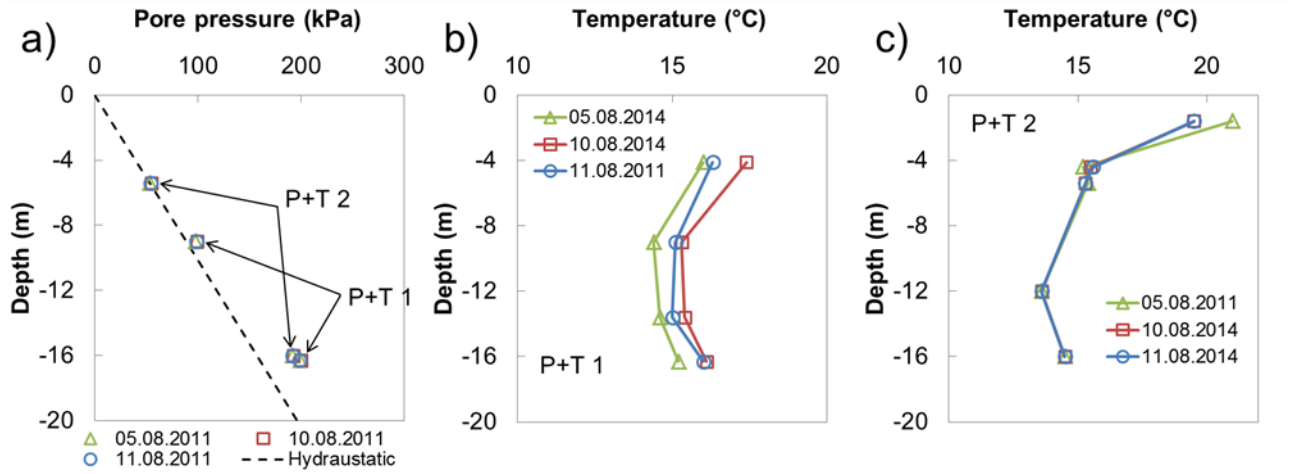

Figure 7:46 (a) Profiles of pore water pressure and temperature along (b) P+T1 and (c) P+T2 during the "free head" test

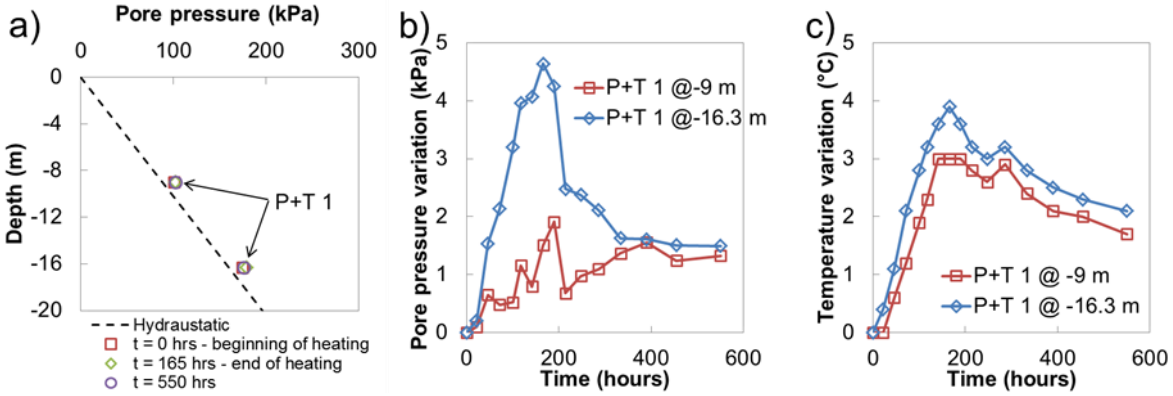

Figure 7:47 Evolution of (a) pore water pressure profile, (b) pore water pressure in time and (c) temperature along P+T 1 during the group test

No variation in soil temperature or in pore water pressure was observed along P+T 1 during the long TRT of pile #3. This indicates that even after 24 days of continuous heating with a heat rate of 125 W/m, the temperature variations induced in pile # 3 did not propagate farther than 3 m.

In conclusion, heat transport is observed within the ground along distances of the order of magnitude of half a meter, suggesting that the main heat storage occurs in the large diameter piles. Despite temperature variations up to 4 °C, pore water pressure is only slightly affected and a near hydrostatic pore water pressure profile is observed.

7.5.3 Conclusion

The thermal response of the piles was investigated using a conventional thermal response test analysis method. A procedure to account for capacitive effects of the large diameter piles was also proposed and evaluated. The length of the test is found to have a significant impact on the estimated soil thermal conductivity and pile thermal resistance. A long thermal response test was therefore carried out during 24 days on a test pile. The ground thermal conductivity and pile thermal resistance were estimated to 3.1 W/(m·K) and 0.048 K/(W/m), respectively.

The thermohydraulic response of the soil in between the piles was monitored using vibrating wire piezometers. Despite temperature variations of 3.5-4 °C were measured half a meter away from the heated pile shafts, no deviation from the hydrostatic profile was observed, suggesting that the ground permeability is high enough to prevent excess pore water pressure from building up.

7.6 Discussions

7.6.1 On the determination of the degree of freedom

The method used to estimate the degree of freedom is based on linear regressions. Therefore, the hysteretic behaviours that could be observed as well as the irreversible strains caused by the elastoplastic response of the soil could affect the accuracy of these estimates. We computed the coefficient of determination along each pile in order to discuss the confidence in the estimated degrees of freedom. We can clearly see that the parts of the piles embedded within the sandstone experience hysteretic responses and/or irreversible strains which are not well represented using linear regressions. Thus, estimates with very low coefficient of determination, i.e. lower than 0.7, are not relevant and estimates with relatively low coefficient of determination, i.e. between 0.7 and 0.8, have greater error. However, portions of the piles above the sandstone exhibit good linear trends (see Table 7:10). Therefore, the scatter observed at -22 and -24 m in the profiles of degree of freedom is associated with this issue.

Table 7:10 Coefficient of determination of the degree of freedom in the different tests

Depth (m)	Free head Pile #1	Single tests				Group test			
		Pile #1	Pile #2	Pile #3	Pile #4	Pile #1	Pile #2	Pile #3	Pile #4
4	0.97	0.81	0.99		0.99	0.88	1.00	-	0.98
6	1.00	0.96	0.99	0.94	0.98	0.96	0.99	0.99	-
8	0.99	0.99	1.00	0.94	0.96	0.98	0.99	0.99	0.97
10	1.00	0.99	1.00	0.97	0.99	0.99	0.99	1.00	0.99
12	0.98	1.00	0.97	0.91	0.98	0.99	0.99	0.98	0.99
14	0.90	0.98	0.98	0.98	0.97	0.98	0.98	0.99	0.99
16	0.81	0.99	0.96	0.78	0.99	0.98	0.99	0.99	0.98
18	0.91	0.98	0.96	0.94	0.98	0.99	0.95	0.98	0.99
20	0.91	0.90	0.92	0.93	0.98	0.98	0.98	0.87	0.97
22	0.63	0.75	0.83	0.81	0.95	0.39	0.51	0.66	0.71
24	0.73	0.75	0.74	0.57	0.82	0.46	0.52	0.25	0.45
26	0.86	0.91	0.89	0.92	0.97	0.69	0.73	0.84	0.84
28	1.00	1.00	0.87	0.97	0.99	0.99	0.80	0.93	0.84

7.6.2 Do blocked radial thermal strains explain the increased axial thermal expansion within the parts of the piles embedded within the bedrock?

The impact of blocked radial thermal strains has been discussed in Section 3.6.1 and it has been shown that the axial thermal expansion can increase by 50 % when radial strains are prohibited. Furthermore, the experimental observations have shown that no radial thermal strains occur along the parts of the piles embedded within the sandstone as well as axial strains are greater in this pile portions. We therefore modified the analyses and used an axial thermal expansion of 15 με/°C instead of 10 με/°C along the lower part of the pile (for measurements at points -20, -22, -24, -26

and -28 m). Comparisons of the profiles are given in Figure 7:49. This correction seems to straighten the profiles, which seems more consistent with the stratigraphy on site.

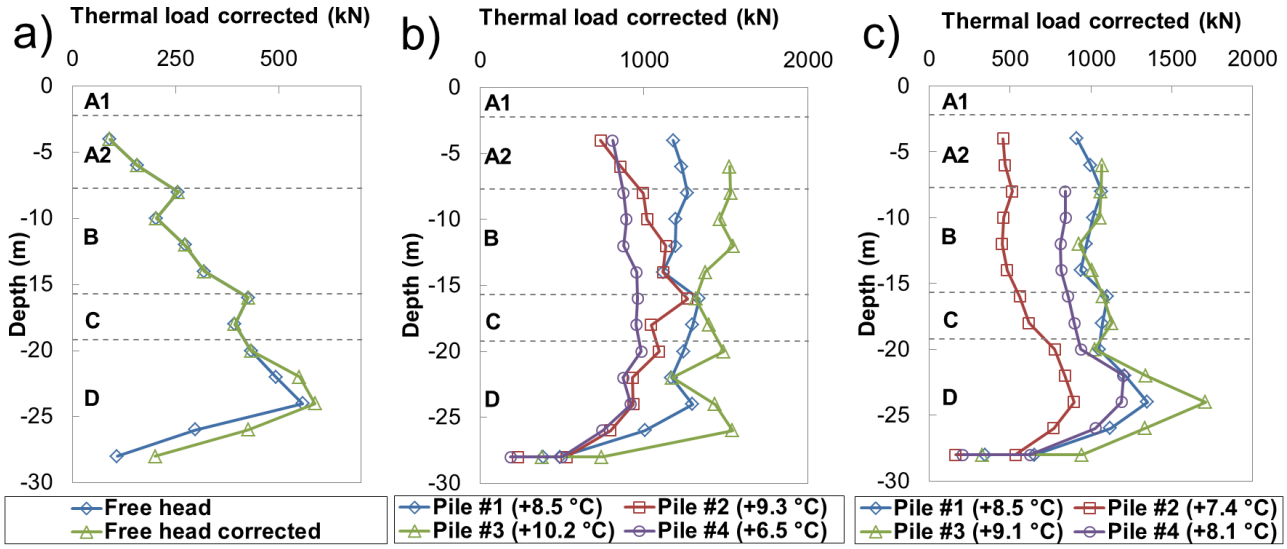

Figure 7:48 Profiles of internal thermal load using the corrected degree of freedom for the (a) "free head" test, (b) the single tests and (c) the group test

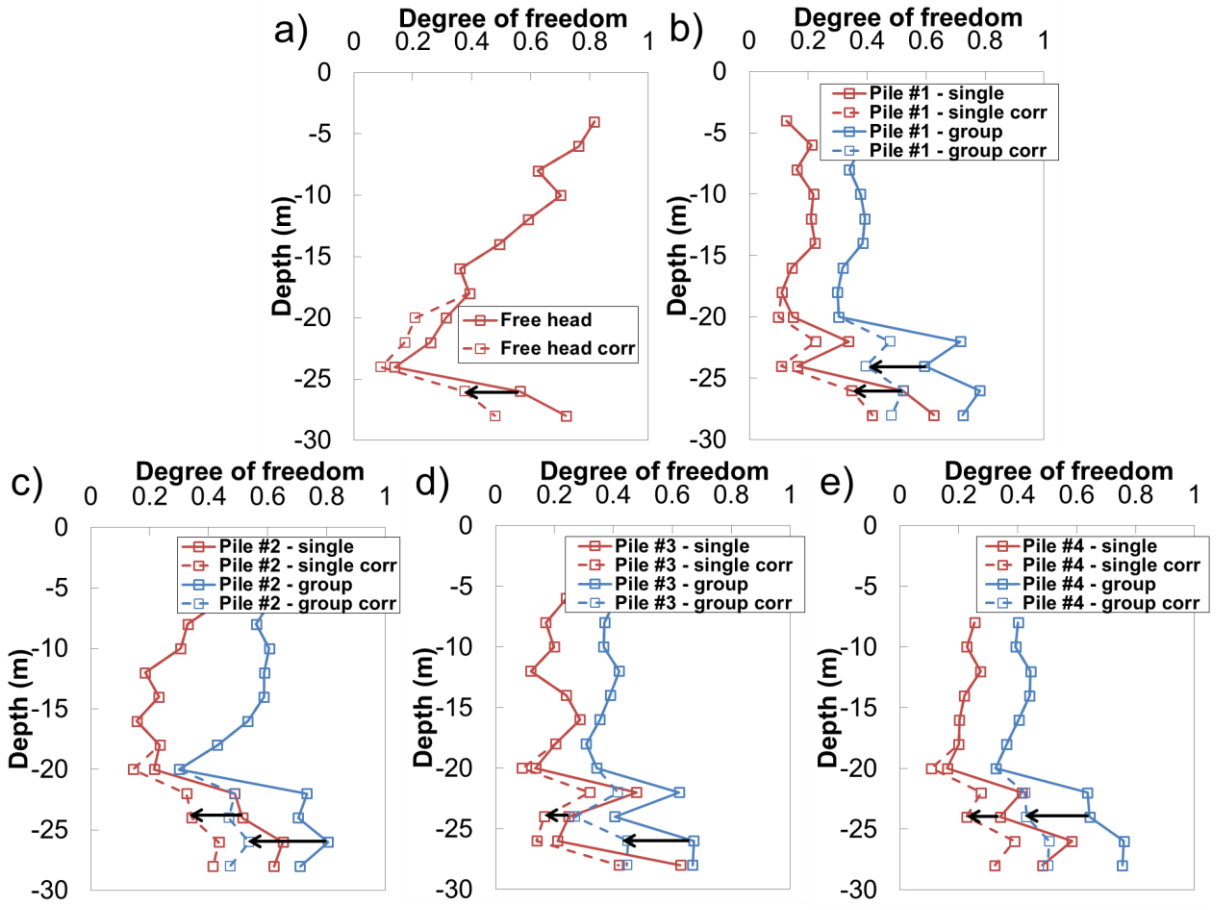

Figure 7:49 Comparison of the profiles of degree of freedom with (dashed line) and without (solid line) the correction for radial strains

The discussion carried out on the radial strains and the mobilizable axial/radial thermal expansions, in Section 3.6.1, may explain a part of the high degree of freedom observed in the lower part of the piles embedded within the molasse. Indeed, strong soil layers may block the radial strains, increasing the axial thermal expansion by 50 %. Therefore, based on the observations of radial strains (see Section 7.4.3.1) which suggest that the sandstone prevents radial strains, we compared the profiles deduced using the linear thermal expansion of 10^{-5} °C^{-1} (free radial thermal strains) and the modified one accounting for the blocked radial strains, $1.5x10^{-5}$ °C$^{-1.}$ The significant increase in degree of freedom observed at the pile tips is significantly reduced when considering that the radial strains are blocked (Figure 7:49). This modification increases the internal thermal efforts along the pile portion embedded within the sandstone (Figure 7:48).

In conclusion, axial and radial strains are closely linked along energy piles when crossing strong soil layers. However, engineering practice may not recommend embedding such a long portion of pile within stiff soil layers, but only a couple of times the pile diameter in order to prevent pile tilting.

7.7 Concluding remarks

This Chapter presented the results from full-scale *in situ* experiments carried out on a group of 4 energy piles. First, pile #1 was tested without any structure on top of it during the "free head" test. This provided information about the ground constraints acting on the piles. The results of the test on pile #1 were generalised to the three other test piles. Then, single tests were achieved once the water retention tank was built. These tests characterised the single thermomechanical response of each pile. It was observed that the tank construction impacts the pile response down to the stiff soil layers while the position of the piles below the raft (i.e. below a corner for the pile #2, an edge for piles #3 and #4 or in the middle of the raft for pile #1) influences only the first 10 meters of the piles. Furthermore, insulating the first 4 m of the test piles allowed observing the load redistribution within the pile group. Pile-to-pile interactions were observed as the heated pile pulled on the adjacent piles, from pile tops (expansive strains) to pile tips (base compression relieves). During the single tests, heated piles exhibited maximum heaves around 0.5 mm and maximum thermal internal efforts of 1500 kN. Finally, the four piles were heated simultaneously. Piles #1 and #4 were heated individually with heat rates of 3 kW while piles #2 and #3 where connected in series to a same heater delivering 6 kW. Comparing the pile responses during the group test with their responses during single tests evidences that group effects are significant. Indeed, heating the group of piles doubled their degrees of freedom, inducing greater thermal strains and therefore greater pile heaves (up to 1 mm) but lower differential settlements and consequently lower internal thermal efforts (up to 1000 kN).

The development of radial thermal strains was investigated using optical fibers deployed around the perimeter of the reinforcing cage in pile #1. It was observed that radial thermal strains are blocked within the stiff soil layers while they can develop in soft layers. As a result, the axial mobilizable thermal expansion may increase by 50 % along the stiff layers and the determination of the degree of freedom should account for it.

Despite the soil layering, the temperature profiles along the piles remained homogeneous during the heating tests. The thermal response of the piles was investigating using a conventional method coupled with a procedure accounting for thermal capacitive effects of large diameter piles. However, the thermomechanical tests were not long enough to reach thermal steady state and a test of 24 days was carried out on pile #3. The retrieved thermal conductivity of the ground is around 3.1 W/(m·K) and the pile thermal resistance is approximately 0.048 K/(W/m).

The thermohydraulic response of the soil in between the pile was monitored using piezometers. Despite temperature variations recorded half a meter away from pile #1 reached 3.5-4°C during the group test, no variation of pore water pressure was observed. This suggests that the soil permeability is high enough to prevent excess pore water pressure from building up under the thermal load applied during the test.

7.8 Acknowledgements

The author thanks Mr. Laurent Gastaldo and Mr. Jean-François Mathier from the Laboratory of Rock Mechanics of the Swiss Federal Institute of Technology Lausanne (Switzerland) who carried the compression tests on concrete samples from the test piles.

Concluding Remarks

Chapter 8 Conclusions

8.1 Thermomechanical response of single energy piles

The impact of radial strains on the axial thermomechanical response of energy piles has been experimentally evidenced on the full-scale *in situ* test. Radial strains were observed in soft soil layers while they were blocked in the sandstone. Furthermore, it was found that axial strains were greater along the portions of the piles where radial strains were entirely blocked compared to portions of piles embedded within soft soil layers. It was then estimated that mobilizable axial thermal expansion may increase by 50 % when radial strains are totally blocked. As a result, a 2 dimensional approach might be more suitable for the analyses. A method based on the *p-y* load transfer curves was therefore proposed to account for these effects in simple design tools.

The impact of cyclic pore water pressure variations on a single energy pile serviceability was investigated using finite element analyses. It was found that pore water pressure may build significantly in soils with very low permeability, reducing the soil-pile effective contact stress and consequently the ultimate bearing resistances. In this case, the bearing mechanisms are driven by the pore water pressure evolution: ultimate pile resistance decreases when heating and increases during cooling. Conversely, pore water pressure may not vary significantly in soils with high permeability and the evolution of the pile bearing resistances is therefore driven by the soil and concrete pile expansions.

8.2 Group effects

Single and group tests carried out on the experimental site of EPFL have shown how significant the group effects are. First, single tests have evidenced that heated piles can pull on the neighbouring piles, inducing effect down to the pile tips. Observed pile head heaves were around 0.5 mm. Then, the group test provided profiles of degree of freedom which where compared to the single tests. This comparison has shown that the degree of freedom doubled when the whole group of pile was heated. As a result, internal thermal efforts were deduced while thermal strains increased. Absolute pile heaves are increased up to 1 mm but differential settlements were reduced which relieved the thermal internal efforts in the piles. Therefore, a simple model coupling the Euler-Bernoulli isostatic beam model to Thermo-Pile was developed to illustrate the capabilities of such a design tool based on the load-transfer method to tackle group effects. This model can be extended to hyperstatic beam cases as well as thin and thick plates or simplified finite element models of rafts.

8.3 Long term performances of energy geostructures

The long term thermal and thermomechanical performances of energy geostructures were numerically investigated.

The impact of thermally induced pore water pressure variations on a single energy pile serviceability was quantified using thermohydromechanical finite element analyses. The pile was subjected to different mechanical loads in different soils. The thermal loading sequence consisted in 40 heating and cooling cycles between -10 and +10 °C. It was observed that small long term accumulation of settlement occurs because of thermal cycles when the soil is permeable enough to prevent pore water pressure increase. However, ultimate bearing resistances of the single energy pile are driven by pore water pressure evolution in soils with very low permeability. Indeed, the

contact effective stress at the soil-pile interface may drastically decrease so that a part of the load carried out through shaft friction is transferred to tip compression with the corresponding settlement. This study nevertheless shows that the design codes used for conventional piles may remain conservative in permeable soils.

Heat production through tunnel anchors and bolts was investigated using thermohydraulic and thermohydromechanical finite element analyses. Two tunnel structures were tested with different characteristics. The cut and cover tunnel was modelled considering the soil-atmosphere thermal interactions as well as unsaturated conditions because of the proximity of the anchors with the soil surface. However, the mechanical implications were neglected because of the buffer effect of the backfill. Conversely, the bored tunnel was assumed to be deep enough to only consider saturated conditions, neglecting the thermal influence of the soil surface while accounting for mechanical implications because of the great confinement of the structure. Pure heat production and seasonal heat storage were optimized on each tunnel structure by maximizing the produced heat while not freezing the soil between the anchors. It was found that seasonal heat storage is necessary to sustain an acceptable production level on the cut and cover tunnel while it is not efficient with the bored tunnel. Extracted heat from the ground ranged from 0.6 to 4.2 GWh per year and per kilometer of tunnel.

8.4 *In situ* estimation of thermal properties of the ground

Thermal properties of the ground are the driving parameters of the thermal design of energy geostructures. These were investigated through full-scale and scaled models of ground heat exchangers.

A method accounting for capacitive effects was presented to interpret thermal response tests carried out on large diameter piles in order to retrieve the ground thermal conductivity. This method considers that a part of the injected heat into the pile test is stored into the concrete, increasing the pile temperature. It assumes that the rate of temperature increase of the concrete is the same as the fluid temperature increase rate. An equivalent heat rate stored into the pile is therefore estimated along the “steady state” portion of the thermal response test and is removed from the injected heat rate during the analysis. However, a long thermal response test carried out over 24 days of heating has shown that the thermomechanical response tests did not last long enough to reach the steady state and therefore underestimate the soil thermal conductivity and overestimate the pile thermal resistances. This long thermal response test gives a soil thermal conductivity of 3.1 W/(m·K) and a pile thermal resistance of 0.048 K/(W/m).

A periodic pumping procedure was tested to estimate the ground thermal diffusivity at the scale of energy geostructures. The potential of this method, inspired from hydraulic engineering, was evaluated at the laboratory scale on a scaled model of heat exchanger borehole embedded within a Bioley silt. The method requires applying a periodic temperature variation in the borehole and recording the temperature variations in the ground. The observed delay between the source and monitoring points in the ground is characteristics for the thermal inertia of the ground while the attenuation is representative for storage and dissipative effects. The test carried out in the study considered a daily temperature variation between -15 and +15 °C. The retrieved thermal diffusivity

on the scaled model is in agreement with values reported in the literature and based on other methods. However, deployment of the method at full-scale was discussed and particular attention should be put in accurately determining the positions of ground thermal probes.

8.5 Perspectives

8.5.1 Industrial perspectives

Energy geostructures are an interesting alternative for the heating and cooling of buildings. Their thermal potential is not to be demonstrated anymore since many significant projects have successfully included these structures (e.g. large buildings, metro stations, railway tunnels, etc.). Design tools for the thermal and thermomechanical aspects exist and are in use in the industry. However, the main design focus is the thermal aspect which is the economic driving factor, the thermomechanical part consisting in validating the pile design based on pile displacements and internal efforts compliance. Therefore, this technology is gaining in confidence despite it is not a current solution proposed for large building projects.

The multidisciplinary design of such structures may bring new interactions between project contractors, such as between the HVAC and geotechnical engineers at an early stage of the project. A reference document, edited by the Ground Source Heat Pump Association in the UK (Ground Source Heat Pump, 2012), may help talking these organization issues.

Promoting this technology using demonstration sites involving both thermomechanical and thermal aspects is of great importance. Indeed, existing pilot sites focused on the thermal performances (e.g. the Dock Midfield, see (Anstett et al., 2005)) while specific thermomechanical aspects were investigated using test piles (e.g. EPFL, Lambeth College). As a result, developing pilot projects monitoring the thermal performances of a global system as well as the thermomechanical response of the energy geostructures involved would bring a global picture of the behaviour of such structures under real service conditions (i.e. intermittent operations) and on the long term. Nevertheless, experimental sites dedicated to the thermomechanical response of energy geostructures may allow investigating extreme temperature conditions considering high temperature seasonal heat storage.

Finally, studies carried out across Switzerland to estimate the geothermal potentials of some Swiss cantons, i.e. Vaud (Wilhelm et al., 2003), Fribourg (Vuataz et al., 2005) and Neuchatel (Vuataz et al., 2008), have shown that energy piles may be in competition with other geothermal resources such as geothermal boreholes or aquifers while requiring more particular conditions such as “weak” soils and large buildings. As a result, proposing the solution of energy piles in the identified areas in priority would greatly improve the promotion of the technology instead of suggesting it in areas where energy piles would be in competition with potentially better (i.e. more efficient and/or more economic) heat sources such as geothermal boreholes and/or aquifers.

8.5.2 Research perspectives

From a research standpoint, some aspects remain weakly investigated such as the *in situ* evolution of the soil-pile interface and pile bearing capacities.

As suggested by Chapter 4, energy piles may be, the most of the time, installed in soils with permeabilities high enough to prevent excessive variations in pore water pressure under reasonable temperature variations. Thus, thermal expansion coefficients of the soil and the concrete might be the driving parameters for the thermomechanical response of energy geostructures. However, *in situ* long term displacements of energy piles are not yet available as the feedbacks on the long term are not yet recorded from test sites. However, one possibility to include the design of energy piles in conventional design practice should be, as suggested by Chapter 4, to estimate the amount of load transferred from shaft friction to tip compression as it is the mechanism inducing long term settlements. From this transferred load, the settlement at the pile tip could be found and therefore the pile settlement could be estimated.

The two-dimensional effects should be better investigated. Indeed, the present work has demonstrated that radial thermal strains may have a significant impact on the axial thermomechanical response of energy piles in particular and energy geostructures in general. The present work presented an a priori method to account for these two-dimensional effects but this could be improved using the thermoelastic response of the pile to accurately quantify the axial and radial mobilizable thermal expansion coefficients.

Cooling was not investigated on the full-scale test site because a lack of cooling machine. This would be a significant improvement for this test site as cooling is expected to induce a reduction in shaft bearing capacity. However, the cooling tests should be achieved at the end of field campaigns as they could induce irreversible pile settlements. Nevertheless, the large margins of safety used for the test piles may also prevent any accumulation of pile settlement as discussed in Chapter 4. Therefore, it is worthwhile testing active cooling on this site.

Large diameter piles remain difficult to test as heat exchanger piles because of inhomogeneity in pile cross-section temperature. It might be useful to get temperature measurements across the pile cross-sections as well as at the pile-soil interface but this remains challenging on real-scale tests.

Table 8:1 Individual and global prices for a virtual global test site with energy piles

	Unit price (CHF)	Number	Total
Pressure cell	800	10	8’000
Strain gauges	200	50-100	10’000 – 20’000
Optical fibers	1000	14-21	14’000 – 21’000
Piezometer	400	10	4’000
Thermistors	150	10	1’500
		Total for instruments (CHF)	37’500 – 54’500

For academic purposes, future constructions including energy piles should/could comprise instrumented energy piles and conventional piles in order to observe the global response of a foundation to real thermal loads. This would not require extensive instrumentation, as an example: a building supported by 100 piles among which 70 are energy piles would require instrumenting maybe 10 % of the energy piles and 10 % of the conventional piles, that is to say 7 energy piles and 3 conventional piles, in different locations. For 20 m long piles, 5 to 10 axial strain gauges plus 2-3 radial optical fibers in the energy piles, depending on the local stratigraphy, plus one pressure cell at

each pile tip would be enough to have a global idea of the foundation thermomechanical response. Thermistors and piezometers could complete the monitoring system. Based on the sensor costs used on the EPFL test site, the cost for providing the sensors for such a site would be around 40'000 – 55'000 CHF (Table 8:1), which remains reasonable compared to the building price. The development of full-scale experimental sites could also be extended to tunnel structures. For example, short portions of cut-and-cover tunnels could be simply equipped with absorber pipes and instrumented using strain gauges, which would provide a first insight in the *in situ* thermomechanical response of such structures which are still marginal but represent a significant potential (Brandl, 2006).

The development of simple design/check tools such as Thermo-Pile would help transferring the technology from punctual use to common acceptance. The software Thermo-Pile could be extended from simply supported beams to hyperstatic thick plates based on the development presented in this thesis. This could help tackling the issues linked to the thermomechanical responses of energy pile groups. Furthermore, long term cyclic effects have been investigated (Pasten and Santamarina, 2014) and degradation models are available (Chin and Poulos, 1991; Shahrour and Rezaie, 1997). At this level, including long term and degradation models as well as group effects would provide an up-to-date tool for the geotechnical design of energy piles.

Finally, a critical design point could be the thermomechanical optimisation of the pile layout, similarly to what can be found for geothermal boreholes with characteristic radiuses of influence. However, this step might be a bit too early in the development process and two different philosophies of design might confront. On one hand, the most straightforward application should consist in taking as much heat as possible from a pile layout which is only based on structural support considerations. On the other hand, the structure of the building could be optimised in such a way that the pile locations are also optimised from a thermal standpoint. This last approach would therefore require that energy piles are considered very early in the project, even at the architectural level. I think that a very first step towards this integrated design of buildings including energy piles should consist in carrying extensive numerical parametric studies using a software such as COMSOL to understand what would be the effect of the number of pipes, concrete cover thickness, heat carrier fluid flow rate and pile aspect ratio on the radius of thermal influence of energy piles. From this extensive study, charts or tables could be used to determine characteristic radiuses of thermal impact for this or that pile, leading to minimal pile to pile distances for thermal optimization if any is to be done. Indeed, piles are generally away from each other of at least 3 times the pile diameter. Therefore, this kind of parametric study would indicate whether thermal optimization is achievable or not.

Chapter 9 Appendix

9.1 Simple cycle of a heat pump

The refrigerant undergoes cyclic adiabatic compression and expansion that can be represented in property diagrams. Among those, we chose to use pressure (P)-enthalpy (H) diagram. This diagram represents three different domains of state of the refrigerant: dry vapour, liquid and vapour-liquid mixture where both phases coexist. These domains are separated by two curves and a point: the bubble point curve delimits the liquid domain from the mixture domain while the dew point curve delimits the vapour domain from the mixture domain; both curves join at the critical point. The bubble curve represent the moment when the first bubble is seen within the liquid while the dew point curve represents the moment when the first droplet of liquid is observed within the vapour (Figure 9:1a). Curves representing the quality of the mixture (i.e. portion of vapour in the mixture) are found within the domain where the mixture exists (x = 0.1, 0.2 …). Obviously, the quality of the mixture is equal to 0 along the bubble point curve and 1 along the dew point curve. Isotherms (i.e. T = constant) are presented across the three domains. Within the mixture domain, the phase changes (i.e. evaporation or condensation) occur at constant temperature; that is to say along isotherms. Isentropic curves (i.e. S = constant) are also provided within the vapour domain as the compression is achieved isentropically (Figure 9:1b). Therefore, the compression phase follows one of these curves.

A typical simple cycle consists in seven phases (see Figure 9:1c):

- **Stage 1:** the refrigerant is vaporized at the contact with the heat source (1 → 2). The thermal contact is ensured through a heat exchanger, conventionally called the evaporator. The heat taken from the heat source is given by:

$$q_{1,2} = (1 - x_1) L_v \left(T_{evap}\right)$$

Equation 9:1 Absorbed heat during evaporation of the refrigerant in the evaporator

where x_1 is the mixture quality at the outlet of the expansion valve, T_{evap} is the temperature at which the evaporation occurs and $L_v(T_{evap})$ is the latent heat of vaporization at the phase change temperature.

- **Stage 2:** the refrigerant is superheated – through a superheater – at constant pressure to ensure that no liquid remains (2 → 3) which could damage the compressor blades. Dry steam is obtained.

- **Stage 3:** the refrigerant is compressed adiabatically (i.e. isentropically), which increases its pressure and temperature (3 → 4). This stage requires the use of Laplace law which links the evolution of temperature and pressure of an ideal gas between a given state a (T_a, P_a) to another state b (T_b, P_b) as:

$$T_a^{\gamma} P_a^{1-\gamma} = T_b^{\gamma} P_b^{1-\gamma}$$

Equation 9:2 Laplace law for ideal gas

where:

$$\gamma = \frac{C_P}{C_V}$$

Equation 9:3 Laplace coefficient for ideal gas

with C_p and C_v the heat capacities at constant pressure and constant volume, respectively. The mechanical work transmitted from the compressor to the refrigerant is given by:

$$W_{3,4} = C_p \left(T_4 - T_3\right)$$

Equation 9:4 Absorbed work by the refrigerant through the compressor

Let ΔP be the increase in refrigerant pressure through the compressor. The temperature of the refrigerant at the outlet of the compressor is therefore given by:

$$T_4 = \left[\frac{P_{evap}}{P_{evap} + \Delta P}\right]^{\frac{1}{\gamma}-1} T_3$$

Equation 9:5 Refrigerant vapour temperature after compression

- **Stage 4:** the refrigerant vapour cools down to the dew point at which pressure it has been compressed (4 → 5). This phase is called desuperheating and some systems use this part to produce hot water. The restituted heat during this stage is given by:

$$q_{4,5} = -C_P \left(T_5 - T_4\right)$$

Equation 9:6 Desuperheating heat

- **Stage 5:** the refrigerant totally condenses as it yields heat to the heat sink through the condenser (5 → 6). The delivered heat to the heat sink during this phase is given by:

$$q_{5,6} = -L_v \left(T_{cond}\right)$$

Equation 9:7 Heat released into the heat sink through the condenser

- **Stage 6:** the liquid refrigerant is slightly over cooled in order to make sure that no vapour remains (6 → 7). The lost heat during this phase is given by:

$$q_{6,7} = -C_P \left(T_7 - T_{cond}\right)$$

Equation 9:8 Heat lost during supercooling

- **Stage 7:** the refrigerant expands adiabatically (i.e. isenthalpically) through the expansion valve and a part of it is vaporized (7 → 1). Assuming that $T_7 \sim T_{cond}$, the final mixture quality is deduced from:

$$\Delta h = 0 = C_{PL}\left(T_{evap} - T_{cond}\right) + x_1.L_v\left(T_{evap}\right) \Rightarrow x_1 = \frac{L_v\left(T_{evap}\right)}{C_{PL}\left(T_{cond} - T_{evap}\right)}$$

Equation 9:9 Mixture quality at the cycle closure

N.B.: positive heat quantities are absorbed by the heat pump while negative heat quantities are restituted to the exterior.

The Coefficient of Performance (CoP) of a HP is given as the ratio between the energy output (i.e. heat at the condenser) and the input (i.e. electricity). CoP of GSHP systems using energy geostructures are around 4 (Brandl, 2006), which means that for four units of extracted heat from the ground (i.e. "free" units) plus one unit provided through the compressor (i.e. paid unit), we get 5 units of energy for heating. However, seasonal application of energy geostructures is more generally characterised using the Seasonal Factor of Performance (SFP) which is equal to the amount of energy produced divided by the amount of consumed energy to produce it. This is generally represented in a Sankey diagram that graphically represents the energy budget of a system with the internal and external energy fluxes.

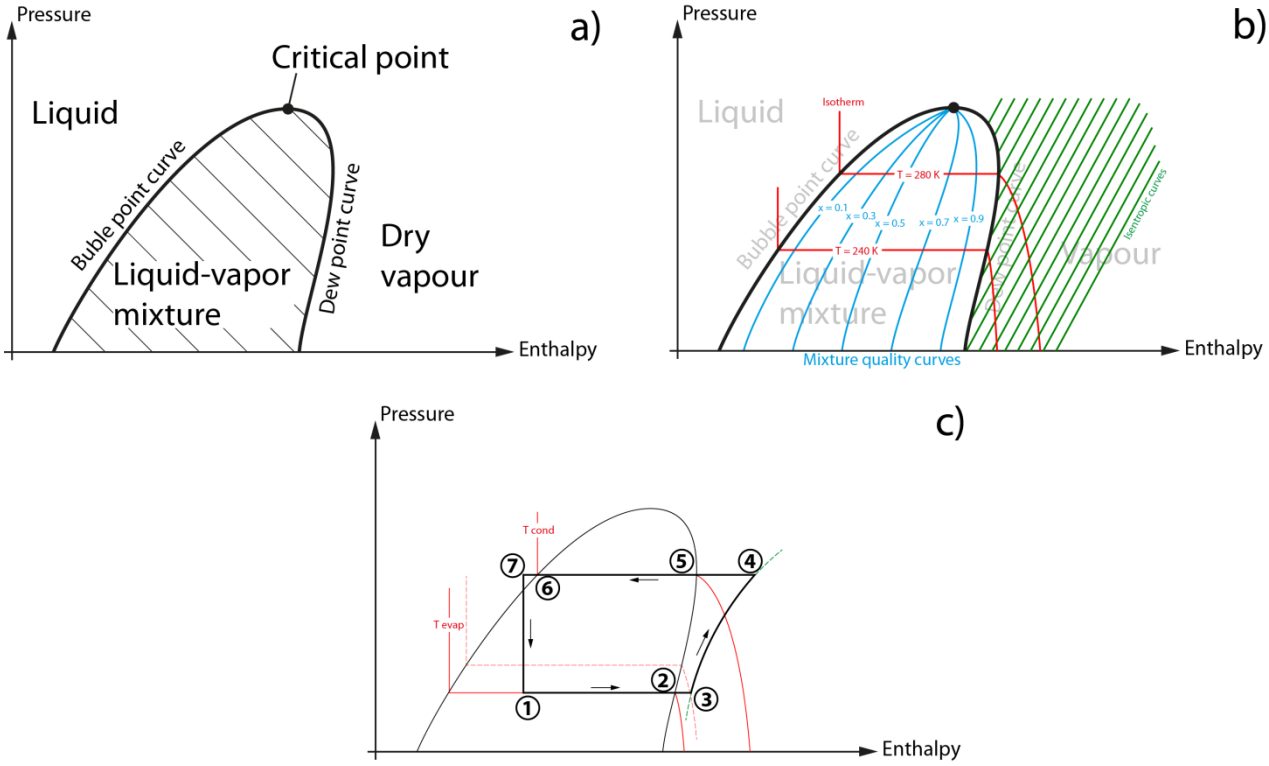

Figure 9:1 H-P diagrams with (a) phase domains, (b) mixture quality and isentropic curves and isotherms and (c) a typical heat pump cycle.

9.2 Evolution of axial (*t-z*) load-transfer curves with radial expansion

The evolution of mobilised shaft friction must be continuous as the temperature varies. Therefore, some modifications for going from one curve to another must be developed. The present method proposes to shift the curves along the displacement axis as show in Figure 9:2. This method remains physically acceptable because:

1/ during heating

- It predicts as greater critical displacement (i.e. displacement at which the ultimate state is reached) for the case when temperature increases from T_0 to $T_1 > T_0$ compared to the isothermal temperature curve at T_1.
- It does not increase the mobilised shaft friction if not axial displacement is observed

2/ during cooling

It might be necessary to recompute the equilibrium of the pile. Indeed, when cooling, the soil-pile contact stress will decrease and induced settlements may develop.

This model however neglects any variation in shear stress induced by the shear strain due to radial expansion. Indeed, thinking of a rectangular element at the soil pile interface (Figure 9:3) may:

- Undergo a shear strain when the pile is mechanically loaded (Figure 9:3b), developing the shear stress required to carry the pile load
- Undergo an increase of its shear strain during heating at it will be "flattened" (Figure 9:3c) and consequent increase in shear stress
- Undergo a decrease of its shear strain during cooling as the pile-soil interface moves toward the pile axis, and there experience a relieve in shear stress

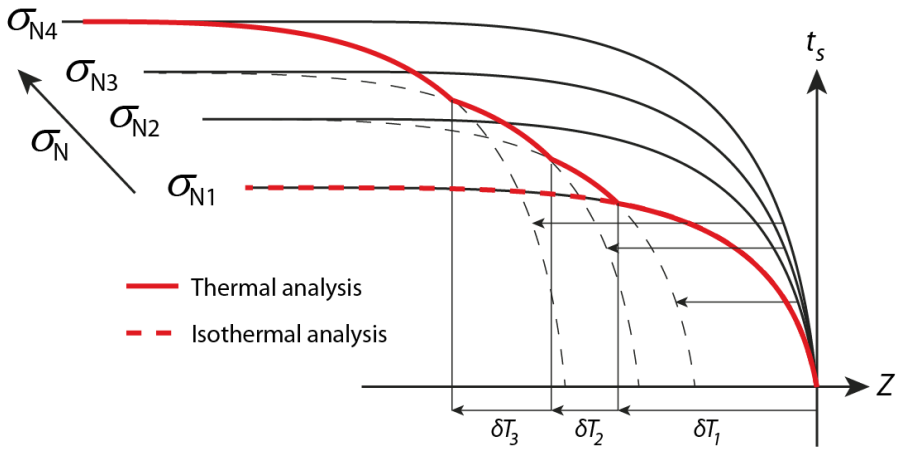

Figure 9:2 The red solid path is followed when temperature increases and load-transfer curve is modified accordingly. The red dashed path is followed under isothermal conditions

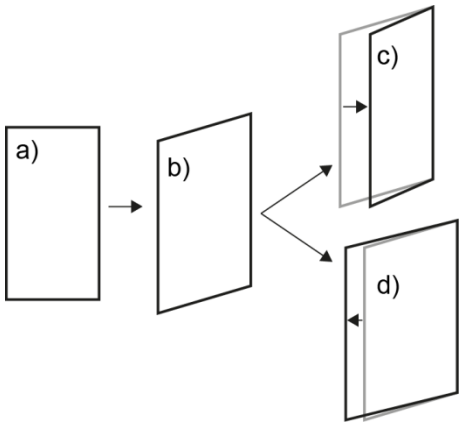

Figure 9:3 Evolution of shear strain of a rectangular element at the pile-soil interface first under to the pile loading (b) and then under either heating (c) or cooling (d).

9.3 Price of the produced heat with thermoactive anchors

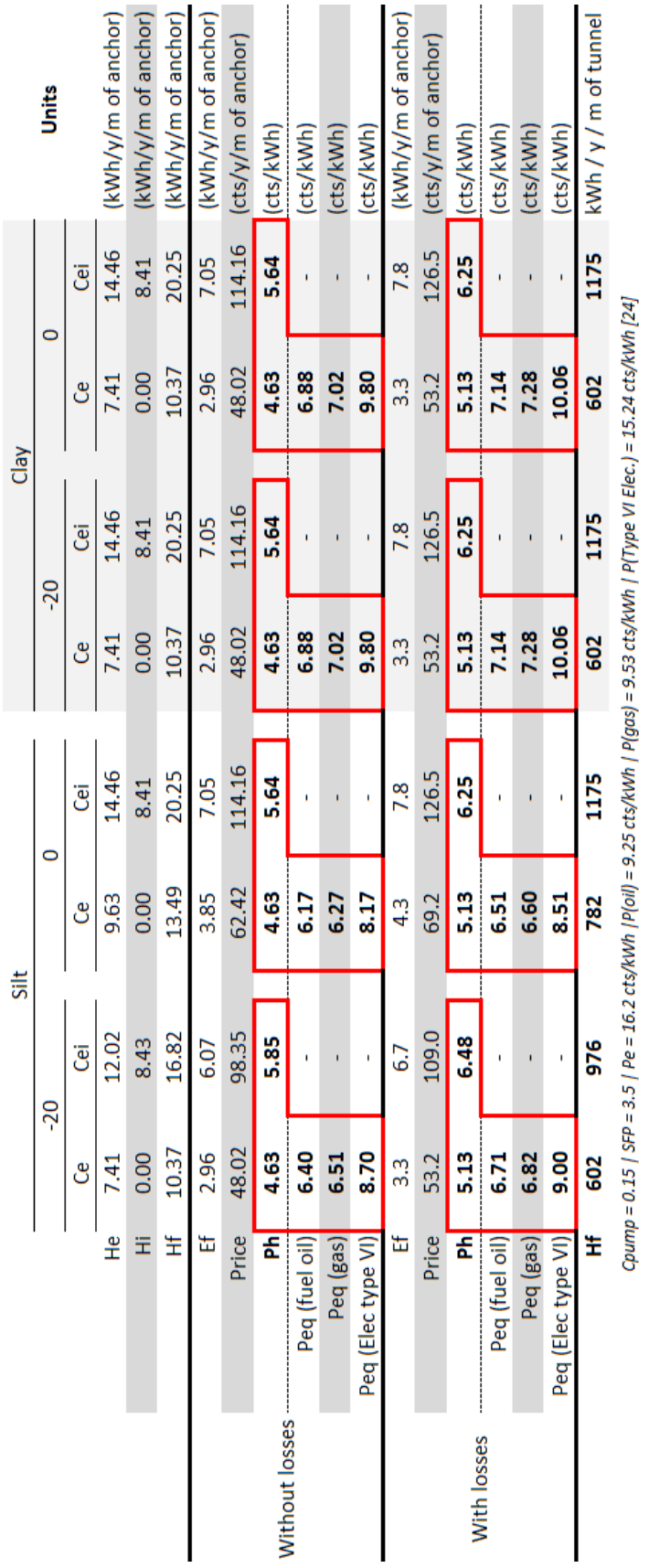

Figure 9:4 Estimated prices of the produced heat on the cut and cover tunnel

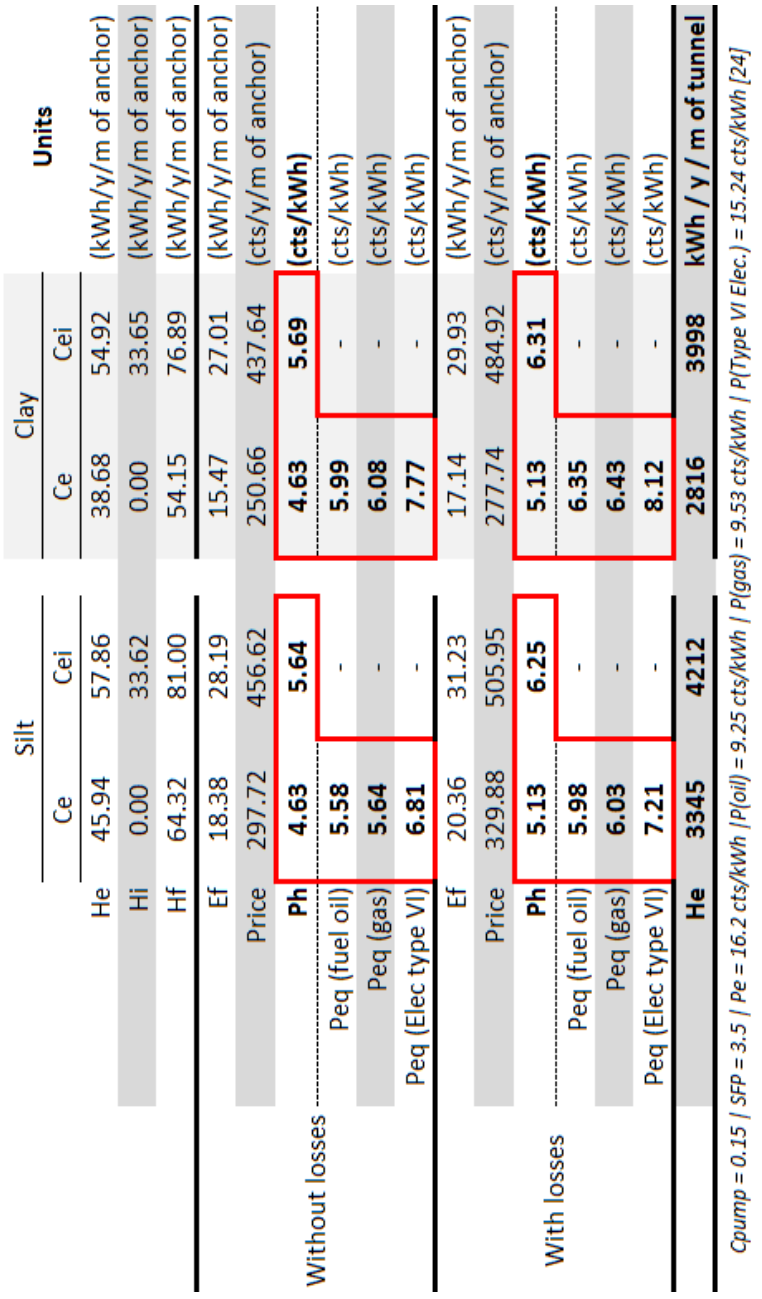

		Silt		Clay		Units
		Ce	Cei	Ce	Cei	
He		45.94	57.86	38.68	54.92	(kWh/y/m of anchor)
Hi		0.00	33.62	0.00	33.65	(kWh/y/m of anchor)
Hf		64.32	81.00	54.15	76.89	(kWh/y/m of anchor)
	Ef	18.38	28.19	15.47	27.01	(kWh/y/m of anchor)
	Price	297.72	456.62	250.66	437.64	(cts/y/m of anchor)
Without losses	**Ph**	**4.63**	**5.64**	**4.63**	**5.69**	**(cts/kWh)**
	Peq (fuel oil)	**5.58**	-	**5.99**	-	(cts/kWh)
	Peq (gas)	**5.64**	-	**6.08**	-	(cts/kWh)
	Peq (Elec type VI)	**6.81**	-	**7.77**	-	(cts/kWh)
	Ef	20.36	31.23	17.14	29.93	(kWh/y/m of anchor)
	Price	329.88	505.95	277.74	484.92	(cts/y/m of anchor)
With losses	**Ph**	**5.13**	**6.25**	**5.13**	**6.31**	**(cts/kWh)**
	Peq (fuel oil)	**5.98**	-	**6.35**	-	(cts/kWh)
	Peq (gas)	**6.03**	-	**6.43**	-	(cts/kWh)
	Peq (Elec type VI)	**7.21**	-	**8.12**	-	(cts/kWh)
	He	**3345**	**4212**	**2816**	**3998**	**kWh / y / m of tunnel**

Cpump = 0.15 / SFP = 3.5 / Pe = 16.2 cts/kWh /P(oil) = 9.25 cts/kWh / P(gas) = 9.53 cts/kWh / P(Type VI Elec.) = 15.24 cts/kWh [24]

Figure 9:5 Estimated prices of the produced heat on the bored tunnel

9.4 Individual estimates of thermal diffusivity

The individual estimates represented in Figure 6:7 are detailed in this appendix. The results were split into four different tables to clarify their contents. Table 9:1 presents estimates based on the phase shift and the boundary condition of no heat flux at infinity. Table 9:2 presents estimates based on the phase shift and the boundary condition of no heat flux at the tank wall. Table 9:3 presents the estimates based on the attenuation and the boundary condition of no heat flux condition at infinity. Table 9:4 presents the estimates based on the attenuation and the boundary condition of no heat flux at the tank wall. Obviously, no estimation can be achieved by comparing a thermocouple to itself or to the other thermocouple at the same distance from the tank axis (pairs T1–T4, T2–T5 and T3–T6).

Table 9:1 Values of retrieved thermal diffusivity D_φ (in 10^{-7} m^2/s) based on phase shift and no heat flux at infinity

	1	2	3	4	5	6
1		0.67	0.91		0.67	1.53
2			0.37	0.35		0.44
3				2.51	0.38	
4					0.35	6.25
5						0.44
6						

Table 9:2 Values of retrieved thermal diffusivity D_φ (in 10^{-7} m^2/s) based on phase shift and no heat flux at R

	1	2	3	4	5	6
1		1.53	1.57		1.53	2.16
2			0.53	0.34		0.73
3				0.28	0.57	
4					0.34	4.51
5						0.73
6						

Table 9:3 Values of retrieved thermal diffusivity D_δ (in 10^{-7} m^2/s) based on attenuation and no heat flux at infinity

	1	2	3	4	5	6
1		122	20.1		122	54.8
2			43.9	26.2		81.6
3				83.4	49.6	
4					31.7	688
5						94.9
6						

Table 9:4 Values of retrieved thermal diffusivity D_δ(in 10^{-7} m^2/s) based on attenuation and no heat flux at R

	1	2	3	4	5	6
1		3.55	1.41		3.71	1.67
2			2.50	2.82		2.77
3				1.78	0.43	
4					2.91	2.27
5						2.84
6						

9.5 Full-scale *in situ* test construction

9.5.1 Construction site report

The following content regroups all the events that were recorded on the construction site from the beginning of the construction until the end of my Ph.D. thesis. This document was translated from French.

Monday 23rd May 2011: Iron frames to install the strain gauges are made by the mechanical workshop of the EPFL
Friday 27th May 2011: Reception of the sensors, testing and initial measurements, beginning of strain gauges installation on supporting frames, installation of absorber pipes postponed because the reinforcing cages were not delivered on time
Saturday 28th May 2011: Gathering the sensors by pile on which they will be installed and listing of their serial numbers
Monday 30th May 2011: Borrowing of the SOFO unit of the ICOM laboratory of EPFL, installation of the SOFO reading unit pilot software on the field laptop and construction of the data base with the sensors (serial number + active length + passive length + position along the piles), end of strain gauges installation of the supporting frames, reinforcing cages delivered
Tuesday 31st May 2011: Beginning of the absorber pipe installation
Wednesday 1st June 2011: Installation of strain gauges on 2 reinforcing cages
Thursday 2nd June 2011: Construction site closed
Monday 6th June 2011: All the reinforcing cages are equipped and ready to be lifted, the boring platform and its access ramp are achieved
Tuesday 7th June 2011: Full construction of pile #3, RAS
Wednesday 8th June 2011: Full construction of Pile #4, because the borehole was too deep, the reinforcing cage was maintained elevated using chains
Thursday 9th June 2011: Full construction of pile #2
Friday 10th June 2011: Full construction of pile #1, installation of switching boxes for VW transducers (strain gauges, load cells, thermistors and piezometers), initial measurements to check sensors integrity
From June 13rd to 17th 2011: Drillings for the piezometers and borehole extensometers are postponed because of a broken drilling machine
From June 20th to 24th 2011: 160 mm diameter boreholes are drilled. They use "lost heads" so that the drilling is achieved without ground removal, but only injection of water and hammering the casing with a peak at the basis
Monday 20th June 2011: The first borehole is drilled for the borehole extensometer between piles #2 and #4. Because we can't drill down to -18 m as first planned, we shorten the last anchor bar from 18 m to 15 m. The borehole extensometer is backfilled with a 80/20 mixture of cement and bentonite
Tuesday 21st June 2011: The borehole for the piezometers between piles #2 and #4 is drilled and sensors are installed: piezometers are put into sand layers sealed with compactonite (highly expansive clay material)
Wednesday 22nd June 2011: installation of the borehole extensometer between piles #2 and #1
Thursday 23rd June 2011: Installation of the piezometers between piles #1 and #2
Monday 27th June 2011: Earthwork starts around the piles. 1.30 m of the drilling platform (i.e. very coarse gravel) is removed
Week 29 of 2011: Initial measurements are made on any sensor. We see that two stain gauges do not provide frequency measurements. The other sensors seem ok

Tuesday 26th July 2011: Pile top trimming starts. This will be achieved without cutting through the concrete in order to not cut the cables or pipes
Wednesday 27th July 2011: Pile top trimming is finished. It was done using electric jackhammers. No damage was caused to the pipes and cables. Reinforcing cages are not retrieved on piles #1 and #4
Friday 29th July 2011: The old (blue) heating module is revised because it didn't work for a very long time. The connecting pipes that were for double U geothermal loops are modified to have only one inlet and one outlet. An electric cable for 10 A/380 V is made (old electric outlets) to test the module in the laboratory. The test is ok
Tuesday 2nd August 2011: The "free head" test is installed on pile #1 in the afternoon. The first phase (i.e. fluid circulation without heating) is launched in the evening. Circuit pressure = 2.8 br and flow rate ~ 21 L/min
Wednesday 3rd August 2011: The first phase of the "free head" test is stopped at 9 AM. A heat rate of 1 kW is then injected into pile #1. The reading head of borehole extensometer #1 is installed
Friday 5th August 2011: Measurements of temperature along the pile are low and it is decided to increase the heat rate up to 2 kW as the schedule of the construction site only gives 1 week of test
Monday 8th August 2011: The "free head" test is stopped and the heating module is removed to let the construction go on. The first layer of concrete is poured just after
Wednesday 10th August 2011: Connecting pipes running from the piles to the future room where modules will be put are installed. These are not thermally insulated because it may compromise the water tightness of the raft
Tuesday 16th August 2011: The installation of the reinforcing cage of the raft starts. The cables and pipes are installed in such a way that they enter the service room at least 20 cm away from the walls to avoid damages during the wall constructions
Wednesday 17th August 2011: Concrete is poured in the raft, vibrated and smoothed
Thursday 18th August 2011: The poured raft is covered with a plastic film and wetted to prevent cracks
End of August, beginning of September 2011: Walls and roof of the water retention tank are built; a 800 mm diameter manhole is installed to access the service room with the sensors. The tank roof is covered with plastic film and wetted to prevent cracks; the manhole is also covered with plastic film
26th to 30th September 2011: 10-15 cm of water infiltrated in the service room because of the concrete wetting, which damaged the switching boxes and the optical fibers. The evacuation grid that was supposed to be used to drain the water was covered with concrete
Thursday 6th October 2011: Switching boxes are installed on walls to prevent damages from future floods and a drier is installed in the room
Friday 7th October 2011: Sensors are checked: three switching boxes are damages as well as several optical fibers connectors
Monday 10th October 2011: Check of the bill with M. Riegler from Marti AG
Wednesday 12nd October 2011: The evacuation grid is retrieved drilling into the room floor slab
Thursday 13th October: SMARTEC SA is consulted to see what we can do with the damaged boxes and sensors
Thursday 17th November 2011: A technician from SMARTEC comes on site to repair what can be done on site (optical fiber connectors) and removes switching boxes from piles #2, 3 and 4 to take them back to SMARTEC and see what can be done. After further investigation, the removed boxes will be replaced
Tuesday 13th December2011: Kruger SA installs a room dryer during one week in order to remove the humidity from the service room
Wednesday 4th January 2012: A single test on pile #1 is installed and launched
Friday 6th January 2012: the heating on pile #1 is stopped (temp. increase only of 4 °C)

Monday 16th January 2012: the new switching box of pile #4 is installed. The heating module is connected to pile #4 and a test is launched on the afternoon. The data logger still does not work as it is not alimented by the module
Tuesday 17th January 2012: A power cut happened during the night. The problem is fixed (broken cable) and the test is launched again
Thursday 19th January 2012: Heating is stopped on pile #4 (afternoon)
Monday 23rd January 2012: The heating module is connected to pile #2 and the switching box of pile #2 is installed. The heating is launched in the afternoon
Wednesday 25th January 2012: Heating on pile #2 is stopped
Saturday 28th January 2012: Switching box of pile #3 is installed and the module is connected to pile #3
Monday 30th January 2012: The heating on pile #3 is started
Wednesday 1st February 2012: Heating is stopped on pile #3
27th March 2012: Thermal diffusivity test is launched using pumping test method with heating steps from 0 to 5 kW with a period of 2 hrs (1 hr heating and 1 hr thermal rest).
November 2012: The test room is covered with a geotechnical platform which prevents reaching the sensors
17th June 2013: The test room is reopened. 10 cm of water is at the bottom of the room but no damage is visible as the boxes were installed on the walls. The room is emptied with a pump
21st June 2013: The room is totally emptied to flow a floor screed for water drainage
15th July to 13rd September 2013: Single tests on piles #1, #3 and #4 are carried out with power cuts sometimes
22nd May 2014: Electrical installation in the room is achieved (light, connectors and panel). Single test on pile #2 is launched
20th June 2014: Three heating modules are installed in the test room: one is connected to pile #1, another one on pile #4 and piles #2 and #3 are connected in series to the same module (pile #3 first).

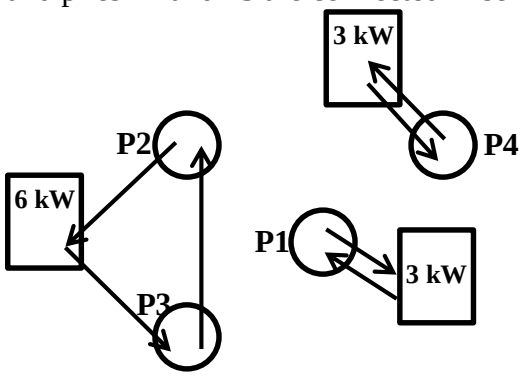

25th June 2014: The group test is launched
1st July 2014: Heating is stopped
18th July 2014: The long TRT is launched on pile #3
12th August 2014: The long TRT on pile #3 is stopped

9.5.2 Experimental site plans

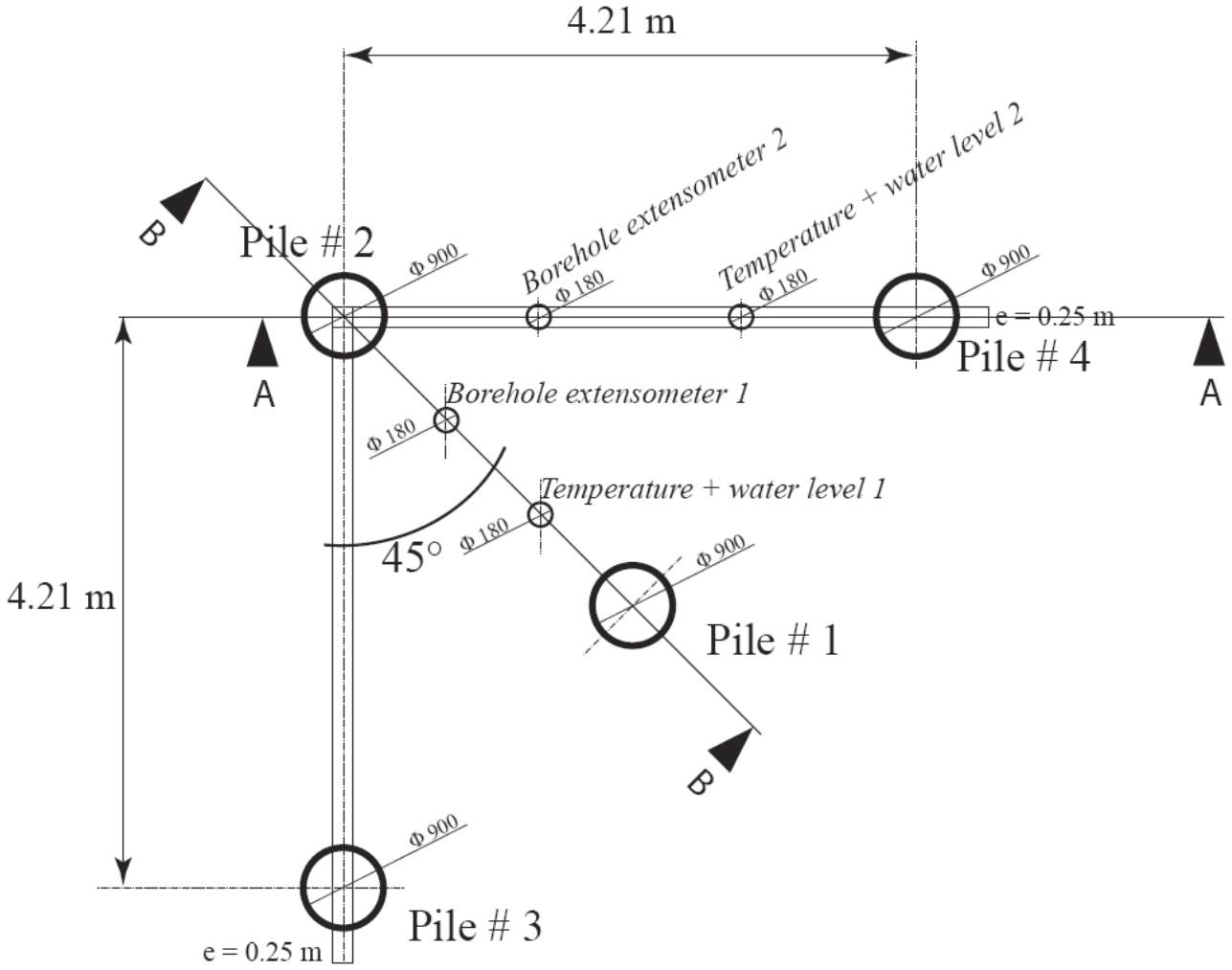

Figure 9:6 Top view of the four test piles and boreholes

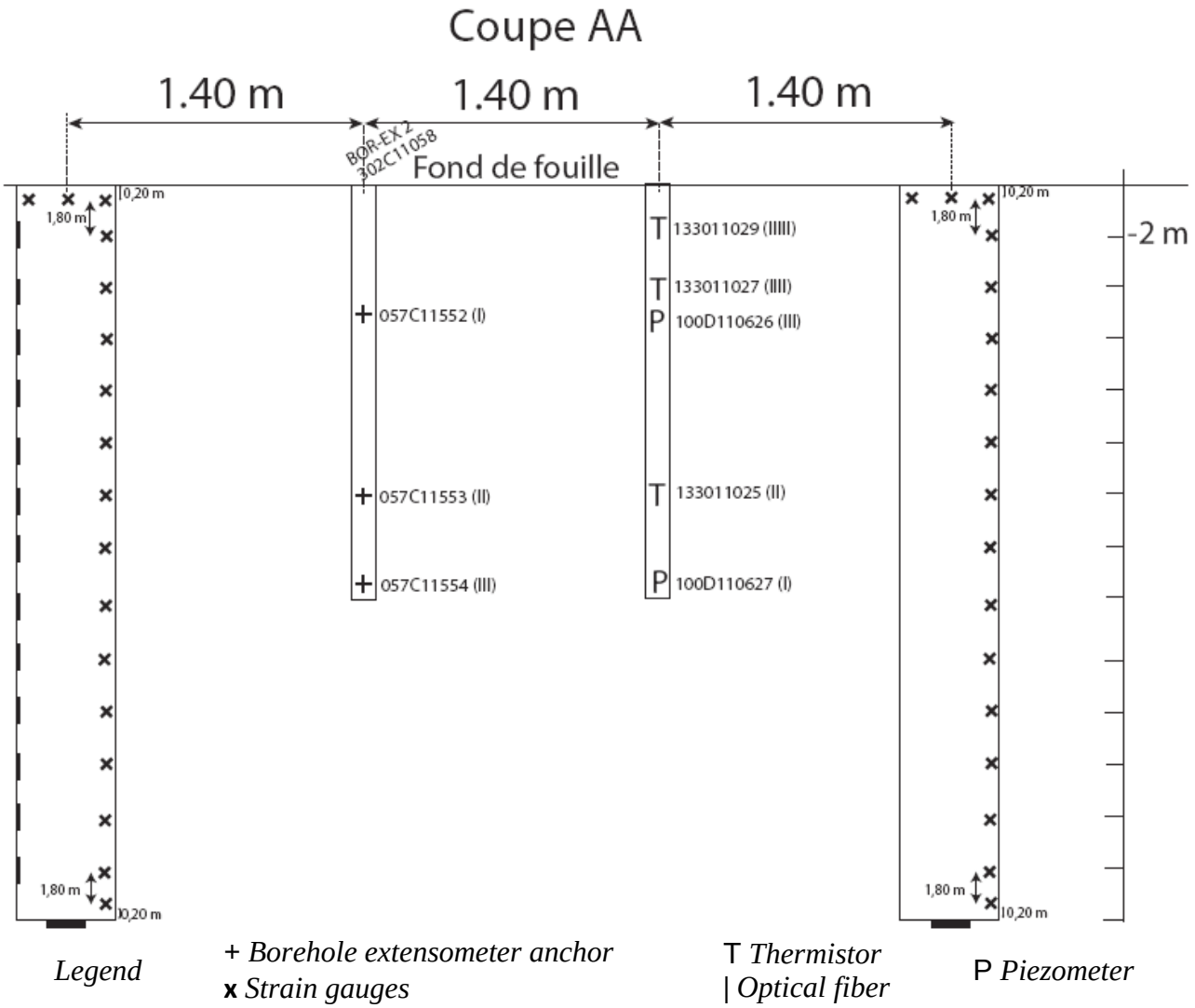

Figure 9:7 Cut AA with piles # 2 (left) and #4 (right)

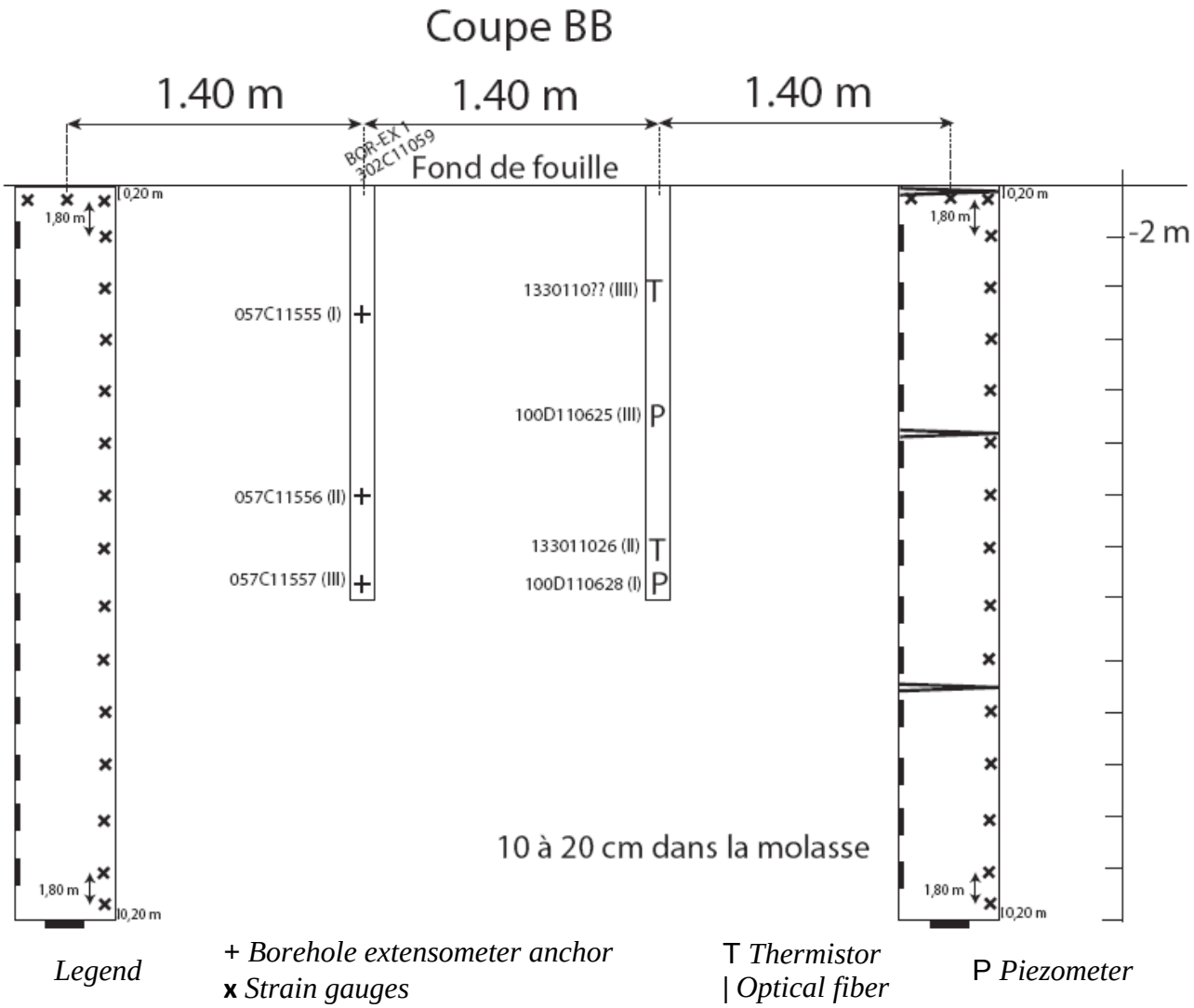

Figure 9:8 Cut BB with piles # 2 (left) and #1 (right)

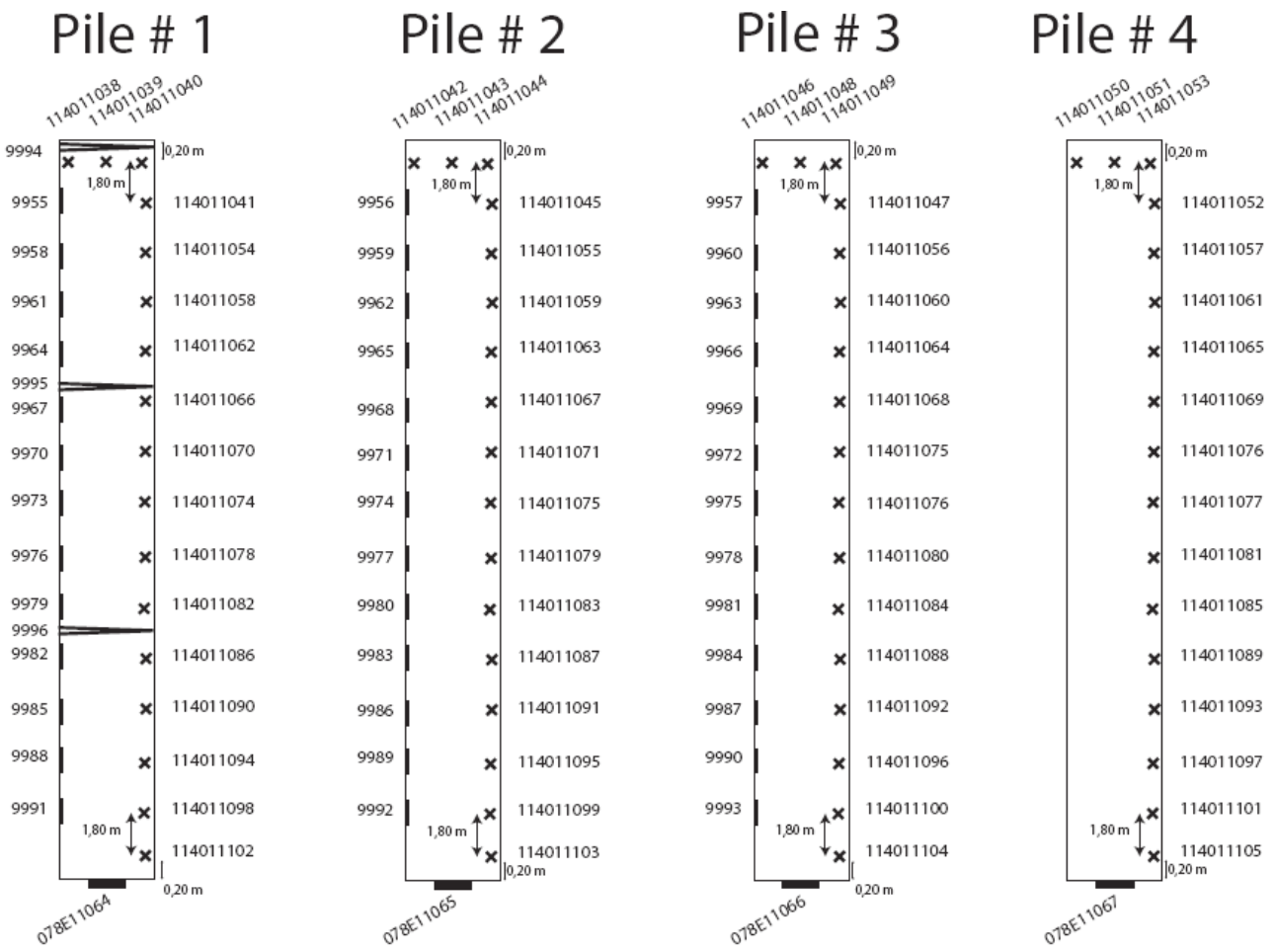

Figure 9:9 All sensors in piles with serial numbers

9.5.3 Mini-module procedures

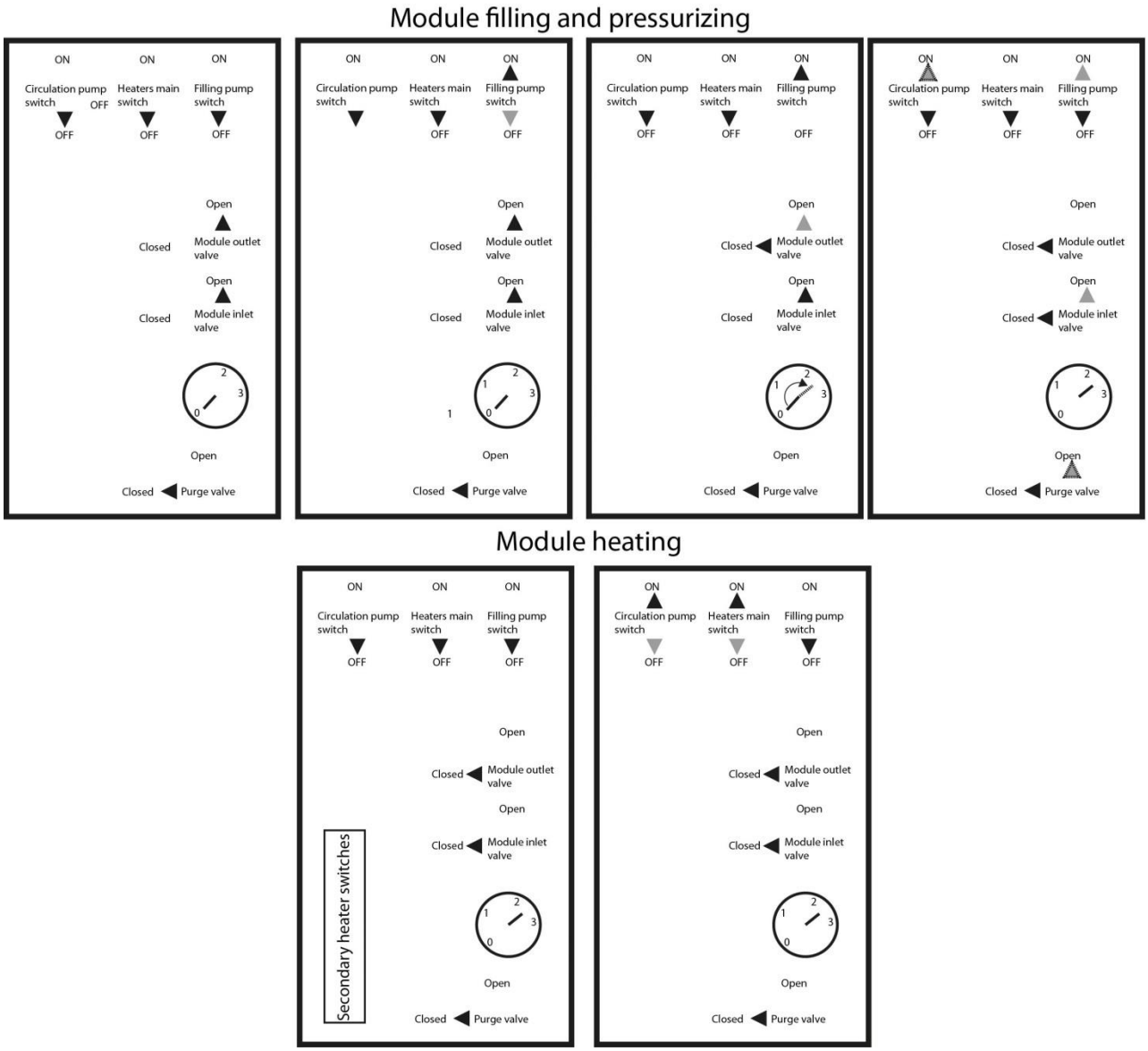

Figure 9:10 Schematic representation of procedures on the mini-module

9.5.4 Calibration sheets for load cells and piezometers

ROCTEST TELEMAC

CALIBRATION DATA SHEET
VIBRATING WIRE PRESSURE TRANSDUCER

Model:	**TPC**
Serial number:	**078E11064**
Range:	**1 000 kPa**
Temperature:	**23.2 °C**
Barometric pressure:	**101.1 kPa**
Cable model:	**IRC-41A**
Cable length:	**35 m**
Thermistor type:	**3 kOhms**

Color code: **red & black (coil) green & white (thermistor)**

Applied pressure kPa	Reading linear unit LU	Error linear % FS	Error polynomial % FS
0.10	4081.4	-0.21	0.02
200.00	3798.9	0.04	0.00
400.00	3514.5	0.16	-0.02
600.00	3228.7	0.19	0.01
800.00	2940.2	0.03	-0.01
1000.10	2650.1	-0.23	0.00
1000.30	2649.8	-0.23	0.00
800.00	2940.5	0.05	0.00
600.00	3229.3	0.23	0.05
400.00	3514.5	0.16	-0.02
199.90	3798.8	0.02	-0.02
-0.10	4081.5	-0.22	0.01
	Maximum error (%):	0.23	0.05

Calculated Pressure:

$P_c = P - P_T - (S-S_0)$

P, P_c = Raw pressure and corrected one
P_T = Temperature correction
S_0, S = Barometric pressure at installation and current one

Linear regression	Polynomial regression
$P = C_f (L - L_0)$ $P_T = C_T (T - T_0)$	$P = AL^2 + BL + C'$ (*) $P_T = C_T (T - T_0)$
C_f = -6.9880E-01 kPa / LU C_T = -8.8865E-02 kPa / °C	A = -8.3448E-06 kPa / LU² B = -6.4263E-01 kPa / LU C_T = -8.8865E-02 kPa / °C
L_0 : Initial reading in LU	(*) C' calculation: please refer to instruction manual, § Initial reading
L : Reading in LU ; T_0, T : Temperatures in °C (initial, current)	

Note : LU = Linear Unit with K = 1.0156, position 4 on the MB-6T readout unit

Certificate: 051311A.xls Traceability: TR-03-03

Calibrated by: Dorina Jugureanu Date: 2011/05/13

Tel: (1) 450-465-1113 · 1-877-ROCTEST (USA, Canada) · 33 (1) 64.06.40.80 (Europe) · www.roctest.com · www.telemac.fr

Figure 9:11 Calibration sheet for TPC #1

ROCTEST TELEMAC

CALIBRATION DATA SHEET
VIBRATING WIRE PRESSURE TRANSDUCER

Model:	**TPC**
Serial number:	**078E11065**
Range:	**1 000 kPa**
Temperature:	**23.2 °C**
Barometric pressure:	**101.1 kPa**
Cable model:	**IRC-41A**
Cable length:	**35 m**
Thermistor type:	**3 kOhms**

Color code: **red & black (coil) green & white (thermistor)**

Applied pressure kPa	Reading linear unit LU	Error linear % FS	Error polynomial % FS
0.00	4052.2	-0.24	0.01
200.00	3791.6	0.01	-0.04
400.00	3530.1	0.19	-0.02
600.00	3266.4	0.20	0.00
800.00	3000.6	0.06	0.01
1000.10	2732.2	-0.27	-0.01
1000.10	2732.6	-0.24	0.01
800.00	3000.3	0.04	-0.02
600.00	3266.5	0.22	0.01
400.00	3531.0	0.26	0.06
199.90	3792.1	0.03	-0.01
-0.10	4052.4	-0.24	0.01
	Maximum error (%):	0.27	0.06

Calculated Pressure:

$P_c = P - P_T - (S-S_0)$

P, P_c = Raw pressure and corrected one
P_T = Temperature correction
S_0, S = Barometric pressure at installation and current one

Linear regression			Polynomial regression		
$P = C_f (L - L_0)$ $P_T = C_T (T - T_0)$			$P = AL^2 + BL + C'$ (*) $P_T = C_T (T - T_0)$		
C_f =	-7.5781E-01	kPa / LU	A =	-1.0957E-05	kPa / LU²
C_T =	-1.2265E-01	kPa / °C	B =	-6.8347E-01	kPa / LU
			C_T =	-1.2265E-01	kPa / °C
L_0 : Initial reading in LU			(*) C' calculation: please refer to instruction manual, § Initial reading		
L : Reading in LU ; T_0, T : Temperatures in °C (initial, current)					

Note : LU = Linear Unit with K = 1.0156, position 4 on the MB-6T readout unit

Certificate: 051311A.xls Traceability: TR-03-03

Calibrated by: Dorina Jugureanu Date: 2011/05/13

Tel: (1) 450-465-1113 · 1-877-ROCTEST (USA, Canada) · 33 (1) 64.06.40.80 (Europe) · www.roctest.com · www.telemac.fr

Figure 9:12 Calibration sheet for TPC #2

ROCTEST TELEMAC

CALIBRATION DATA SHEET
VIBRATING WIRE PRESSURE TRANSDUCER

Model:	**TPC**
Serial number:	**078E11066**
Range:	**1 000 kPa**
Temperature:	**23.2 °C**
Barometric pressure:	**101.1 kPa**
Cable model:	**IRC-41A**
Cable length:	**35 m**
Thermistor type:	**3 kOhms**

Color code: **red & black (coil) green & white (thermistor)**

Applied pressure kPa	Reading linear unit LU	Error linear % FS	Error polynomial % FS
0.00	3749.1	-0.28	-0.02
200.00	3427.0	0.07	0.02
400.00	3101.5	0.22	0.01
600.00	2774.1	0.24	0.03
800.00	2442.5	0.01	-0.04
1000.00	2110.3	-0.26	0.01
999.80	2110.7	-0.25	0.01
800.00	2443.2	0.05	0.00
600.00	2773.5	0.21	-0.01
400.00	3101.2	0.20	-0.01
199.90	3426.7	0.04	-0.01
-0.10	3749.5	-0.26	0.00
	Maximum error (%):	0.28	0.04

Calculated Pressure:

$P_c = P - P_T - (S - S_0)$

P, P_c = Raw pressure and corrected one
P_T = Temperature correction
S_0, S = Barometric pressure at installation and current one

Linear regression	Polynomial regression
$P = C_f (L - L_0)$ $P_T = C_T (T - T_0)$	$P = AL^2 + BL + C'$ (*) $P_T = C_T (T - T_0)$
C_f = -6.1008E-01 kPa / LU	A = -7.3468E-06 kPa / LU²
C_T = -7.7583E-02 kPa / °C	B = -5.6703E-01 kPa / LU
	C_T = -7.7583E-02 kPa / °C
L_0 : Initial reading in LU	(*) C' calculation: please refer to instruction manual, § Initial reading
L : Reading in LU ; T_0, T : Temperatures in °C (initial, current)	

Note : LU = Linear Unit with K = 1.0156, position 4 on the MB-6T readout unit

Certificate: 051311A.xls Traceability: TR-03-03

Calibrated by: Dorina Jugureanu Date: 2011/05/13

Tel: (1) 450-465-1113 · 1-877-ROCTEST (USA, Canada) · 33 (1) 64.06.40.80 (Europe) · www.roctest.com · www.telemac.fr

Figure 9:13 Calibration sheet for TPC #3

ROCTEST TELEMAC

CALIBRATION DATA SHEET
VIBRATING WIRE PRESSURE TRANSDUCER

Model:	**TPC**
Serial number:	**078E11067**
Range:	**1 000 kPa**
Temperature:	**23.2 °C**
Barometric pressure:	**101.1 kPa**
Cable model:	**IRC-41A**
Cable length:	**35 m**
Thermistor type:	**3 kOhms**

Color code: **red & black (coil) green & white (thermistor)**

Applied pressure kPa	Reading linear unit LU	Error linear % FS	Error polynomial % FS
0.00	3923.6	-0.25	-0.01
200.00	3652.7	0.09	0.04
400.00	3378.5	0.18	0.00
600.00	3102.6	0.15	-0.03
800.00	2826.2	0.09	0.04
1000.00	2546.1	-0.24	-0.01
999.80	2546.3	-0.25	-0.01
799.90	2826.1	0.07	0.02
600.00	3103.1	0.19	0.00
400.00	3378.0	0.15	-0.04
200.00	3652.0	0.04	-0.01
-0.10	3924.0	-0.23	0.00
	Maximum error (%):	0.25	0.04

Calculated Pressure:

$$P_c = P - P_T - (S - S_0)$$

P, P_c = Raw pressure and corrected one
P_T = Temperature correction
S_0, S = Barometric pressure at installation and current one

Linear regression	Polynomial regression
$P = C_f (L - L_0)$ $P_T = C_T (T - T_0)$	$P = AL^2 + BL + C'$ (*) $P_T = C_T (T - T_0)$
C_f = -7.2592E-01 kPa / LU	A = -9.1870E-06 kPa / LU²
C_T = -1.0490E-01 kPa / °C	B = -6.6647E-01 kPa / LU
	C_T = -1.0490E-01 kPa / °C
L_0 : *Initial reading in LU*	(*) C' calculation: please refer to instruction manual, § Initial reading
L : Reading in LU ; T_0, T : Temperatures in °C (initial, current)	

Note : LU = Linear Unit with K = 1.0156, position 4 on the MB-6T readout unit

Certificate: 051311A.xls Traceability: TR-03-03

Calibrated by: Dorina Jugureanu Date: 2011/05/13

Tel: (1) 450-465-1113 · 1-877-ROCTEST (USA, Canada) · 33 (1) 64.06.40.80 (Europe) · www.roctest.com · www.telemac.fr

Figure 9:14 Calibration sheet for TPC #4

ROCTEST TELEMAC

CALIBRATION DATA SHEET
VIBRATING WIRE PRESSURE TRANSDUCER

Model:	**PWS**
Serial number:	**100D110625**
Range:	**350 kPa**
Temperature:	**22.6 °C**
Barometric pressure:	**101.1 kPa**
Cable model:	**IRC-41A**
Cable length:	**40 m**
Thermistor type:	**3 kOhms**

Color code: **red & black (coil) green & white (thermistor)**

Applied pressure kPa	Reading linear unit LU	Error linear % FS	Error polynomial % FS
0.10	4160.8	-0.07	0.03
70.10	3891.7	0.00	-0.01
140.10	3622.2	0.05	-0.02
210.00	3352.9	0.08	0.00
280.00	3082.6	0.06	0.04
350.00	2810.3	-0.11	-0.01
349.90	2810.7	-0.11	-0.02
280.00	3082.3	0.04	0.02
210.00	3352.8	0.07	-0.01
140.00	3623.0	0.08	0.01
70.00	3892.2	0.01	0.00
-0.10	4161.1	-0.10	-0.01
	Maximum error (%):	0.11	0.04

Calculated Pressure:

$P_c = P - P_T - (S-S_0)$

P, P_c = Raw pressure and corrected one
P_T = Temperature correction
S_0, S = Barometric pressure at installation and current one

Linear regression	Polynomial regression
$P = C_f (L - L_0)$ $P_T = C_T (T - T_0)$	$P = AL^2 + BL + C'$ (*) $P_T = C_T (T - T_0)$
C_f = -2.5919E-01 kPa / LU	A = -1.3406E-06 kPa / LU²
C_T = -6.2263E-02 kPa / °C	B = -2.4984E-01 kPa / LU
	C_T = -6.2263E-02 kPa / °C
L_0 : *Initial reading in LU*	(*) C' calculation: please refer to instruction manual, § Initial reading
L : Reading in LU ; T_0, T : Temperatures in °C (initial, current)	

Note : LU = Linear Unit with K = 1.0156, position 4 on the MB-6T readout unit

Certificate: 042711A.xls Traceability: TR-03-03

Calibrated by: Dorina Jugureanu Date: 2011/04/27

Tel: (1) 450-465-1113 · 1-877-ROCTEST (USA, Canada) · 33 (1) 64.06.40.80 (Europe) · www.roctest.com · www.telemac.fr

Figure 9:15 Calibration sheet for the first piezometer in P+T 1

ROCTEST TELEMAC

CALIBRATION DATA SHEET
VIBRATING WIRE PRESSURE TRANSDUCER

Model:	**PWS**
Serial number:	**100D110626**
Range:	**350 kPa**
Temperature:	**22.6 °C**
Barometric pressure:	**101.1 kPa**
Cable model:	**IRC-41A**
Cable length:	**40 m**
Thermistor type:	**3 kOhms**

Color code: **red & black (coil) green & white (thermistor)**

Applied pressure kPa	Reading linear unit LU	Error linear % FS	Error polynomial % FS
0.10	4162.1	-0.13	0.02
70.00	3891.3	0.01	-0.02
140.10	3620.1	0.18	0.06
210.00	3346.4	0.10	-0.02
280.00	3072.1	0.02	-0.01
350.10	2796.5	-0.14	0.02
350.00	2796.6	-0.15	0.00
280.00	3072.1	0.02	-0.01
210.00	3346.4	0.10	-0.02
140.00	3620.1	0.15	0.03
70.00	3891.2	0.00	-0.03
-0.10	4162.3	-0.17	-0.02
	Maximum error (%):	0.18	0.06

Calculated Pressure:

$$P_c = P - P_T - (S - S_0)$$

P, P_c = Raw pressure and corrected one
P_T = Temperature correction
S_0, S = Barometric pressure at installation and current one

Linear regression	Polynomial regression
$P = C_f (L - L_0)$ $P_T = C_T (T - T_0)$	$P = AL^2 + BL + C'$ (*) $P_T = C_T (T - T_0)$
C_f = -2.5631E-01 kPa / LU C_T = -6.8731E-02 kPa / °C	A = -2.1713E-06 kPa / LU² B = -2.4120E-01 kPa / LU C_T = -6.8731E-02 kPa / °C
L_0 : Initial reading in LU	(*) C' calculation: please refer to instruction manual, § Initial reading
L : Reading in LU ; T_0, T : Temperatures in °C (initial, current)	

Note : LU = Linear Unit with K = 1.0156, position 4 on the MB-6T readout unit

Certificate: 042711A.xls Traceability: TR-03-03

Calibrated by: Dorina Jugureanu Date: 2011/04/27

Tel: (1) 450-465-1113 · 1-877-ROCTEST (USA, Canada) · 33 (1) 64.06.40.80 (Europe) · www.roctest.com · www.telemac.fr

Figure 9:16 Calibration sheet for the first piezometer in P+T 2

ROCTEST TELEMAC

CALIBRATION DATA SHEET
VIBRATING WIRE PRESSURE TRANSDUCER

Model:	**PWS**
Serial number:	**100D110627**
Range:	**350 kPa**
Temperature:	**22.6 °C**
Barometric pressure:	**101.1 kPa**
Cable model:	**IRC-41A**
Cable length:	**40 m**
Thermistor type:	**3 kOhms**

Color code: **red & black (coil) green & white (thermistor)**

Applied pressure kPa	Reading linear unit LU	Error linear % FS	Error polynomial % FS
0.00	4151.5	-0.08	0.01
69.90	3871.6	-0.03	-0.04
140.00	3591.9	0.10	0.03
210.00	3310.7	0.09	0.01
280.00	3028.1	-0.01	-0.03
350.10	2746.1	-0.05	0.04
350.00	2745.5	-0.12	-0.03
280.00	3028.7	0.02	0.00
210.00	3310.5	0.07	0.00
140.00	3591.9	0.10	0.03
69.90	3871.7	-0.02	-0.04
-0.10	4151.9	-0.08	0.01
	Maximum error (%):	0.12	0.04

Calculated Pressure:

$P_c = P - P_T - (S-S_0)$

P, P_c = Raw pressure and corrected one
P_T = Temperature correction
S_0, S = Barometric pressure at installation and current one

Linear regression	Polynomial regression
$P = C_f (L - L_0)$ $P_T = C_T (T - T_0)$	$P = AL^2 + BL + C'$ (*) $P_T = C_T (T - T_0)$
C_f = -2.4905E-01 kPa / LU C_T = -6.4001E-02 kPa / °C	A = -1.2284E-06 kPa / LU² B = -2.4058E-01 kPa / LU C_T = -6.4001E-02 kPa / °C
L_0 : Initial reading in LU	(*) C' calculation: please refer to instruction manual, § Initial reading
L : Reading in LU ; T_0, T : Temperatures in °C (initial, current)	

Note : LU = Linear Unit with K = 1.0156, position 4 on the MB-6T readout unit

Certificate: 042711A.xls Traceability: TR-03-03

Calibrated by: Dorina Jugureanu Date: 2011/04/27

Tel: (1) 450-465-1113 · 1-877-ROCTEST (USA, Canada) · 33 (1) 64.06.40.80 (Europe) · www.roctest.com · www.telemac.fr

Figure 9:17 Calibration sheet for the second piezometer in P+T 2

ROCTEST TELEMAC

CALIBRATION DATA SHEET
VIBRATING WIRE PRESSURE TRANSDUCER

Model:	**PWS**
Serial number:	**100D110628**
Range:	**350 kPa**
Temperature:	**22.6 °C**
Barometric pressure:	**101.1 kPa**
Cable model:	**IRC-41A**
Cable length:	**40 m**
Thermistor type:	**3 kOhms**

Color code: **red & black (coil) green & white (thermistor)**

Applied pressure kPa	Reading linear unit LU	Error linear % FS	Error polynomial % FS
0.00	4117.3	-0.11	0.02
69.90	3837.3	0.03	0.00
140.00	3555.6	0.10	0.00
210.00	3273.1	0.09	-0.01
280.00	2990.3	0.06	0.03
350.00	2705.1	-0.14	-0.01
350.00	2705.1	-0.14	-0.01
280.00	2989.8	0.02	0.00
210.00	3273.6	0.13	0.02
140.00	3555.3	0.08	-0.03
70.00	3837.0	0.03	0.01
-0.10	4117.2	-0.15	-0.02
	Maximum error (%):	0.15	0.03

Calculated Pressure:

$P_c = P - P_T - (S-S_0)$

P, P_c = Raw pressure and corrected one
P_T = Temperature correction
S_0, S = Barometric pressure at installation and current one

Linear regression			Polynomial regression		
$P = C_f (L - L_0)$ $P_T = C_T (T - T_0)$			$P = AL^2 + BL + C'$ (*) $P_T = C_T (T - T_0)$		
C_f =	-2.4791E-01	kPa / LU	A =	-1.7416E-06	kPa / LU²
C_T =	-5.2630E-02	kPa / °C	B =	-2.3603E-01	kPa / LU
			C_T =	-5.2630E-02	kPa / °C
L_0 : Initial reading in LU			(*) C' calculation: please refer to instruction manual, § Initial reading		
L : Reading in LU ; T_0, T : Temperatures in °C (initial, current)					

Note : LU = Linear Unit with K = 1.0156, position 4 on the MB-6T readout unit

Certificate: 042711A.xls Traceability: TR-03-03

Calibrated by: Dorina Jugureanu Date: 2011/04/27

Tel: (1) 450-465-1113 · 1-877-ROCTEST (USA, Canada) · 33 (1) 64.06.40.80 (Europe) · www.roctest.com · www.telemac.fr

Figure 9:18 Calibration sheet for the second piezometer in P+T 1

9.5.5 Illustration of construction phases

Figure 9:19 Instrumentation of the 4 reinforcing cages on the construction site, in the background, we can see two boring machines with temporary casings

Figure 9:20 Augering of pile #3

Figure 9:21 Lifting of an equipped 28 m long reinforcing cage

Figure 9:22 Insertion of the reinforcing cage into the temporary casing

Figure 9:23 Sensor cables coming out from an instrumented pile (optical fibers in white and vibrating wires in black) through the protective PVC tube

Figure 9:24 Drilling of the boreholes for the piezometers and ground extensometers

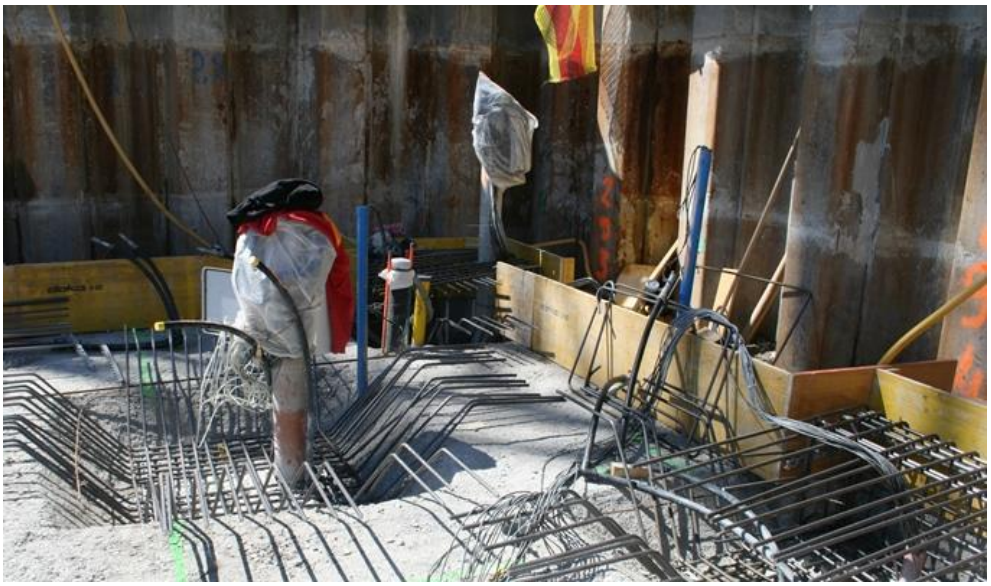

Figure 9:25 Installation of the reinforcing rods in the raft

9.5.6 Compression tests on concrete and grout samples

LABORATOIRES DE MECANIQUE DES SOLS ET DES ROCHES

COMPRESSION UNIAXIALE

Exécuté selon la norme SN 670 353 et LMS+R ER.520

ÉCOLE POLYTECHNIQUE FÉDÉRALE DE LAUSANNE

No éprouvette		Titre de l'étude	Commettant		
			nom		adresse
R0703PIEU1		AULA EPFL	EPFL-LMS		LAUSANNE
No sond.	Prof. [m]	Nature échantillon	Echantillon prélevé par	Date réception	Date essai
P1	-	BETON 28 JOURS	COMMETTANT	10.06.11	11.07.11
Mode conservation		Mode préparation éprouvette	Ingénieur responsable		Opérat.
			nom	signature	
HUMIDITE CONTROLEE		SCIE, RECTIFIE	J.-F. Mathier		LG

Haut. [mm]	Diam. [mm]	ρ [t/m³]	w [%]	Ep50% [MN/m²]	Er50% [MN/m²]	σ_c [MN/m²]
300.0	158.0	2.44	-	24300	28000	41.0

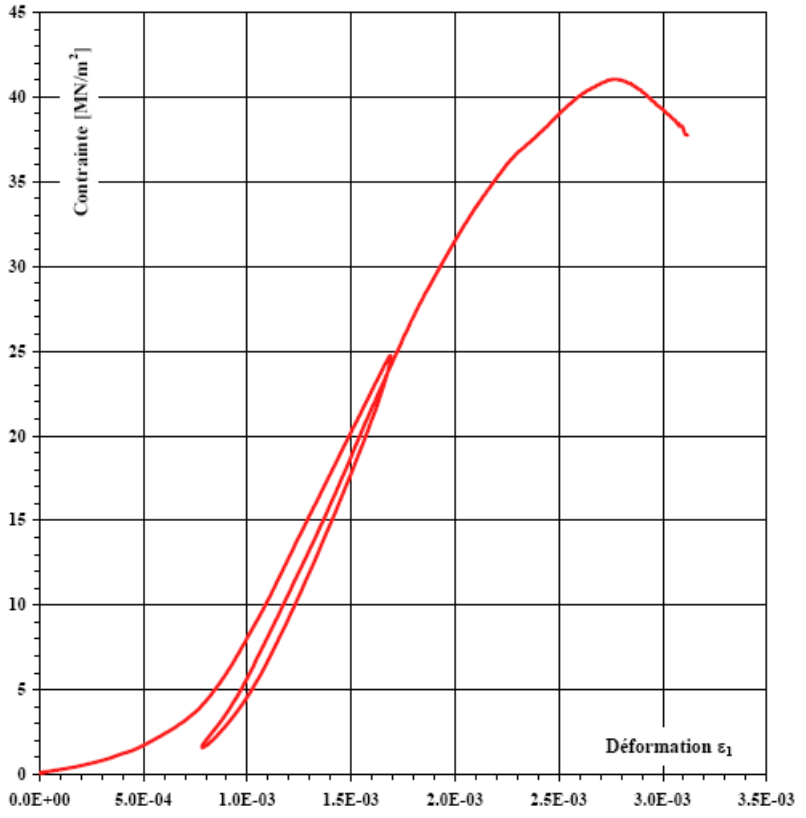

Observations:

Ce protocole ne peut être reproduit partiellement et son contenu ne concerne que l'éprouvette testée
En outre, il fait partie d'une série d'essais, voir page "Rapport d'essais"

Page 1/1
ER.520 07/09
R0703pieu1.xls

Figure 9:26 Compression test on pile #1 sample a

LABORATOIRES DE MECANIQUE DES SOLS ET DES ROCHES

COMPRESSION UNIAXIALE

Exécuté selon la norme SN 670 353 et LMS+R ER.520

ÉCOLE POLYTECHNIQUE FÉDÉRALE DE LAUSANNE

No éprouvette		Titre de l'étude	Commettant		
			nom		adresse
R0703PIEU1b		AULA EPFL	EPFL-LMS		LAUSANNE
No sond.	Prof. [m]	Nature échantillon	Echantillon prélevé par	Date réception	Date essai
P1b	-	BETON 28 JOURS	COMMETTANT	10.06.11	11.07.11
Mode conservation		Mode préparation éprouvette	Ingénieur responsable		Opérat.
			nom	signature	
HUMIDITE CONTROLEE		SCIE, RECTIFIE	J.-F. Mathier		LG

Haut. [mm]	Diam. [mm]	ρ [t/m³]	w [%]	Ep50% [MN/m²]	Er50% [MN/m²]	σ_c [MN/m²]
304.0	158.0	2.46	-	24300	27100	40.5

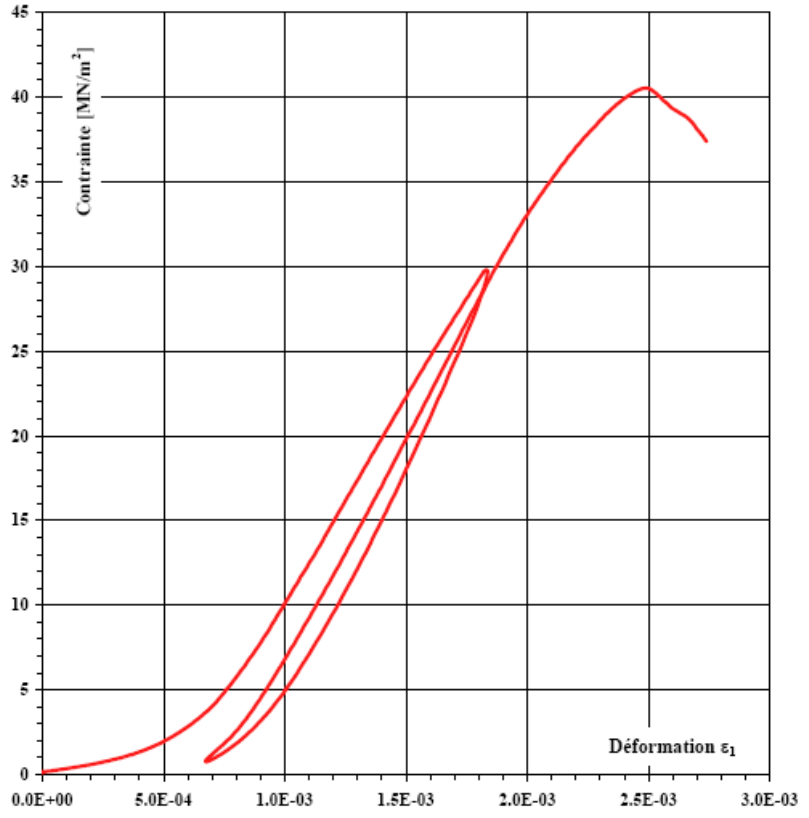

Observations:

Ce protocole ne peut être reproduit partiellement et son contenu ne concerne que l'éprouvette testée
En outre, il fait partie d'une série d'essais, voir page "Rapport d'essais"

Page 1/1
ER.520 07/09
R0703pieu1b.xls

Figure 9:27 Compression test on pile #1 sample b

LABORATOIRES DE MECANIQUE DES SOLS ET DES ROCHES

COMPRESSION UNIAXIALE

Exécuté selon la norme SN 670 353 et LMS+R ER.520

ÉCOLE POLYTECHNIQUE FÉDÉRALE DE LAUSANNE

No éprouvette	Titre de l'étude	Commettant	
		nom	adresse
R0703PIEU2	AULA EPFL	EPFL-LMS	LAUSANNE

No sond.	Prof. [m]	Nature échantillon	Echantillon prélevé par	Date réception	Date essai
P2	-	BETON 28 JOURS	COMMETTANT	09.06.11	11.07.11

Mode conservation	Mode préparation éprouvette	Ingénieur responsable		Opérat.
		nom	signature	
HUMIDITE CONTROLEE	SCIE, RECTIFIE	J.-F. Mathier		LG

Haut. [mm]	Diam. [mm]	ρ [t/m³]	w [%]	Ep50% [MN/m²]	Er50% [MN/m²]	σ_c [MN/m²]
302.0	158.0	2.45	-	26000	-	44.7

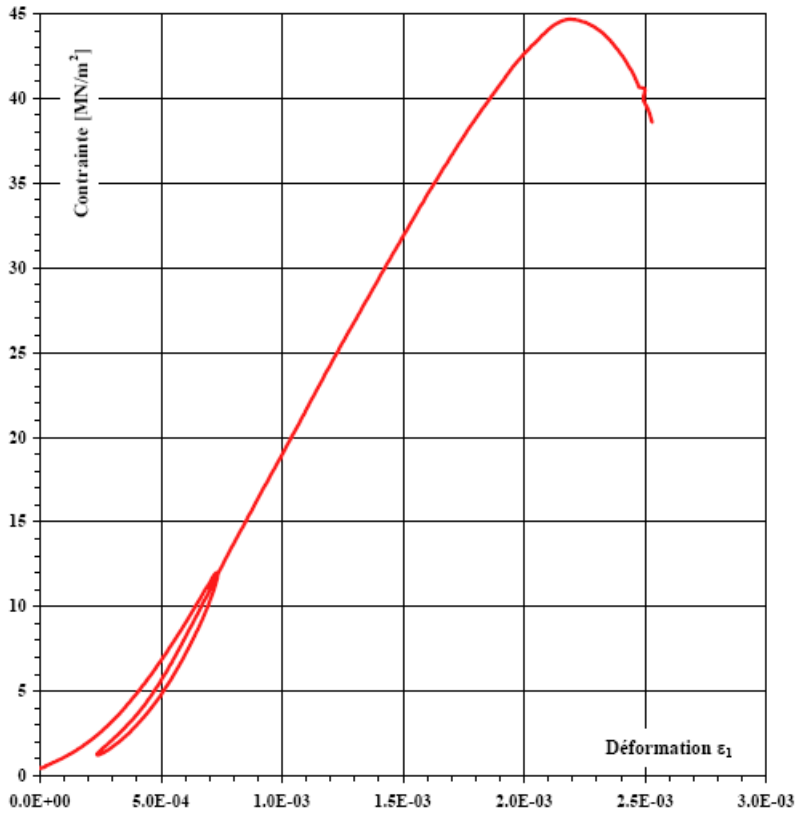

Observations:

Ce protocole ne peut être reproduit partiellement et son contenu ne concerne que l'éprouvette testée
En outre, il fait partie d'une série d'essais, voir page "Rapport d'essais"

Page 1/1
ER.520 07/09
R0703pieu2.xls

Figure 9:28 Compression test on pile #2 sample a

LABORATOIRES DE MECANIQUE DES SOLS ET DES ROCHES

COMPRESSION UNIAXIALE

Exécuté selon la norme SN 670 353 et LMS+R ER.520

ÉCOLE POLYTECHNIQUE FÉDÉRALE DE LAUSANNE

No éprouvette	Titre de l'étude	Commettant	
		nom	adresse
R0703PIEU2b	AULA EPFL	EPFL-LMS	LAUSANNE

No sond.	Prof. [m]	Nature échantillon	Echantillon prélevé par	Date réception	Date essai
P2b	-	BETON 28 JOURS	COMMETTANT	09.06.11	11.07.11

Mode conservation	Mode préparation éprouvette	Ingénieur responsable		Opérat.
		nom	signature	
HUMIDITE CONTROLEE	SCIE, RECTIFIE	J.-F. Mathier		LG

Haut. [mm]	Diam. [mm]	ρ [t/m³]	w [%]	Ep50% [MN/m²]	Er50% [MN/m²]	σ_c [MN/m²]
303.0	158.5	2.46	-	17500	21100	30.3

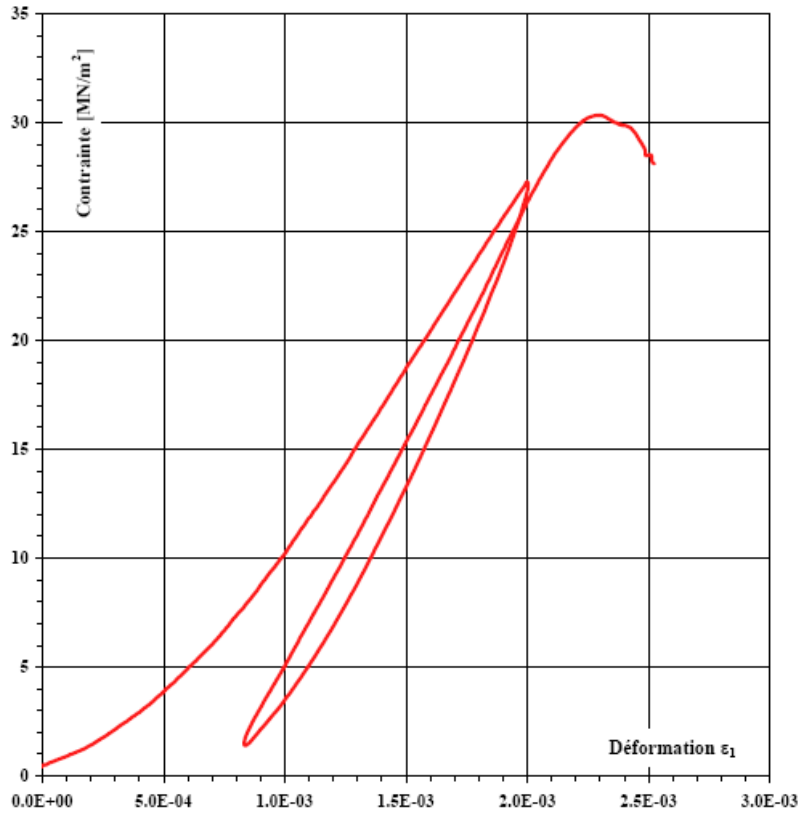

Observations:

Ce protocole ne peut être reproduit partiellement et son contenu ne concerne que l'éprouvette testée
En outre, il fait partie d'une série d'essais, voir page "Rapport d'essais"

Page 1/1
ER.520 07/09
R0703pieu2b.xls

Figure 9:29 Compression test on pile #2 sample b

LABORATOIRES DE MECANIQUE DES SOLS ET DES ROCHES

COMPRESSION UNIAXIALE

Exécuté selon la norme SN 670 353 et LMS+R ER.520

ÉCOLE POLYTECHNIQUE FÉDÉRALE DE LAUSANNE

No éprouvette	Titre de l'étude	Commettant	
		nom	adresse
R0703PIEU3	AULA EPFL	EPFL-LMS	LAUSANNE

No sond.	Prof. [m]	Nature échantillon	Echantillon prélevé par	Date réception	Date essai
P3	-	BETON 28 JOURS	COMMETTANT	07.06.11	08.07.11

Mode conservation	Mode préparation éprouvette	Ingénieur responsable		Opérat.
		nom	signature	
HUMIDITE CONTROLEE	SCIE, RECTIFIE	J.-F. Mathier		LG

Haut. [mm]	Diam. [mm]	ρ [t/m³]	w [%]	Ep50% [MN/m²]	Ej50% [MN/m²]	σ_c [MN/m²]
303.0	157.0	2.45	-	23300	-	57.9

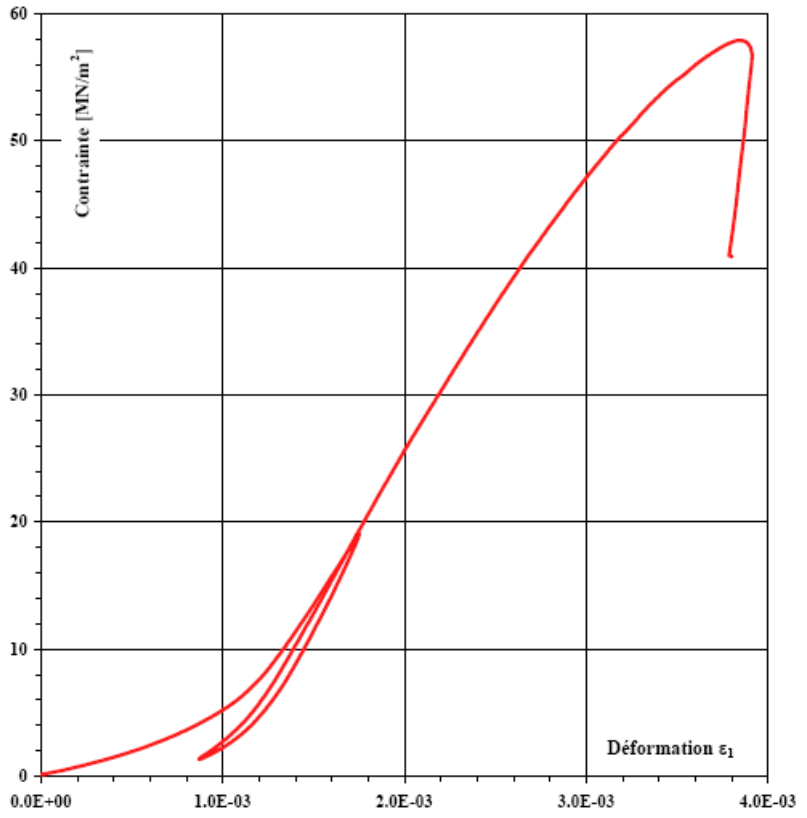

Observations:

Ce protocole ne peut être reproduit partiellement et son contenu ne concerne que l'éprouvette testée
En outre, il fait partie d'une série d'essais, voir page "Rapport d'essais"

Page 1/1
ER.520 07/09
R0703pieu3.xls

Figure 9:30 Compression test on pile #3 sample a

LABORATOIRES DE MECANIQUE DES SOLS ET DES ROCHES

COMPRESSION UNIAXIALE

Exécuté selon la norme SN 670 353 et LMS+R ER.520

ÉCOLE POLYTECHNIQUE FÉDÉRALE DE LAUSANNE

No éprouvette	Titre de l'étude	Commettant	
		nom	adresse
R0703PIEU3b	AULA EPFL	EPFL-LMS	LAUSANNE

No sond.	Prof. [m]	Nature échantillon	Echantillon prélevé par	Date réception	Date essai
P3b	-	BETON 28 JOURS	COMMETTANT	07.06.11	11.07.11

Mode conservation	Mode préparation éprouvette	Ingénieur responsable		Opérat.
		nom	signature	
HUMIDITE CONTROLEE	SCIE, RECTIFIE	J.-F. Mathier		LG

Haut. [mm]	Diam. [mm]	ρ [t/m³]	w [%]	Ep50% [MN/m²]	Er50% [MN/m²]	σ_c [MN/m²]
301.0	158.0	2.45	-	28200	32400	55.2

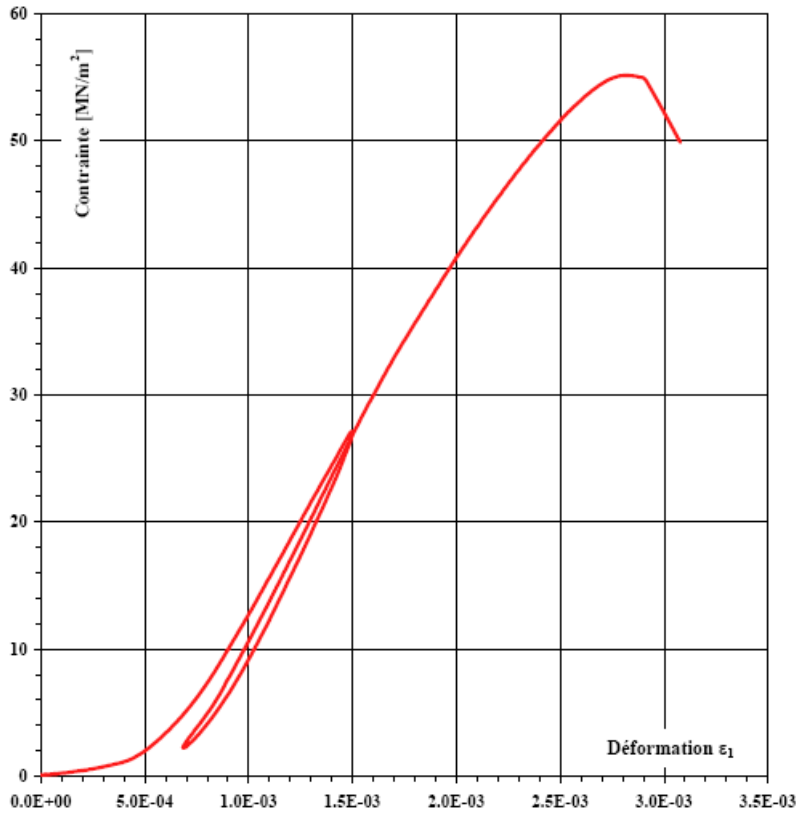

Observations:

Ce protocole ne peut être reproduit partiellement et son contenu ne concerne que l'éprouvette testée
En outre, il fait partie d'une série d'essais, voir page "Rapport d'essais"

Page 1/1
ER.520 07/09
R0703pieu3b.xls

Figure 9:31 Compression test on pile #3 sample b

LABORATOIRES DE MECANIQUE DES SOLS ET DES ROCHES

COMPRESSION UNIAXIALE

Exécuté selon la norme SN 670 353 et LMS+R ER.520

ÉCOLE POLYTECHNIQUE FÉDÉRALE DE LAUSANNE

No éprouvette		Titre de l'étude	Commettant		
			nom		adresse
R0703extensoA		AULA EPFL	EPFL-LMS		LAUSANNE
No sond.	Prof. [m]	Nature échantillon	Echantillon prélevé par	Date réception	Date essai
EXTENSO	-	COULIS 28 JOURS	COMMETTANT	16.06.11	22.07.11

Mode conservation	Mode préparation éprouvette	Ingénieur responsable		Opérat.
		nom	signature	
HUMIDITE CONTROLEE	SCIE, RECTIFIE	J.-F. Mathier		LG

Haut. [mm]	Diam. [mm]	ρ [t/m³]	w [%]	Ep50% [MN/m²]	Er50% [MN/m²]	σ_c [MN/m²]
303.0	157.0	1.54	-	2980	-	7.6

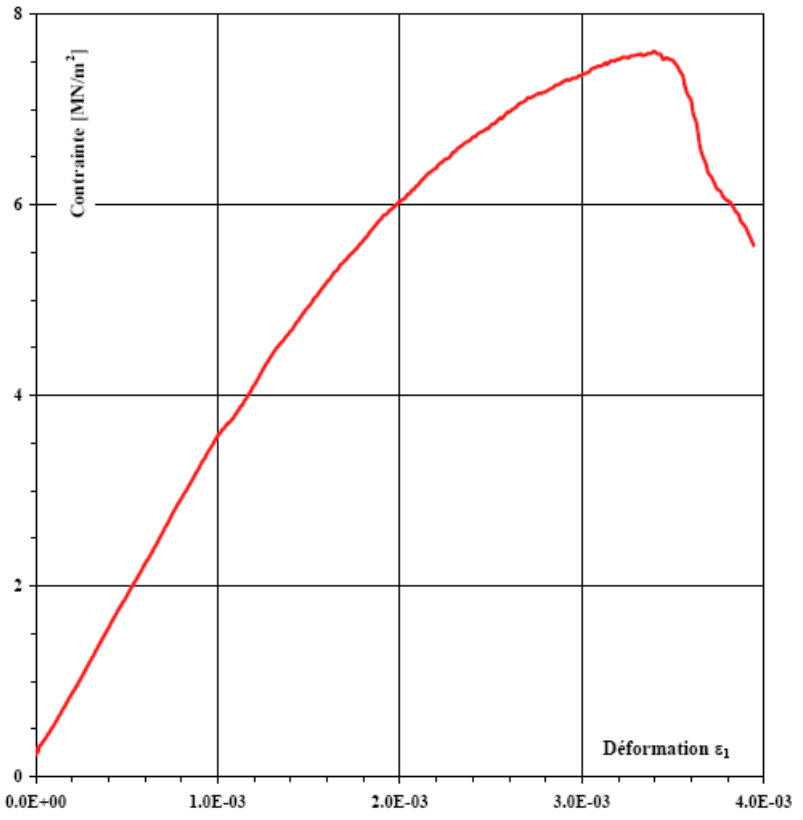

Observations:

Ce protocole ne peut être reproduit partiellement et son contenu ne concerne que l'éprouvette testée
En outre, il fait partie d'une série d'essais, voir page "Rapport d'essais"

Page 1/1
ER.520 07/09
R0703extensoA.xls

Figure 9:32 Compression test on borehole extensometer grout sample a

LABORATOIRES DE MECANIQUE DES SOLS ET DES ROCHES

COMPRESSION UNIAXIALE

Exécuté selon la norme SN 670 353 et LMS+R ER.520

ÉCOLE POLYTECHNIQUE FÉDÉRALE DE LAUSANNE

No éprouvette		Titre de l'étude	Commettant		
			nom		adresse
R0703extensoB		AULA EPFL	EPFL-LMS		LAUSANNE
No sond.	Prof. [m]	Nature échantillon	Echantillon prélevé par	Date réception	Date essai
EXTENSO	-	COULIS 28 JOURS	COMMETTANT	16.06.11	22.07.11

Mode conservation	Mode préparation éprouvette	Ingénieur responsable		Opérat.
		nom	signature	
HUMIDITE CONTROLEE	SCIE, RECTIFIE	J.-F. Mathier		LG

Haut. [mm]	Diam. [mm]	ρ [t/m³]	w [%]	Ep50% [MN/m²]	Er50% [MN/m²]	σ_c [MN/m²]
302.0	158.0	1.53	-	2580	3900	6.4

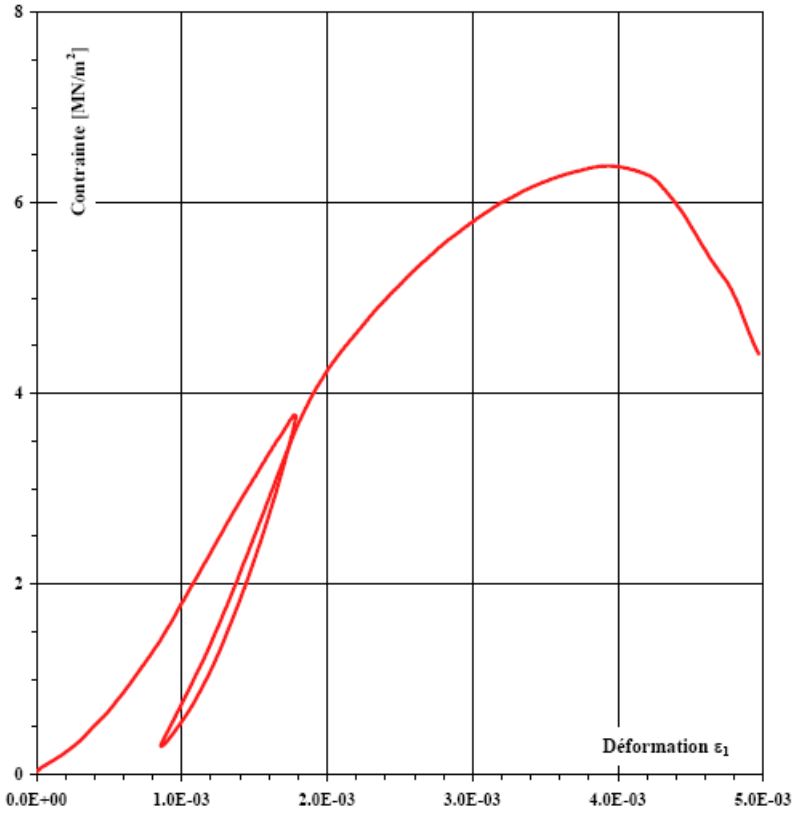

Observations:

Ce protocole ne peut être reproduit partiellement et son contenu ne concerne que l'éprouvette testée
En outre, il fait partie d'une série d'essais, voir page "Rapport d'essais"

Page 1/1
ER.520 07/09
R0703extensoB.xls

Figure 9:33 Compression test on borehole extensometer grout sample b

9.5.7 Retrieved positions of pile top strain gauges

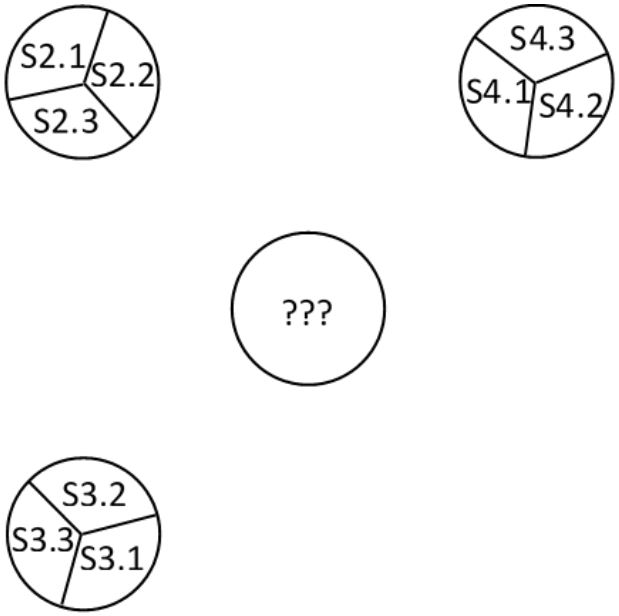

Figure 9:34 Retrieved positions of pile top strain gauges

9.5.8 Individual strain-temperature histories

This section regroups the different strain-temperature histories of each of the strain gauge. These curves were used to determine the profiles of degree of freedom of the piles.

9.5.8.1 Free head test

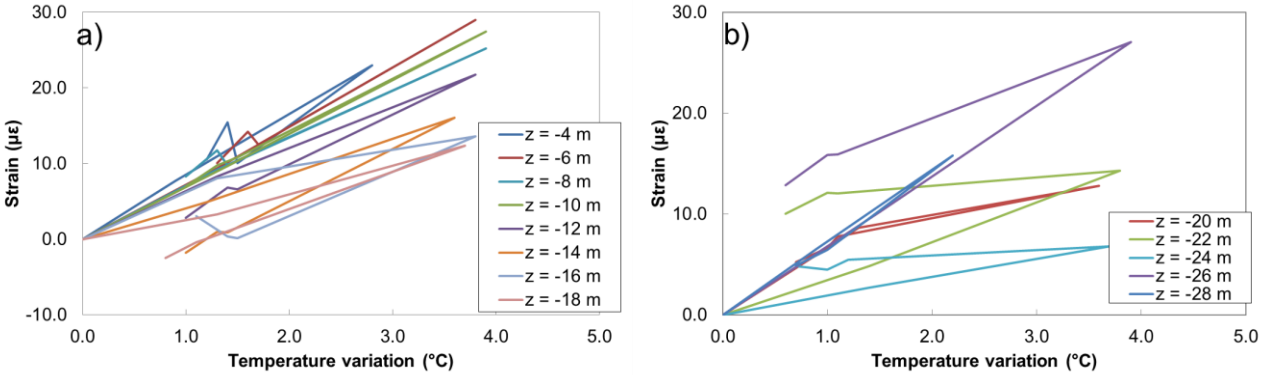

Figure 9:35 Temperature – strain histories along pile #1 in (a) the weak soil layers and (b) the molasse bedrock during the free head test

9.5.8.2 Single tests

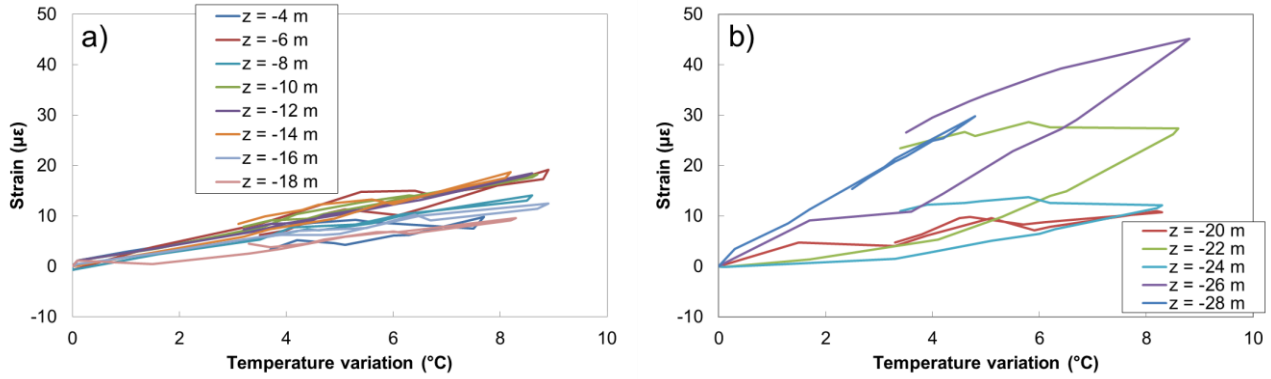

Figure 9:36 Temperature – strain histories along pile #1 in (a) the weak soil layers and (b) the molasse bedrock during the single test 1

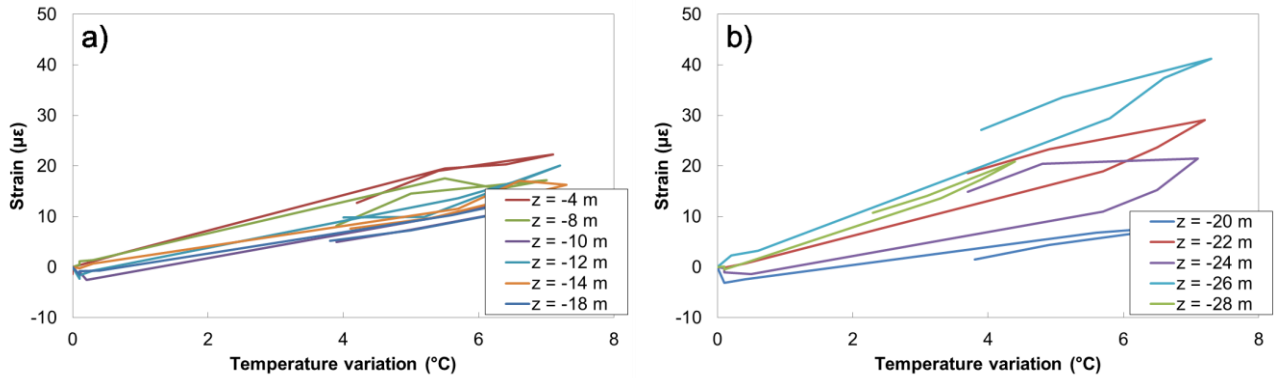

Figure 9:37 Temperature – strain histories along pile #4 in (a) the weak soil layers and (b) the molasse bedrock during the single test 2

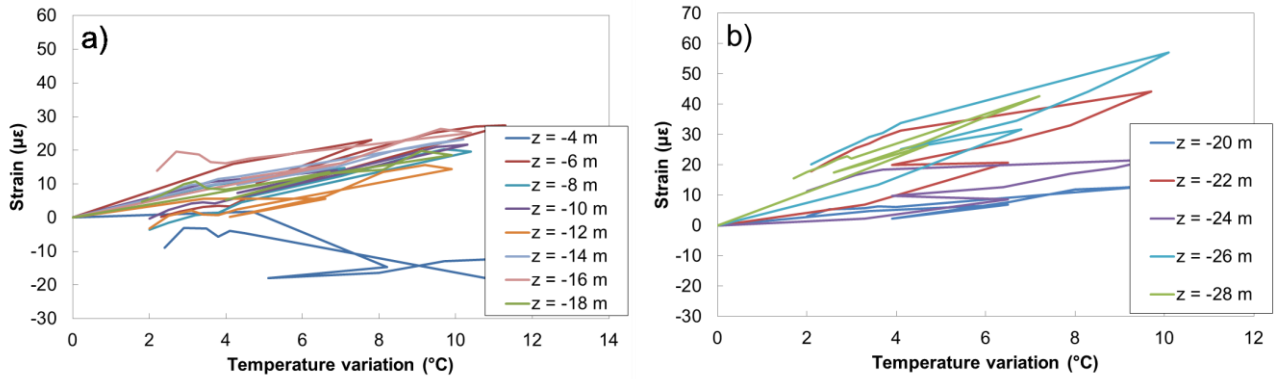

Figure 9:38 Temperature – strain histories along pile #3 in (a) the weak soil layers and (b) the molasse bedrock during the single test 3

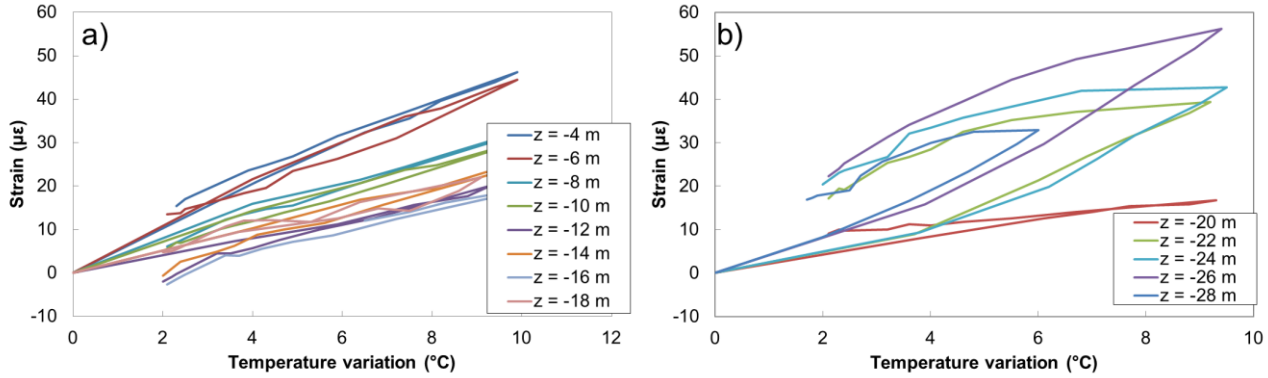

Figure 9:39 Temperature – strain histories along pile #2 in (a) the weak soil layers and (b) the molasse bedrock during the single test 4

9.5.8.3 Group test

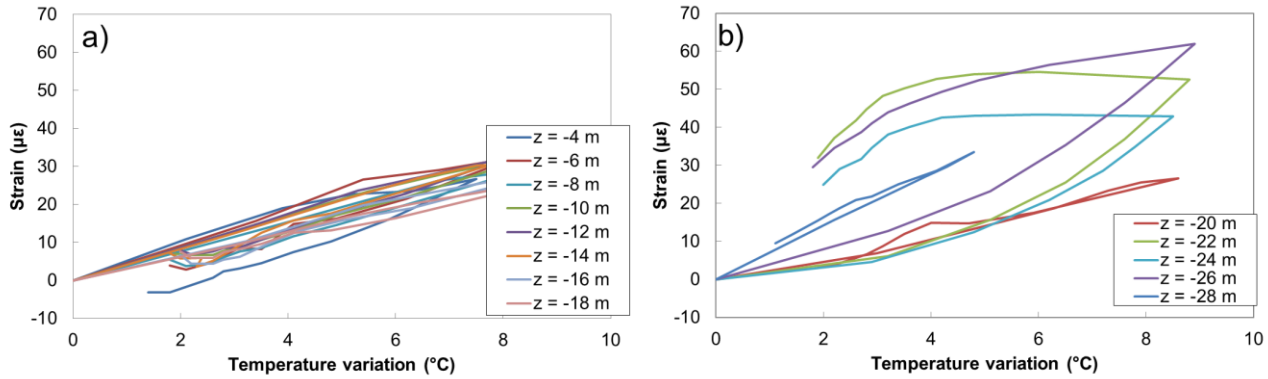

Figure 9:40 Temperature – strain histories along pile #1 in (a) the weak soil layers and (b) the molasse bedrock during the group test

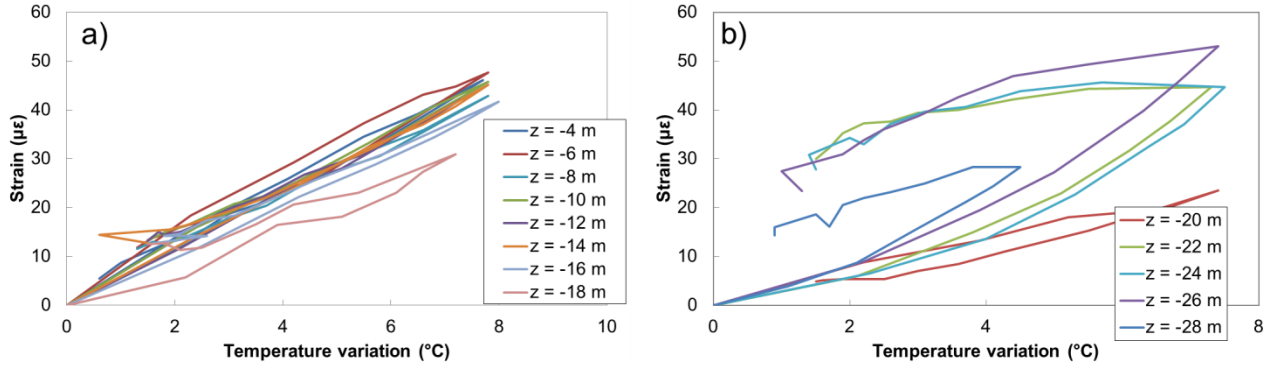

Figure 9:41 Temperature – strain histories along pile #2 in (a) the weak soil layers and (b) the molasse bedrock during the group test

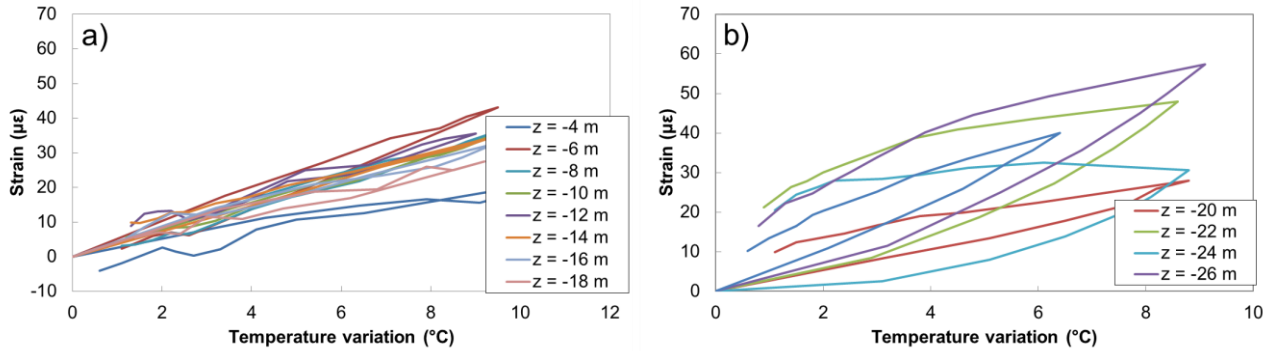

Figure 9:42 Temperature – strain histories along pile #3 in (a) the weak soil layers and (b) the molasse bedrock during the group test

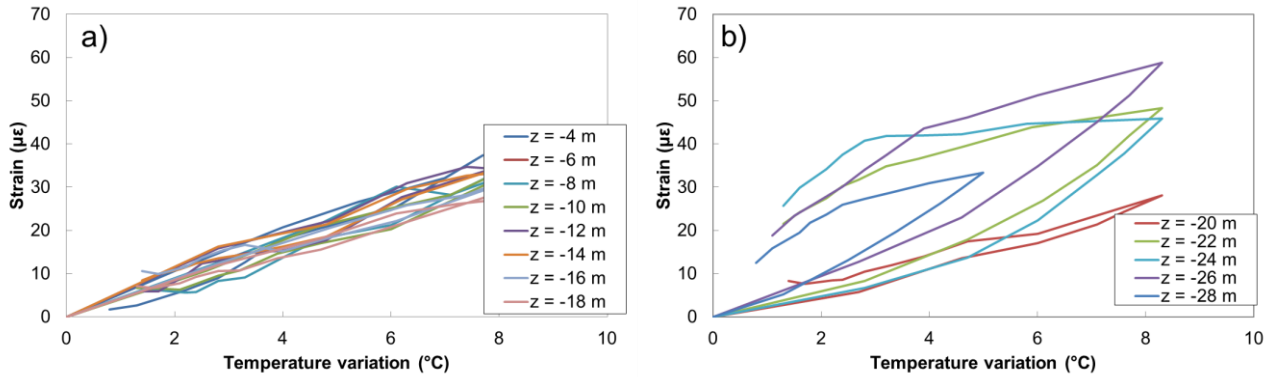

Figure 9:43 Temperature – strain histories along pile #4 in (a) the weak soil layers and (b) the molasse bedrock during the group test

9.5.9 *Thermal response tests*

9.5.9.1 *Free head test – pile #1*

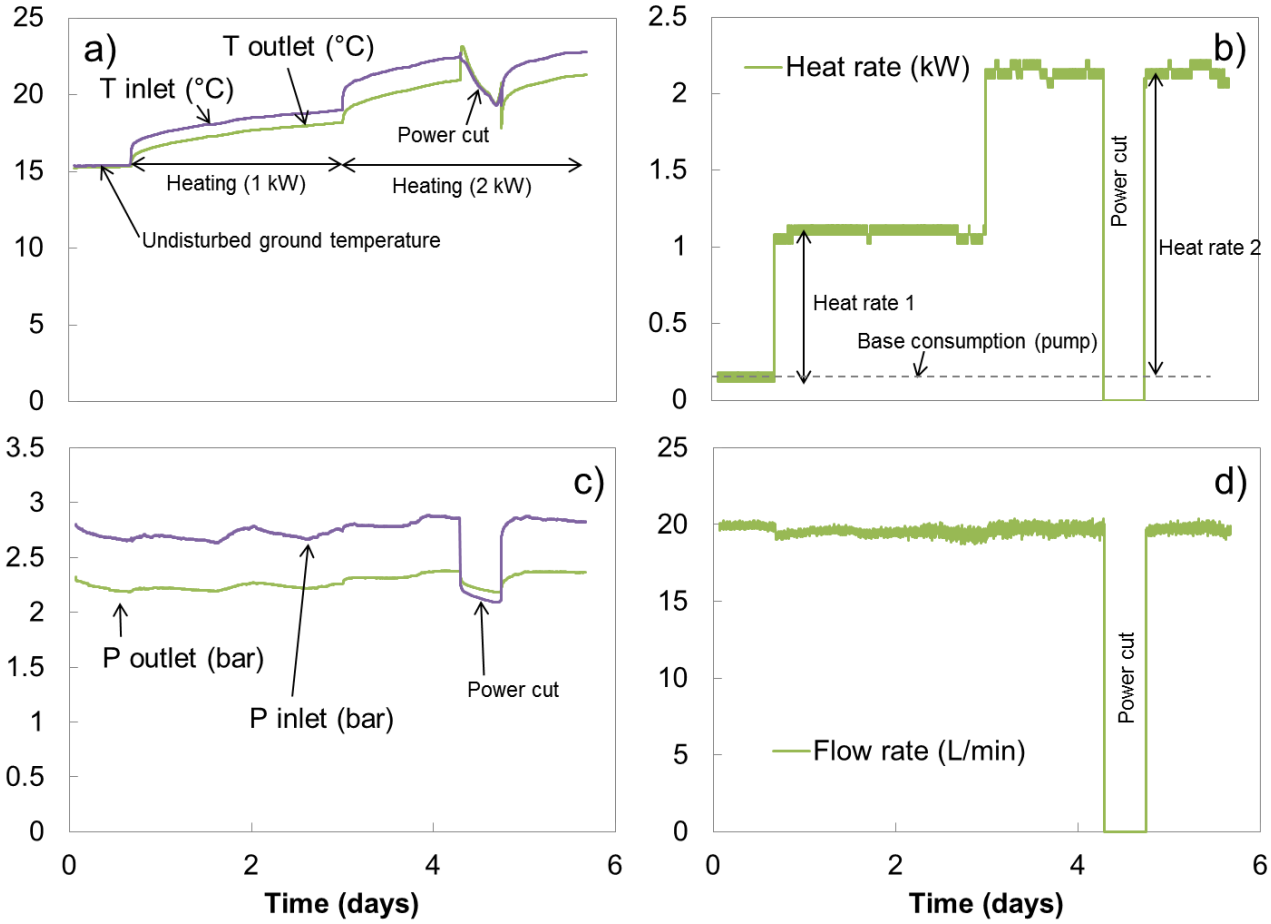

Figure 9:44 Main outputs of the TRT on pile #1 during the "free head" test with (a) inlet and outlet fluid temperatures, (b) module power consumption, (c) inlet and outlet fluid pressures and (c) flow rate

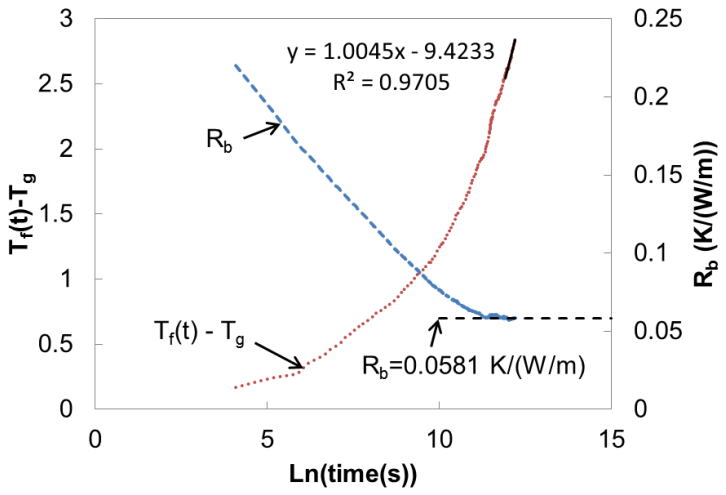

Figure 9:45 Evolution of pile #1 temperature anomaly and thermal resistance during the "free head" test, only during the first phase of the TRT with P=1 kW

9.5.9.2 Single test – pile #1

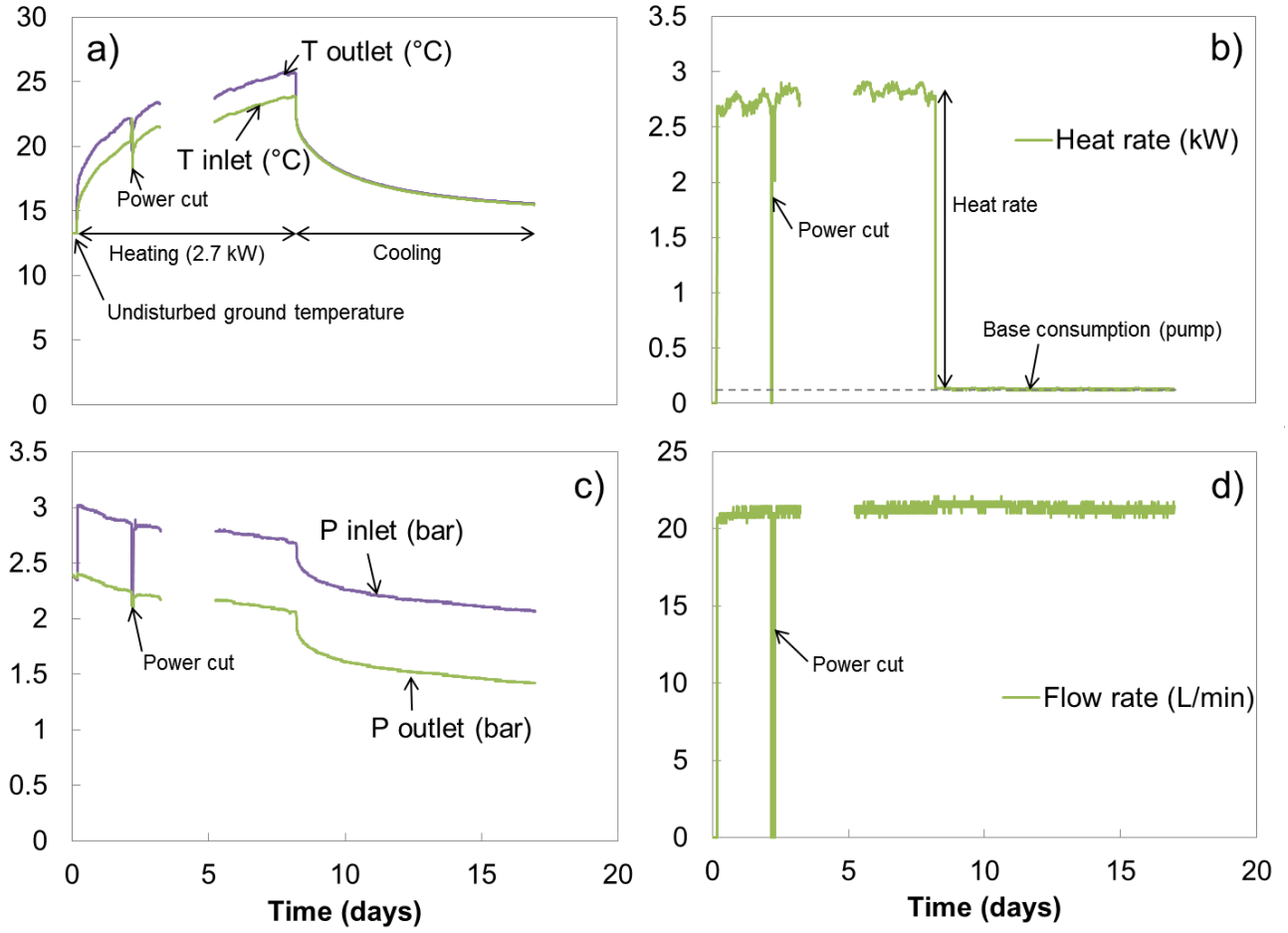

Figure 9:46 Main outputs of the TRT on pile #1 during the tests "single pile" with (a) inlet and outlet fluid temperatures, (b) module power consumption, (c) inlet and outlet fluid pressures and (c) flow rate

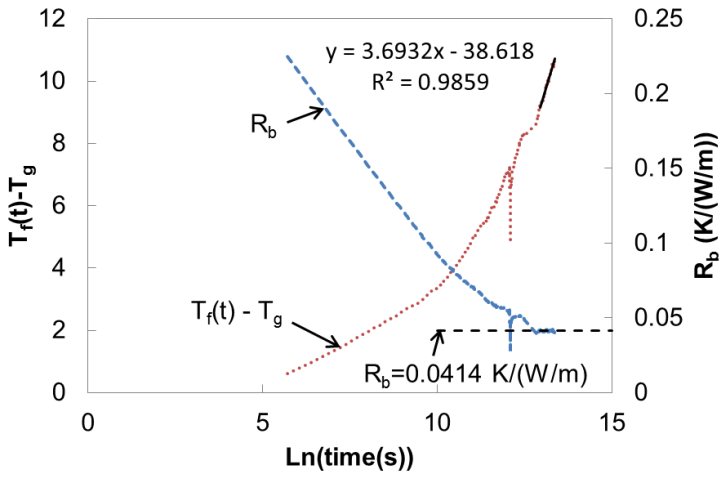

Figure 9:47 Evolution of pile #1 temperature anomaly and thermal resistance during the tests "single pile"

9.5.9.3 Single test – pile #2

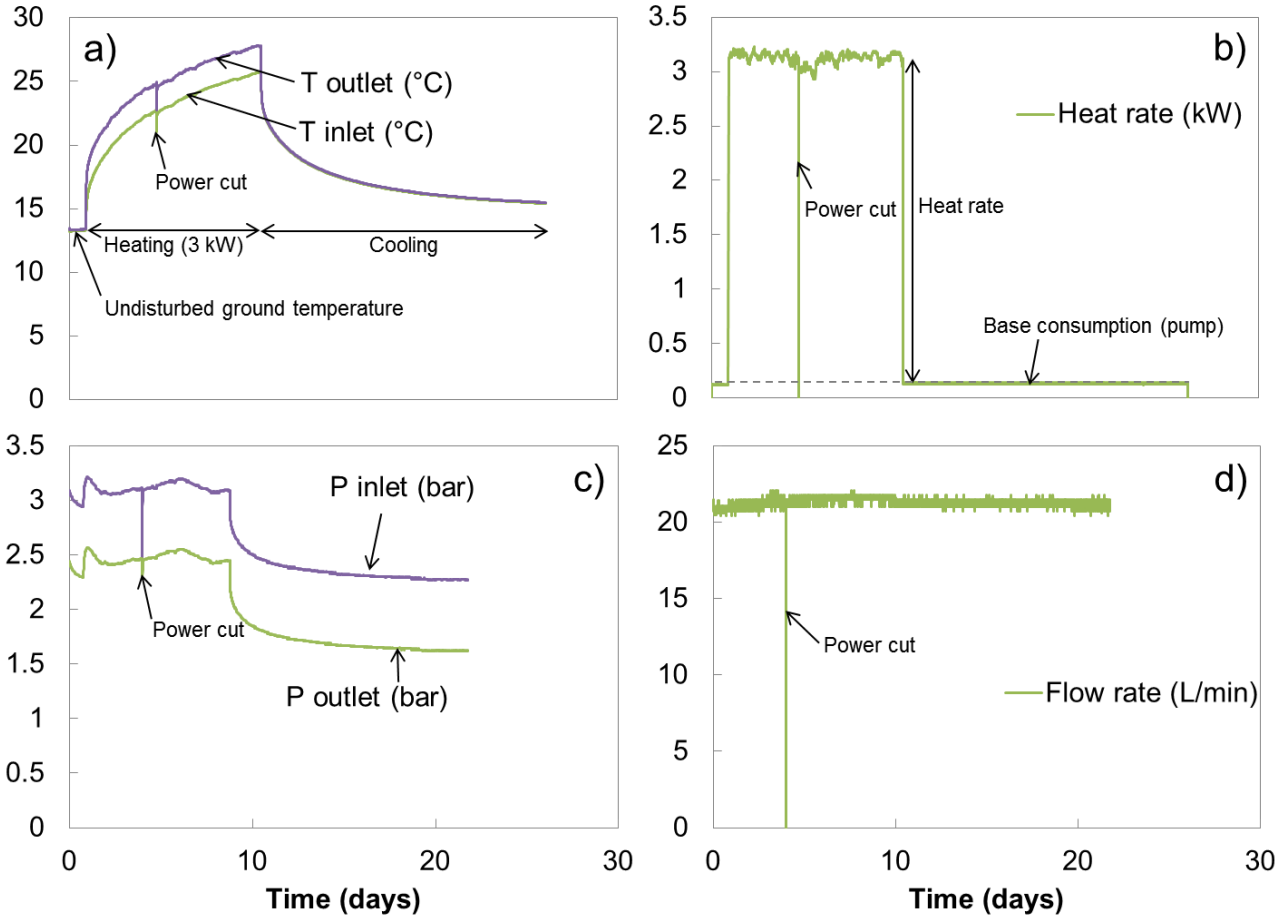

Figure 9:48 Main outputs of the TRT on pile #2 during the tests "single pile" with (a) inlet and outlet fluid temperatures, (b) module power consumption, (c) inlet and outlet fluid pressures and (c) flow rate

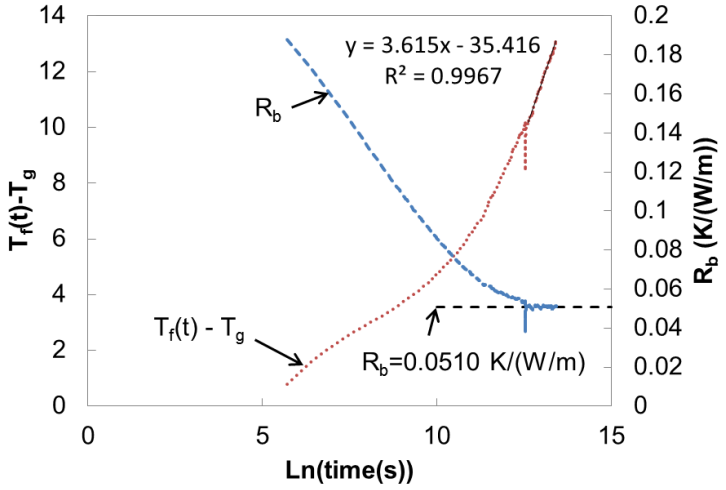

Figure 9:49 Evolution of pile #2 temperature anomaly and thermal resistance during the tests "single pile"

9.5.9.4 Single test – pile #4

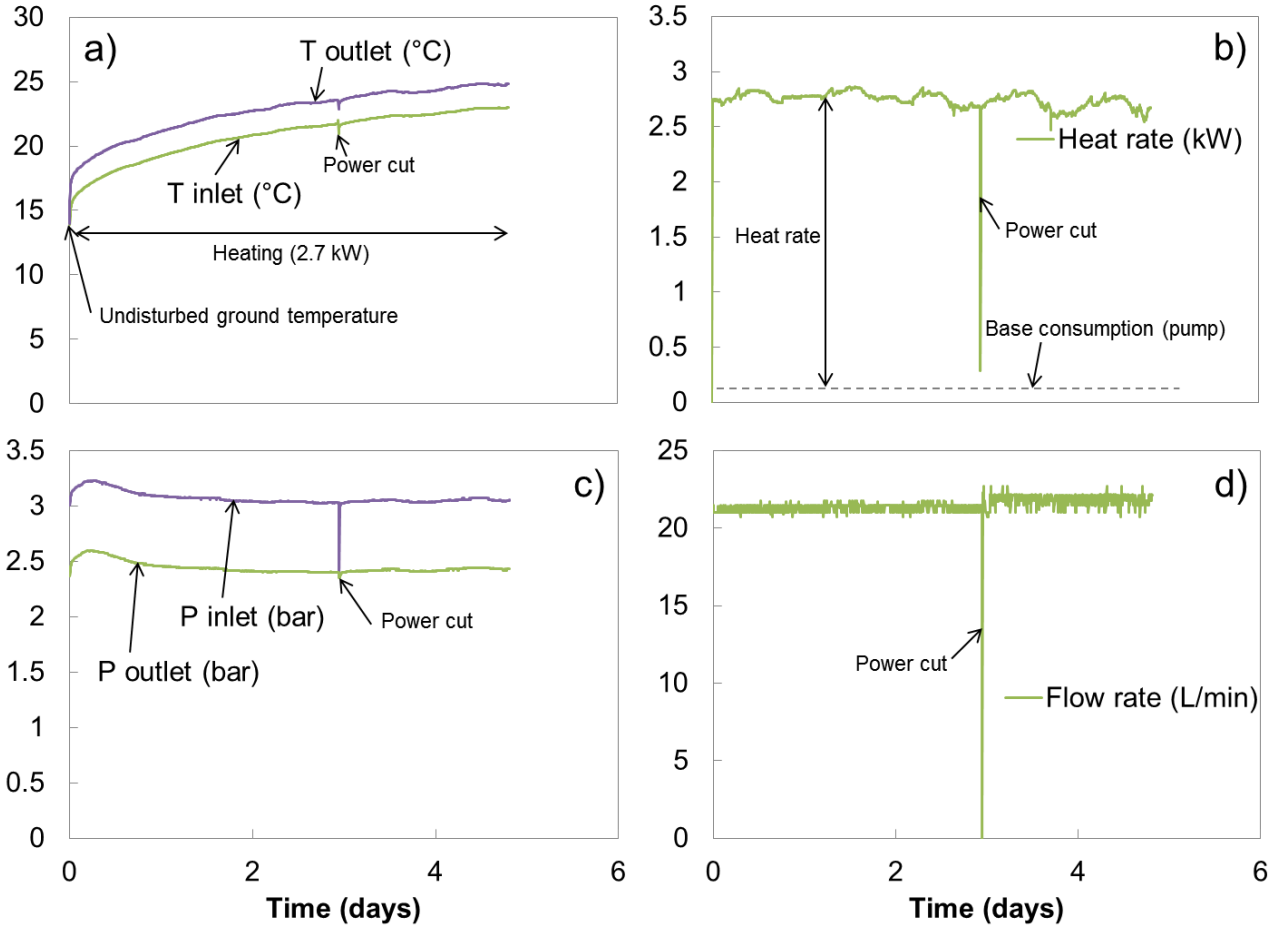

Figure 9:50 Main outputs of the TRT on pile #4 during the tests "single pile" with (a) inlet and outlet fluid temperatures, (b) module power consumption, (c) inlet and outlet fluid pressures and (c) flow rate

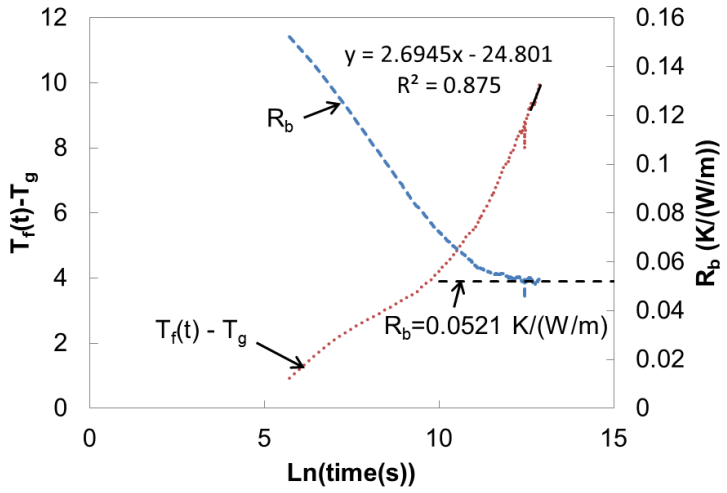

Figure 9:51 Evolution of pile #4 temperature anomaly and thermal resistance during the tests "single pile"

9.5.9.5 Group test – pile #1

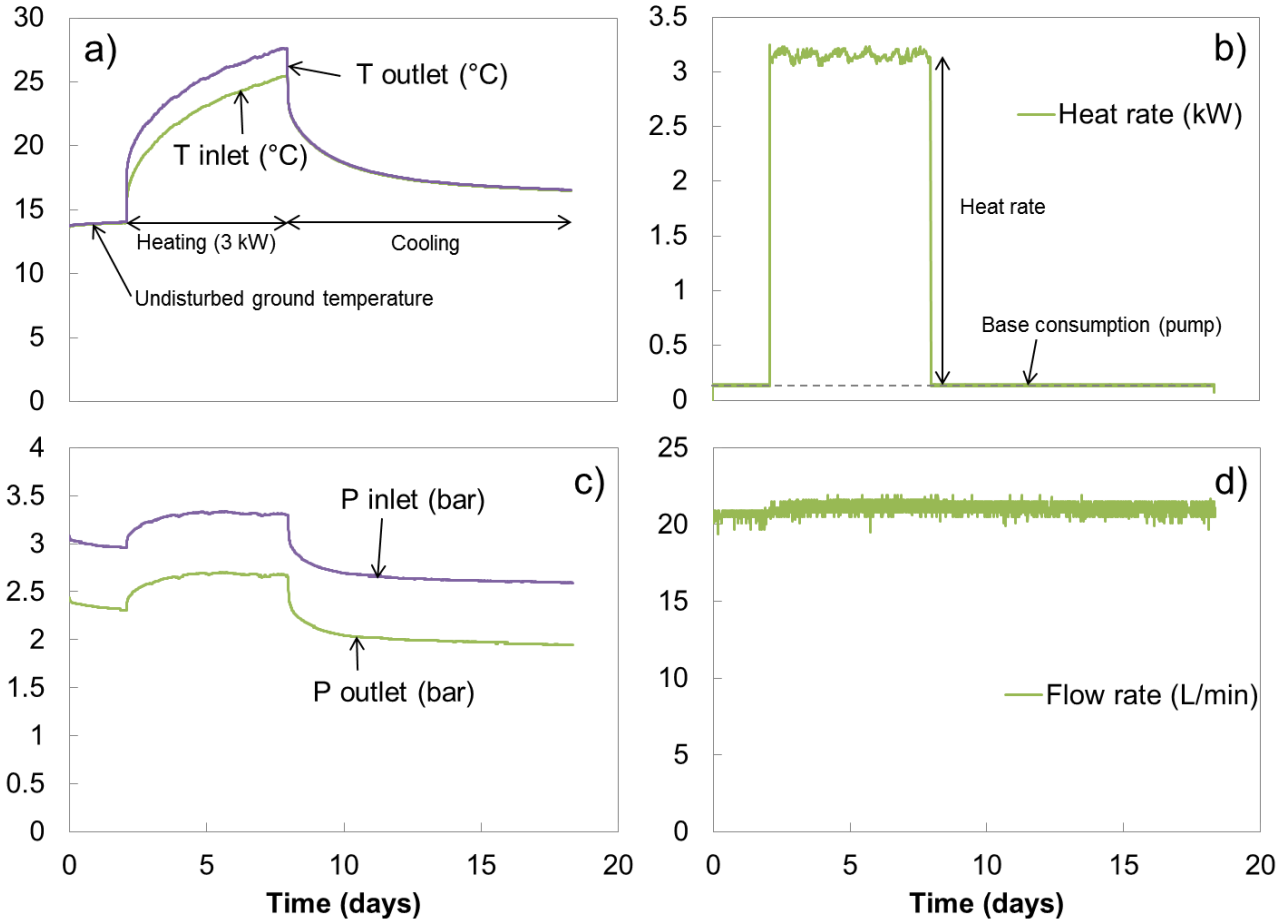

Figure 9:52 Main outputs of the TRT on pile #1 during the group test with (a) inlet and outlet fluid temperatures, (b) module power consumption, (c) inlet and outlet fluid pressures and (c) flow rate

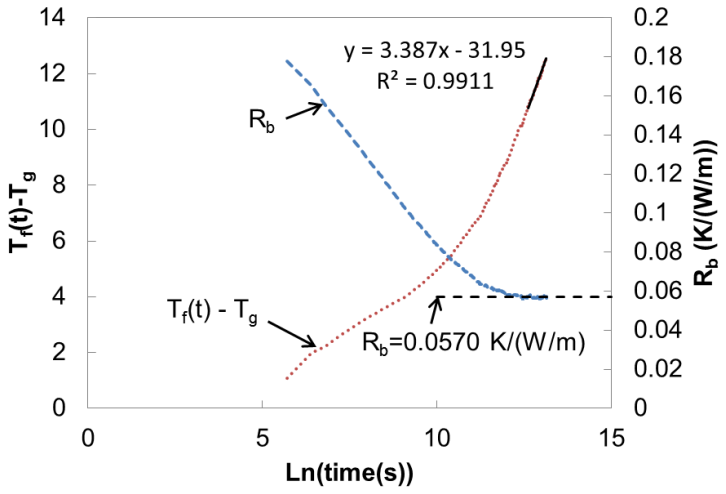

Figure 9:53 Evolution of pile #1 temperature anomaly and thermal resistance during the group test

9.5.9.6 Group test – piles #2 and 3

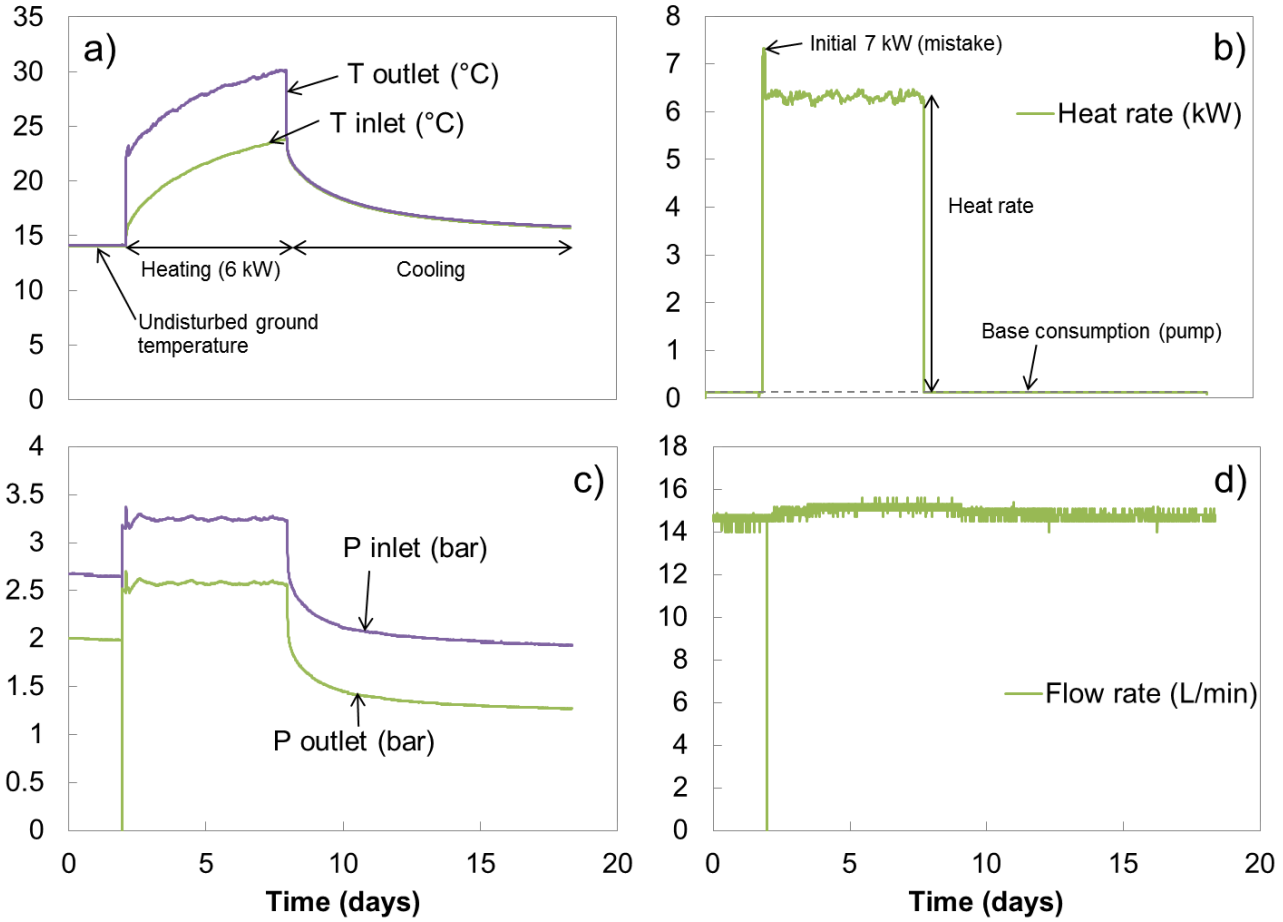

Figure 9:54 Main outputs of the TRT on piles #2 and #3 (connected in series) during the group test with (a) inlet and outlet fluid temperatures, (b) module power consumption, (c) inlet and outlet fluid pressures and (c) flow rate

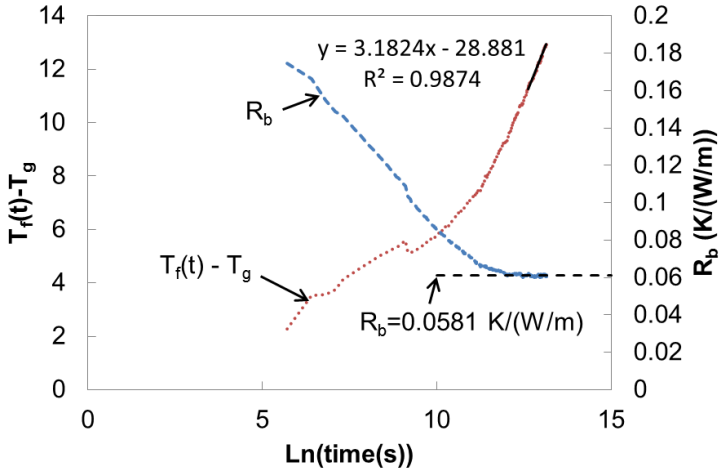

Figure 9:55 Evolution of piles #2 and #3 (connected in series) temperature anomaly and thermal resistance during the group test

9.5.9.7 Group test – pile #4

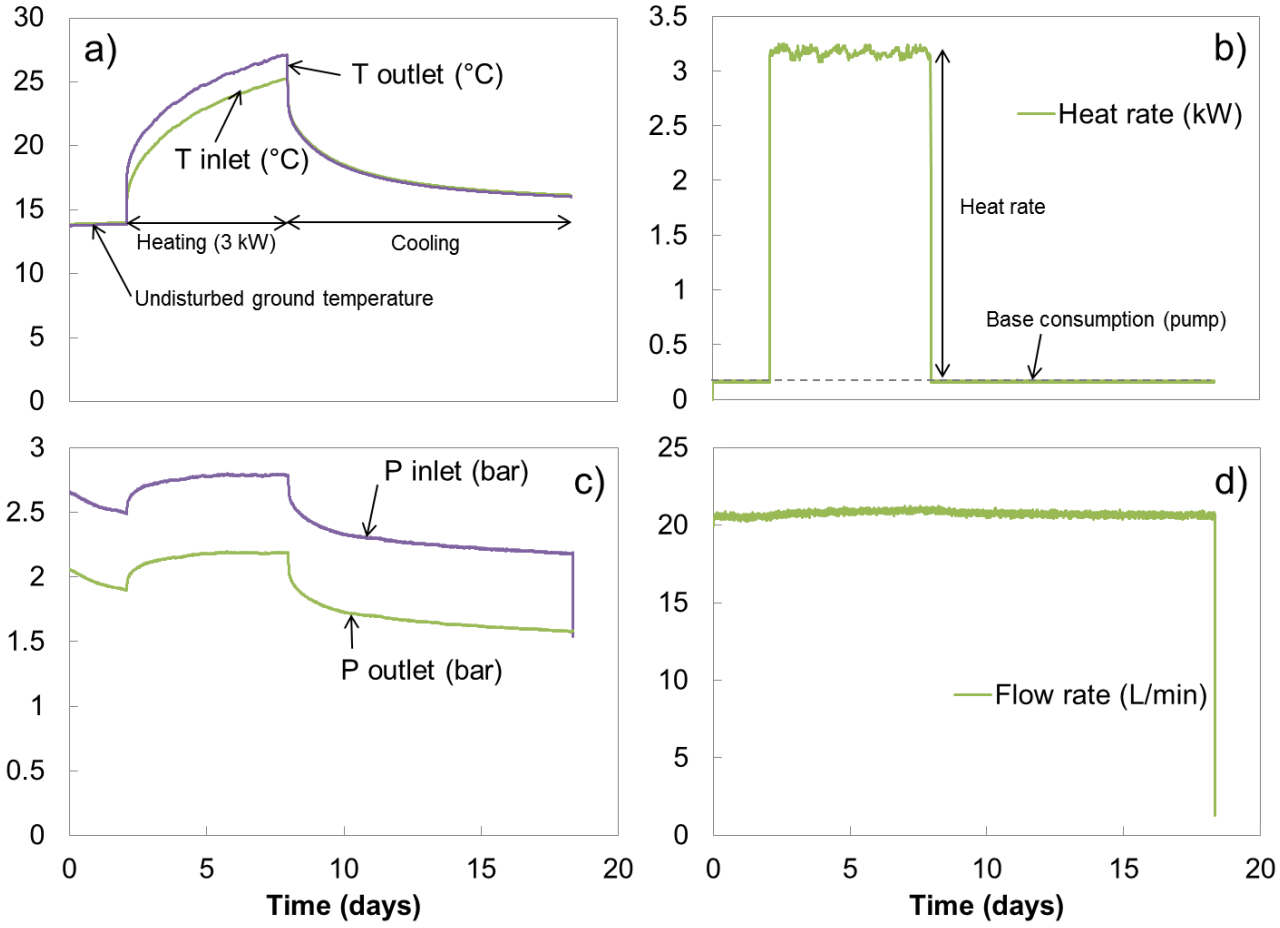

Figure 9:56 Main outputs of the TRT on pile #4 during the group test with (a) inlet and outlet fluid temperatures, (b) module power consumption, (c) inlet and outlet fluid pressures and (c) flow rate

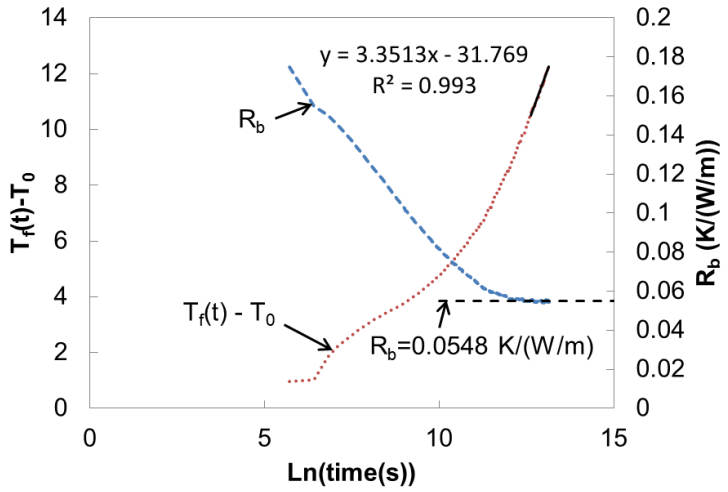

Figure 9:57 Evolution of pile #4 temperature anomaly and thermal resistance during the group test

9.5.9.8 Long thermal response test – pile #3

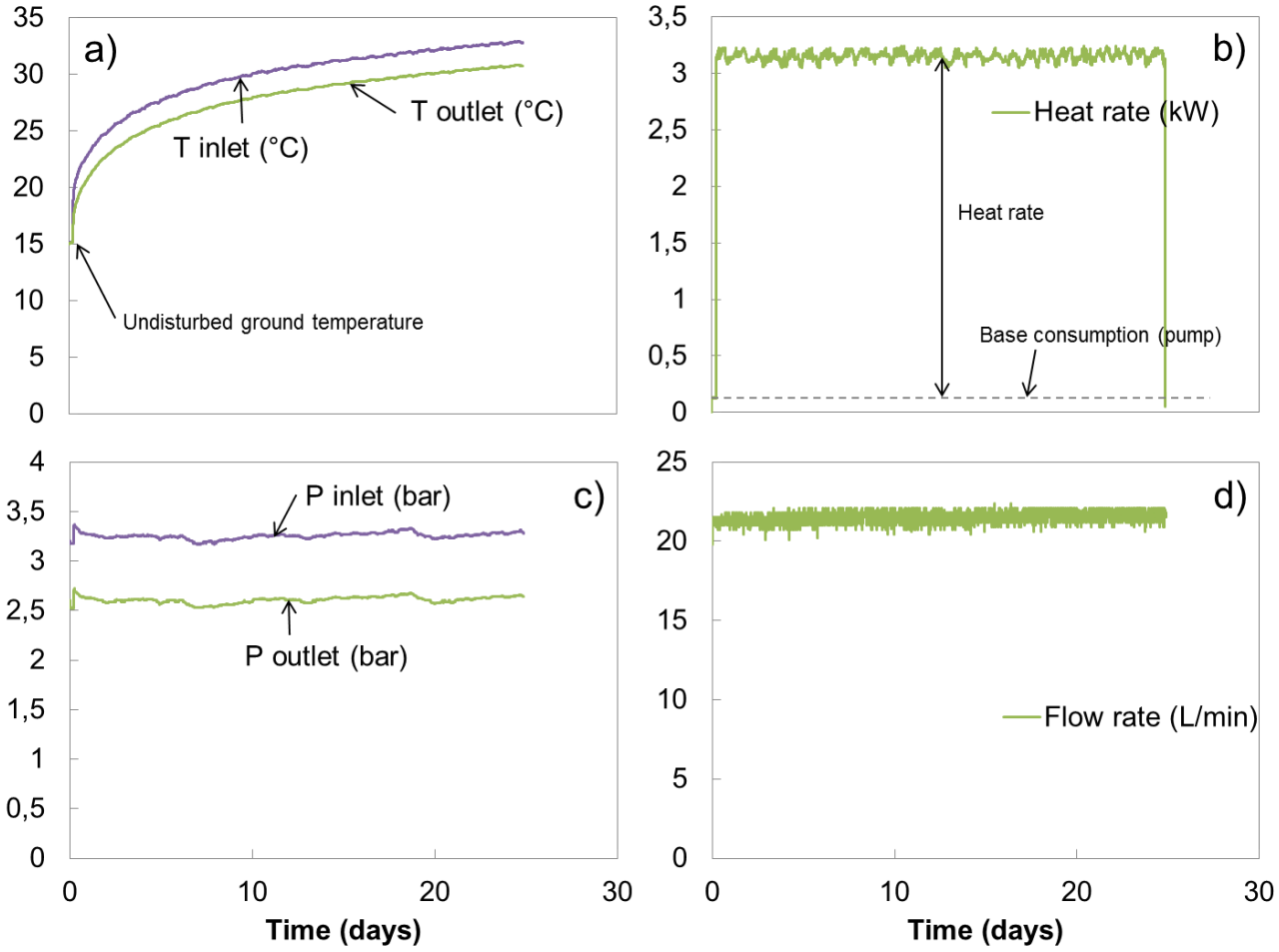

Figure 9:58 Main outputs of the TRT on pile #3 during the long thermal response test with (a) inlet and outlet fluid temperatures, (b) module power consumption, (c) inlet and outlet fluid pressures and (c) flow rate

References

Adam D. (2008a). Tunnels as Energy Sources: Technology and Case Histories. Tunnel. **Special edition:** 83-86.

Adam D. (2008b). Increased efficiency of ground storage (in Greman), presentation, Ringvorlesung ökologie - TU Wien.

Adam D. and Markiewicz R. (2009). Energy from earth-coupled structures, foundations, tunnels and sewers. *Géotechnique* **59**(3): 229-236.

Adams W. M. (2006). The Future of Sustainability: Re-thinking Environment and Development in the Twenty-first Century, The World Conservation Union (IUCN). Report of the IUCN Renowned Thinkers Meeting, 29-31 January 2006.

Al Nakshabandi G. and Kohnke H. (1965). Thermal conductivity and diffusivity of soils as related to moisture tension and other physical properties. *Agricultural Meteorology* **2**: 271-279.

Amar S., Clarke B. G. F., Gambin M. P. and Orr T. L. L. (1991). The application of pressuremeter test results to foundation desing in Europe, Part 1: Predrilled pressuremeters - selt-boring pressurementers., European Soil Mechanics and Foundation Engineering. European Regional Technical Committee N°. 4. A. A. Balkema, Rotterdam, The Netherlands.

Amatya B. L., Soga K., Bourne-Webb P. J., Amis T. and Laloui L. (2012). Thermo-mechanical behaviour of energy piles. *Géotechnique* **62**(6): 503-519.

Amis T. and Robinson C. A. W. (2010). Inserting geothermal loops into the diaphragm walls of the Knightsbridge Palace Hotel project, www.slideshare.net.

Amis T. and Loveridge F. (2014). Energy piles and other thermal foundations for GSHP - developments in UK practice and research. *REHVA*(1): 32-35.

Anstett M., Hubbuch M., Laloui L., Matthey B., Morath M., Pahud D., Parriaux A., Rybach L., Schönbächler M., Tacher L. and Wilhelm J. Using the heat from the ground heat through foundation and retaining concrete structures (in French), Documentation 0190, S. S. o. e. a. architects, 2005.

Armaleh S. and Desai C. (1987). Load deformation response of axially loaded piles. *Journal of Geotechnical Engineering* **113**(12): 1483-1500.

Axelsson G. (2010). Sustainable geothermal utilization – Case histories; definitions; research issues and modelling. *Geothermics* **39**(4): 283-291.

Bauchau O. A. and Craig J. I. (2009). Euler-Bernoulli beam theory. Structural Analysis. O. A. Bauchau and J. I. Craig, Springer Netherlands. **163:** 173-221.

Baudoin A. (1988). Stockage intersaisonnier de chaleur dans le sol par batterie d'échangeurs baionnette verticaux: modèle de prédimensionnement. Ph.D Thesis, Université de Reims, Reims, France.

Bear J. and Cheng A. H. D. (2010). Modeling Groundwater Flow and Contaminant Transport. Springer,

Bengt H. F. (1980). The analysis of results from routine pile load tests. *Ground Engineering*: 19-31.

Bonvin M. and Cordier P. (2002). Energy piles with hot and cold distributions integrated within the building structure (in French, Peiux énergétiques avec distribution de chaleur et de froid intégrée dans la structure), Geothermal Energy program, Swiss Federal Office of Energy. DIS-P 33846 / DIS-C 74140.

Bordas Freitas T. M., Cruz Silva F. and Bourne-Webb P. J. (2013). The response of energy foundations under thermo-mechanical loading. 18th International Conference on Soil Mechanics and Geotechnical Engineering, Paris.

Bouazza A., Wang B. and Singh R. M. (2013). Soil effective thermal conductivity from energy pile thermal tests. Coupled Phenomena in Environmental Geotechnics. Torino, Italy**:** 211-219.

Bourne-Webb P. J., Amatya B., Soga K., Amis T., Davidson C. and Payne P. (2009). Energy pile test at Lambeth College, London: geotechnical and thermodynamic aspects of pile response to heat cycles. *Géotechnique* **59**(3): 237-248.

Bourne-Webb P. J. (2013). Observed response of energy geostructures. Energy Geostructures: Innovation in Underground Engineering. L. Laloui and A. Di Donna. Hoboken, ISTE Ltd. and John Wiley and Sons**:** 45-67.

Brandl H. (2006). Energy foundations and other thermo-active ground structures. *Géotechnique* **56**(2): 81-122.

Brettman T. and Amis T. (2011). Thermal conductivity evaluation of a pile group using geothermal energy piles. Geo-Frontiers 2011. Dallas, Texas, USA**:** 499-508.

Bristow K. L., Campbell G. S. and Calissendorff K. (1993). Test of a Heat-Pulse Probe for Measuring Changes in Soil Water Content. *Soil Sci. Soc. Am. J.* **57**(4): 930-934.

Brodbaek K. T., Moller M., Sorensen S. P. H. and Augustesen A. H. (2009). Review of p-y relationships in cohesionless soil, Aalbrog University, Department of Civil Engineering, Water & Soil. Aalborg, Denmark.

Caichu X., Meng S., Guozhu Z., Suguang X. and Yichuan Z. (2012). Experimental study on geothermal heat exchangers buried in diaphragm walls. *Energy and Buildings* **52**: 50-55.

Callari C. (2004). Coupled numerical analysis of strain localization induced by shallow tunnels in saturated soils. *Computers and Geotechnics* **31**: 193-207.

Cao J. (2010). Numerical modelling of sand-pile interface for large numbers of cycles: Development of a cycles jumping method (in French). University of Lille, Lille, France.

Carslaw H. S. and Jaeger J. C. (1947). Conduction of Heat in Solids. Oxford University Press, New York, NY, USA.

Cekerevac C. and Laloui L. (2004). Experimental study of thermal effects on the mechanical behaviour of a clay. *International Journal for Numerical and Analytical Methods in Geomechanics* **28**(3): 209-228.

Charlier R. (1987). Unified approach to some nonlinear problems in continuum mechanics by the finite element method (in French). Ph.D. Thesis, University of Liège, Liège, Belgium.

Charlier R., Raud J. P. and Collin F. (2001). Numerical modelling of coupled transient phenomena. *Revue Française de Génie Civil* **5**(6): 719-741.

Chin J. T. and Poulos H. G. (1991). A "T-Z" approach for cyclic axial loading analysis of single piles. *Computers and Geotechnics* **12**: 289-320.

Collin F., Li X., Radu J. P. and Charlier R. (2002). Thermo-hydro-mechanical coupling in clay barriers. *Engineering Geology* **64**: 179-193.

Collin F. (2003). Thermo-hydro-mechanica couplings in partially saturated soil and soft rocks (in French). Ph.D. Thesis, Department of Applied Engineering, University of Liège, Liège, Belgium.

Coyle H. M. and Reese L. C. (1966). Load transfer for axially loaded piles in clay. *Journal of the Soil Mechanics and Foundations Division* **92**(2): 1-26.

CSTB T. a. S. C. f. B. Dynamic simulation tools. from http://www.valpac.fr/wacom.aspx?idarchitecture=50&Country=.

Cui P., Li X., Man Y. and Fang Z. (2011). Heat transfer analysis of pile geothermal heat exchangers with spiral coils. *Applied Energy* **88**(11): 4113-4119.

Delaleux F., Py X., Olives R. and Dominguez A. (2012). Enhancement of geothermal borehole heat exchangers performances by improvement of bentonite grouts conductivity. *Applied Thermal Engineering* **33–34**(0): 92-99.

Di Donna A., Dupray F. and Laloui L. (2013). Numerical study of the heating-cooling effects on the geotechnical behaviour of energy piles. International symposium on Coupled Phenomena in Environmental Geotechnics, Torino, Italy, Taylor & Francis Group.

Di Donna A. (2014). Thermo-mechanical aspects of energy piles. School of Architecture, Civil and Environmental Engineering, Civil Engineering, Swiss Federal Institute of Technology Lausanne, Lausanne, Switzerland.

Diao N. R., Qinyun L. and Zhaohong F. (2004a). Heat transfer in ground heat exchangers with groundwater advection. *International Journal of Thermal Sciences* **43**: 1203-1211.

Diao N. R., Zeng H. Y. and Fang Z. H. (2004b). Improvement in modeling of heat transfer in vertical ground heat exchangers. *HVAC & R Research* **10**(4): 459-470.

Diot J. (2012). On estimating the needs, criteria and examples, Journées de la Géothermie en région Centre, 21 et 22 février 2012. Orléan, France.

Dupray F., Laloui L. and Kazangba A. (2014). Numerical analysis of seasonal heat storage in an energy pile foundation. *Computers and Geotechnics* **55**: 67-77.

Eskilson P. (1987). Thermal Analysis of Heat Extraction Boreholes. Ph.D Thesis, Department of Mathematical Physics, University of Lund, Lund, Sweden.

European Committee for Standardization (2004): Eurocode 7: Geotechnical design. EN 1997-1:2004:E.

Farouki O. T. (1986). Thermal properties of soils. Trans Tech Pub., Rockport, MA.

Forbes J. D. (1849). Account of some experiments on the temperature of the Earth at different depths, and in different soils, near Edinburgh. *Transactions of the Royal Society of Edinburgh* **10**: 189-236.

Fourier J. (1822). Analytical theory of heat (in French). Paris.

Franco A. and Vaccaro M. (2012). An integrated " Reservoir-Plant" strategy for a sustainable and efficient use of geothermal resources. *Energy* **37**(1): 299-310.

Frank R. and Zhao S. R. (1982). Estimation of axially loaded pile settlements with pressiometric paramters for bored piles in thin-grained soils (in French). *Bull Liaison Lab Ponts Chaussées, Paris, France* **119**: 17-24.

Frank R., Kalteziotis N., Bustamante M., Christoulas S. and Zervogiannia H. (1991). Evaluation of performance of two piles using pressuremeter method. *Journal of Geotechnical Engineering* **117**(5): 695-713.

Franzius J. N. and Pralle N. (2011). Turning segmental tunnels into sources of renewable energy. *Proceedings of the Institution of Civil Engineers-Civil Engineering* **164**(1): 35-40.

Fredlung D. G. and Xing A. (1994). Equations for tghe soil-water characteristic curve. *Canadian Geotechnical Journal* **31**(3): 521-532.

Frodl S., Franzius J. N. and Bartl T. (2010). Design and construction of the tunnel geothermal system in Jenbach. *Geomechanichs and Tunnelling* **3**(5): 658-668.

Fromentin A., Pahud D., Laloui L., Moreni M., Kapp C. and Roth K. (1998). Heat exchanger piles - Noth district of EPFL, Preliminary study of technical and economic feasability (in French), Swiss Institute of Technology Lausanne. LMS SY40 / LASEN 120.105.

Garber D., Choudhary R. and Soga K. (2013). Risk based lifetime costs assessment of a ground source heat pump (GSHP) system design: Methodology and case study. *Building and Environment* **60**(0): 66-80.

Glišić B. and Simon N. (2000). Monitoring of concrete at very early age using stiff SOFO sensor. *Cement and Concrete Composites* **22**(2): 115-119.

Goode J., III and McCartney J. S. (2014). Centrifuge modeling of energy foundations in sand and clay. 8th International Conference on Physical Modelling in Geotechnics (ICPMG2014), Perth, Australia.

Ground Source Heat Pump G. A. (2012): Thermal Pile, Installation & Materials Standards.

Heidari M., El Naggar H., Jahanandish M. and Ghahramani A. (2014). Generalized cyclic p-y curve modeling for analysis of laterally loaded piles. *Soil Dynamics and Earthquake Engineering* **63**: 138-149.

Heizen Mit Öl. (2012). Preisvergleich Jahresmittel. from http://www.erdoel-vereinigung.ch/fr/heizenmitoel/Peise/PreisvergleichJahresmittel.aspx.

Hellstrom G. (1991). Ground heat storage, Thermal Analysis of Duct Storage Systems. Departement of Mathematical Physics, University of Lund, Lund, Sweden.

Hemmingway P. and Long M. (2013). Energy piles: site investigation and analysis. *Proceedings of the ICE - Geotechnical Engineering* **166**: 1-15.

Hermansson Å., Charlier R., Collin F., Erlingsson S., Laloui L. and Sršen M. S. (2009). Heat Transfer in Soils. Water in Road Structures. D. Andrew, Springer Netherlands. **5:** 69-79.

Hinkel K. M. (1997). Estimating seasonal values of thermal diffusivity in thawed and frozen soils using temperature time series. *Cold Regions Science and Technology* **26**(1): 1-15.

Hoekstra P., Delaney A. and Atkins R. (1973). Measuring the thermal properties of cylindrical specimens by the use of sinusoidal temperature waves., CRREL Technical Report 244. AD 770425.

Imhasly S., Signorelli S. and Rybach L. (2013). Staticis of geothermal utilisation in Switzerland, Edition 2012 (in German), Swiss Society of Geothermal Energy (SVG/SSG). Zürich.

Inaudi D., Laloui L. and Steinmann G. (2000). Looking below the surface. *Concrete Engineering International* **4**(3).

Ingersoll L. R. and Plass H. J. (1948). Theory of the ground pipe heat source for the heat pump. *ASHVE Transactions* **54**: 119-122.

Ingersoll L. R., Zobel O. and Ingersoll A. (1954). Heat Conduction with engineering, geological, and other applications. McGraw-Hill, New York.

Jin M., Dickinson R. E. and Vogelmann A. M. (1997). A Comparison of CCM2–BATS Skin Temperature and Surface-Air Temperature with Satellite and Surface Observations. *Journal of Climate* **10**(7): 1505-1524.

Kemmler A., Piégsa A., Ley A., Keller M., Jakob M. and Catenazzi G. (2013). Analysis of the Swiss energy consumption according to end use, from 2000 to 2012 (in german), Swiss Federal Office of Energy. Bern.

Kersten M. B. (1949). Laboratory research for the determination of the thermal properties of soils,

Knellwolf C., Péron H. and Laloui L. (2011). Geotechnical analysis of heat exchanger piles. *Journal of Geotechnical and Geoenvironmental Engineering* **137**(10): 890-902.

Kovari K. and Tisa A. (1998). Computational model and charts for cut and cover tunnels. Colloquium tunnel structures. I. a. f. b. a. s. engineering. Stockholm, Sweden.

Kramer A. C. and Basu P. (2014). Performance of a model geothermal pile in sand. 8th Internation Conference on Physical Modelling in Geotechnics, Perth, Australia.

Kürten S. (2011). Use of geothermal enery with thermo-active seal panels. 21st European young geotechnical engineers'conference. F. B. J. Barends, J. Breedeveld, R. B. J. Brinkgreve, M. Korff and L. A. v. Paassen. Rotterdam, the Netherlands**:** 327-332.

Laloui L., Moreni M., Steinmann G., Vulliet L., Fromentin A. and Pahud D. (1999). Test of a static pile foundation submitted to thermomechanical loads under real service conditions (in French), Swiss Federal Office of Energy (SFOE). Lausanne.

Laloui L. (2001). Thermomechanical behaviour of soils. *Revue Française de Génie Civil* **5**(6): 809-843.

Laloui L. and Cekerevac C. (2003). Thermo-plasticity of clays: An isotropic yield mechanism. *Computers and Geotechnics* **30**(8): 649-660.

Laloui L., Moreni M. and Vulliet L. (2003). Behaviour of a dual-purpose pile foundation, support and heat exchanger. *Canadian Geotechnical Journal* **40**(2): 388-402.

Laloui L., Nuth M. and Vulliet L. (2006). Experimental and numerical investigations of the behaviour of a heat exchanger pile. *International Journal for Numerical and Analytical Methods in Geomechanics* **30**(8): 763-781.

Laloui L. and Cekerevac C. (2008). Non-isothermal plasticiy model for cyclic behaviour of soils. *International Journal for Numerical and Analytical Methods in Geomechanics* **32**: 437-460.

Laloui L. and François B. (2009). ACMEG-T: Soil thermoplasticity model. *Journal of Engineering Mechanics* **135**(9): 932-944.

Laloui L. and Di Donna A. (2011). Understanding the behaviour of energy geo-structures. *Proceedings of the ICE - Civil Engineering* **164**(4): 184-191.

Laloui L. and Di Donna A., Eds. (2013). Energy Geostructures Innovation in Underground Engineering. Hoboken.

Lang H. J. and Huder J. (1978). Soil Mechanics and Foundation Engineering: The behavior of soils and the major basic structural concepts (in German).

Lee I.-M. and Nam S.-W. (2001). The study of seepage forces acting on the tunnel lining and tunnel face in shallow tunnels. *Tunnelling and Underground Space Technology* **16**(1): 31-40.

Lloret S., Inaudi D., Glisic B., Kronenberg P. and Vurpillot S. (2000). Optical set-up development for the monitoring of structural dynamic behavior using SOFO sensors. Smart Structures and Materials 2000: Sensory Phenomena and Measurement Instrumentation for Smart Structures and Materials. R. O. Claus and W. B. Spillman. Bellingham, Spie-Int Soc Optical Engineering. **3986:** 199-205.

Loveridge F., Brettman T., Olgun C. G. and Powrie W. (2014a). Assessing the applicability of thermal response testing to energy piles. Global Perspectives on the Sustainability Execution of Foundations Works. Stockholm, Sweden.

Loveridge F. and Powrie W. (2014). 2D thermal resistance of pile heat exchangers. *Geothermics* **50**(0): 122-135.

Loveridge F., Powrie W. and Nicholson D. P. (2014b). Comparison of two different models for pile thermal response interpretation. *Acta Geotechnica* **9**: 367-384.

Man Y., Yang H., Diao N., Liu J. and Fang Z. (2010). A new model and analytical solutions for borehole and pile ground heat exchangers. *International Journal of Heat and Mass Transfer* **53**(13–14): 2593-2601.

Materials A. S. f. T. a. (1963): Thermal conductivity of materials by means of guarded hot plate.

Matlock H. (1970). Correlation for design of laterally loaded piles in soft clay. Second annual offshore technology conference, Houston, Texas.

Mattsson N., Steinmann G. and Laloui L. (2008). Advanced compact device for the in situ determination of geothermal characteristics of soils. *Energy and Buildings* **40**(7): 1344-1352.

McCartney J. S. and Rosenberg J. E. (2011). Impact of heat exchange on side shear in thermo-active foundations. Geo-Frontiers 2011, Dallas, TX.

Mikkelsen P. M. (2002). Cement-bentonite grout backfill for borehole instruments. *Geotechnical Instrumentation News* **December 2002**: 38-42.

Mimouni T., Dupray F. and Laloui L. (2013). Estimating the geothermal potential of heat exchanger anchors on a cut and cover tunnel. *Geothermics* **51**: 380-387.

Mimouni T. and Laloui L. (2014). Towards a secure basis for the design of geothermal piles. *Acta Geotechnica* **9**(3): 355-366.

Mochlinski K. (1964). Some industrila measurments of thermal properties of soil. International Study Group on Soils, Cambridge, England.

Mogensen P. (1983). Fluid to duct wall heat transfer in duct system heat storages. International Conference of Subsurface Heat Storage in Theory and Pratice, Swedish Council for Building Research.

Molina-Giraldo N., Blum P., Zhu K., Bayer P. and Zhaohong F. (2011). A moving finite line source model to simulate borehole heat exchangers with groundwater advection. *International Journal of Thermal Sciences* **50**(12): 2506-2513.

Monfort J. (2012). Design of UTES (Underground Thermal Energy Storage) for shallow geothermal systems (in French). Intersol'2012, Paris.

Murchison J. M. and O'Neill M. W. (1984). Evaluation of p-y relationships in cohesionless soils. Analysis and Design of Pile Foundations. Proceedings of a Symposium in conjunction with the ASCE National Convention.

Murphy K. D. and McCartney J. S. (2012). Behavior of full-scale energy foundations in Denver, Colorado. GeoChallenges**:** 217-229.

Murphy K. D. and McCartney J. S. (2014). Seasonal response of energy foundations during building operation. *Geotechnical and Geological Engineering*.

Murphy K. D., McCartney J. S. and Henry K. S. (2014a). Evaluation of thermo-mechanical and thermal behavior of full-scale energy foundations. *Acta Geotechnica*.

Murphy K. D., McCartney J. S. and Henry K. S. (2014b). Thermo-mechanical characterization of a full-scale energy foundation. From soil behaviour fundamentals to innovations in geotechnical engineering.

Network T. C. R. E. (2002). Commercial Earth Energy Systems: A Buyer's Guide, Renewable and Electrical Energy Division, Energy and Resources Branch, Natural Resources Canada, Gouvernment of Canada.

Nguyen Pham P. T. (2008). In situ and laboratory testing of natural clayey soils under small strains (in French). Laboratoire des Ponts et Chaussées, Ecole National des Ponts et Chaussées, Paris.

Nicholson D. P., Chen A. Q., Pillai A. and Chendorain M. (2013). Developments in thermal pile and thermal tunnel linings for city scale GSHP systems. Thirty-Eight Workshop on Geothermal Reservoir Engineering, Standford University, Stanford, California.

OFEN (2012). Schweizerische Gesamtenergiestatistik 2011, OFEN.

Ouyang Y., Soga K. and Leung Y. F. (2011). Numerical back-analysis of energy pile test at Lambeth College, London. Geo-Frontiers 2011, Dallas, TX.

Pahud D. (1999). Simulation tool for heating/cooing systems with heat exchanger piles or boreholes heat exchangers, Swiss Federal Office of Energy.

Pahud D. and Matthey B. (2001). Comparison of the thermal performance of double U-pipe borehole heat exchangers measured in situ. *Energy and Buildings* **33**(5): 503-507.

Pahud D. and Hubbuch M. (2007). Monitoring and optimising the energy pile installation at the dock Midfield of Zurich airport, Swiss Federal Office of Energy. DIS-Project Nr 37373.

Pahud D. (2013). A case study: the dock Midfield of Zurich airport. Energy Geostructures: Innovation in Underground Engineering. L. Laloui and A. Di Donna. Hoboken, ISTE Ltd. and John Wiley and Sons.

Paksoy H. O., Andersson O., Abaci S., Evliya H. and Turgut B. (2000). Heating and cooling of a hospital using solar energy coupled with seasonal thermal energy storage in an aquifer. *Renewable Energy* **19**(1–2): 117-122.

Panet M. (1995). Le calcul des tunnels par la méthode convergence-confinement. Presses de l'Ecole Nationale des Ponts et Chaussées, Paris, France.

Park H., Lee S.-R., Yoon S. and Choi J.-C. (2013). Evaluation of thermal response and performance of PHC energy pile: Field experiments and numerical simulation. *Applied Energy* **103**(0): 12-24.

Pasquier P. and Marcotte D. (2012). Short-term simulation of ground heat exchanger with an improved TRVM. *Renewable Energy* **46**: 92-99.

Pasten C. and Santamarina J. C. (2014). Thermally induced long-term displacement of thermoactive piles. *Journal of Geotechnical and Geoenvironmental Engineering* **140**(5): 06014003.

Pérez-Lombard L., Ortiz J. and Pout C. (2003). A review on buildings energy comsuption information. *Energy and Buildings* **40**(3): 394-398.

Peron H., Hueckel T., Laloui L. and Hu L. B. (2009). Fundamentals of desiccation cracking of fine-grained soils: experimental characterisation and mechanisms identification. *Canadian Geotechnical Journal* **46**(10): 1177-1201.

Philippe M., Bernier M. and Marchio D. (2009). Validity ranges of three analytical solutions to heat transfer in the vicinity of single boreholes. *Geothermics* **38**(4): 407-413.

Potts D. M. and Zdravkovic L. (2001). Finite element analysis in geotechnical engineering: application. Thomas Telford Ltd, London.

Poulos H. G. and Hull T. S. (1989). Role of the analytical geomechanics in foundation engineering. Foundation Engineering Conference. F. H. Kulhawy. Evanston, Illinois, USA**:** 1578-1606.

Randolph M. F. and Wroth C. P. (1978). Analysis of deformation of vertically loaded piles. *Journal of the Geotechnical Engineering Division* **104**(GT12): 1465-1488.

Reese L. C., Cox R. W. and Koop F. D. (1974). Analysis of laterally loaded piles in sand. OTC conference. Dallas, Texas**:** N° OTC 2080.

Rehau (2012). Tunnel Energy Lining, Turning infrastructures into energy sources.

Remund C. P. (1999). Borehole thermal resistance: laboratory and field studies. *ASHRAE Transactions* **105**(1): 439-445.

Renner J. and Messar M. (2006). Periodic pumping tests. *Geophysical Journal International* **167**: 479-493.

Rybach L. and Eugster W. J. (2010). Sustainability aspects of geothermal heat pump operation, with experience from Switzerland. *Geothermics* **39**(4): 365-369.

Sangseom J., Hyunsung L., Joon K. L. and Junghwan K. (2014). Thermally induced mechanical response of energy piles in axially loaded pile groups. *Applied Thermal Engineering* **71**: 608-615.

Sanner B. (2001). Shallow geothermal energy. *Geo-Heat Center (GHC) bulletin*.

Sanner B., Karytsas C., Mendrinos D. and Rybach L. (2003). Current status of ground source heat pumps and underground thermal energy storage in Europe. *Geothermics* **32**(4-6): 579-588.

Sass I. and Lehr C. (2011). Improvements on the thermal response test evaluation applying the cylinder source theory. Thirty-sixth Workshop on Geothermal Reservoir Engineering, Stanford University, Stanford, California.

Schaap M. G., Leij F. J. and Van Genuchten M. T. (2001). Rosetta: A computer program for estimating soil hydraulic parameters with hierarchical pedotransfer functions. *Journal of Hydrology* **251**: 163-176.

Scott R. F. (1964). Heat exchange at the ground surface,

Seed H. B. and Reese L. C. (1957). The action of soft clay along friction piles. *Transactions of the American Society of Civil Engineering* **122**: 731-754.

Shahrour I. and Rezaie F. (1997). An elastoplastic constitutive relation for the soil-structure interface under cyclic loading. *Computers and Geotechnics* **21**(1): 21-39.

Shannon W. L. and Wells W. A. (1947). Tests for thermal diffusivity of granular materials. Proceedings of the American Society for Testing and Materials.

Stewart M. A. and McCartney J. S. (2014). Centrifuge modeling of soil-structure interaction in energy foundations. *Journal of Geotechnical and Geoenvironmental Engineering* **140**(4): 04013044-04013041-04013011.

Suryatriyastuti M. E., Mroueh H., Burlon S. and Habert J. (2013). Numerical analysis of the bearing capacitiy in thermo-active piles under cyclic axial loading. Energy geostructures: Innovation in Underground Engineering. L. Laloui and A. Di Donna. Hoboken, ISTE Ltd. and John Wiley and Sons**:** 139-154.

Suryatriyastuti M. E., Mroueh H. and Burlon S. (2014). A load transfer approach for studying the cyclic behavior of thermo-active piles. *Computer and Geotechnics* **55**: 378-391.

van Genuchten M. T. (1980). A closed-form equation for predicting the hydraulic conductivity of unsaturated soils. *Soil Science Society of America Journal* **44**(5): 892-898.

Vuataz F. D., Bossy F., Colliard B. and Wilhelm J. (2005). Estimation of the geothermal potential of the Fribourg canton (in French), Canton de Fribroug, Direction de l'économie et de l'emploi, Service des transports et de l'énergie, Section énergie.

Vuataz F. D., Affolter M., Matthey B., Peguiron E., Robert-charrue C. and Wilhelm J. (2008). Estimation of the geothermal potential of the Neuchatel canton (in French), Centre de REchecher en GEothermie (CREGE).

Wilhelm J., Bianchetti G. and Sierre F. D. (2003). Estimation of the geothermal potential of the Vaud canton (in French), Etat de Vaud, Departement de la sécurité et de l'environnement, Service de l'environnement et de l'énergie, Division de l'énergie. 46'094/86'175.

Williams G. P. and Gold L. W. (1976). Ground Temperatures. *Canadian Building Digest* **180**.

Wolfe L. M. and Thieme J. O. (1964). Physical and thermal properties of frozen soils and ice. *Journal of the Society of Petroleum Engineers*(March): 67-72.

Yavari N., Tang A. M. and Pereira J. M. (2014). Experimental study on the mechanical behaviour of a heat exchanger pile using physical modelling. *Acta Geotechnica* **9**(3): 385-398.

You S., Cheng X., Guo H. and Yao Z. (2014). In-situ Experimental Study of Heat Exchange Capacity of CFG Pile Geothermal Exchangers. *Energy and Buildings*(0).

Zeng H., Diao N. and Fang Z. (2003). Heat transfer analysis of boreholes in vertical ground heat exchangers. *International Journal of Heat and Mass Transfer* **46**(23): 4467-4481.

Zhang W. K., Yang H. X., Lu L. and Frang Z. H. (2013). The analysis on solid cylindrical heat source model of foundation pile ground heat exchangers with ground water flow. *Energy* **55**: 417-425.

Thomas Mimouni

Route de la Maladière 28
1022 Chavannes-près-Renens
Mobile : +41 (0)77 41 54 368
E-mail : thomas.mimouni@epfl.ch

27 ans
Nationalité: Française
Permis de travail : B

- **Docteur en Géotechnique**
- **Ingénieur hydraulicien**
- **Anglais courant**

Expérience professionnelle

2011-2014 — **Assistant-doctorant en géotechnique (3.5 ans)** — LMS, EPFL Lausanne, Suisse

Caractérisation thermomécanique des géostructures énergétiques (Dir. Prof. L. Laloui)

- **Conception** et **gestion** d'un site expérimental échelle 1:1 au Swiss Tech Convention Center de l'EPFL (budget 300'000 frs)
- **Développement** de tests expérimentaux uniques sur un groupe de pieux
- **Elaboration** d'un test *in situ* pour la mesure de paramètres thermiques du sol
- **Développement** et **commercialisation** du logiciel Thermo-Pile
- **Rédaction** de documents pour lever des fonds (EPFL : 300'000 frs, OFEN : 20'000 frs)

2007-2010 — **Coordinateur sécurité (3 ans)** — ISS Sécurité Grenoble, France

Coordination de la sécurité sur le secteur nord du stade des Alpes

- **Gestion** du plus grand secteur du stade
- **Supervision** d'une trentaine de collaborateurs répartis en 4 équipes

Formation

2011-2014 — **Docteur ès sciences en géotechnique** — LMS, EPFL Lausanne, Suisse

2008-2010 — **Ingénieur en Hydraulique, Ouvrages et Environnement** — ENSE³, INP Grenoble, France

2007-2008 — **Bachelor en Sciences de l'Ingénieur** — ENSE³, INP Grenoble, France

2005-2007 — **Classes Préparatoires aux Grandes Ecoles** — Lycée P. de Fermat Toulouse, France

Projets

2011 — **Assistant de recherche (2 mois)** — LMS, EPFL Lausanne, Suisse

Développement d'un logiciel de dimensionnement pour les pieux énergétiques

- **Développement** du logiciel Thermo-Pile
- **Mise à jour** de la documentation utilisateur

2010-2011 — **Assistant de recherche (7 mois)** — EFLUM, EPFL Lausanne, Suisse

Analyse adimensionnelle et prédiction de la profondeur de la couche limite atmosphérique basée sur le bilan d'énergie à la surface de la Terre (Dir. Prof. M. Parlange)

- **Traitement de données** provenant de campagnes de mesures internationales
- **Analyse** adimensionnelle des groupes de données

2010 — **Thèse de master (8 mois)**

Décroissance de la turbulence convective et stratification de l'humidité au-dessus d'une

région agricole (Dir. Dr. D. Nadeau)

- **Traitement de données** provenant de capteurs météorologiques
- **Analyse** de la décroissance de la turbulence convective
- **Analyse** du comportement de l'humidité au-dessus d'une zone agricole

EFLUM, EPFL
Lausanne, Suisse

2009 **Stage « ingénieur » (3 mois)**

Etude du flux atmosphérique au travers d'un environnement construit
(Dir. Dr. D. Nadeau)

EFLUM, EPFL
Lausanne, Suisse

- **Reconstruction** du campus de l'EPFL (Gambit) et simulation avec Ansys Fluent
- **Evaluation** de différents modèles (RANS, URANS, LES)
- **Détermination** de l'emplacement optimal d'une petite éolienne sur le campus

Compétences

Langues

- **Français** : langue maternelle
- **Anglais** : Courant (niveau C2)

Technique

- **Analyses** aux éléments finis de géostructures
- **Expert** pour les revues scientifiques Geothermics et Acta Geotechnica
- **Développement** et optimisation de protocoles expérimentaux
- **Dimensionnement** des capteurs géothermiques : formation continue *geoth14* de la Société Suisse de Géothermie
- **Surveillance** d'ouvrages d'art
- **Relations** client, **vente** et **support technique**
- **Acquisition** de matériel, commandes, **gestion** de budget

Informatique

- Suite Microsoft Office, Suite Adobe
- Développement **Java** (IDE NetBeans)
- Notions de **Fortran** et **C/C++**
- Logiciels de dimensionnement: **EED**, **PileSim**, **Thermo-Pile**
- Codes éléments finis géotechniques: **Plaxis**, *Lagamine*
- CFD : Gambit + **Ansys Fluent**
- Autres : **Matlab**, **Hec-Ras**, **Grass GIS**

Centres d'intérêts

Sports & voyages

- **Football américain** : joueur **international** français jusqu'en 2011, **champion d'Europe** junior 2006 / **coach et joueur** au club lausannois depuis 2011
- **Alpinisme** : autonome dans les courses F/PD – **Escalade** : Falaise, grandes voies, autonome jusqu'en AD
- **Nouvelle-Zélande** : tour des deux îles et treks en autonomie (Abel Tasman Coastal track, Keppler track et Tongariro Northern Circuit)

Publications / Conférences

Articles de Journaux

- **T. Mimouni** and L. Laloui (2014). Towards a secure basis for the design of geothermal piles, Acta Geotechnica 9(3), p. 355-366.
- **T. Mimouni**, F. Dupray and L. Laloui (2013). Estimating the geothermal potential of heat exchanger anchors on a cut-and-cover tunnel, Geothermics 51, p. 380-387.
- **T. Mimouni**, L. Lei and L. Laloui (2014). Estimating the soil thermal diffusivity with interference analyses, Acta Geotechnica, DOI: 10.1007/s11440-014-0325-0.
- **T. Mimouni** and L. Laloui (soumis). Behaviour of a group of energy piles, Canadian Geotechnical Journal.

Articles de conférences

- L. Laloui, **T. Mimouni** and F. Dupray. Advances in the analysis of thermo-active foundations, International symposium on Coupled Phenomena in Environmental Geotechnics, Torino, Italy, July 1-3, 2013.
- L. Laloui, **T. Mimouni** and F. Dupray. Advances in thermo-active foundations and underground structures, European Geothermal Congress, Pisa, Italy, June 3-7, 2013.

Chapitres de Livres

- **T. Mimouni** and L. Laloui. Full-scale in situ testing of energy piles, in Energy Geostructures: Innovation in Underground Engineering, L. Laloui and A. Di Donna (Eds.), Hoboken, ISTE Ltd. Wiley and Sons, p. 23-42, 2013.
- F. Dupray, **T. Mimouni** and L. Laloui. Alternative uses of heat exchanger geostructures, in Energy Geostructures: Innovation in Underground Engineering, L. Laloui and A. Di Donna (Eds.), Hoboken, ISTE Ltd. Wiley and Sons, p. 119-137, 2013.
- **T. Mimouni** and L. Laloui. Thermo-Pile: a numerical tool for the design of energy piles, in Energy Geostructures: Innovation in Underground Engineering, L. Laloui and A. Di Donna (Eds.), Hoboken, ISTE Ltd. Wiley and Sons, p. 265-278, 2013.

Rapports

- **T. Mimouni**, F. Dupray, S. Minon and L. Laloui (2013). Heat Exchanger Anchors for Thermo-active Tunnels, Swiss Association of Road and Transportation Experts.

Conférences

- **T. Mimouni**, A. Di Donna, F. Dupray and L. Laloui. When foundations heat and cool the buildings (in French), Meeting of the Club Ravel, Lausanne, Switzerland, February 5, 2013.
- **T. Mimouni**, F. Dupray and L. Laloui. Geotechnical aspects of heat production through foundation structures, Fall Meeting of the Swiss Society for Soils and Rocks Mechanics, Bienna, Switzerland, November 7, 2013.
- **T. Mimouni**, F. Dupray and L. Laloui. On using tunnel anchors and bolts as heat exchangers with the ground, International Workshop on Geomechanics and Energy, Lausanne, Switzerland, November 26-28, 2013.
- **T. Mimouni** and L. Laloui. Pieux géothermiques, test au Swiss Tech Convention Center, Swiss Tech Convention Center, EPFL, Lausanne, Switzerland, May 7, 2014.